



**UNIVERSITY OF TM
KWAZULU-NATAL**

**INYUVESI
YAKWAZULU-NATALI**

**THE DESIGN AND ANALYSIS OF A NOVEL 5 DEGREE OF
FREEDOM PARALLEL KINEMATIC MANIPULATOR**

**Submitted by: Mr. Wesley Emile Dharmalingum (BScEng, UKZN) –
209516218**

Supervisor:

Dr. Jared Padayachee

Co-Supervisor:

Prof. Glen Bright

November 2019

Submitted in the fulfilment of the academic requirements for the degree of
Master of Science in Engineering at the School of Mechanical Engineering,
University of KwaZulu-Natal.

DECLARATION 1: SUBMISSION

As the candidate's supervisor, I agree to the submission of this dissertation.

Supervisor:  _____ Date: 29 June 2020
Dr. Jared Padayachee

As the candidate's co-supervisor, I agree to the submission of this dissertation.

Co-supervisor:  _____ Date: 01 July 2020
Prof. Glen Bright

DECLARATION 2: PLAGIARISM

I, Wesley Emile Dharmalingum, declare that,

- i. The research reported in this dissertation, except where otherwise indicated, is my original research.
- ii. This dissertation has not been submitted for any degree or examination at any other university.
- iii. This dissertation does not contain other persons' data, pictures, graphs or other information, unless specifically acknowledged as being sourced from other persons.
- iv. This dissertation does not contain other persons' writing, unless specifically acknowledged as being sourced from other researchers. Where other written sources have been quoted, then:
 - a. Their words have been re-written but the general information attributed to them has been referenced;
 - b. Where their exact words have been used, then their writing has been placed in italics and inside quotation marks, and referenced.
- v. This dissertation does not contain text, graphics or tables copied and pasted from the Internet, unless specifically acknowledged, and the source being detailed in the dissertation and in the References sections.

Signed:  _____ Date: 29 June 2020

DECLARATION 3: PUBLICATIONS

Details of contribution to peer-reviewed publications that include research presented in this dissertation. The undersigned agree that the following submissions were published and submitted as described and that the content therein is contained in this research.

Publication 1 (Published): International Conference on Competitive Manufacturing 2019 (COMA'19)

W. Dharmalingum, J. Padayachee and G. Bright, "The Design of a 5 Degree of Freedom Parallel Kinematic Manipulator for Machining Applications", in proceedings of the 2019 International Conference on Competitive Manufacturing (COMA'19), 2019, pp 227-233 (7 pages).

The paper was published and presented on 30 January 2019 in Stellenbosch, South Africa.

Wesley Dharmalingum was the lead author of this paper and conducted all research and experimentation under the supervision of Doctor Jared Padayachee and Professor Glen Bright.

Publication 2 (Submitted): South African Journal of Industrial Engineering (SAJIE)

W. Dharmalingum, J. Padayachee and G. Bright, "Synthesis of a Novel 5 Degree of Freedom Parallel Kinematic Manipulator", in the South African Journal of Industrial Engineering (SAJIE), vol. TBD, pp. TBD (16 Pages).

The paper was submitted on 25 June 2020.

Wesley Dharmalingum was the lead author of this paper and conducted all research and experimentation under the supervision of Doctor Jared Padayachee and Professor Glen Bright.

Signed: _____


Date: _____
29 June 2020

ACKNOWLEDGEMENTS

I thank my Lord and Saviour Jesus Christ for the wisdom, knowledge, understanding, strength and perseverance to complete this research. I also take this opportunity to appreciate my mum, sister and brother for all the love, support, strength and sacrifices that were made for me. Your efforts have been a tremendous help to me beyond what words can describe. I would also like to thank Chanelle Maduray for all her inspiration and encouragement.

Special gratitude goes to my supervisor Dr. Padayachee for all the conversations, support, inspiration and motivation and the belief in me. I thank you for all the advice and guidance given to me regarding my studies and beyond the scope of my studies. I also thank my co-supervisor Prof. Glen Bright for the guidance, assistance and support during my research.

I thank the Mechanical Engineering workshop staff for the assistance during my research and all the work performed in the fabrication of components. I would like to appreciate Mrs. Kogie Naicker, Ms. Nashlene Bedasee and Ms. Wendy Janssens for the administrative support and assistance received.

I acknowledge my postgraduate colleagues and friends for all the motivation, encouragement, advice, insights and assistance that you have given to me in various ways through this research. I appreciate it. The conversations we shared were priceless.

I acknowledge the University of KwaZulu-Natal for the Reino Stegen scholarship and National Research Foundation (NRF) for the financial aid received. The running expenses of the project was covered by the NRF THUTHUKA FUNDING INSTRUMENT TTK170421228180.

ABSTRACT

To remain internationally competitive, local manufacturers require technologically competitive equipment and need to produce reasonably priced goods to the South African market. South Africa has faced economic challenges such as the growing rate of inflation and higher interest rates. The manufacturing sector needs upliftment. A review of Parallel Kinematic Manipulators (PKMs) was performed to establish a research gap. Research showed that affordable PKMs for industrial applications do not exist. These platforms have the potential to be adopted by small to medium size companies to aid the manufacturing sector in South Africa.

The concept of using parallel kinematic robotic platforms for machining tasks has received attention in recent years. This research included the synthesis of a novel 5 Degree of Freedom (DOF) PKM for the validation of machining, part handling, sorting and general positioning applications. The PKM possessed a parasitic rotation. The PKM was designed in SolidWorks® and a desktop prototype was produced through Additive Manufacturing (AM). A novel inverse kinematic analysis was developed which is an extension of the geometric method. All kinematic calculations were tested and validated through MATLAB®. The inverse and forward kinematic simulations produced high accuracy results, with most errors attributed to rounding off errors. The workspace of the robot was solved through the extension of the inverse kinematic analysis. Point clouds were generated and a triangulation algorithm wrapped a surface around the point cloud to determine volume. Five different types of workspaces were investigated.

Testing and experimentation conducted on the prototype validated the design, kinematic analyses, electronic and software system. An Optical Computer Mouse (OCM) was used as a low-cost displacement sensor. A resolution of 0.2 mm/pixel was realised through the tests conducted on the OCM. The linear actuators were produced through AM and tests showed an accuracy and repeatability of approximately 0.2 mm. The tests validated its performance and its use in the accuracy and repeatability testing of the PKM. The inverse kinematic testing was conducted to determine the accuracy and repeatability of the PKM. The accuracy and repeatability values were approximately 2 mm and 2° for position and rotation respectively. The inverse kinematic tests validated the potential for machining, part handling and sorting applications. Payload testing showed that the PKM lifted a maximum payload of 25.23 kg before failure occurred. This illustrated the high payload advantage that PKMs possess over serial robotic platforms.

The PKM displayed anisotropic motion characteristics. The accuracy and repeatability were pose-dependent which indicated that the platform possessed anisotropic mechanical strength in its workspace. The weight distribution of the PKM was not uniform due to its architectural layout. This indicated anisotropic inertial properties and therefore reaffirmed anisotropic mechanical strength. The results from testing and experimentation validated the potential use for machining, part handling, sorting and general positioning applications. This research is beneficial to manufacturers requiring robotic platforms for multiple tasks and to the robotics research community.

TABLE OF CONTENTS

DECLARATION 1: SUBMISSION	i
DECLARATION 2: PLAGIARISM	i
DECLARATION 3: PUBLICATIONS	ii
Publication 1 (Published): International Conference on Competitive Manufacturing 2019 (COMA'19)	ii
Publication 2 (Submitted): South African Journal of Industrial Engineering (SAJIE)	ii
ACKNOWLEDGEMENTS	iii
ABSTRACT	iv
LIST OF ACRONYMS AND ABBREVIATIONS	xii
NOMENCLATURE	xiii
LIST OF FIGURES	xv
LIST OF TABLES	xviii
1. INTRODUCTION	1
1.1 Project Background and Motivation	1
1.2 Existing Research and Research Gap	3
1.3 Research Aim and Objectives	3
1.4 Methodology	4
1.5 The Scientific Contribution of Dissertation	4
1.6 Overview of Dissertation	4
1.7 Chapter Summary	5
2. LITERATURE REVIEW	6
2.1 Current Manufacturing Challenges and Trends	6
2.2 Machine Architectures	7
2.2.1 Serial Kinematic Architectures	7
2.2.2 Parallel Kinematic Architectures	9
2.2.3 Comparative Analysis of Serial and Parallel Architectures	11
2.2.4 Hybrid Architectures	12
2.3 Review of Parallel Kinematic Architectures	13
2.3.1 Two DOF Systems	13
2.3.2 Three DOF Systems	15
2.3.3 Four DOF Systems	16

2.3.4	Five DOF Systems.....	17
2.3.5	Six DOF Systems	20
2.3.6	Specifications of 5-DOF and 6-DOF PKMs.....	23
2.4	Chapter Summary	23
3.	CONCEPT GENERATION AND SELECTION	25
3.1	Introduction.....	25
3.2	Machine Synthesis	25
3.2.1	Joint Selection and Limb Topology.....	26
3.2.2	Architectural Selection, DOFs and Dedicated Motors per Limb.....	28
3.2.3	Configuration of Joints on the End Effector and Base	29
3.2.4	The Direction of the Applied Force of the Actuators and z-axis.....	29
3.2.5	Machine Synthesis Insights	30
3.3	Description of the architecture	30
3.3.1	Manipulator Structure.....	30
3.3.2	Machine Novelties and Characteristics	32
3.4	Quality Function Deployment.....	33
3.4.1	Relationship between Customer Requirements and Engineering Metrics	34
3.4.2	Relationship between Engineering Metrics	34
3.4.3	Importance Ratings, Relative Weight and Difficulty of Target.....	34
3.4.4	Target Specifications	35
3.4.5	Competitive Analysis	36
3.5	Chapter Summary	37
4.	MECHANICAL DESIGN	38
4.1	Mechanical Design Methodology	38
4.2	System Decomposition Diagram.....	39
4.3	Design for Additive Manufacturing	39
4.3.1	Material Selection.....	39
4.3.2	Material Wastage, Manufacturing Time and Clearances.....	40
4.3.3	Linear Actuator.....	40
4.3.4	Revolute Joints	41
4.3.7	End Effector and Base	42

4.3.8	Mounting Brackets and Spacing Blocks.....	42
4.3.9	Spacing Blocks.....	43
4.4	PKM Specifications	43
4.5	Sub-assembly Precedence Diagrams.....	44
4.6	Assembly Precedence Diagram.....	47
4.7	Chapter Summary	48
5.	KINEMATIC ANALYSIS	49
5.1	Introduction.....	49
5.2	Homogenous Transformation Matrix.....	49
5.3	Inverse Kinematics.....	49
5.3.1	Extension of the Geometric Method.....	50
5.3.2	Inverse Kinematic Relationships through the Outer Vector Loop Method	51
5.3.3	Inverse Kinematic Relationships through the Inner Vector Loop Method	52
5.3.4	Inverse Kinematic Simulink Model.....	57
5.4	Forward Kinematics	59
5.4.1	Newton Raphson Method	60
5.4.2	Derivation of the Constraint Equations	60
5.5	Chapter Summary	63
6.	SINGULARITY AND WORKSPACE ANALYSIS.....	64
6.1	Introduction.....	64
6.2	Singularity Analysis.....	64
6.2.1	Types of Singularities.....	64
6.2.2	Singularities of the 2R(Pa-IQ)RR, R(Pa-IQ)R PKM.....	66
6.3	Workspace Analysis.....	67
6.3.1	Methods of Workspace Calculation	68
6.3.2	Constant Orientation (Translational) Workspace	70
6.3.3	Alpha Rotation and Translational Workspace	72
6.3.4	Beta Rotation and Translational Workspace	73
6.3.5	Maximal Workspace Excluding Parasitic Motion	75
6.3.6	Inclusive Orientation Workspace	76
6.3.7	Constant Orientation Workspace Height Investigation	77

6.4	Chapter Summary	79
7.	ELECTRONIC AND SOFTWARE SYSTEM	80
7.1	Introduction	80
7.2	Flow Diagram of System	80
7.3	Description of Selected Components	80
7.3.1	Motor Selection	80
7.3.2	Stepper Motor Drivers	81
7.3.3	Microcontroller Board Layout and Selection	81
7.3.4	Power Supply	82
7.3.5	Sensor Selection	82
7.4	Wiring Diagrams	83
7.5	Control Box	85
7.6	Software System	85
7.7	Chapter Summary	87
8.	SYSTEM PERFORMANCE AND TESTING	88
8.1	Introduction	88
8.2	Testing System	88
8.2.1	Translation Testing System	88
8.2.2	Rotation Testing System	89
8.3	Method of Calibration	90
8.4	Linear Actuator Accuracy and Repeatability	90
8.4.1	Aim	90
8.4.2	Apparatus	90
8.4.3	Methodology	90
8.4.4	Results	91
8.4.5	Analysis	93
8.4.6	Conclusion	93
8.5	Inverse Kinematic Analysis Simulations	93
8.5.1	Aim	93
8.5.2	Apparatus	93
8.5.3	Methodology	93

8.5.4	Results	94
8.5.5	Analysis	95
8.5.6	Conclusion.....	95
8.6	PKM Accuracy and Repeatability	95
8.6.1	Aim.....	95
8.6.2	Apparatus	95
8.6.3	Methodology	95
8.6.4	Results	98
8.6.5	Analysis	102
8.6.6	Conclusion.....	103
8.7	Payload Testing.....	104
8.7.1	Aim.....	104
8.7.2	Apparatus	104
8.7.3	Methodology	104
8.7.4	Results	105
8.7.5	Analysis.....	106
8.7.6	Conclusion.....	107
8.8	Forward Kinematic Simulations for Repeatability – MATLAB® and SolidWorks®	107
8.8.1	Aim.....	107
8.8.2	Apparatus	107
8.8.3	Methodology	107
8.8.4	Results	107
8.8.5	Analysis.....	107
8.8.6	Conclusion.....	108
8.9	Forward Kinematic Simulations – Guess Deviations Analysis.....	108
8.9.1	Aim.....	108
8.9.2	Apparatus	108
8.9.3	Methodology	108
8.9.4	Results	108
8.9.5	Analysis.....	111
8.9.6	Conclusion.....	112

8.10	Chapter Summary	112
9.	DISCUSSION	114
9.1	Chapter Introduction	114
9.2	Concept Overview, Justification and Literature	114
9.3	Synthesis and Design of a Novel PKM	116
9.4	Singularity and Workspace Analysis	118
9.5	Physical Testing and Performance	119
9.5.1	Inverse Kinematics	119
9.5.2	Forward Kinematics	121
9.6	Implications of the Research	122
9.7	Chapter Summary	123
10.	CONCLUSION	124
10.1	Introduction	124
10.2	Research Contribution.....	124
10.3	Insights of the Novel PKM	124
10.4	Limitations of the Research.....	125
10.5	Recommendations	125
10.6	Future Work	125
10.7	Chapter Summary	126
	REFERENCES	127
	APPENDICES	139
	Appendix A – Testing Results.....	139
	A.1 Linear Actuator Accuracy and Repeatability	139
	A.2 Inverse Kinematic Simulations – MATLAB® and SolidWorks®.....	142
	A.3 PKM Accuracy and Repeatability	149
	A.4 Payload Tests	151
	A.5 Forward Kinematic Simulations – MATLAB® and SolidWorks®.....	152
	A.6 Forward Kinematic Simulations – Guess Deviations Analysis.....	165
	A.7 Mouse Resolution	168
	Appendix B – Code from Software	182
	B.1 Inverse Kinematics: MATLAB® Code.....	182

B.2 Inverse Kinematics: Arduino Code	193
B.3 Forward kinematics MATLAB® Code	195
B.4 Workspace MATLAB® Code.....	203
Appendix C – Calculations	205
C.1. Power Screw Analysis.....	205
C.2. Steps per Linear Movement	205
C.3. Buckling Analysis	206
C.4. Rotated CD Vector Analysis	207
Appendix D – Quality Function Deployment	212
Appendix E – Project Costs	216
Appendix F – Linear Actuator Concepts.....	217
F.1 Concept 1: Aluminium Sheet Concept	217
F.2 Concept 2: Additive Manufactured Bracket Concept	217
F.3 Concept 3: Additive Manufactured Casing with Guides and Slots.....	218
F.4 Linear Actuator Pugh Selection Matrix	218
Appendix G – PKM DOFs	219
G.1 Alpha Rotation	219
G.2 Beta Rotation	219
G.3 Parasitic Gamma Rotation.....	221
G.4 Translation along x, y and z Axes	222
Appendix H – Engineering Drawings	223

LIST OF ACRONYMS AND ABBREVIATIONS

2D:	Two-Dimensional
3D:	Three-Dimensional
ABS:	Acrylonitrile Butadiene Styrene
AM:	Additive Manufacturing
BRIC:	Brazil, Russia, India, China
BRICS:	Brazil, Russia, India, China, South Africa
CAD:	Computer-Aided Design
CNC:	Computer Numerical Control
CR:	Control Resolution
DH:	Denavit-Hartenberg
DOF:	Degree of Freedom
GDP:	Gross Domestic Product
IDE:	Integral Development Environment
IoT:	Internet of Things
IQ:	Irregular Quadrilateral
NR:	Newton Raphson
OCM:	Optical Computer Mouse
Pa:	Parallelogram
PCD:	Pitch Circle Diameter
PID:	Proportional-Integral-Derivative
PKM:	Parallel Kinematic Manipulator
PLA:	Polylactic Acid
PMT:	Parallel Machine Tool
PWM:	Pulse Width Modulation
QFD:	Quality Function Deployment

NOMENCLATURE

Latin alphabet

A	Area
AP	Position accuracy
d	Diameter
d_c	Collar diameter
d_m	Mean diameter
d_p	Pitch diameter
E	Young's Modulus of Elasticity
f	Friction coefficient between the lead screw and nut
f_c	Friction coefficient for the collar of the power screw system
I	Area moment of inertia
$J_{\alpha \text{ and } \tau}$	Jacobian matrix for isolated alpha rotation with translation
K	Effective-length factor
\bar{l}	Mean value with respect to deviations between the j^{th} reached positions
L	Length
m	Gradient
M_t	Torque
p	Pitch
P_{cr}	Critical load
r	Radius of gyration
RP	Positional repeatability
S_l	Standard deviation of l
W	Load
\bar{x}	Mean of x values
x_c	Commanded x position

Greek alphabet

α	Euler angle describing rotation about the x-axis
α_n	Thread angle divided by 2
β	Euler angle describing rotation about the y-axis
γ	Euler angle describing rotation about the z-axis
Δ	Change
η	Efficiency
λ	Intermediate angle in the CD vector calculations
ξ	Intermediate angle in the CD vector calculations
ρ	Scaling factor matrix
σ_{cr}	Critical stress
ς	Perspective transformation matrix
Σ	Sum
ψ	Angle to determine the final value of the components of the CD vectors

LIST OF FIGURES

Figure 1-1: Index of industrial production for BRICS countries [2]	1
Figure 1-2: South African Manufacturing Statistics [6]	2
Figure 1-3: Industry growth rates for the first quarter of 2019 [7]	2
Figure 2-1: Depiction of the industrial revolutions [22].....	6
Figure 2-2: The three levels required to form a CPS [22]	7
Figure 2-3: A serial robot developed by FANUC corporation of Japan [26]	8
Figure 2-4: Stiffness testing of a serial robot [13].	8
Figure 2-5: Different architectural designs of PKMs [8, 35].	9
Figure 2-6: Desktop 3 DOF parallel kinematic milling machine [39]	10
Figure 2-7: The Quickstep machining centre and the kinematic structure of the manipulator [8].....	11
Figure 2-8: The hybrid Tricept-type PKMs [8]	12
Figure 2-9: Architectural design of the Exechon [48]	13
Figure 2-10: Examples of 2-DOF PKMs [50, 51]	14
Figure 2-11: Examples of 3-DOF PKMs [57, 62]	16
Figure 2-12: Examples of 4-DOF PKMs [8, 76]	17
Figure 2-13: Examples of 5-DOF PKMs [84, 88, 90, 91].	19
Figure 2-14: Examples of 6-DOF PKMs [40, 95, 96]	21
Figure 2-15: Commercialised 6-DOF PKMs [11, 40]	22
Figure 3-1: PKM synthesis [40]	25
Figure 3-2: The different types of joints [35]	26
Figure 3-3: An example of a universal joint and a parallelogram joint.	26
Figure 3-4: The branched-chain used by Qui et al [89].	27
Figure 3-5: The actuated parallelogram joint.....	27
Figure 3-6: The spatial 3-DOF PKM designed by Liu and Kim [60]......	29
Figure 3-7: Base and end effector mounting points.....	29
Figure 3-8: Geometric layout of the PKM.....	31
Figure 3-9: Machine Topology	31
Figure 4-1: Mechanical design process for a PKM [37].....	38
Figure 4-2: Mechanical system decomposition diagram	39
Figure 4-3: Linear actuator concept 4.....	40
Figure 4-4: Revolute joints	41
Figure 4-5: The end effector	42
Figure 4-6: Mounting brackets and spacing block.....	43
Figure 4-7: Thrust bearing sub-assembly diagram	44
Figure 4-8: Linear Actuator sub-assembly diagram	44
Figure 4-9: PKM sub-assembly diagram	45
Figure 4-10: XY mouse sub-assembly diagram.....	46
Figure 4-11: Testing frame for translation sub-assembly diagram	46
Figure 4-12: Testing frame for rotation sub-assembly diagram.....	47

Figure 4-13: Project assembly diagram	47
Figure 5-1: General vector diagram with the top view of the PKM	50
Figure 5-2: Outer vector loop	51
Figure 5-3: Two different views illustrating the coplanar nature of a pair of legs.....	52
Figure 5-4: Inner vector loop for leg 1 and leg 2	53
Figure 5-5: One of the cases of the x and z components of vector CD being altered	55
Figure 5-6: Simulink model for the inverse kinematics.....	57
Figure 5-7: A close-up typical calculation using various blocks	59
Figure 5-8: A graphical representation of the execution of the NR method	60
Figure 5-9: The location of theta 1 and theta 5	61
Figure 6-1: Mechanical resistance of a mechanism without the use of force or torque.....	65
Figure 6-2: Loss of a DOF for a serial robot wrist [129]	65
Figure 6-3: Sudden uncontrollable movement of the end effector and the gaining of a DOF[129]	66
Figure 6-4: An example of a workspace boundary singularity	66
Figure 6-5: Singularity poses in which unpredictable motion could occur under certain conditions	67
Figure 6-6: An example of a point cloud, surface wrap and point cloud distribution.....	69
Figure 6-7: Flow chart for searching for the robot workspace	70
Figure 6-8: Results of the translation workspace analysis	71
Figure 6-9: Workspace results that was obtained by Xialong et al. [90].	72
Figure 6-10: Alpha rotation and translational workspace	73
Figure 6-11: Beta rotation and translational workspace	74
Figure 6-12: A physically impossible pose.....	75
Figure 6-13: Maximal workspace of the PKM	76
Figure 6-14: Inclusive orientation workspace for angles ranging from 8° up to and including 10°	77
Figure 6-15: The xy view of the workspace at different heights for constant orientation	78
Figure 6-16: Isometric view of slices of the constant orientation workspace at different heights	79
Figure 7-1: Flow Diagram of Electronic Hardware	80
Figure 7-2: The TB6560 stepper motor driver.....	81
Figure 7-3: Schematic Diagram of the Arduino Mega [145].....	82
Figure 7-4: Mean Well S-320-24.....	82
Figure 7-5: The optical mouse sensor selected	83
Figure 7-6: Wiring diagram of the electronic system	84
Figure 7-7: Close-up wiring diagram of a stepper motor to a TB6560 Stepper motor driver [152]	84
Figure 7-8: The SolidWorks® model and fully assembled control box	85
Figure 7-9: The integration of the electronic and software system with the prototype.....	86
Figure 7-10: A typical Simulink model that can be used communicate with an Arduino board	87
Figure 8-1: Testing system designs for translation and rotation	89
Figure 8-2: Mouse and end effector attachments.....	89
Figure 8-3 Calibration of an actuator.....	90
Figure 8-4: Calibration of the digital depth gauge Vernier Calliper	91

Figure 8-5: Set-up and measurement of actuator lengths	91
Figure 8-6: Graph of standard deviation versus actuation length	92
Figure 8-7: The region of testing points. The regions are equally spaced along the y-axis.....	94
Figure 8-8: Testing the translational motion of the end effector.	96
Figure 8-9: Measuring the angle of tilt for an alpha rotation.	97
Figure 8-10: The PKM performing a positive alpha rotation.	97
Figure 8-11: The tilt bias of the end effector when the mirror was placed on the end effector.	97
Figure 8-12: SolidWorks confirmation of no PKM movement when all actuators are locked.....	98
Figure 8-13: Translational Accuracy and Repeatability vs. Y Displacement.	100
Figure 8-14: Alpha Rotation Accuracy and Repeatability vs. Alpha Angle.....	101
Figure 8-15: Alpha Rotation Accuracy and Repeatability vs. Y Displacement.....	101
Figure 8-16: Beta Rotation Accuracy and Repeatability vs. Beta Angle.....	102
Figure 8-17: Beta Rotation Accuracy and Repeatability vs. Y Displacement	102
Figure 8-18: Mass validation of calibrated weights.....	104
Figure 8-19: Graph of Mass vs. Leg Actuation Error	105
Figure 8-20: The PKM lifting various weights vertically by 50.42 mm.....	105
Figure 8-21: Failed components after lifting a 25.23 kg load.....	106
Figure 8-22: The weakest point of the PKM where the failure occurred.....	106
Figure 8-23: Translation Guess Deviation vs. Number of Iterations for position.....	109
Figure 8-24: Translation Guess Deviation vs. Number of Iterations for angular values	109
Figure 8-25: Guess deviation results for alpha rotation with translation – position	110
Figure 8-26: Guess deviation results for alpha rotation with translation - angles.....	110
Figure 8-27: Guess deviation results for beta rotation with translation – position	111
Figure 8-28: Guess deviation results for beta rotation with translation - angles.....	111

LIST OF TABLES

Table 2-1: Comparison between serial and parallel kinematics.....	11
Table 2-2: Specifications of a sample of PKMs	23
Table 3-1: The different classes of parallel kinematic manipulators	28
Table 3-2: Differences between the novel architecture and the Hexapod.....	33
Table 3-3: Target Specifications.....	35
Table 4-1: Comparison between ABS and PLA	40
Table 4-2: PKM specifications	44
Table 4-3: Thrust bearing sub-assembly description and bill of materials	44
Table 4-4: Linear actuator sub-assembly description and bill of materials	45
Table 4-5: PKM sub-assembly description and bill of materials	45
Table 4-6: XY mouse optical sensor sub-assembly description and bill of materials	46
Table 4-7: Testing frame for translation sub-assembly description and bill of materials	46
Table 4-8: Testing frame for rotation sub-assembly description and bill of materials	47
Table 4-9: Project assembly description and bill of materials	47
Table 5-1: The 13 different cases of inverse kinematic solutions.....	56
Table 5-2: Description of Simulink function blocks used	57
Table 6-1: Summary of the workspace boundaries for constant orientation.....	70
Table 6-2: PKM constraints for alpha rotation	72
Table 6-3: Limits for the beta workspace analysis	73
Table 7-1: Determining the wire pairs for the stepper motors	81
Table 8-1: Accuracy and repeatability of actuator 1 to 6.....	92
Table 8-2: Regions for sampling testing points	94
Table 8-3: Accuracy results for translational motion.....	99
Table 8-4: Repeatability results for translational motion.....	100
Table 8-5: Summary of leg actuation errors as a function of load.....	105

1. INTRODUCTION

1.1 Project Background and Motivation

In light of the growing competition from emerging markets of Europe and Asia, South Africa needs to implement strategies to uplift its manufacturing sector. Local manufacturers are required to remain technologically competitive. The manufacturing industry has experienced economic challenges through recent years, which include the growing inflation rate, weaker Rand and higher interest rates. These pose as inhibitors to small and medium-size local manufactures to overcome start-up costs. Manufacturing equipment needs to possess the required functionality and be affordable to remain competitive and manufacture goods of equivalent quality as global manufacturers.

The five major emerging countries are Brazil, Russia, India, China and South Africa (BRICS). The BRICS countries make up 42% of the world's population, 23% Gross Domestic Product (GDP) and 18% of the trade globally. Brazil, Russia, India and China (BRIC) was renamed as BRICS when South Africa joined the BRIC group in 2011. Some of the countries within the BRICS group's cooperation areas include economic and financial cooperation, Health and Science, Technology and Innovation [1]. The BRICS Joint Statistical Publication [2] showed that South Africa's industrial progress had not increased significantly since 2014. Figure 1-1 shows the graph of the index of industrial production in comparison to other countries.

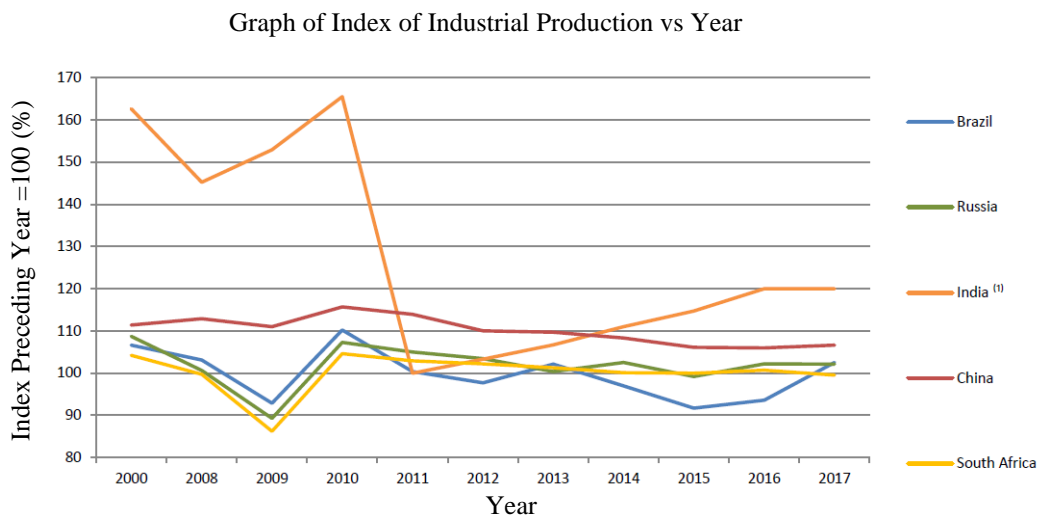


Figure 1-1: Index of industrial production for BRICS countries [2]

Research on the global manufacturing market predicts China, India and Southeast Asia regions to be the fastest-growing regions forecast up to 2023 [3]. A report on global robotics forecasted that the robotics industry would continue to grow up to 2022. There are no notable African competitors in the global robotics space [4]. The report on global Computer Numerically Controlled (CNC) machine tools displays the same trend whereby African competitors fail to feature [5]. According to Stats SA [6], the manufacturing sector was on the rise for 2018 and increased by 1.2% after the contraction of 0.5% in 2017. Figure 1-2 depicts the manufacturing trends of the South African Manufacturing sector. Stats SA [7] also revealed that the South African economy has struggled in the first three months of 2019, indicated by a drop in 3.2%, shown in Figure 1-3. The manufacturing, mining and trade were the sectors that struggled the most.

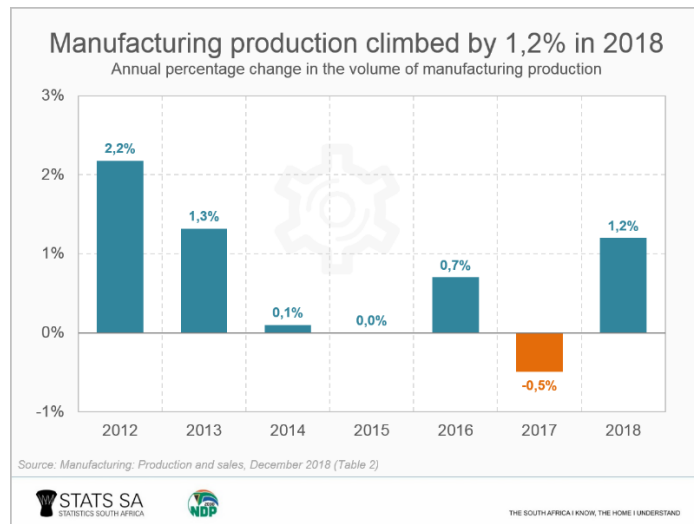


Figure 1-2: South African Manufacturing Statistics [6]

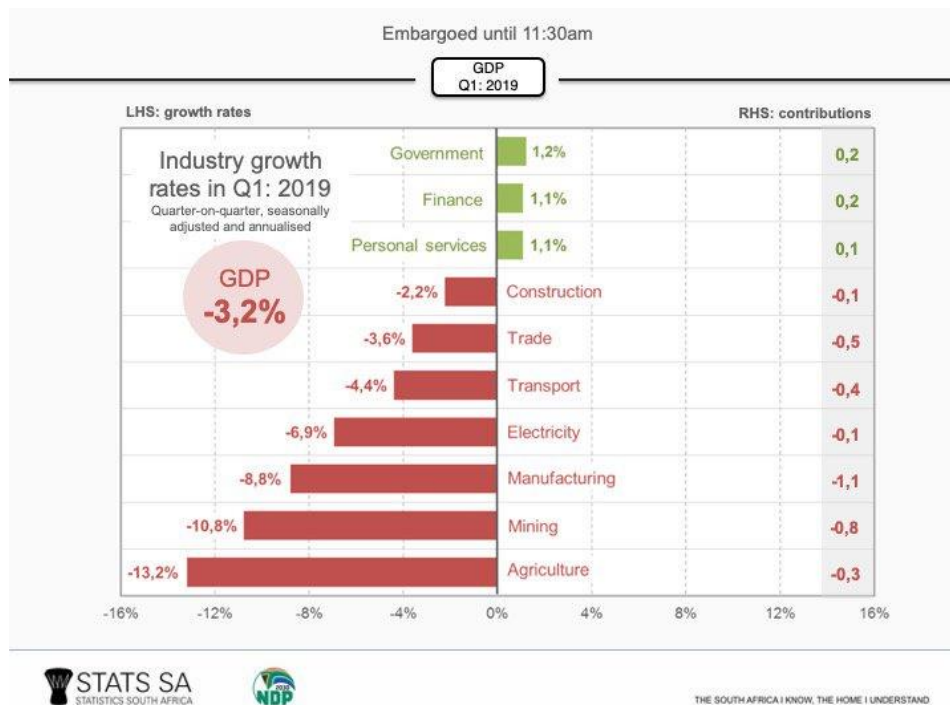


Figure 1-3: Industry growth rates for the first quarter of 2019 [7]

Robotic platforms have been adopted to assist in manufacturing tasks to lower lead times and produce high quality goods. These platforms aid the economy. Importing manufacturing equipment, coupled with their large costs and the cost of starting up a manufacturing plant, inhibits the start-up of small and medium-size local manufacturers. Cost-effective robotic platforms can assist current and potential small and medium-size local manufacturers to aid the economy. Pandilov and Dukovski [8] documented the variety of tasks that serial robots and Parallel Kinematic Manipulators (PKMs) can accomplish. Serial robots can perform welding, palletising, assembly line applications, packaging and part handling. PKMs can be employed for fine positioning, pick and place applications, machining, motion platforms and surgical applications [8-11].

A PKM is a robotic platform with two or more closed-loop kinematic chains. Each kinematic chain connects to a common base and end effector. PKMs possess high mechanical rigidity, the ability for fine positioning of the end effector, high payload to weight ratio and there is non-cumulative error propagation. The drawbacks of PKMs are a relatively small workspace, complex kinematic analyses and sophisticated calibration methods [10, 12]. Serial robots possess an open-loop kinematic chain. They possess a large workspace, high workspace to robot size ratio and simple forward kinematic analysis. However, they suffer from joint error propagation, relatively low mechanical stiffness and are susceptible to vibrations [13, 14]. Each type of robotic platform has its own merits and drawbacks. This research proposed the concept of using a novel PKM to validate positioning, machining, part handling and sorting applications. Industrial companies could adopt a large-scale version of the PKM.

1.2 Existing Research and Research Gap

PKMs have received growing attention in past decades and their high payload to weight ratio has been attractive to researchers [8]. The concept of robot machining originated in the early 1990s to accomplish CNC machine-type tasks [15]. CNC machines perform machining applications in the automotive and aerospace industries. They are capable of machining with high precision. However, the drawbacks of these machines are that they are large, heavy and expensive [16, 17]. Affordable industrial robots for machining applications are currently not realised in the industry.

In comparison to CNC machines, industrial robots possess a low capital investment and the flexibility to be applied to various applications [18]. The flexibility and reusability of robotic systems make them a viable alternative for various tasks [14]. Robotic systems possess a better workspace to installation space ratio than CNC machines [8]. According to Brüning et al. [18] and Karim and Verli [17], industrial robots have high economic potential for machining applications in the automotive and aerospace industries.

There is a research gap in the development of affordable robotic manufacturing systems to assist small to medium size companies to enter the South African market. The proposed robotic system served to validate part handling, sorting, general positioning and robotic machining applications. A large-scale, more robust architecture could perform these tasks as industrial applications. Some of the industries that could benefit from this research are the automotive, mining and aerospace industries. Research suggests that a PKM can be developed to suit specific user workspace requirements, therefore, reducing costs and eliminating unused machine functionality [19]. This research explored different joint combinations to achieve a higher range of rotation. These joint combinations could provide additional stiffness and tighter machine tolerances.

The novel 5 Degree of Freedom (DOF) PKM explored the exclusive use of revolute and prismatic joints. A desktop prototype was produced through Additive Manufacturing (AM) and was tested as a proof-of-concept. The inverse kinematic analysis was solved which aided in the forward kinematics, singularity and workspace analyses.

1.3 Research Aim and Objectives

Aim

This research aimed to design and investigate a novel 5-DOF parallel kinematic robotic system that can be used to validate machining, part handling, sorting and general positioning applications.

Project Objectives

1. Research and establish insights in parallel kinematic robotic systems.
2. Synthesise a novel PKM that possesses 5 DOFs through an established methodology.
3. Research, develop and simulate the kinematic models for the robotic platform.
4. Research and simulate the workspace and identify singularities.
5. Research, design and construct a desktop prototype.
6. Research, design and implement a suitable electronic system to automate the mechanical platform.
7. Research and develop experiments and methods of data collection to verify the performance of different types of movements that validate the application in machining, part handling, sorting and general positioning tasks.

1.4 Methodology

The research conducted followed the steps listed below:

- Perform research on parallel kinematic robotic systems.
- Research various types of PKMs and establish directions for machine synthesis.
- Perform the mechanical design concurrently with the design for workspace and kinematic modelling.
- Identify the physical limitations of the machine to establish its workspace and singularities.
- Construct a desktop prototype through additive manufacturing.
- Research, design and implement a suitable electronic and software system.
- Research, design, plan and execute a series of experiments and tests that verify the kinematic models and payload characteristics.
- Report on the findings of this research in an MSc. dissertation and in conference and journal publications.

1.5 The Scientific Contribution of Dissertation

This research study made the following contributions:

- i. A novel 5-DOF PKM with a higher range of rotation than most 5-DOF and 6-DOF PKMs.
- ii. A novel inverse kinematic model also used to develop the forward kinematic equations and perform the workspace analyses.
- iii. An Optical Computer Mouse (OCM) used as a low-cost position sensor and its implementation.
- iv. Insights on the kinematics, workspace and isotropic characteristics of the robotic platform.

Research Question: Can a novel PKM be developed for 3 translational and 2 rotational DOFs to validate part handling, sorting, general positioning and robotic machining capabilities?

1.6 Overview of Dissertation

Chapter 1: Introduces the reader to the background of this research, motivation for the study, the resulting scientific contributions, and methodology. This chapter also presented the aim and objectives.

Chapter 2: Presents the comparison between serial and parallel kinematic manipulators and a review on PKMs. A critical reflection of the literature is presented.

Chapter 3: Documents the concept generation of the PKM and a Quality Function Deployment (QFD) analysis.

Chapter 4: Presents the design methodology and mechanical design of the robotic platform.

Chapter 5: Presents the inverse and forward kinematic analyses.

Chapter 6: Presents the singularities and the workspace analyses.

Chapter 7: This chapter discusses the selection of electronic components and software systems.

Chapter 8: Presents the system performance and testing of the PKM under different conditions of motion.

Chapter 9: This chapter discusses the design and performance of the PKM, considering the aim and objectives.

Chapter 10: Concludes the dissertation with key insights, limitations, recommendations and future work.

1.7 Chapter Summary

This chapter introduced the reader to the manufacturing challenges faced by South Africa. This chapter also presented the motivation for this research, a background to robotic platforms and a research gap. The aim and objectives of this research and the contribution of the study were presented. The methodology was presented before an overview of the dissertation was presented. The next chapter presents the literature review of the study. Manufacturing challenges and trends are discussed. The relevance of this research is placed within the context of Industry 4.0. A review of different DOF PKMs is presented and insights are discussed regarding their novelties, merits, challenges and applications.

2. LITERATURE REVIEW

2.1 Current Manufacturing Challenges and Trends

Industry 4.0 is defined as follows: “a collective term for technologies and concepts of value chain organisation which draws together Cyber-Physical Systems, the Internet of Things (IoT), and the Internet of Services” [20]. The objective of Industry 4.0 is to, therefore, drive fundamental improvements to industrial processes centred on manufacturing facilities, engineering, material handling and supply chain and life cycle management. The aim is to create a “Smart Factory” through the collaboration between the IoT and Cyber-Physical Systems [21]. Figure 2-1 shows the evolution of the various industrial revolutions.

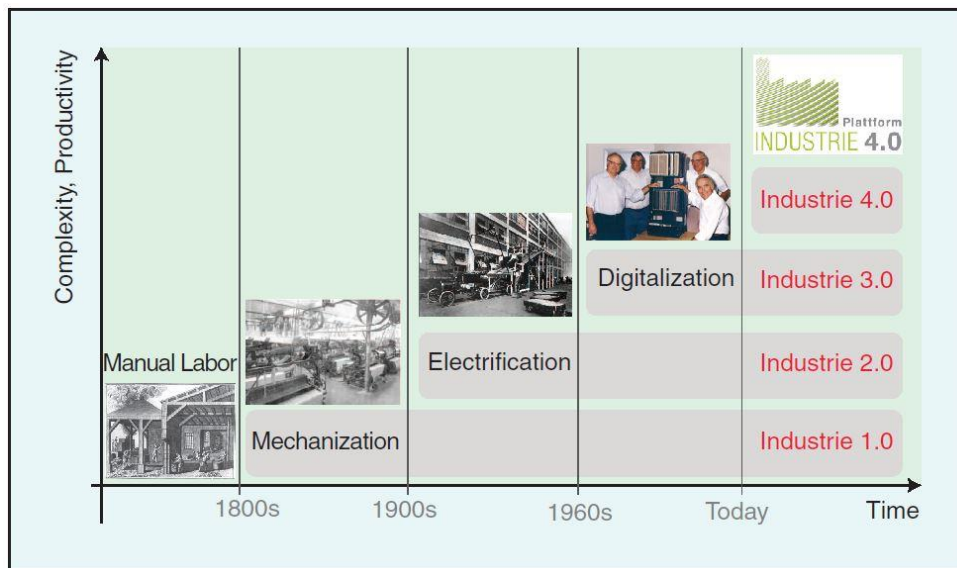


Figure 2-1: Depiction of the industrial revolutions [22]

The IoT encapsulates the following necessities: flexibility, adaptability, the efficiency of people and processes, quicker response time to decision making, customization, integration of business partners and value processes concerning cyber-physical systems [23]. The IoT mainly focusses on the inter-networking of devices and machines. These, in turn, must possess communication capability. As the rate of communication and information exchange increases, this directly improves efficiencies in a manufacturing environment.

Cyber-Physical Systems makes use of advanced technologies that manage interconnected systems, which are its physical assets and computational capabilities [24]. These interconnected systems are a family of software, sensors, machines, workpieces, other physical objects and the communication system which monitors physical processes, creates a virtual reality and can make decentralised decisions in order to exhibit intelligent behaviour. This intelligent behaviour is meant to occur whilst machines communicate with each other, humans and a centralized communication system [20].

Figure 2-2 depicts the three levels that are required for a Cyber-Physical System to exist. The physical objects can store documents and knowledge about themselves on a network, which could be a cloud-based network. This information can be updated and augmented in order to create another identity for them on the network as data objects. The data objects are searchable and can be explored and analysed. The data objects form a knowledge base for different applications. Algorithms make use of this knowledge base and optimize the autonomy and

intelligent behaviour exhibited by the physical objects. Through these algorithms and the availability of bulk information, services that were previously not possible can now be developed [22].

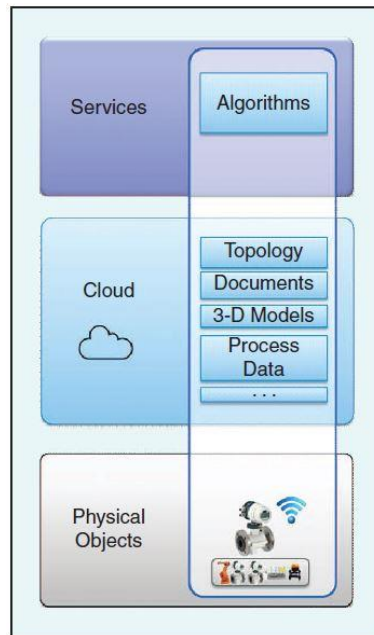


Figure 2-2: The three levels required to form a CPS [22]

The emergence of Industry 4.0 demands that manufacturing industries incorporate new technologies and methodologies in order to stay competitive. Through the exploitation of internet capabilities and embedded systems, countries like Germany have already started adopting this paradigm [20, 22]. The adoption of the paradigm has the potential of creating a variety of new products and market share will soon be gained by those that possess the best technological competitiveness. South Africa cannot neglect to adapt to this change or it risks falling further behind in manufacturing competitiveness.

Robotic platforms can provide the needed flexibility for manufacturing and assembly lines and whilst innovation can lead to more cost-effective robotic platform solutions to address the needs of the South African manufacturing sector. Manufacturing environments can use serial, parallel and hybrid robotic platforms with the serial architecture currently the most widely adopted [8]. This research provides a novel robotic platform to validate industrial applications. Interconnected systems can be implemented to further develop the PKM into an Industry 4.0 applicable robotic system.

2.2 Machine Architectures

2.2.1 Serial Kinematic Architectures

The serial robot is an open-loop kinematic chain characterized by links connected in series through one type or different types of joints [25]. A serial robot has a fixed base and an end effector attached to the last link in the chain. The type of end effector employed is dependent on the application. Serial manipulators have an industrial presence, especially in factories. Some applications include handling of radioactive elements, automotive assembly lines, space exploration, welding and palletizing [25] [8].

The advantages of the serial manipulator are its large workspace to installation ratio, simple calibration, easy forward kinematic analysis and modelling and solving its dynamics characteristics is relatively simple [8]. Drawbacks of the serial architecture include propagation of joint errors, low stiffness, high inertia, low payload to weight ratio and low speed and acceleration [8]. Figure 2-3 depicts a serial robot developed by FANUC corporation of Japan [26].



Figure 2-3: A serial robot developed by FANUC corporation of Japan [26]

In light of extending the functionality of serial robots, researchers have explored overcoming its low stiffness and complex programming characteristics. The serial robot has a high workspace to installation space ratio. Wang et al. [13] developed a feed-forward compensation scheme to compensate for robot deformation induced by machining forces. The machine stiffness was improved and produced a better surface finish to a milled aluminium block. Figure 2-4 depicts the serial robot used for the investigation. Karim and Verl [17] and Chen and Dong [15] surveyed recent advancements in using serial robots in high stiffness applications with a focus on trajectory planning, vibration/chatter analysis, advanced and flexible programming and the optimisation of mechanical stiffness.



Figure 2-4: Stiffness testing of a serial robot [13].

Schneider et al. [14] researched and developed a position control system for a serial robot for machining using an optical measurement system. Schneider et al. [27] proceeded to combine advanced programming and simulation

to create an ideal path for the robot under machining forces. Domroes et al. [28] developed a flexible programming concept, which enabled the robot to mill water pump impellers autonomously. The flexible programming concept enabled this to occur along a dynamically adapted path. This innovation enhanced the quality of robotic machined components and improved productivity. Kubela et al. [29] proposed an online controller to compensate for accuracy errors in KUKA serial robots due to backlash from drive reversion. The concept of an online controller was validated and improved the system with almost no additional cost.

Klimchik et al. [30] analysed the modelling of manipulator stiffness and estimation of the cutting force. The method was used to rank the performance of available industrial robots concerning several machining tasks. Research conducted by Dumas et al. [31] evaluated the joint stiffness values for translational and rotational displacements of the robot's end effector for a specified force and torque. The research aimed to optimize machining operations and assist in motion planning. Zargarbashi et al. [32] researched posture optimization through the development of a performance index. The performance index evaluated the torque of the actuators and the joint rates in accomplishing a specified robot posture during machining. A study performed by Lin et al. [33] examined the posture optimization of industrial robots in order to reduce machining errors. Researchers agree that the mechanical properties of serial robots limit the accuracy and efficiency achievable for high stiffness applications such as robotic machining applications [13, 15, 27, 28, 30, 33, 34].

2.2.2 Parallel Kinematic Architectures

A PKM is a mechanism that possesses at least two independent closed-loop kinematic chains. Each closed-loop kinematic chain is attached to a fixed platform (base) and an end effector [35]. PKMs find its niche in automated manufacturing systems, motion simulators, surveillance, positioning, machining and pick and place applications [8]. PKMs can either move spatially or be restricted to move along a plane permitting rotation about the axis normal to the plane. Figure 2-5 (a) shows a spatial 6-DOF PKM for fine positioning applications possessing 3 translational and 3 rotational DOFs. Figure 2-5 (b) depicts a planar PKM with revolute joints [35].

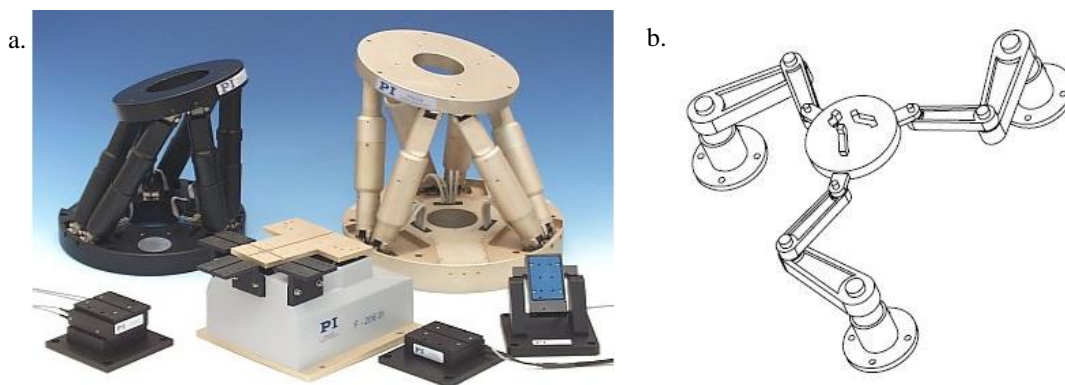


Figure 2-5: Different architectural designs of PKMs [8, 35].

- a. PKMs used for fine positioning applications [8].
- b. The 3RRR PKM with planar motion capabilities [35].

PKM architectures reduce the effect of cumulative joint positioning errors by averaging errors, thus providing high accuracy and repeatability. Other advantages are high speed and acceleration, low inertia of moving masses for certain architectural types and a relatively high payload to weight ratio [36]. PKMs possess a limited range of

motion and small workspace for a relatively high number of actuators. Since the joints are interdependent, mathematical modelling becomes complex concerning the forward kinematic analysis [36]. Calibration can also be complicated [8]. For these reasons, parallel and serial manipulators find relevance in different types of applications although not limited to those applications.

There have been successful PKMs that have been adopted by industry which includes the Stewart-Gough Platform developed by Dr. Eric Gough [37]. Its initial application was for testing the properties of tyres under different loads [37]. Flight simulators also use the Stewart-Gough Platform. The Delta robot was developed by Clavel [38] which used the concept of parallelograms in its architecture; Bosch GmbH commercialised this robot for the packaging industry [8]. The flex-picker was developed and commercialised by ABB. The Delta robot provided a basis for the design of the flex-picker [38]. The flex-picker performed rapid pick and place applications.

Concerning machining applications, a significant study was the free leg hexapod by researchers such as Olarra et al. [19] for miniature machining applications. The different foot configurations altered the workspace, which was aided by machine programming. This allowed the optimization of foot configurations for the intended application. Glavonjic et al. [39] performed research, design and construction of a desktop 3-axis parallel kinematic milling machine. The PKM was an educational desktop model. The PKM machined soft material and the concept was proven. The machine, however, could not be commercialised. Figure 2-6 illustrates the prototype.



Figure 2-6: Desktop 3 DOF parallel kinematic milling machine [39]

The Okuma's Cosmo Centre PM600 and the FANUC F-200iB are commercially available platforms. The Cosmo Centre PM600 performs machining applications and the FANUC F-200iB can accomplish positioning and machining tasks [8, 40, 41]. These platforms are described further in Section 2.3. Metrom Mechatronische Maschinen GmbH and Krause and Mauser have also produced milling machining centres which are large [8, 42]. The Quickstep, developed by Krause and Mauser, is shown in Figure 2-7 [8].

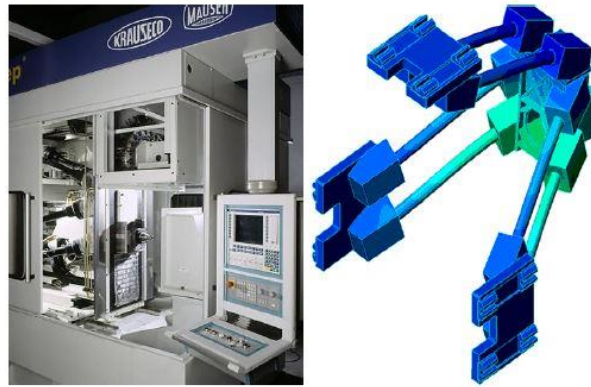


Figure 2-7: The Quickstep machining centre and the kinematic structure of the manipulator [8]

2.2.3 Comparative Analysis of Serial and Parallel Architectures

Table 2-1 depicts a comparative analysis between serial and parallel kinematic manipulators [8].

Table 2-1: Comparison between serial and parallel kinematics

Feature	Serial Kinematic Manipulator	Parallel Kinematic Manipulator
Workspace	Large	Small
Solving the forward kinematics	Easy	Difficult
Solving the inverse kinematics	Difficult	Easy
Position error	Accumulates	Averages
Force error	Averages	Accumulates
Maximum force	Minimum actuator force limits the maximum force	All actuator forces summed together
Stiffness	Low	High
Dynamics characteristics	Poor. Worsens with increased size	High
Modelling and solving dynamics	Relatively simple	Complex
Inertia	High	Low
Payload to weight ratio	Low	High
Speed and acceleration	Low	High
Accuracy	Low	High
Calibration	Simple	Complex
Workspace to robot size ratio	High	Low

2.2.4 Hybrid Architectures

Open and closed-loop kinematic chains characterize hybrid architectures. These mechanisms may be connected in series, known as a conventional hybrid structure, or in parallel, known as a cooperative structure. There are 3 types of conventional hybrid structures: parallel-parallel type, serial-parallel type or parallel-serial type [43]. Hybrid architectures find their niche in machining applications such as metal cutting, polishing, woodworking and spot welding. Hybrid mechanisms are also capable of holding a laser and saw cutting tools. Automobile and aerospace manufacturers make use of this type of machine architecture for component assembling, welding, fabrication of turbine blades, impellers, high-speed milling and other items that require contouring [8, 44].

The hybrid manipulator was designed and developed by Karl-Erik Neumann in 1987. Figure 2-8 (a) depicts the patent known as the Tricept robot. Neos Robotics, Inc commercialised it. It possessed 3 degrees of freedom (2 rotational and 1 translational degree). The initial obstacle for the design was that the computational power required for intended functionality was unavailable. Comau Pico produced the first multiprocessor controller and overcame the challenge of computational power. The controller and open architecture made it possible to process the complex kinematics exhibited by this mechanism. The hybrid architecture performed machining applications. Figure 2-8 (b) depicts the Tricept 805. It combines the flexibility from serial robots and the stiffness of a parallel robotic system [8].

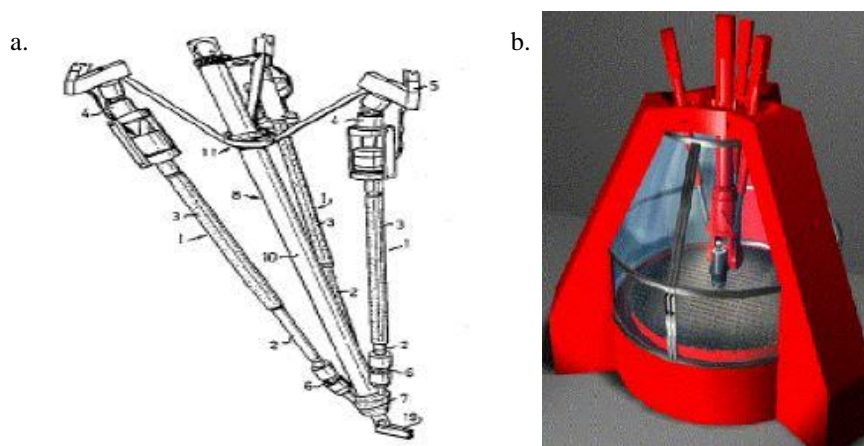


Figure 2-8: The hybrid Tricept-type PKMs [8]

- a. The patented design of the Tricept by Karl-Erik Neumann comprised of a parallel architecture with a serial architecture end effector [8].
- b. The Tricept 805 comprised of a parallel architecture with a serial architecture end effector [8].

In 2002, ABB and SMT Tricept launched the IRB 940. The IRB 940 performed heavy-duty cleaning and pre-machining of aluminium parts [8]. The Trivariant hybrid structure was commercialised and formed part of the HSC milling centre. Like the Tricept, the Trivariant possesses 5 DOFs [44, 45]. The Exechon machining centre is a hybrid architecture with 5 DOFs. It has an over-constrained kinematic structure with eight links and nine joints [46, 47]. It has excellent potential in drilling applications with high flexibility. Siemens [48] developed the controller for the system. Figure 2-9 displays the Exechon.

Dörries Scharmann Technologie GmbH developed the ECOSPEED and ECOLINER machining centres which incorporate the Sprint Z3 tool head. The tool head is a parallel kinematic tool head that can move in translationally

in one direction and tilt in all directions. The serial component is incorporated through a planar cross slide. This hybrid machining centre finds its applications in high-speed machining of large aluminium structural components. In the aerospace automotive and tool and die industry, it is useful in the production of small to medium size components [40]. The VERNE Machine was developed by Fatronik for IRCCyN. It consists of a parallel module which provides the translational movement. A tilting worktable imparts rotation about two orthogonal axes, thus classified as hybrid architecture. It machined complex parts especially in the moulding industry [49]. The TriCenter machine was based on the kinematics of the Tricept and aimed to improve rigidity. Its architecture was similar to the Tricept whereby it possessed a 3-DOF parallel manipulator with a 2 axis serial milling head [40].



Figure 2-9: Architectural design of the Exechon [48]

Hybrid architectures, therefore, seek to retain the large workspace and high dexterity of serial manipulators and high payload to weight ratio and high stiffness of PKMs while minimizing the disadvantages of both [43]. Despite the advantages of hybrid kinematic systems, there is no systematic method that enables the design of a hybrid kinematic system without having to perform a separate synthesis for each of the mechanisms that would be attached. This drawback was examined by Campos et al. [43] but the method presented does not use computer algorithms, which may result in chain isomorphisms. According to Harib et al. [46], a comprehensive study and understanding of the kinematics, dynamics and design of hybrid architectures are still lacking. The investigation of an exclusive serial robot or PKM leads to more straightforward kinematic analyses and programming. The PKM architecture possesses attractive stiffness characteristics and a high payload to weight ratio is presented in Section 2.3.

2.3 Review of Parallel Kinematic Architectures

2.3.1 Two DOF Systems

Duan et al. [50] developed a 2-DOF spherical PKM. It possessed two rotational DOFs and could be used for vibration isolation, precision manipulation applications and as a 2-DOF orientation and force/torque sensor. Figure 2-10 (a) illustrates the prototype. Qu et al. [51] researched a piezo-driven 2-DOF PKM for high precision alignment applications as shown in Figure 2-10 (b). The PKM found relevance in orientation adjustment to ensure

alignment between two flat surfaces. The design used flexure-hinge based mechanisms and piezoelectric stack actuators. A resolution of 1 μ rad was achieved. Bozorgi et al. [52] performed the design, development, dynamic analysis and control for a 2-DOF spherical PKM. A robust algorithm for dynamic modelling was proposed and was validated by the end effector following the prescribed trajectory. Lagrangian and Newtonian approaches were used.

Reconfiguration analysis was performed by Kong [53] on a 2-DOF 3-4R PKM. The robotic platform was found to possess 14 different operation modes while using the minimum number of actuated joints. Yang et al. [54] proposed a modified robust control system for a 2-DOF PKM with planar translation motion. Yang et al. [54] designed the diamond-shaped PKM for high speed and high precision part handling and assembly. Experimental results validated the modified control system. The control method produced more accurate trajectories in comparison to using traditional potential difference methods. Niu et al. [55] produced a novel 2-DOF PKM with rotational DOFs. The PKM was designed with uncoupled and isotropic movements that possessed a larger workspace, simple mathematical analysis, ease of control, high stiffness and dexterity. Applications include aiming applications such as radar scanners, telescopes and cameras.

2-DOF PKMs exhibit exclusive rotation or translation of the end effector. 2-DOF PKMs are designed for a specific category of applications. The flexibility and reusability of 2-DOF PKMs are limited. 2-DOF PKMs are cost-effective are characterized by more straightforward mathematical analyses. They do, however, lack the mechanical rigidity of a PKM possessing more legs. 2-DOF PKMs have not been widely adopted by industry. High precision positional and rotational applications are well suited to 2-DOF PKMs due to the smaller workspaces. High speed planar applications can be accomplished by 2-DOF PKMs. Greater depth of analysis, regarding aspects such workspace and singularities, on 2-DOF PKMs are aided by their simpler mathematical analyses.

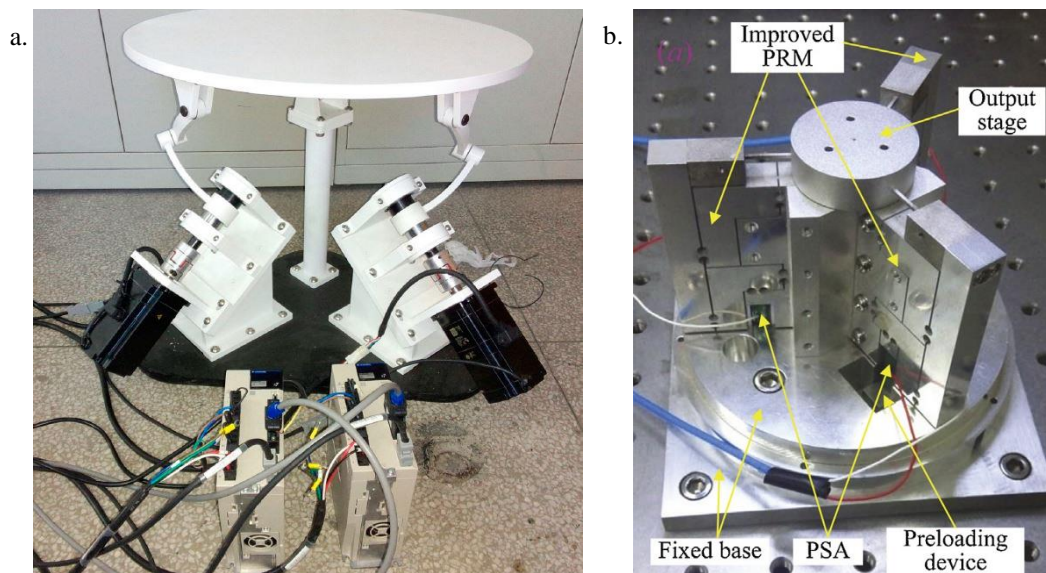


Figure 2-10: Examples of 2-DOF PKMs [50, 51]

- a. The spherical PKM developed by Duan et al. [50].
- b. The piezo-driven, high precision PKM [51].

2.3.2 Three DOF Systems

A biologically-inspired PKM, producing realistic eye movements, was developed by Bang et al. [56]. The prototype was an improvement made to the Agile Eye developed by Gosselin and Hamel in terms of encasing the PKM behind a layer of a humanoid face [56]. The PKM possessed only rotational movement of the end effector. The Agile Wrist was also derived from the Agile Eye and was altered by using cylindrical joints as investigated by Al-Widyan et al. [57]. The cylindrical joint was employed to alleviate manufacturing errors for spherical PKMs. The PKM was designed to hold and orient a tool for shot-peening applications as is illustrated in Figure 2-11 (a). A notable 3-DOF PKM, called the Orthoglide, was developed by Chablat and Wenger [58] for exclusive translational motion. The Orthoglide had the potential to be used for machining applications. Dahmouche et al. [59] further investigated the Orthoglide. The purpose of their investigation was to determine if high-speed vision-based computed torque control for dynamic control. The method was successfully employed and could be used for robots that experience flexibility and backlash.

Liu and Kim [60] proposed a novel 3-DOF spatial PKM capable of large rotations of the end effector. The PKM possessed 1 rotational and 2 translational DOFs. The footpoints were actuated and only single DOF joints were used. The PKM explored the ease of assembly and disassembly through magnetic joints. Carbonari et al. [61] designed a novel reconfigurable 3-DOF PKM. Metamorphic universal joints imparted the reconfigurability into the PKM. The end effector could achieve either pure translation or pure rotation. Singularities were shared for the different end effector motion cases and in the space of the actuation parameters. Nurahmi and Gan [62] also explored the notion of a metamorphic 3-DOF PKM which used reconfigurable revolute joints located at the base of the device. The end effector of this PKM exhibited operation modes of 3-DOF coupled rotations, 3-DOF planar motion and 1 translation with 2 rotation movement. Figure 2-11 (b) illustrates the PKM.

Ahangar et al. [63] designed a 3-DOF delta PKM with 1-DOF redundancy attached to its base. The purpose of the investigation was to save time and energy saving for pick and place applications along a conveyor. Al-Naimi et al. [64] used machine vision in the development of a pick and place PKM for industrial applications. A novel collision-free workspace method was explored for a 3-DOF delta PKM by Ataei et al. [65]. Kinetostatic indices were used to measure the performance of the PKM. The novel algorithm was successful and can be used for path planning. Other delta type PKMs were explored by various authors [66-68]. These investigations included using a system of cams with a single drive [66], kinematic sensitivity evaluation [67] and applications in endonasal surgery [68]. Arian et al. [69] investigated the dynamic characteristics of a planar 3-DOF PKM. A novel geometric approach was used to solve the inverse kinematic models. The dynamic rigid-body model developed reduced computation time by 58%.

3-DOF PKMs can exhibit 2 translation and 1 rotation, 1 translation and 2 rotations, pure translations or pure rotations. The different combinations of translational and rotational DOFs allows 3-DOF PKMs to be employed for a wider range of applications than 2-DOF PKMs. The 3-DOF class of PKM exhibits large differences in appearance due to the nature of joint combinations and architectural layout. The delta and spatial type of PKMs are most widely researched with the delta-type PKMs having an industrial presence. Sorting tasks are one of the most common industrial application of 3-DOF PKMs. Many platforms require future work before being implemented for industrial applications.

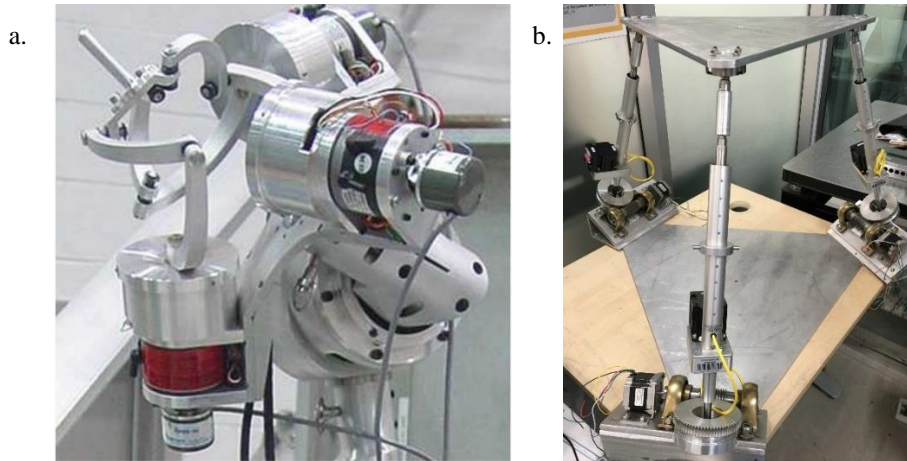


Figure 2-11: Examples of 3-DOF PKMs [57, 62]

- a. The spherical PKM developed for shot peening applications [57].
- b. The metamorphic 3-DOF PKM that was developed by Nurahmi and Gan [62].

2.3.3 Four DOF Systems

Niche applications of 4-DOF PKMs are packaging, picking, packing and palletizing tasks. Reymond Clavel investigated the use of parallelograms to create a PKM that possessed one rotational and three translational DOFs. A link directly connected from base to the end effector provides the rotational degree of freedom. His patent was known as the Delta robot. This design was useful for pick and place applications [8, 70]. SIG Pack systems (part of Bosch Packaging Technology division) and ABB Automation commercialised the Delta robot. Their products, are known as the C33/CE33 Delta robots and the IRB 340 Flex Picker Robot, are shown in Figure 2-12 (a), respectively [8].

Rasoulzadeh and Masouleh [71] investigated singularity configurations analysis using Grassman-Cayley Algebra. Kang et al. [72] investigated the kinematic modelling, analysis and load distribution algorithm of a 4-DOF PKM that was redundantly actuated. Singularity analysis was performed on a novel surgical PKM by Khalifa et al. [73]. Mohammadi et al. [74] explored the concept of kinematics concerning modelling and weighted kinematic sensitivity. Screw theory is generally used to assist when obtaining the Jacobian matrix structure [71-73].

A simulation study of a Delta robot was conducted by Azmoun et al. [75], which used a Proportional-Integral-Derivative (PID) and Sliding-Mode controller based on the inverse kinematic analysis. Akhbari et al. [76] developed a novel asymmetrical 4-DOF delta PKM for milling applications, as depicted in Figure 2-12 (b). The results showed that the asymmetric configuration and different link lengths improved the singularity avoidance and dexterity. Apostolescu and Ionaşcu [77] developed a new delta 4-DOF PKM for pick and place and stacking tasks. The PKM was able to detect new objects in its workspace and rotate objects irrespective of initial orientation. Control and vision of a 4-DOF PKM were investigated by Rouhollahi et al. [78] to improve pick and place tasks from a conveyor belt. Physical experimentation validated the use of the proposed system.

The most common topology discovered for 4-DOF parallel manipulators is the delta structure with 3 translational and 1 rotational DOFs. Some 4-DOF PKMs have been implemented industrially exclusively for pick and place applications. 4-DOF PKMs are generally larger than 2-DOF and 3-DOF PKMs hence they possess a larger

workspace. Recently, 4-DOF PKMs have been employed for AM applications. Actuation of 4-DOF PKMs are generally in the form of a rotational input thus the motors are situated on the base. The low inertia allows fast movements of the end effector but this architectural type suffers from poor mechanical rigidity. Actuation redundancy has been explored for 4-DOF PKMs which aimed to reduce singularity challenges.

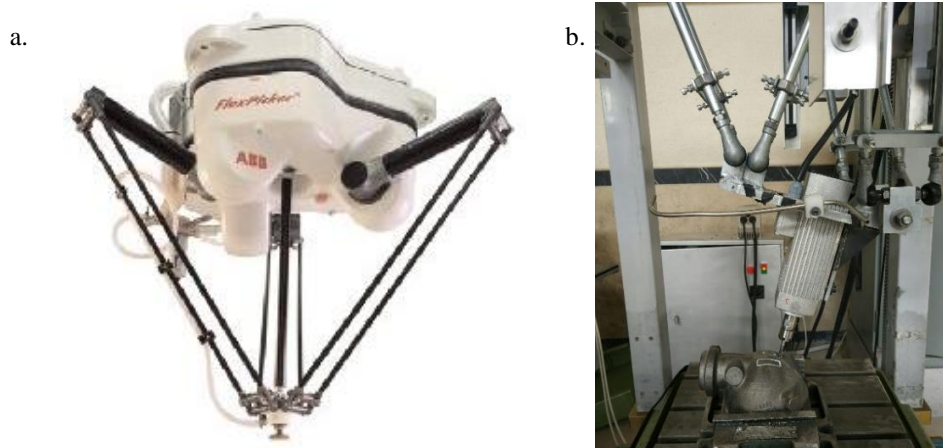


Figure 2-12: Examples of 4-DOF PKMs [8, 76]

- a. The ABB IRB 340 Flex Picker [8].
- b. The asymmetric delta robot developed by Akhbari et al [76].

2.3.4 Five DOF Systems

Early research mainly concentrated on 6-DOF hexapod type PKMs however, 6-DOF PKMs have a relatively small workspace. Some industrial applications do not require 6 DOFs. Therefore, it's beneficial to study PKMs with fewer than 6-DOFs. Advantages of PKMs that possess fewer than 6-DOFs include a more straightforward mechanical design, fewer components, thus more cost-effective, larger workspace and a simpler controller can be used. Except for the delta type architecture for 4-DOF PKMs, there are relatively few papers on 4-DOF and 5-DOF PKMs. There exist a difficulty to design 4-DOF and 5-DOF PKMs with identical limb structure [79]. Fang and Tsai [79] presented a systematic structure synthesis of a class of 4-DOF and 5-DOF PKMs that possess identical limb structure. Various joint and layout combinations were enumerated, inclusive of the number of DOFs permitted. Hairong et al. [80] used screw theory to analyse the motion screw and constraint screw of the limbs and end effector, respectively. Screw theory was used to create a synthesis procedure for the development of a symmetrical 5-DOF PKM. This method was validated through simulations done on PKMs possessing 3 rotational and 2 translational DOFs.

Li et al. [81] investigated the type synthesis of a 3 rotational and 2 translational (3R2T) 5-DOF parallel manipulator, which makes use of Lie Group of Displacements. Fourteen novel architectures are revealed for the 3R2T 5-DOF parallel manipulator. This method can be used for the enumeration of lower mobility PKMs. Fiore et al. [82] performed a dimensional synthesis of a 5-DOF parallel manipulator for AM applications. The parameters were optimized using a genetic algorithm to generate the workspace. The control system was outlined. The PKM could achieve larger movements that were not feasible with general AM machines.

Guo et al. [83] developed a ship active vibration isolation system, which was based on a novel 5-DOF PKM. PID control and force-position redundant control was employed. ADAMS®-MATLAB Simulink® simulations were

conducted to improve the control of the PKM. The dynamic model was obtained through the Lagrange method and the control system based on ship motion. A 5-DOF Parallel Machine Tool (PMT) developed by Zheng et al. [84], possessed 3 translational and 2 rotational DOFs. The PKM had 1 passive and 5 active limbs. Multi-axis simultaneous control was investigated in detail in order to control the path traced by the machine tool. Course interpolations algorithms and mapping transformations were implemented. The PKM accomplished 5-axis machining with high position accuracy and low vibrations.

Further work conducted on the PMT involved a motion control algorithm investigated by Cheng et al. [85]. A concise motion control algorithm was deduced from the Euler angles of the end effector and was developed in conjunction with the inverse kinematic solution. This algorithm was successfully applied to the PMT and results showed that the positional and repeatable errors were reduced. Figure 2-13 (a) depicts the PMT. Ersoy et al. [86] developed a 5-DOF PKM for beating heart surgery. It was designed as a lightweight PKM. The purpose of the PKM was to track the heartbeat motion during a coronary artery bypass procedure. This unique 5-DOF PKM uses two separate subsystems to position the end effector accurately. It possessed a 3-DOF remote stage and a 2-DOF fixed stage. Simulations and experimentations showed that the heartbeat motion data was tracked with a 0.66mm error.

A novel hybrid 5-DOF PKM, named the T5, was designed for machining applications by Song et al. [87], which comprised of 2 PKM subsystems in series. A flow path is presented to synthesise a PKM which was accomplished in 4 steps. The design of this PKM was patented and was intended for high precision machining applications on large-scale structural aircraft components. Screw theory was applied for the kinematic analysis and a kinematic performance index was defined. The research also presented multi-objective dimensional optimization using a nondominated sorting genetic algorithm. The T5 was further explored by Sun et al. [88]. The authors addressed the improvement of PKM geometric errors at the design stage through a design optimisation method. The research aimed to minimize vibration and deformation through an electrodynamic optimization method. The geometric errors were treated as parameter uncertainty. Figure 2-13 (b) illustrates the T5 PKM.

Qiu et al. [89] presented a method of Three-Dimensional (3D) modelling of a 5-DOF PKM possessing branched chains. The PKM possessed 2 rotational and 3 translational DOFs. Concerning the branched chain, a notable feature was the attachment of limbs to upright brackets and with the brackets themselves possessing additional joints. Xiaolong et al. [90] proposed a 5-DOF PKM with redundant actuation as is illustrated in Figure 2-13 (c). The PKM consisted of 4-SPS limbs and 2-RPS limbs. The PKM could perform 3 rotational and 2 translational movements. The PKM had 4 limbs mounted symmetrically around its base and the 2-RPS joints were located along a plane across on centre of the base. A notable feature was the restriction of one transitional DOF through the arrangement of the revolute joints.

Zhu et al. [91] investigated the limb and actuation singularities of a fully symmetrical 5-DOF PKM which could be used for simulating the motion of a spinal column. This is another 5-DOF PKM possessing 3 rotational and 2 translational DOFs. The singularity analysis was performed using screw theory and Grassmann geometry. The PKM employed revolute joints, which passively restricted a translational DOF and is depicted in Figure 2-13 (d).

Liu et al. [92] developed a 5-DOF portable machining robot named DiaRoM for the processing of large structural elements and remote maintenance on large equipment or components. The Grassmann Line Geometry and Line-

graphs were used to synthesise the design. Flexible 5-axis machining was achieved and with the ability to transform between horizontal and vertical machining modes. Huang et al [93] developed a novel 5-DOF PKM with 5 active legs and 1 passive leg. The passive leg was positioned at the center of a circular base and the PKM was designed to be symmetrical. This PKM possessed 3 rotational and 2 translational DOFs. The inverse kinematics, velocity and accelerations were validated through simulations. Metrom developed a 5-axis Pentapod machine with a unique end effector design which allowed each of the 5 actuators to be attached to it by individual revolute joints. The end effector achieved rotations of up to and including 90° . The workpiece was mounted on a rotary work table, which imparted an additional DOF to the machining centre but did not affect the PKM structure. A control strategy was implemented to take into account the movements of the rotary worktable [94].

5-DOF PKMs include numerous novel architectures and unique architectural layouts in comparison to other DOF PKMs. The most common motion type of the end effector is 3 rotational and 2 translational DOFs. There are rare instances of the PKM possessing 2 rotational and 3 translations DOFs. 5-DOF PKMs generally exist as hybrid systems and there are examples of hybrid PKMs having some but little industrial presence [8]. Many experimental 5-DOF PKMs have been developed and many have only been analysed from a computational standpoint. Many authors have not followed through with functional prototypes and the implementation of a 5-DOF pure PKM system in the industry is lacking. The category of 5-DOF PKMs has received lesser attention relative to 3-DOF, 4-DOF and 6-DOF PKMs. Most 4-DOF PKMs possess the delta structure whilst most 6-DOF PKMs are exploited for their high stiffness characteristics. 5-DOF PKMs can therefore utilise advantages of 4-DOF and 6-DOF PKMs and be positioned to improve specific applications carried out by 4-DOF and 6-DOF PKMs.

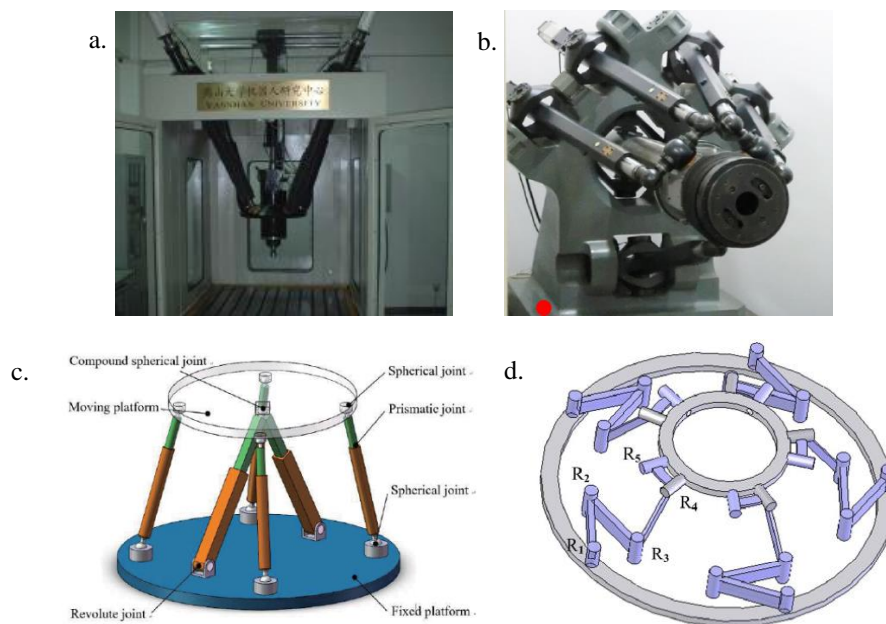


Figure 2-13: Examples of 5-DOF PKMs [84, 88, 90, 91].

- a. The PMT developed by Zheng et al. [84].
- b. The T5 PKM machining system [88].
- c. A redundant actuated 5-DOF PKM [90].
- d. The PKM designed by Zhu et al. which makes exclusive use of revolute joints [91].

2.3.5 Six DOF Systems

6-DOF PKMs possess 3 rotational and 3 translational DOFs. Since it is trivial that all DOFs are permitted for 6-DOF PKMs, research into these platforms include optimisation of PKM parameters, increasing workspace, different calibration techniques, the potential use for new applications, improving control, methods of synthesis, path planning, vibration analyses and a variety of other aspects. An early functional 6-DOF PKM was used for the tyre testing which was developed by Gough and Figure 2-14 (a) [40] illustrates the platform. These types of PKMs are referred to as “Hexapods” [40]. 6-DOF PKMs have been extensively researched and used for flight simulation, micro-positioning, machining tools, light positioning in surgical labs and other many other applications [8].

McCann and Dollar [95] developed a novel 6-PKM for grasping and dexterous spatial manipulation, as illustrated in Figure 2-14 (b). A notable advantage was that the PKM could grasp objects with minimal sensing. The PKM encountered challenges when grasping highly irregular objects. Spherical joints were used at the fingertip of the robot to conform to firmly grasping objects passively but inaccurate grasping occurred that the limits of the workspace for certain poses. Gonzalez and Asada [96] designed and developed a novel extendable PKM, called the TSE, for use in aircraft assembly applications. The PKM was designed to reach high ceilings and to possess a large workspace. The actuation of the robot’s foot points allowed a greater reach and the architectural layout could be altered to suit the intended work envelope. The prototype could reach a maximum height of 1.62 meters. Figure 2-14 (c) illustrates the TSE PKM.

Stenzel et al. [97] used a 6-DOF parallel manipulator to simulate the motion characteristics of an emergency vehicle for selected manoeuvres for obstacle avoidance. Forces were measured that act on a vehicle when driving over a speed bump or during obstacle avoidance. The PKM was found to generate undesirable vibrations of higher frequencies during testing. Becerra-Vargas et al. [98] explored a robust joint space control for a 6-DOF parallel robot. This research sought to apply a robust inverse dynamic control with the control strategy based on the Lyapunov stability theory. Simulations validated that the joint control structure overcomes the real-time implementation for the forward kinematics.

Trajectory planning was researched by Hasnaa and Mohammed [99]. The inverse kinematic model was established for a 6-DOF PKM, named HEXA. The PKM was designed with rotary actuation of the joints instead of prismatic joints and this allowed large workspaces to be achieved. The PKM was simulated in MATLAB® to trace various trajectories. The kinematic models and path tracing were successful. Beiki and Irani-Rahaghi used a nonlinear dynamic optimisation procedure for energy-efficient path planning. The energy consumption of the actuators was analysed and the accuracy error of the end effector was investigated. The optimisation tool was based on a finite element method. Simulation results based on dynamic modelling were performed in MATLAB® and planning a minimum energy consumption path validated the method employed.

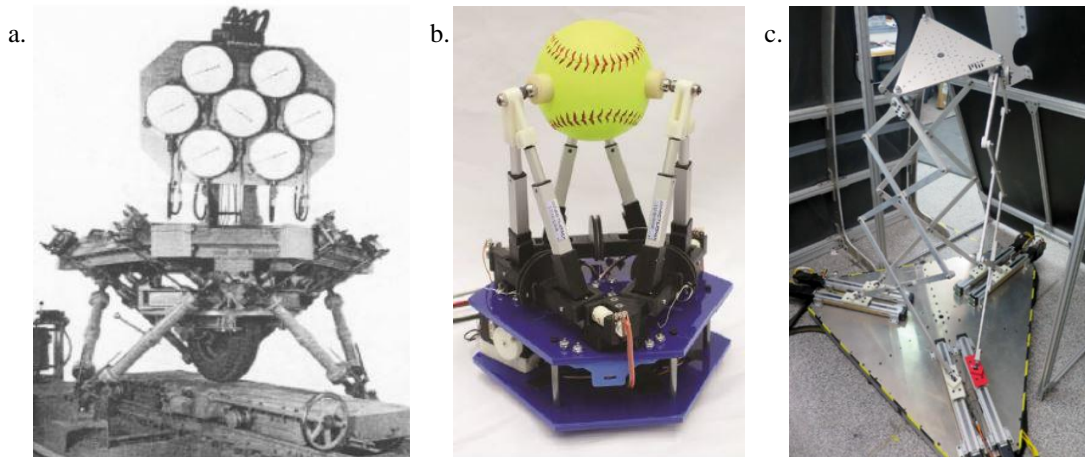


Figure 2-14: Examples of 6-DOF PKMs [40, 95, 96]

- a. The tyre testing PKM developed by Gough [40].
- b. A dexterous grasping PKM prototype [95].
- c. The TSE PKM for aircraft assembly tasks [96].

Ding et al. [100] presented a statistical approach to reducing pose errors of a 6-DOF PKM. The structure of joint clearance was analysed. The drawback encountered from this method was long computational time. Ghorbani and Omurlu [101] investigated 3 different numerical methods to solve the coupled nonlinear forward kinematic equations of a 6-DOF flight simulator PKM. The Adaptive-Network-based Fuzzy Inference System, Multilayer Perceptron and Radial Base Function and Neural Network methods were implemented. Through experimentation, the Adaptive-Network-based Fuzzy Inference System method proved to be the best of the 3 approaches. The inverse kinematics and workspace analyses were conducted on a novel 6-PSS PKM by Xu et al. [102]. The design explored the use of triangle rail trusses and sliders for the actuation of the footpoints. The largest workspace was largely influenced by one of the angles of interest. The workspace was dependent on the actuator layout angle. The feasibility was validated through SolidWorks® and MATLAB® simulations.

A novel 6-DOF PKM was designed by Harada and Angeles [103] which uses only 2 limbs but possessed kinematic and actuation redundancy. The kinematic redundancy influenced singularity and collision avoidance which generated a larger workspace. Actuation redundancy improved position accuracy. Simulations conducted on MATLAB® demonstrated that collisions were avoided successfully while the PKM maintained its prescribed position and orientation of the end effector.

The FANUC F-200iB, depicted in Figure 2-15 (a) is a successfully commercialised PKM used for welding, loading, dispensing and material removal applications. The robot has exceptional rigidity and repeatability in comparison to serial robots [8]. This robotic platform is expensive and not affordable to small and medium-size manufacturing companies [41]. Barnfather et al. [11] investigated the machining capability of the FANUC F-200iB to establish and minimise the position errors during non-cutting operations. The research was undertaken to facilitate higher tolerance machining. The errors discovered were in the micron range and were attributed mainly to the pose of the machine. The PKM could not machine to high tolerances due to static errors and systematic errors were more dominant than random errors. It was suggested that a possible solution to reduce positional errors is to perform in-situ process monitoring.

OKUMA PM 600, shown in Figure 2-15 (b), was successfully commercialised and resembles the Stewart Platform design. It was designed for machining aluminium components and dies and moulds that require less polishing. The machine could perform high-speed machining and be suitable for continuous operation. The drawback of the machine is that it is large and heavy [40]. Ibaraki et al. [104] expanded on the research of the OKUMA PM600 and performed kinematic calibration by circular tests to improve the contouring accuracy when performing circular tasks. The calibration method was validated experimentally.

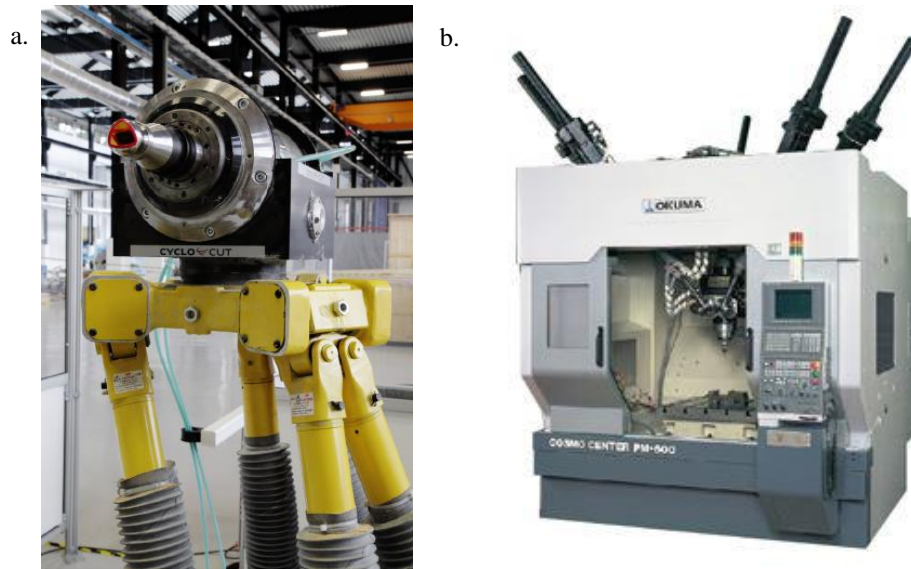


Figure 2-15: Commercialised 6-DOF PKMs [11, 40]

- a. The FANUC F-200iB with a machining tool [11].
- b. The OKUMA PM 600 [40].

6-DOF PKMs are exploited for their high stiffness characteristics since they possess 6 legs. 6-DOF PKMs generally have an architectural layout similar to the hexapod layout. The high mechanical rigidity provided by 6-DOF PKMs makes them attractive for, but not limited to, machining, general positioning and high vibration applications. These reasons have led authors to focus attention more on applications and to improve PKM performance indices. There was more novelty of machine architectural layout and limb configurations observed in the 5-DOF PKMs in comparison to the 6-DOF PKMs. 6-DOF PKMs have been attractive thus, more research was conducted on these platforms and there is more commercialisation of 6-DOF PKMs than 5-DOFs. The rotational capability of 5-DOF PKMs is generally better than 6-DOF PKMs and the Pentapod PKM developed by Metrom is an example [94].

The hexapod-type layout for 5-DOF and 6-DOF PKMs generally possess prismatic joints thus, the PKM has higher inertia. The higher inertia of these PKMs makes them better suited for low-speed tasks but still possesses the functionality to be used for pick and place operations that require a short distance to move parts. Workspace can be designed to suit the application but the PKM's kinematic, singularity and workspace analyses need to be solved first. There is a tradeoff between large workspace and machine stiffness. Larger workspaces require all motors to be mounted at footpoints but reduces mechanical rigidity. Mathematical kinematic and workspace modelling is generally performed in MATLAB® while additional software such as ADAMS® and SolidWorks® were used for motion analysis and 3D Computer-Aided Design (CAD) modelling respectively.

2.3.6 Specifications of 5-DOF and 6-DOF PKMs

Novel architectures are developed to improve specific parameters of current PKMs. Research can also investigate the optimisation of certain parameters of an existing PKM. It is then worth presenting the specifications of some of the prominent and current PKMs for benchmarking. Table 2-2 presents the specifications of a sample of PKMs. A comprehensive list of PKM specifications can be found in the research conducted by Weck and Staimer [94] and details of some commercially realised PKMs were presented by Pandilov [40].

Table 2-2: Specifications of a sample of PKMs

PKM	Workspace X*Y*Z (mm)	Rotation (degrees)	Accuracy	Repeatability
Fanuc F-200iB [41]	$\pm 520 * \pm 510.93 * 437.27$	Depends on end effector mounting.	N/A	± 0.1 mm
Hexabot [10]	$\pm 152.2 (X-Y) * 178$	± 25	N/A	10 μ m
OKUMA PM 600 [105, 106]	$\text{Ø}600 (X-Y) * 400$	± 25	5 μ m	N/A
Mikrolar P1500 [107]	$\text{Ø}725 (X-Y) * 273$	± 25	50 μ m	25 μ m
Mikrolar Hex-A-Jet P3000 [108]	$\text{Ø}1219 (X-Y) * 508$	± 15 (X, Y Axis) ± 5 (Z Axis)	± 0.05 mm	0.03 mm
Metrom Pentapod P800 [94, 109]	$\text{Ø}600 (X-Y) * 400$	± 90	± 0.020 mm	0.003 mm
Hexact [94]	200*200*100	± 15 (X, Y Axis) ± 5 (Z Axis)	± 20 μ m	<5 μ m
Hexapode 300 [94]	700*700*300	N/A	8 μ m/300 mm	± 1 μ m
Geodetic G500 [94]	500*500*500	N/A	± 25 μ m	± 5 μ m
Giddings&Lewis Variax [94]	700*700*750	± 25	12 μ m	N/A

The workspace is directly proportional to the length of linear actuators used however, the rotational range should theoretically remain the same assuming all components are scaled by the same factor. There are a few 5-DOF and 6-DOF PKMs that exceed a rotational range of $\pm 30^\circ$. Concerning 5-DOF PKMs that are parallel (not hybrid), only the Metrom P800, Sena Eclipse and the Tekniker Seyanka PKMs included and exceeded a rotational range of $\pm 30^\circ$. There is a niche for the development of 5-DOF PKMs with high rotational capabilities that exceed rotational capabilities of 6-DOF PKMs to give them more industrial relevance. There is also a challenge to produce affordable PKMs that are also lightweight and mobile.

2.4 Chapter Summary

This chapter presented the concept of Industry 4.0 and the relevance of this research within this context. Serial, parallel and hybrid robotic architectures were investigated and a comparative analysis was performed on serial and parallel kinematic architectures. A review of different DOF PKMs was researched regarding their novelties,

merits and challenges of each and their applications. Specifications of some 5-DOF and 6-DOF PKMs were presented with the establishment of a research gap.

The literature suggested that 2-DOF PKMs exhibit either rotation or translation of the end effector. 2-DOF PKMs are designed for specific applications, they are cost-effective and possess simpler mathematical analyses. 2-DOF PKMs lack the mechanical rigidity and have not been widely adopted by industry. 3-DOF PKMs exhibit a combination of translational and rotational DOFs and can be designed to possess only translations or rotations of the end effector. The delta and spatial types are most commonly researched while many 3-DOF PKMs require future work. The delta structure is the most common topology of 4-DOF PKMs and is used mainly for pick and place applications. 4-DOF PKMs have been employed for AM applications. 4-DOF PKMs possess low inertia permitting high-speed movements but lack mechanical rigidity.

5-DOF PKMs generally possess 3 rotational and 2 translational DOFs. 5-DOF PKMs commonly exist as hybrid systems and hybrid PKMs having some industrial presence. Many experimental 5-DOF PKMs have been developed but have not been commercialised. The category of 5-DOF PKMs has received lesser attention than others. 6-DOF PKMs are exploited for their high stiffness characteristics and are generally similar in appearance to the Hexapod-type layout. Some 6-DOF PKMs have been commercialised. The rotational capability of 5-DOF PKMs are generally higher than 6-DOF PKMs and 5-DOF PKMs possesses more novelty than 6-DOF PKMs. 4-DOF PKMs possess larger workspaces than 5-DOF and 6-DOF PKMs. There is a tradeoff between large workspace and machine stiffness.

The succeeding chapter discusses the PKM concept generation and selection. A sequential synthesis for the architectural design of the PKM is presented. Insights of the machine synthesis are discussed. The architectural design and PKM novelties are presented. A QFD analysis was performed to aid in the development of target specifications. Potential customer requirements and their relationships to engineering metrics were reviewed. The relationship between the different engineering metrics were investigated.

3. CONCEPT GENERATION AND SELECTION

3.1 Introduction

This chapter presents the synthesis methodology for the development of a novel PKM. Concepts and ideas from Section 2.3 were explored to give insights into the development of a new joint. The architecture is described with its novelties. A QFD process was used to develop target specifications and to understand the different relationships within the design process.

3.2 Machine Synthesis

Figure 3-1 illustrates the synthesis of PKM topologies. Pandilov and Dukovski, and Weck [40, 94] described the process. The systematic methodology was broken down into the following steps:

1. Joint selection and limb topology.
2. Selection of architectural type, DOFs and motors dedicated to each limb.
3. Configuration of joints on the base.
4. Configuration of joints on the end effector.
5. Direction of the applied force of the actuators.
6. The direction of the z-axis.

The subsections of Section 3.2 present the step by step synthesis methodology.

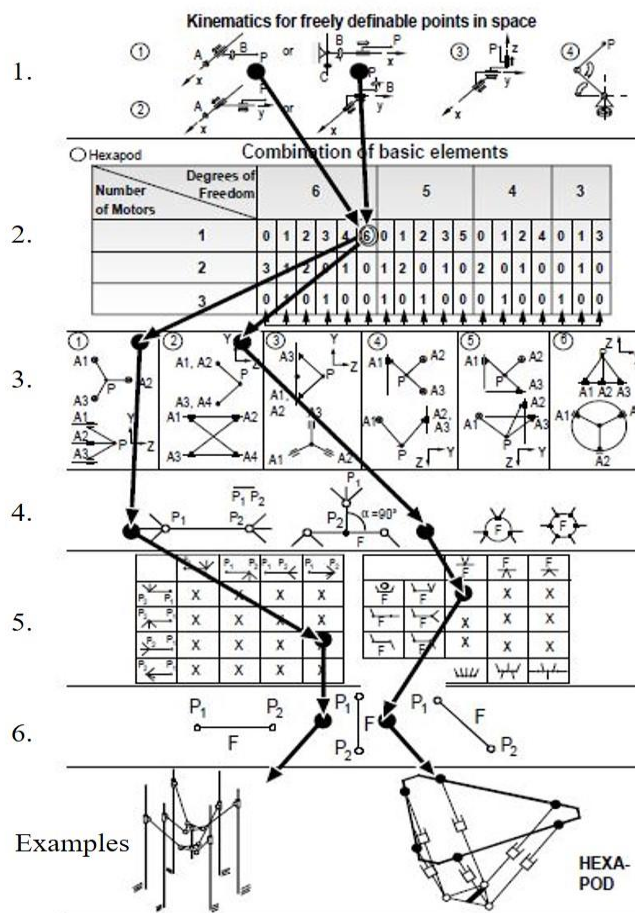


Figure 3-1: PKM synthesis [40]

3.2.1 Joint Selection and Limb Topology

A kinematic pair is established when two rigid links are coupled, resulting in restrained relative motion. Kinematic pairs are classified as either a lower or an upper kinematic pair. A lower kinematic pair is established when two rigid bodies maintain surface contact. An upper pair is restrained such that the two rigid bodies that keep a line or point contact [35]. An example of an upper kinematic pair is a pair of gears. There are six types of lower kinematic pairs, as listed below and categorized in terms of their DOFs [35]. Figure 3-2 depicts the different type of joints:

- Prismatic (P): Allows translation along 1 axis (1 DOF)
- Revolute (R): Allows paired elements to rotate concerning each other about 1 axis (1 DOF)
- Cylindrical (C): Allows translation and independent rotation about 1 axis (2 DOFs)
- Helical (H): Allows translation and independent rotation about 1 axis (2 DOFs)
- Spherical (S): Allows paired elements to rotate concerning each other about 3 axes (3 DOFs)
- Planar (E): Allows translation along 2 axes and rotation about 1 axis (normal to the plane) (3 DOFs)

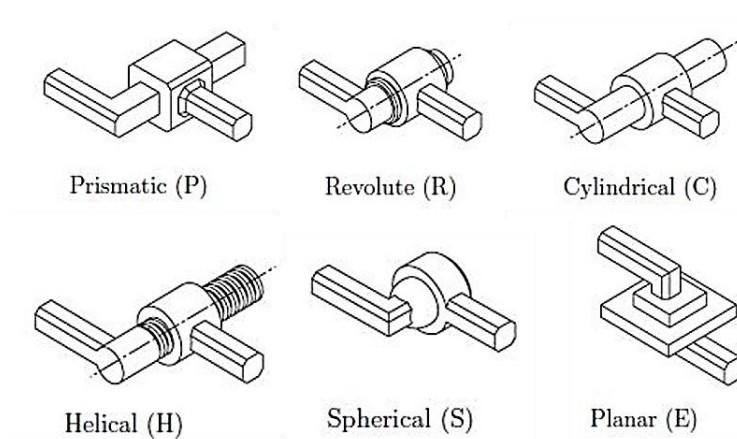


Figure 3-2: The different types of joints [35]

A Universal joint (U) combines two revolute joints to permit rotation about two axes that are perpendicular to each other. This joint allows 2 rotational DOFs as shown in Figure 3-3 (a). The Parallelogram (Pa) joint is comprised of 4 links and adds to the stability of the limb structure. The Pa joint is illustrated in Figure 3-3 (b). The Pa joint allows 1 DOF.

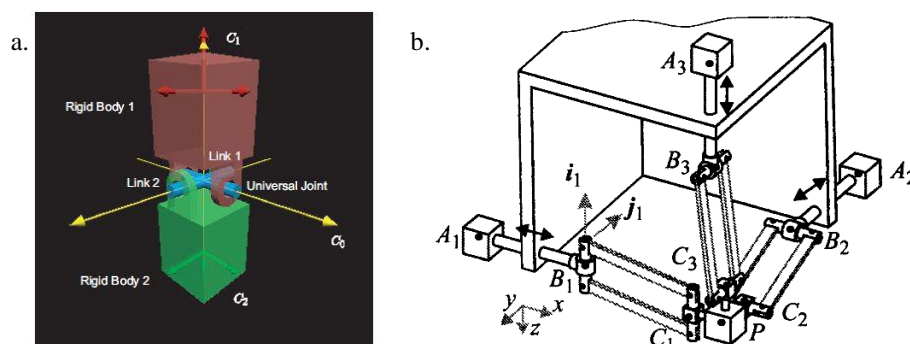


Figure 3-3: An example of a universal joint and a parallelogram joint.

- A Universal (U) joint [110].
- A Parallelogram (Pa) joint [58].

PKMs are described alphanumerically according to the types of joints that make up their kinematic chains. For example, the 3 UPU PKM. The number indicates that the PKM is comprised of 3 identical kinematic chains. The sequence of upper-case letters indicates that the sequence of joints from the base to the end effector. First is a Universal joint, then a Prismatic joint and finally another Universal joint. The underlined letter specifies the actuated joint [35].

Inspiration was drawn from the passive parallelogram joint [58]. Universal joints were split into two revolute joints which aimed at increasing accuracy and providing tighter tolerances. The concept of splitting a universal joint into two revolute joints with offsets was found to be attractive as it would be easier to manufacture and possesses fewer geometric constraints [111]. Yu et al. [111] also stated that the RR joint would increase the workspace of a PKM and could increase its stiffness by a factor of 2 due to its more straightforward bearing structure as opposed to a universal joint. The branched-chain limb, from the study conducted by Qiu et al. [89], also served as a basis for merging concepts to generate a new joint. Figure 3-4 illustrates the branched-chain.

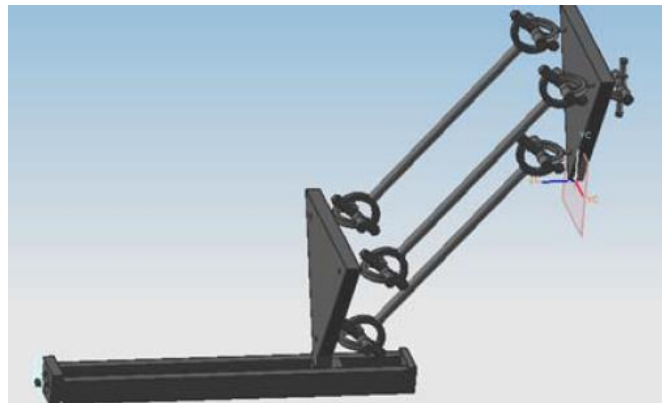


Figure 3-4: The branched-chain used by Qiu et al [89].

When the two legs comprising the joint are actuated by the same distance, a parallelogram shape is maintained as depicted in Figure 3-5 (a). If the legs are actuated to different distances, the joint then becomes an Irregular Quadrilateral (IQ) as shown in Figure 3-5 (b). The novel joint is therefore named the Pa-IQ joint.

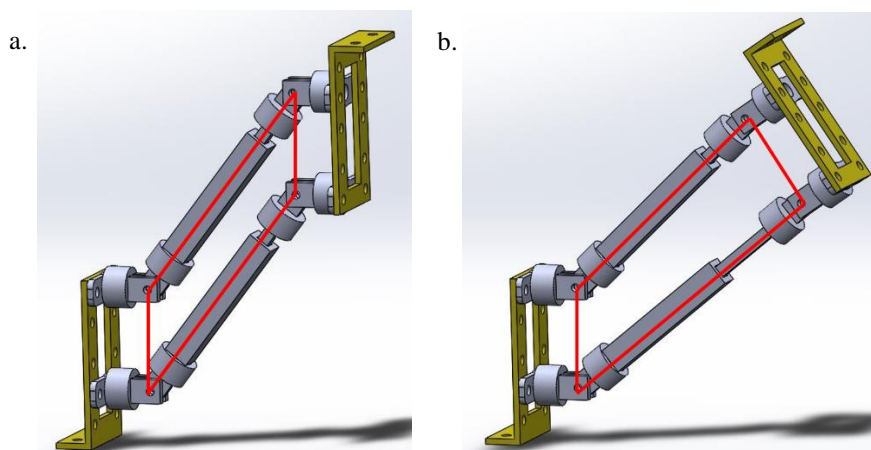


Figure 3-5: The actuated parallelogram joint.

- a. The parallelogram shape exhibited.
- b. The irregular quadrilateral shape exhibited.

3.2.2 Architectural Selection, DOFs and Dedicated Motors per Limb

According to Koseki et al. [112], parallel kinematic manipulators can be classified into three categories as presented in Table 3-1.

Table 3-1: The different classes of parallel kinematic manipulators

Type	Rotary	Prismatic	Fixed Linear
Force of output	Small	Large	Large
Location of actuator	Base	On the leg	Base
Moving mass	Small	Large	Small
Speed capability	Fast	-	Fast
Rigidity	Poor	Good	Good
Workspace	Large	Small	Large
Overall structure	Simple and compact	Large moving parts	Large footprint

The PKM in this study aimed to validate part handling, pick and place, general positioning and machining applications. The rotary type cannot be considered for machining applications due to its small output force and poor rigidity. This category of PKMs does not possess the mechanical strength to absorb the vibration and chatter induced from machining tasks. The PKM was aimed to possess a small footprint, thus, the fixed linear type of PKMs was not considered.

The prismatic type was the most applicable to suit the applications of this research. It possesses good rigidity and has a smaller footprint than the fixed linear type, although it has the drawback of large moving masses. Accuracy is valued over speed for robotic machining and fine positioning applications. The prismatic type can also be used for sorting and pick and place applications that do not require the workpiece to be moved relatively large distances.

Machining applications and general positioning applications, such as movable cinema seats, do not require the rotation about the axis normal to the base. Since Pa-IQ joints are used, both legs within the pair are always coplanar. This can be exploited to restrict the independent rotation about the axis normal to the base and permit the motion as a parasitic rotation. Xiaolong et al. [90] and Zhu et al. [91] used revolute joints to restrict a translational DOF. The same methods can be applied to convert an independent motion to a dependent motion to realise other machine advantages. Xiaolong et al. [90] used 6 actuators to produce a redundant actuated 5-DOF PKM.

At least 5 actuators were required to control 5-DOF independently but the Pa-IQ joints required 2 actuated limbs per pair therefore, 6 actuators were considered. This made up 3 pairs of legs. The arrangement of the 3 pairs is discussed in Section 3.3.

3.2.3 Configuration of Joints on the End Effector and Base

Inspiration for the end effector and leg layout was drawn from the spatial 3-DOF PKM design by Liu and Kim [60]. Figure 3-6 illustrates the PKM capable of high rotational ranges. The end effector was designed to accommodate the leg layout. Two parallelogram joints are arranged in a “stacked” manner and the other parallelogram joint has the links side-by-side. A similar approach was used and the end effector mounting points for the PKM in this study are displayed in Figure 3-7. The base mounting points were designed to be 120° apart to aid in isotropic movement. Three mounting points were needed on the base. The shape of the base is irrelevant except that the mounting brackets are mounted on a Pitch Circle Diameter (PCD), as illustrated in Figure 3-7.

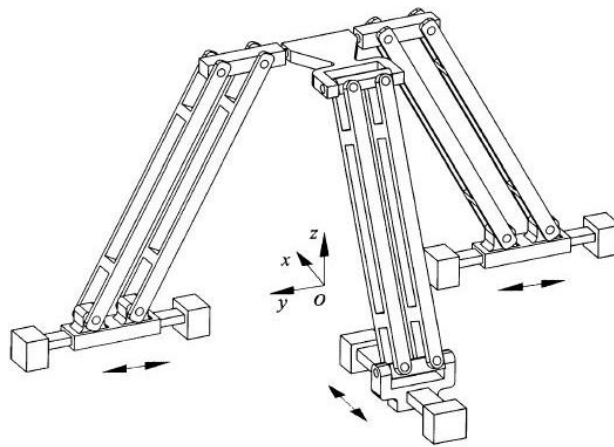


Figure 3-6: The spatial 3-DOF PKM designed by Liu and Kim [60].

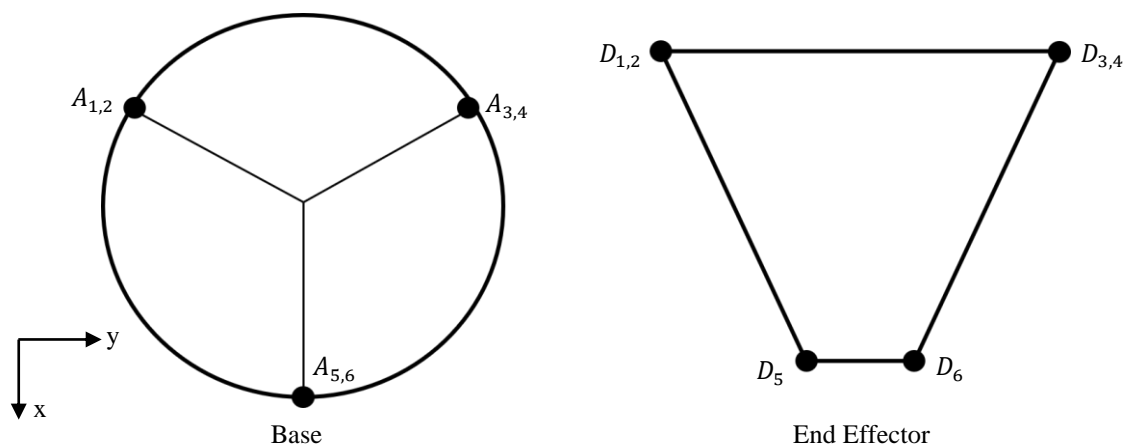


Figure 3-7: Base and end effector mounting points

3.2.4 The Direction of the Applied Force of the Actuators and z-axis

The actuators apply a force axially along the length of the threaded rod to cause the extension and contraction of the actuators. This is due to the linear actuation of the telescoping arm instead of rotational actuation. The z-axis is normal the base. A local coordinate system was placed on the end effector to resolve vectors to a global

coordinate system. The local z-axis was also normal to the end effector. The axes of the global coordinate system are displayed in Figure 3-7.

3.2.5 Machine Synthesis Insights

Joint combinations can be used to restrict DOFs or convert independent motions to dependent motions by changing the mounting orientation. Offsets permit relative motion between joints and a frame of reference. The selection of the correct architectural type needs to be established at an early stage. There are numerous possibilities of limb combinations and architectural layouts to develop a PKM, therefore, the application needs to be established before the synthesis procedure is conducted. The literature review provided inspiration and direction for innovation of the limb topology and end effector design. Aspects such as mechanical rigidity, tolerance of different types of joints, force transfer through joints, the strength of linkages, reconfigurability, modularity and portability should be considered when experimenting with prototype designs.

3.3 Description of the architecture

3.3.1 Manipulator Structure

Figure 3-8 depicts the geometric layout. The arrangement of the pair of legs restricts the independent rotation about the axis normal to the base and permits the rotation as a parasitic rotation. Lin et al. [113] defined parasitic motion as a dependent motion that accompanies other independent motions. Parasitic motion is therefore a resultant of other motions and cannot occur independently. The kinematic phenomenon of parasitic motion poses disadvantages such as unwanted motion, lower accuracy and more difficult calibration procedures. Parasitic motion can be advantageous by performing tasks by lower DOF mechanisms which leads to lower costs, sometimes lower complexity of kinematics and easier control.

An over-constrained (or redundant) mechanism exhibits an increase in rigidity according to Pashkevich et al. [114]. The PKM designed in this study was classified as a redundant mechanism due to a greater number of actuators than DOFs [10]. The 5 DOFs are comprised of 3 translational and 2 rotational DOFs. The restriction of the independent rotation about the axis normal to the base was influenced by machining applications not requiring it and general positioning, part handling and sorting tasks can still be accomplished without the independent rotation about the axis normal to the base. The configuration of the joints on the base and end effector follows from Figure 3-7.

The PKM was named the 2R(Pa-IQ)RR, R(Pa-IQ)R manipulator. Figure 3-9 depicts the topology. Each of the pairs of legs leans toward the centre of the base and are spaced at 120 degrees from each other. The individual legs are comprised of the following:

- A common revolute joint shared by another leg in its leg pair.
- An individual revolute joint.
- A prismatic joint.
- An individual revolute joint.
- A common revolute joint shared with the same leg as per the first revolute joint.
- The first and second pairs of legs possess an additional common revolute joint which is attached to the end effector.

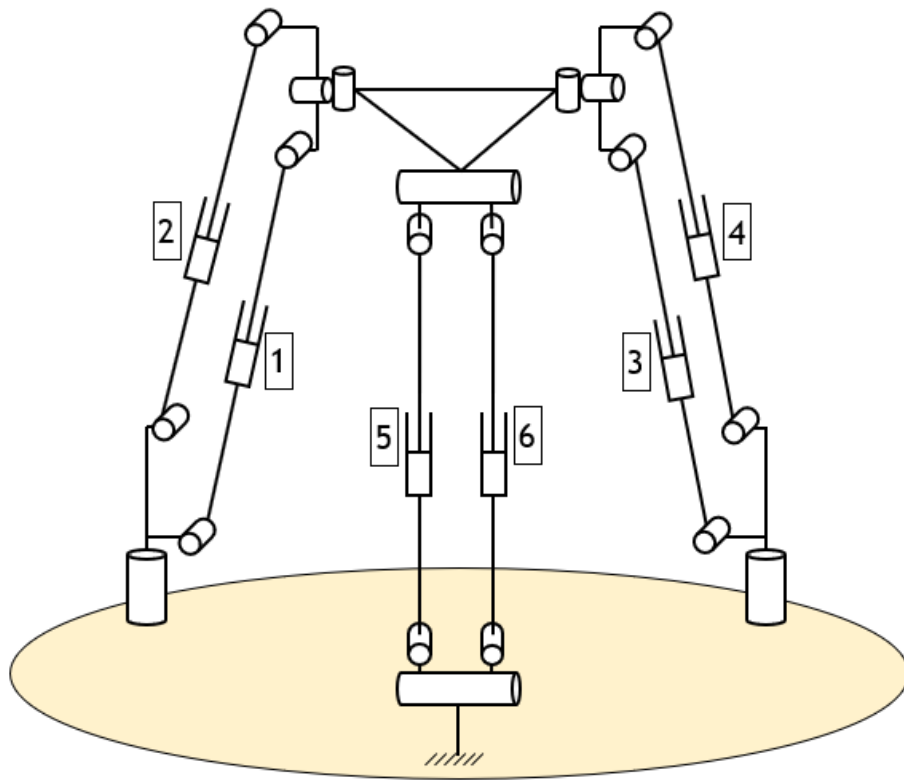


Figure 3-8: Geometric layout of the PKM

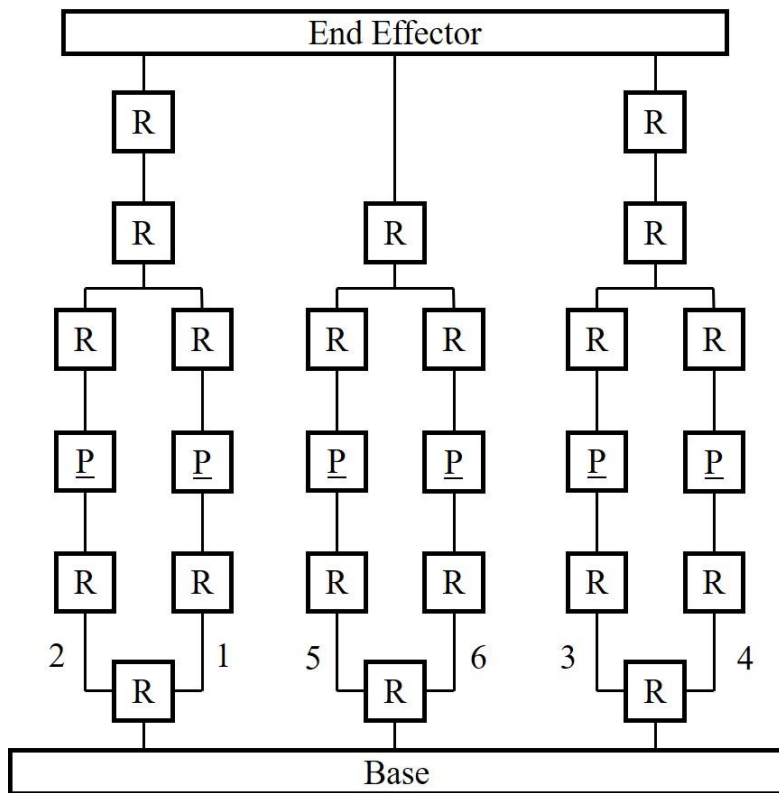


Figure 3-9: Machine Topology

3.3.2 Machine Novelties and Characteristics

The 2R(Pa-IQ)RR, R(Pa-IQ)R possessed the following novelties and characteristics:

- All prismatic joints are actuated and all potential universal joints have been decoupled into revolute joints.
- The position and orientation of the pairs of legs collectively restricts the independent rotation about the axis normal to the base (z-axis) and permits the rotation as a parasitic rotation.
- When the end effector exhibits translation, then the pairs of legs maintain a parallelogram structure as each pair is actuated by equal stroke lengths. Each pair of legs could be actuated by a different stroke length to another pair.
- The arrangement of the revolute joints constrains each of the legs within a pair to be coplanar.
- The rotation was achieved when the legs within a pair are actuated to different lengths. The parallelogram structure changes into an irregular quadrilateral.

The DOF of a PKM is generally calculated by using the Grubler or Kutzbach criterion and is presented below [9]:

$$F = \lambda(n - j - 1) + \sum_i f_i \quad (3.1)$$

Where $\lambda = 6$ for spatial manipulators, n is the number of links of the mechanism, j is the number of joints with the assumption that all joints are binary and f_i is the relative motion allowed by joint i . For the PKM developed in through this study the aforementioned parameters are as follows:

- $\lambda = 6$ as this is a spatial manipulator.
- $n = 28$ as this is the total number of links.
- $j = 32$ as the manipulator possesses 20 binary joints and 6 ternary joints which (counts as 2 binary joints each). Therefore, the total number of joints is the sum of these two values.
- $f_i = f_1 = 26$ as there are 6 prismatic joints and 20 revolute joints and each of these joints permits one DOF thus, the total number of one DOF joints is 26.

The DOFs can be calculated using the Grubler/Kutzbach equation.

$$F = 6(28 - 32 - 1) + 26 = -4 \quad (3.2)$$

A robotic manipulator cannot possess a negative number of DOFs. The negative value is interpreted as the PKM being an over-constrained mechanism, as stated by Merlet [10]. Over-constrained mechanisms can potentially increase rigidity. These mechanisms constrain the end effector to prevent one or more translations or rotations. The over-constrained nature includes more complicated kinematic and stiffness modelling [114]. It was previously stated that the PKM possessed 5 DOFs and a parasitic rotation. This was identified through observations and measurements conducted in SolidWorks® due to the breakdown of the Grubler/Kutzbach equation for over-constrained mechanisms. Appendix G illustrates the different DOFs exhibited by the PKM confirming its 5 DOFs with a parasitic rotation.

Lin et al. [113] suggested that parallel mechanisms exhibiting parasitic motion should be classified according to type of parasitic motion, scale and motion pattern. The PKM developed was classified as follows:

- **Type:** The PKM possessed a rotational parasitic motion induced by 2 independent rotations of the end effector hence the parasitic motion characteristic is symbolised as $R\oplus\{R\}$. The term within the brackets, represents the dependent motion and in this instance the symbol R refers to rotation.
- **Scale:** The scale refers to the amplitudes of the independent and dependent motions relative to each other. In terms of scale, the PKM was classified as Finite-Finite since the dependent motion can sometimes be greater than one of the independent rotations that cause its occurrence and all motions were finite. The parasitic motion was not infinitesimal and was therefore not classified as Finite-Infinitesimal. The parasitic motion was not always smaller than both independent rotations and therefore could not be classified as Finite-Small.
- **Motion pattern:** The motion pattern summarises the representation of motions. The PKM possess 3 and 2 independent translations and rotations respectively and is represented as $3T2R$. Considering the parasitic motion, the motion pattern of the PKM is then represented as $3T2R\oplus\{R\}$. Due to one parasitic motion incurred, the dimension of parasitic motion is 1.

The PKM possessed similarities to the Hexapod (Stewart-Gough Platform) in appearance [8]. Differences between the $2R(Pa-IQ)RR$, $R(Pa-IQ)R$ PKM and the Hexapod are listed in Table 3-2.

Table 3-2: Differences between the novel architecture and the Hexapod

Architecture	$2R(Pa-IQ)RR$, $R(Pa-IQ)R$	Hexapod
DOF	5	6
Joints	Prismatic and revolute	Various combinations of prismatic, revolute, spherical and universal joints
Pairs of legs	Yes	No
Common joints	Yes	Sometimes
Attachment points to base	3	6
Attachment points to end effector	4	6
Some actuators move completely in space	Yes	No

3.4 Quality Function Deployment

The QFD analysis is performed to assist in generating target specifications. The QFD analysis relates the customers' requirements into engineering metrics. Engineering metrics can, therefore, clash with each other and reasonable trade-offs are required. The QFD analysis also helps the designer to benchmark the product against its competitors thus establishing the product's advantages and disadvantages. Obtaining target specifications is a priority of performing the QFD analysis. The aim is to produce a product that results in customer satisfaction however, the difficulty to change different engineering metrics is not equal. The QFD analysis reveals which engineering metrics are critical to the designer/engineer[115]. This research used the House of Quality QFD template. Appendix D presents the QFD.

3.4.1 Relationship between Customer Requirements and Engineering Metrics

Each customer requirement has at least one strong relationship with an engineering metric. The rotation about the x and y axes had the highest number of strong relationships with engineering metrics. This indicated that the rotational capability of the machine is the most sensitive customer requirement for changes in engineering parameters. Most customer requirements have approximately 4 strong relationships with engineering metrics. The durable and lightweight customer requirements have only 2 strong relationships with engineering metrics and are, therefore the least affected by changes in engineering metrics. The stroke length of the linear actuators possessed the highest number of strong relationships with customer requirements. This engineering metric is, therefore, one of the most important metrics to consider.

There are also moderate and weak relationships that exist between customer requirements and engineering metrics. An example of a medium relationship exists between the customer requirement of a modular PKM and the mass of the motors. If the motors are heavy, it makes modularity challenging in terms of reconfiguration, assembly and decommissioning. A weak relationship was observed between the PKM being portable and the volume of the end effector. The volume of the end effector, therefore, its mass, influences the portability of the robotic platform but the relationship does not bear strong nor moderate influences to be of significant concern.

3.4.2 Relationship between Engineering Metrics

Engineering metrics can either be supportive or conflicting. An example of a strong positive (supportive) relationship is the relationship between the range of motion along the x-axis the stroke length of the linear actuators. The stroke length of the actuator significantly affects the range of motion along the x-axis. When the stroke length of the linear actuator is increased, the range of motion in the x-direction is increased. These parameters are intended to be increased and therefore, they have a strong positive correlation. A positive correlation was observed between the mass of the motors and the mass of the actuators. These parameters are aimed to be minimised to create a lightweight PKM. When the mass of the motors is decreased, the mass of the linear actuators is decreased and is, therefore, a supportive relationship.

A conflicting relationship was discovered between the range of motion along the x-axis and number of singularities. The range of motion is aimed to be increased but an increase in range of motion allows the possibility of more singularities to occur within the workspace of the robot. The number of singularities was aimed to be a minimum. This was noted as a negative correlation. A strong negative relationship was discovered between the stroke length of the actuators and the number of singularities. The stroke length should be as large as possible but also increases the likelihood of the number of singularity points that can exist. The rest of the engineering metrics were assessed in the same way as presented.

3.4.3 Importance Ratings, Relative Weight and Difficulty of Target

The importance rating considers the relationship strength between the various customer requirements and engineering metrics. The relative weight value highlights the significance of each engineering metric relative to each other. For example, the stroke length of the linear actuator was ranked with the highest importance due to its strong relationship with many customer requirements. The second-highest ranked engineering parameters were accuracy and repeatability. These parameters require more design and investigation than others that ranked lower. For example, accuracy should require more design and investigation than the mass of the linear actuators.

The difficulty in reaching the target specification was vital because it also influenced how much time should be spent to optimise a parameter and highlighted how dependant a parameter is on others. For example, the target value for the motor of an actuator is 2 kg and rated with a difficulty of 2/10. The mass can be easily achieved through purchasing off-the-shelf motors and is not dependent on other factors. However, the accuracy is rated as 8/10. The difficulty is due to the high dependence on other components and cannot be easily achieved as the mass of the motor. This understanding was carried forward into the detailed mechanical design.

3.4.4 Target Specifications

One of the aims of the QFD analysis was to develop target specifications. Table 3-3 presents the engineering metrics, target specifications and justifications. The target specifications influenced the design of the components presented in Section 4.

Table 3-3: Target Specifications

Engineering Metric	Target Specification	Justification
Mass of motors (Total)	2 kg	6 x NEMA 17 motors should not exceed a mass of 2 kg. NEMA 17 motors are chosen for a compact prototype.
Mass of linear actuators (Total)	4kg	The prototype is aimed to be lightweight.
Range of motion in the x-direction	200 mm	Reasonable estimations were made since this is dependent on the stroke length of the linear actuators.
Range of motion in the y-direction	250 mm	
Range of motion in the z-direction	100 mm	
Minimum degrees of tilt about X and Y-Axis	At least 60°	Most commercially available 5-DOF and 6-DOF PKMs have a range of 50°.
Stroke length of linear actuators	65 mm	A reasonable estimation for a compact prototype.
Area of base	1 m ²	The base should easily account for changes made to the mounting pattern if required.
Volume of end effector	0.00004 m ³	A reasonable estimation for a compact prototype.
Spacing between actuators	90 mm	There would be enough clearance to avoid self-clashing of the actuator legs whilst not designing mounting brackets to be too large.
Volume of footprint (compactness)	0.003 m ³	A compact prototype was aimed to be developed as proof of concept. This was estimated to be a tetrahedron when the PKM is fully retracted.
Singularities in workspace volume	0	Ideal case for any robotic platform.
Tolerance of joints	≤1 mm	To aim for high accuracy and repeatability.
Accuracy	2 mm and 2°	A desktop prototype developed through AM was used for experimentation without the use of high accuracy components.
Repeatability	2 mm and 2°	

3.4.5 Competitive Analysis

A competitive analysis was conducted between industrial PKMs and the PKM developed in this research. The PKM developed was the most favourable concerning weight, cost, modularity and portability. These criteria possessed a strong relationship to each other. The PKM was specified to be developed through AM. This allowed the PKM to be lightweight, be considerably cheaper and more portable than industrial PKMs. The modularity criterion was ranked favourably due to the ease at which the machine can be reconfigured aided by AM.

The PKM was the least favourable concerning translation along the x, y and z axes, durability, high precision and use for different applications. The PKM was aimed to be developed as a desktop prototype hence, considerably smaller than industrial PKMs. The size of the PKM is influenced by the stroke length of the linear actuators. A target specification aimed to produce actuators that possessed a 65 mm stroke length therefore the translation along the x, y and z axes were the least favourable in comparison to industrial PKMs. The PKM was the least durable due to AM. AM permits larger joint tolerances than industrial joints therefore tasks prone to vibrations would cause the PKM to be the least durable. Moreover, the PKM would be the least durable under heavy loads as opposed to industrial PKMs. The larger joint tolerances would pose a challenge in obtaining high accuracy and repeatability.

The PKM's use in different applications was ranked the lowest due to the limitations induced through AM. All PKMs in the competitive analysis were capable of being employed for multiple functions and the PKM developed could also be used in this manner should a large-scale prototype be developed. The target specification of at least 60° of rotation about the x and y axes was favourable since only the Metrom Pentapod P800 possessed larger ranges of tilt. Other PKMs ranges of tilt generally did not exceed $\pm 25^\circ$. The FANUC F-200iB and the Hexapode 300 were ranked the best concerning its use for different applications which is strongly influenced by the portability criterion.

The Metrom Pentapod P800 and the FANUC F-200iB were the best PKMs for benchmarking. The Metrom Pentapod P800 ranked the best on three instances and ranked the least favourable only once. The FANUC F-200iB was the least favourable and most favourable only once. It was consistently competitive against industrial PKMs. The Metrom Pentapod P800 and the FANUC F-200iB can both be used for drilling and milling operations however the FANUC F-200iB is generally mounted in different orientations since it is more portable. The PKM in this study aimed to improve the rotational capabilities of industrial PKMs as well as being relatively lightweight. Larger PKMs such as the OKUMA PM600 and the Metrom Pentapod P800 generally possess higher accuracy and repeatability than other PKMs but possess drawbacks of poor portability, high costs and are extremely heavy. The PKM in this study possessed extreme characteristics by ranking the best and least favourable in 4 instances each. This was strongly influenced by the production through AM. The QFD competitive analysis was not a true reflection of machine performance as it compared customer requirements and not engineering ratios such as actuator stroke length to translation along the x, y and z axes and others. The size of the robotic platform determined many machine characteristics hence, performance and engineering ratios are better suited as a method of comparison.

3.5 Chapter Summary

This chapter discussed the PKM synthesis procedure and presented the sequential formulation of the architectural design. The structure and the PKM novelties were presented and the robotic platform was classified as an over-constrained mechanism. The PKM possessed 5 DOFs and a parasitic rotation. The QFD analysis was presented which aided in generating target specifications. Potential customer requirements and their relationships to engineering metrics were reviewed. The relationships between the various engineering metrics were analysed. A competitive analysis was conducted between industrial PKMs and the PKM developed in the study.

The next chapter presents the mechanical design of the PKM. A design methodology and a system decomposition diagram are presented. The prototype was designed for AM and the design considerations are discussed. The various components designed are presented. The PKM specifications, sub-assembly and assembly precedence diagrams are presented.

4. MECHANICAL DESIGN

The mechanical design methodology is described. A detailed mechanical design was performed using the target specifications obtained from the QFD analysis. Component designs are presented with consideration for AM. A low-cost desktop prototype was designed and built to demonstrate the motion characteristics of the PKM. The final specifications are presented. Sub-assembly and assembly precedence diagrams are presented.

4.1 Mechanical Design Methodology

The mechanical design process is illustrated in Figure 4-1. Shaik [37] presented and followed this process to develop a sensor system for a pick and place PKM. The method was also described by Merlet [116]. The structural and dimensional syntheses were performed concurrently. The machine topology, regarding the PKM type, was addressed in Section 3. Concerning, the actuators, the position of the foot points of the legs relative to each other was 120° as per Figure 3-7. The PCD of the footpoints, the actuator stroke length and mounting distance between actuators in a leg pair were iteratively designed through 3D CAD modelling.

Components were iteratively designed on SolidWorks® due to designing for workspace preferences concurrently. SolidWorks® allowed the joints and assembly to move and measurements were taken, shown in Figure 5-3. Dimensional synthesis concerning workspace and singularities was addressed iteratively. Final engineering drawings are presented in Appendix H. Workspace was dependent on the range of motion along the x, y and z axes. The range of motion was mainly dependant on actuator stroke length, PCD of the footpoints, mounting distance between actuators in a leg pair and end effector design. The PKM was designed to be compact and with sufficient strength for demonstration. A high range of motion along the x and y axes was preferred to define the workspace. Workspace is the most significant factor that influences geometric parametrisation of the PKM as per Figure 4-1.

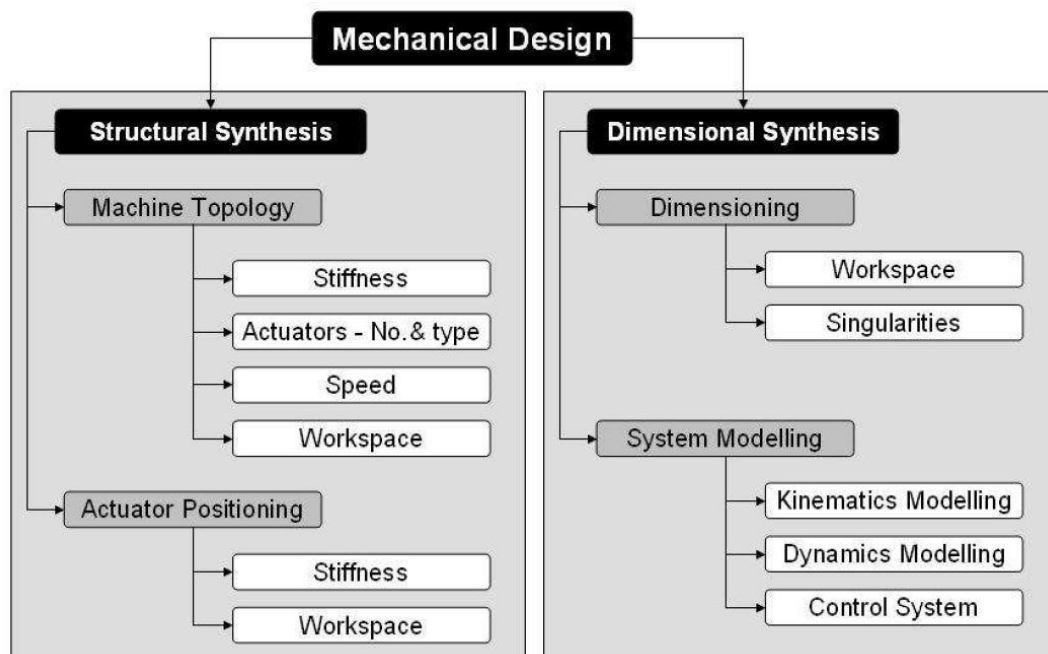


Figure 4-1: Mechanical design process for a PKM [37]

4.2 System Decomposition Diagram

Figure 4-2 illustrates the system decomposition diagram.



Figure 4-2: Mechanical system decomposition diagram

4.3 Design for Additive Manufacturing

AM machines possess parameters such as infill density, layer height, infill pattern and type of scaffolding that alter the print quality. These factors were taken into account. All drawings for the components are presented in Appendix H.

4.3.1 Material Selection

Table 4-1 compares the properties of Acrylonitrile Butadiene Styrene (ABS) and Polylactic Acid (PLA), according eSun [117]. PLA filament was selected as the material for production due mainly to its lower print and bed temperature. The lower bed temperature allowed a faster production of components. PLA possesses a higher tensile strength and bending strength than ABS filament. ABS printed components are more susceptible to warpage. Appendix E presents the cost of the materials.

Table 4-1: Comparison between ABS and PLA

Property	ABS	PLA
Print temperature (°C)	220-260	190-210
Bed temperature (°C)	110	No Heat/(60-80)
Density (g/cm ³)	1.04	1.24
Distortion temperature (°C, 0.45MPa)	78	56
Melt flow index (g/10min)	12 (220 °C/10kg)	5 (190 °C/2.16kg)
Tensile strength (MPa)	43	65
Elongation at break (%)	22	8
Bending strength (MPa)	66	97
Flexural modulus (MPa)	2348	3600
IZOD impact strength (KJ/m ²)	19	4

4.3.2 Material Wastage, Manufacturing Time and Clearances

Manufacturing time was considered due to the large number of components designed. A print infill of 80% was used with a layer height of 0.2 mm. Print orientation was considered to reduce the scaffolding produced while maximising the strength of the component.

A revolute joint was used as the test piece for testing joint tolerances. The forked end of the revolute joint was printed with a gap of 8 mm. Various complimenting test pieces with different widths were printed. The tests revealed that the best clearance for press fits and joints was 0.1 mm and 0.2 mm respectively. When scaffolding was produced, the press-fit clearance changed from 0.1 mm to 0.3 mm. All components were designed with these clearances.

4.3.3 Linear Actuator

The linear actuator affects mechanical strength, rigidity, inertia, workspace and cost. Appendix F presents the various linear actuator concepts and the selection matrix used to select the most suitable concept. The final concept was a variation of concept 3. The guides from the outer casing and the slots from the telescoping arm from concept 3 were removed due to the cantilever effect at the front of the actuator. This increased accuracy. The disadvantage was that it required more scaffolding than concept 3, and therefore, light filing was required to smoothen the areas where scaffolding was developed. The linear actuators had a stroke length of 66 mm. Figure 4-3 depicts an exploded view of concept 4. Appendix C.1 and C.2 presents the power screw and buckling analysis respectively. The buckling analysis revealed that the critical load was 16.80 kN. Appendix H presents the technical drawings.

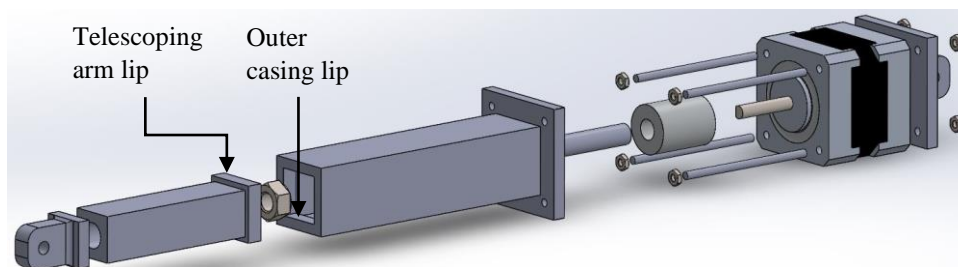


Figure 4-3: Linear actuator concept 4

4.3.4 Revolute Joints

4.3.5 Revolute joints on end effector and linear actuators

The revolute joints follow a clevis joint design with one end in the form of a fork and the other end a matching rod end. The revolute joints were designed with sufficient height to avoid self-clashing. Figure 4-4 (a) to (e) illustrates the forked and rod components of the revolute joints. The gap of forked end of the revolute joints was 8 mm in width and the thickness of each protrusion was 8 mm.

There was a design variation between the revolute joints shown in Figure 4-4 (b) and (c). Actuators 5 and 6 are positioned side-by-side as opposed to one being vertically above the other. The revolute joints in Figure 4-4 (c) were designed to be mounted to an aluminium rod.

4.3.6 Thrust bearing revolute joint

The mounting bracket for the bottom of actuators 1-4 was designed to rotate. Figure 4-4 (f) shows an exploded view the thrust bearing revolute joint. It comprised of 7 components. The radial bearings allowed smooth rotation of the bolt which locked the entire unit together with the lock nut. The top housing component served as a swivel plate for the linear actuator mounting bracket. Specifications for the radial bearing and the thrust bearing are provided by 3D Printing Store and RS components respectively [118, 119]

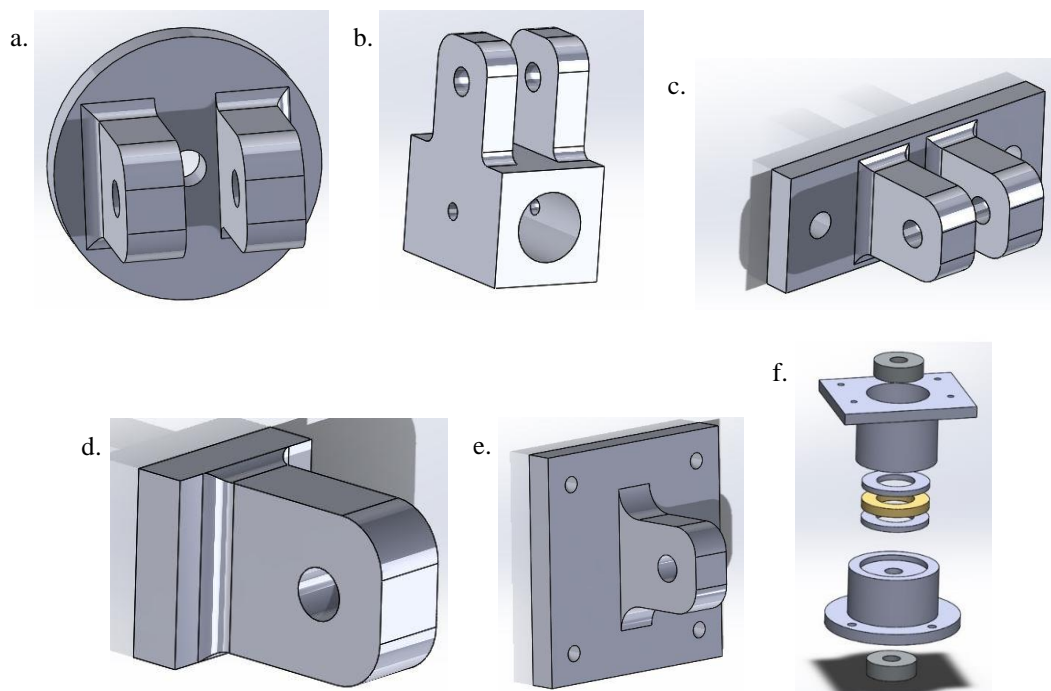


Figure 4-4: Revolute joints

- Revolute joint attached to the end effector
- Revolute joint attached to the top and bottom of actuator 5 and 6
- Revolute joint attached to the top and bottom of actuator 1-4
- Revolute joint attached to the telescoping arm
- Revolute joint attached to the back of the stepper motor
- Exploded view of the revolute joint attached to the mounting bracket for the bottom of actuators 1-4

4.3.7 End Effector and Base

4.3.7.1 End effector and related revolute joints

The end effector was designed to be triangular with revolute joints at each of its corners to accommodate for the three pairs of legs. One corner of the end effector was designed to possess revolute joint oriented horizontally to accommodate the third pair of legs which were side-by-side. An aluminium rod rotated within the horizontal hole. The end effector designed was based on an equilateral triangle and possessed a thickness of 8 mm. Figure 4-5 displays the end effector.

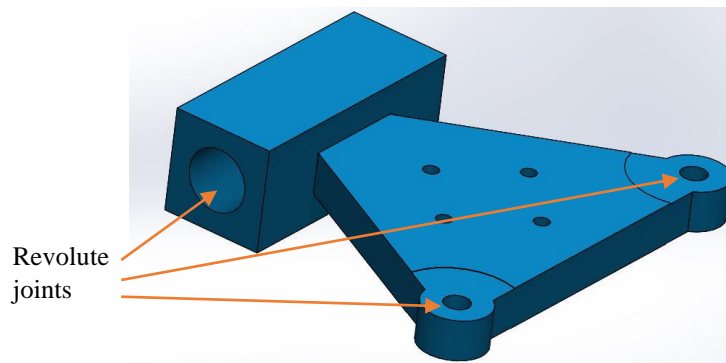


Figure 4-5: The end effector

4.3.7.2 Base and spacing of mounting points

The distance from the center of the base to the leg mounting points and the angular spacing between them are factors that influence workspace, singularities, stiffness, etc. A leg spacing of 120° relative to each other and distance of 150 mm from the base center was chosen. Depending on the intended workspace, the mounting points on the base can be altered.

4.3.8 Mounting Brackets and Spacing Blocks

4.3.8.1 Mounting bracket for the bottom of actuators 1-4

The bottom bracket for the bottom of actuators 1-4 was designed with mounting points at for each actuator in the leg pair. Two brackets were implemented for the first and second pairs of legs. This bracket is connected to the thrust bearing revolute joint.

This bracket was designed with a reinforcing gusset to restrict bending. There can be various mounting points designed into the vertical length of the bracket to allow for reconfigurability. The height of the bracket could also be extended to increase the distance between mounting points. The mounting bracket for the bottom of actuators 1-4 is shown in Figure 4-6 (a).

4.3.8.2 Mounting bracket for the top of actuators 1-4

The mounting bracket for the top of actuators 1-4, illustrated in Figure 4-6 (b), was designed to mirror the vertical face of the bottom mounting bracket with the same layout for the attachment points of the revolute joints. This ensured the pair of legs remain parallel when the end effector exhibits translational motion. The revolute joint shown in Figure 4-4 (a) connects the mounting bracket for the top of actuators 1-4 to the end effector.

4.3.8.3 Mounting bracket for the bottom of actuator 5 and 6

The mounting bracket for the bottom of actuator 5 and 6 was designed with a common revolute joint shared by actuator 5 and 6. The bracket possessed a supporting gusset on either side to increase rigidity. An aluminium rod passed through the top of the bracket and could freely rotate. The revolute joints at the bottom of linear actuator 5 and 6 were bolted onto the aluminium rod. The bracket is depicted in Figure 4-6 (c).

4.3.9 Spacing Blocks

The spacing blocks were designed to assist in the prevention of self-clashing of the legs within the same pair. The spacing blocks were designed to suit the length and width of the mounting brackets at the top and bottom of the linear actuators. The height of the spacing blocks was chosen to be 20 mm as it suffices to prevent self-clashing of the legs in the rest position. The height of the spacing blocks can be designed to suit the angle at which the legs lean forward to prevent self-clashing if other machine parameters are changed. Figure 4-6 (d) illustrates the spacing block.

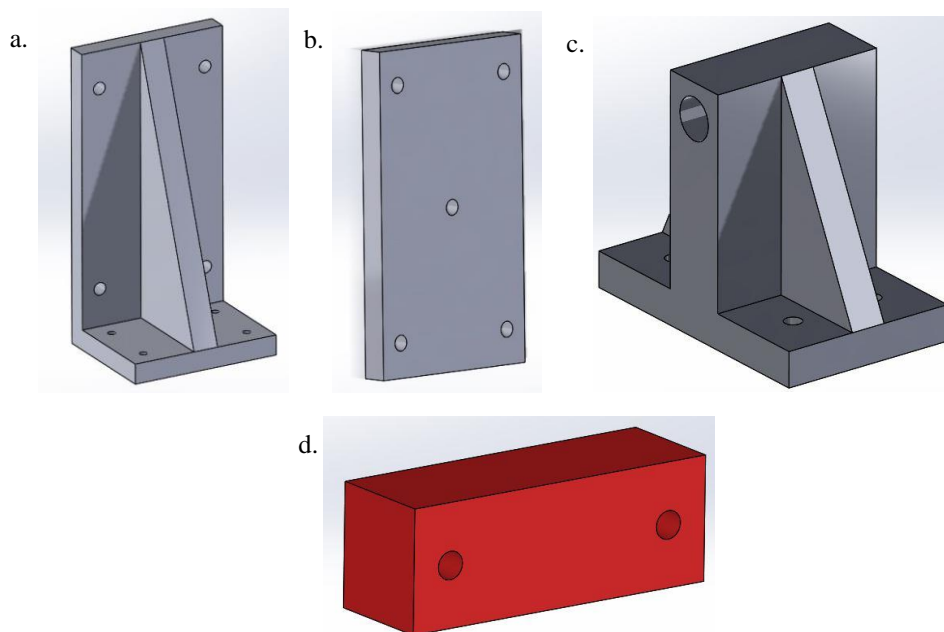


Figure 4-6: Mounting brackets and spacing block

- a. Mounting bracket for the bottom of actuators 1-4
- b. Mounting bracket for the top of actuators 1-4
- c. Mounting bracket for the bottom of actuator 5 and 6
- d. Spacing block

4.4 PKM Specifications

Once the PKM components were design and assembled in SolidWorks®, the machine specifications could be determined. All parameters were reasonably close to the target specifications from the QFD analysis except for the area of the base. This was reduced by 60%. Table 4-2 presents the PKM specifications.

Table 4-2: PKM specifications

Aspect	Specification
Mass of linear actuators (Total)	3.5 kg
Range of motion in the x-direction	188.64 mm
Range of motion in the y-direction	272.24 mm
Range of motion in the z-direction	94.6 mm
Degrees of tilt about the x-axis	71.46°
Degrees of tilt about the y-axis	63.97°
Stroke length of linear actuators	66 mm
Area of base	0.4 m ²
Volume of end effector	0.00035 m ³
Spacing between actuators	80 mm
Tolerance of joints	≤1 mm

4.5 Sub-assembly Precedence Diagrams

The sub-assembly precedence diagrams are presented. Figure 4-7 shows the thrust bearing sub-assembly diagram and Table 4-3 presents the components descriptions and quantities. There are 2 identical thrust bearing assemblies and Figure 4-7 describes the sub-assembly for 1 unit.

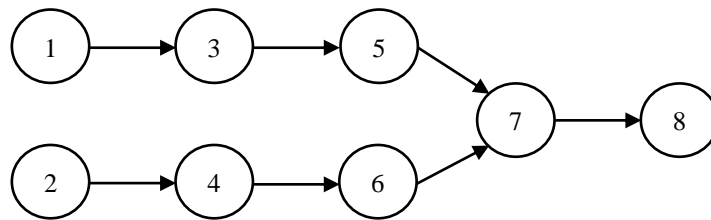


Figure 4-7: Thrust bearing sub-assembly diagram

Table 4-3: Thrust bearing sub-assembly description and bill of materials

Item	Description	Quantity	Item	Description	Quantity
1	Bottom housing	1	5	Bottom race	1
2	Top housing	1	6	Top race	1
3	Bottom radial bearing	1	7	Inner race	1
4	Top radial bearing	1	8	Bolt and lock nut	1

Figure 4-8 shows the linear actuator sub-assembly diagram for one actuator. There are 6 actuators used in the design. Table 4-4 displays the corresponding descriptions and quantities.

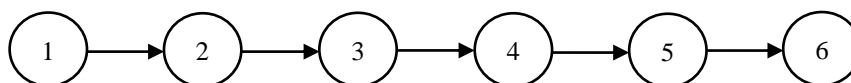


Figure 4-8: Linear Actuator sub-assembly diagram

Table 4-4: Linear actuator sub-assembly description and bill of materials

Item	Description	Quantity	Item	Description	Quantity
1	Joint B part 2	1	4	Threaded rod	1
2	Stepper motor	1	5	Telescoping arm	1
3	Flexible coupling	1	6	Actuator casing	1

The assembly of the PKM is described by Figure 4-9. The subassembly of path 2 is applicable to leg pair 1 and 2 and leg pair 3 and 4 since they are identical. Table 4-5 describes the components used and the quantities.

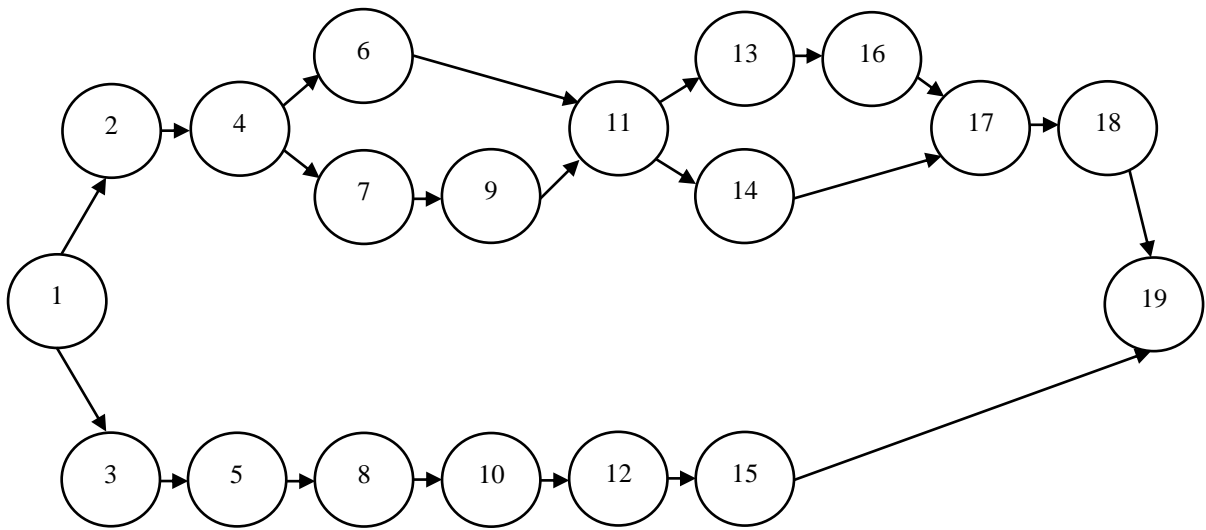


Figure 4-9: PKM sub-assembly diagram

Table 4-5: PKM sub-assembly description and bill of materials

Item	Description	Quantity	Item	Description	Quantity
1	Wooden base	1	11	Actuator sub-assembly	4
2	Thrust bearing sub-assembly	2	12	Revolute joints	2
3	Joint B bracket variation 2	1	13	Spacer block	2
4	Leg 1/3 and 2/4 Joint B bracket variation 1	2	14	Revolute joint	2
5	Aluminium rod	1	15	Aluminium rod	1
6	Revolute joint	2	16	Revolute joint	2
7	Spacer block	2	17	End effector mounting bracket	2
8	Revolute joints	2	18	Revolute joint	2
9	Revolute joint	2	19	End effector	1
10	Actuator sub-assembly	2			

XY optical mouse sensor sub-assembly diagram is shown by Figure 4-10 and the component description and quantities are listed in Table 4-6.

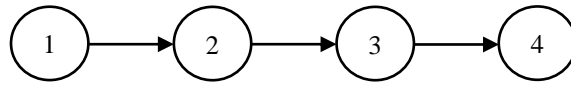


Figure 4-10: XY mouse sub-assembly diagram

Table 4-6: XY mouse optical sensor sub-assembly description and bill of materials

Item	Description	Quantity	Item	Description	Quantity
1	End effector	1	3	XY optical mouse	1
2	XY mouse bracket 2	1	4	XY mouse bracket 1	1

The testing frame developed for this research was set up differently to accommodate testing for translation and rotation. Figure 4-11 shows the testing frame sub-assembly diagram for translation testing. Table 4-7 describes the various components and quantities.

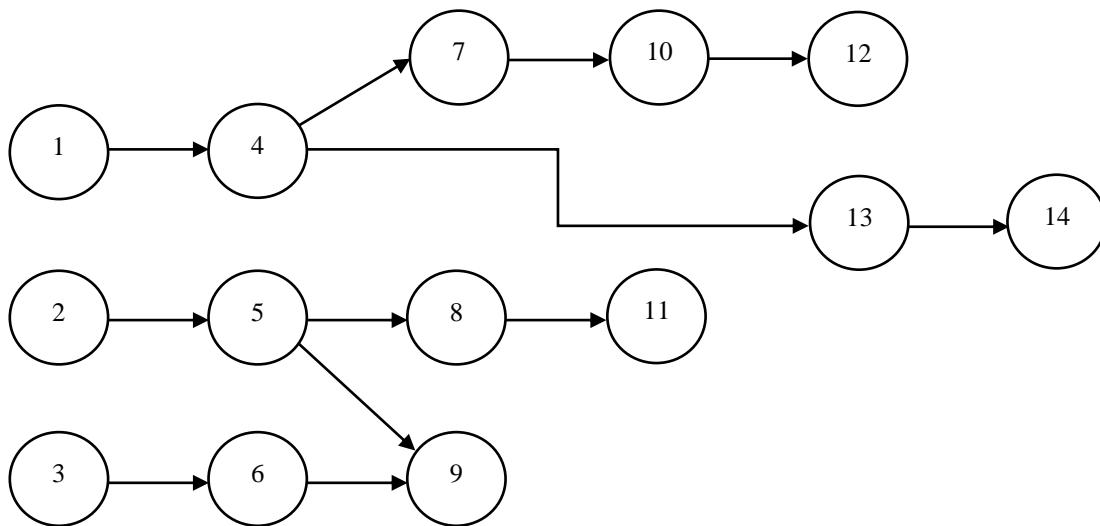


Figure 4-11: Testing frame for translation sub-assembly diagram

Table 4-7: Testing frame for translation sub-assembly description and bill of materials

Item	Description	Quantity	Item	Description	Quantity
1	Aluminium profiles	12	8	Linear bearings	4
2	XY mouse sensor sub-assembly	1	9	Mouse bracket 2	1
3	Z optical mouse	1	10	Mirror bracket 1	2
4	90° connectors	20	11	Chromed linear shaft	4
5	Wooden platform	1	12	Mirror	1
6	Mouse Z bracket 1	1	13	Bottom shaft supports	4
7	Mirror bracket 2	2	14	Top shaft supports	4

The testing frame for rotation testing is shown in Figure 4-12. An additional level comprised of aluminium extruded profiles were required. Table 4-8 shows the components used and quantities.

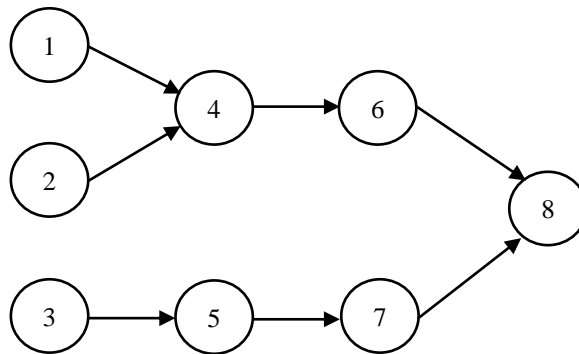


Figure 4-12: Testing frame for rotation sub-assembly diagram

Table 4-8: Testing frame for rotation sub-assembly description and bill of materials

Item	Description	Quantity	Item	Description	Quantity
1	Aluminium extruded profiles basic frame	12	5	Mirror bracket	1
2	Aluminium extruded profiles additional level	7	6	Vernier calliper brackets	2
3	End effector	1	7	Mirror	1
4	90° connectors	50	8	Vernier calliper	1

4.6 Assembly Precedence Diagram

Figure 4-13 shows the assembly diagram. Table 4-9 provides the descriptions and quantities of the components shown in Figure 4-13.

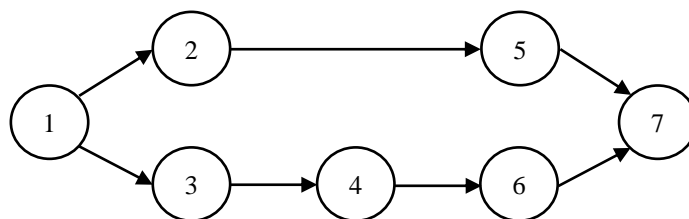


Figure 4-13: Project assembly diagram

Table 4-9: Project assembly description and bill of materials

Item	Description	Quantity	Item	Description	Quantity
1	Wooden base	1	5	Control Box	1
2	PKM sub-assembly	1	6	Testing frame sub-assembly	1
3	Wood inserts	16	7	PC	1
4	Aluminium 90° supports	8			

4.7 Chapter Summary

This chapter presented the mechanical design methodology and the system decomposition diagram. This chapter also described the mechanical design of the various components while considering AM parameters. The PKM specifications were documented. The sub-assembly and assembly precedence diagrams were presented. The following chapter discusses kinematic analysis. The inverse kinematic analysis is first presented which discusses the selected method of analysis and the homogenous transformation matrix. A novel extension of the geometric method is presented. The top layer of Simulink model for the inverse kinematics is presented with a tabulation of the various functions used to develop the model. The forward kinematic analysis is presented. The Newton Raphson (NR) method was employed and the constraint equations are presented.

5. KINEMATIC ANALYSIS

5.1 Introduction

The inverse kinematic analysis solves the actuator lengths or joint angles for a specified position and orientation of the end effector. The forward kinematic analysis solves the position and orientation of the end effector for a given set of actuator lengths or joint angles. The two commonly used methods for position and orientation analysis are the Denavit-Hartenberg (DH) method and the geometric method. The geometric method generates a vector loop to solve the position and orientation of the end effector. The DH method can be easily used for serial manipulators but is complicated for multiple closed-loop kinematic chains. Tsai [9] presented numerous examples of the geometric method and it was concluded as a feasible approach.

5.2 Homogenous Transformation Matrix

Concerning robotics, multiple coordinate systems are employed to assist in the computations of a robot's parameters such as inverse and forward kinematics, velocities and accelerations. The placement and number of coordinate systems used are up to the designer. However, the positions and orientations need to be homogeneously mapped from one coordinate system to another using a homogenous transformation matrix. This matrix is divided into four submatrices and is shown in Equation 5.1 [9]:

$$T_B^A = \begin{bmatrix} R_B^A (3 \times 3) & \vdots & q^A (3 \times 1) \\ \dots & \vdots & \dots \\ \varsigma (1 \times 3) & \vdots & \rho (1 \times 1) \end{bmatrix} \quad (5.1)$$

The upper left submatrix holds the orientation matrix of the moving frame B with respect to frame A (the fixed frame). The upper right submatrix describes the position of the origin of the moving frame B with respect to frame A and is a position vector. The lower left submatrix denotes at perspective transformation and the lower right submatrix represents a scaling factor. The study of robotic manipulators and kinematics of mechanisms sets the scaling factor to 1 and the perspective transformation to zero. The matrix is presented in Equation 5.2 [9]:

$$T_B^A = \begin{bmatrix} R_B^A (3 \times 3) & \vdots & q^A (3 \times 1) \\ \dots & \vdots & \dots \\ 0 \ 0 \ 0 & \vdots & 1 \end{bmatrix} \quad (5.2)$$

5.3 Inverse Kinematics

The methodology that was employed to generate, solve and validate the inverse kinematic equations is listed below:

1. Establish a rotation sequence.
2. Perform the outer vector loop analysis.
3. Perform the inner vector loop analyses.
4. Develop a MATLAB® script to solve the inverse kinematic equations.
5. Validate the equations via SolidWorks®.
6. Develop the Simulink model.
7. Validate the Simulink model via SolidWorks.

The Roll, Pitch and Yaw rotation sequence was used. The order of rotations is not commutative therefore, a rotation sequence needed to be established [9]. The order of rotation takes place about the x-axis (Roll), then the y-axis (Pitch) and finally the z-axis (Yaw). The rotation matrix is given by Equation 5.3.

$$R(\gamma, \beta, \alpha) = \begin{bmatrix} c\gamma c\beta & c\gamma s\beta s\alpha - s\gamma c\alpha & c\gamma s\beta c\alpha + s\gamma s\alpha \\ s\gamma c\beta & s\gamma s\beta s\alpha + c\gamma c\alpha & s\gamma s\beta c\alpha - c\gamma s\alpha \\ -s\beta & c\beta s\alpha & c\beta c\alpha \end{bmatrix} \quad (5.3)$$

Where $c = \text{cosine}$ and $s = \text{sine}$

The case of parasitic motion was not investigated in this study therefore the rotation about the z-axis was regarded as $\gamma = 0$. For $\gamma = 0$, the simplified rotation matrix is shown in Equation 5.4.

$$R(\beta, \alpha) = \begin{bmatrix} c\beta & s\beta s\alpha & s\beta c\alpha \\ 0 & c\alpha & -s\alpha \\ -s\beta & c\beta s\alpha & c\beta c\alpha \end{bmatrix} \quad (5.4)$$

5.3.1 Extension of the Geometric Method

The geometric method applied to solve the inverse kinematics is a novel extension due to the existence of offset revolute joints. The offsets introduce passive angles, therefore, more variables [111, 120]. The architectural design was exploited. Outer and inner vector loops were employed. Figure 5-1a shows a side view of the PKM and a vector loop generally employed. The general vector loop uses four points of interest to construct the vector loop. The vector over-arching the linear actuator is meant to be the only unknown variable (vector). The vector of interest, as shown in Figure 5-1, is identified in red. The red vector, representing the vector from the base to the bottom of the actuator, changes as the end effector moves is, therefore, a free variable as depicted in Figure 5-1b and Figure 5-1c. The position of the bottom of the linear actuator moves along an arc, represented in orange, as the PKM moves.

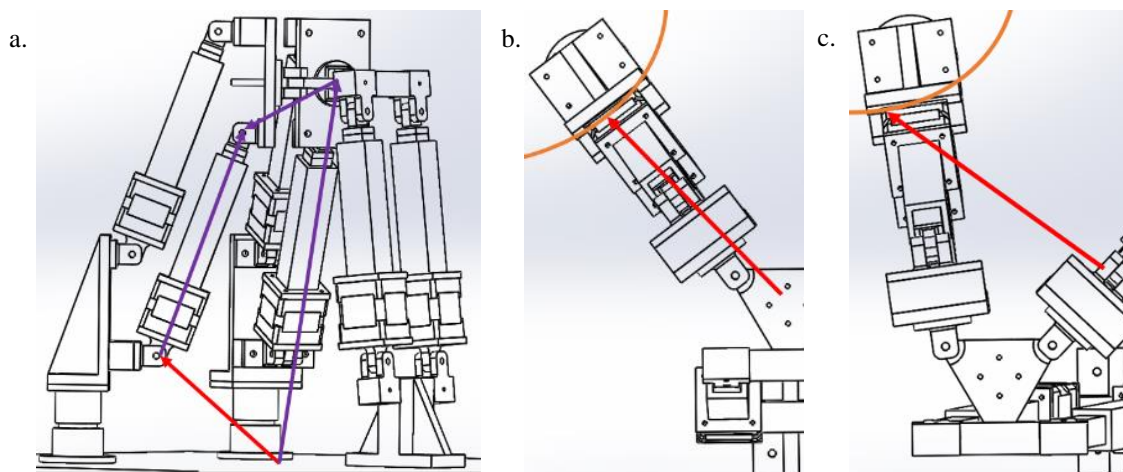


Figure 5-1: General vector diagram with the top view of the PKM

- The red arrow highlighting the vector from O to B .
- The end effector in its home position.
- The change in the length and direction of the red vector.

5.3.2 Inverse Kinematic Relationships through the Outer Vector Loop Method

Figure 5-2 depicts the outer vector loop for actuators 1 and 2. The outer vector loop was developed such that the passive rotations occurring at points A, B, C and D do not need to be known in order to perform the inverse kinematic analysis. Two different paths are taken from point O to point D .

The vectors used in Equation 5.5 were chosen such that \overrightarrow{OA} and \overrightarrow{PD} are machine parameters. Point P is a user-defined input of the position of the end effector. It follows that vector \overrightarrow{OP} is a user-defined vector. The only unknown is the vector \overrightarrow{AD} . The coordinates of vector \overrightarrow{PD} are known relative to a local coordinate frame placed at point P . Vector \overrightarrow{PD} rotates and a rotational matrix was multiplied to it to resolve its position relative to the global coordinate frame placed at point O . The resulting equation can be applied to the leg pair 3 and 4 as well as for leg pair 5 and 6. The generic outer vector loop equation is given by Equation 5.5

$$\overrightarrow{OA} + \overrightarrow{AD} = \overrightarrow{OP} + R(\gamma, \beta, \alpha)\overrightarrow{PD} \quad (5.5)$$

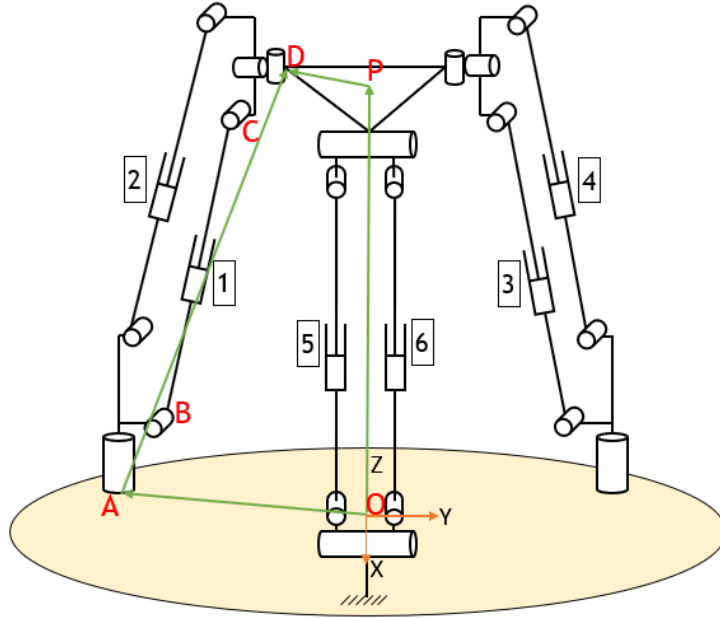


Figure 5-2: Outer vector loop

Equation 5.6 describes the outer vector shown in Figure 5-2. Equation 5.6 is expanded to Equation 5.7 and 5.8 to illustrate the methodology of performing the outer vector loop analysis.

$$\overrightarrow{OA_{1,2}} + \overrightarrow{A_{1,2}D_{1,2}} = \overrightarrow{OP} + R(\beta, \alpha)\overrightarrow{PD_{1,2}} \quad (5.6)$$

$$\begin{bmatrix} (\overrightarrow{OA_{1,2}})_x \\ (\overrightarrow{OA_{1,2}})_y \\ (\overrightarrow{OA_{1,2}})_z \end{bmatrix} + \begin{bmatrix} (\overrightarrow{A_{1,2}D_{1,2}})_x \\ (\overrightarrow{A_{1,2}D_{1,2}})_y \\ (\overrightarrow{A_{1,2}D_{1,2}})_z \end{bmatrix} = \begin{bmatrix} (\overrightarrow{OP})_x \\ (\overrightarrow{OP})_y \\ (\overrightarrow{OP})_z \end{bmatrix} + \begin{bmatrix} c\beta & s\beta & s\alpha & s\beta & c\alpha \\ 0 & c\alpha & -s\alpha & & \\ -s\beta & c\beta & s\alpha & c\beta & c\alpha \end{bmatrix} \begin{bmatrix} (\overrightarrow{PD_{1,2}})_x \\ (\overrightarrow{PD_{1,2}})_y \\ (\overrightarrow{PD_{1,2}})_z \end{bmatrix} \quad (5.7)$$

$$\begin{bmatrix} (\overrightarrow{A_{1,2}D_{1,2}})_x \\ (\overrightarrow{A_{1,2}D_{1,2}})_y \\ (\overrightarrow{A_{1,2}D_{1,2}})_z \end{bmatrix} = \begin{bmatrix} (\overrightarrow{OP})_x + c\beta(\overrightarrow{PD_{1,2}})_x + s\beta s\alpha(\overrightarrow{PD_{1,2}})_y + s\beta c\alpha(\overrightarrow{PD_{1,2}})_z - (\overrightarrow{OA_{1,2}})_x \\ (\overrightarrow{OP})_y + c\alpha(\overrightarrow{PD_{1,2}})_y - s\alpha(\overrightarrow{PD_{1,2}})_z - (\overrightarrow{OA_{1,2}})_y \\ (\overrightarrow{OP})_z - s\beta(\overrightarrow{PD_{1,2}})_x + c\beta s\alpha(\overrightarrow{PD_{1,2}})_y + c\beta c\alpha(\overrightarrow{PD_{1,2}})_z - (\overrightarrow{OA_{1,2}})_z \end{bmatrix} \quad (5.8)$$

Let each equation be isolated as for simplicity as presented by Equation 5.9 to 5.11.

$$L = (\overrightarrow{OP})_x + c\beta(\overrightarrow{PD}_{1,2})_x + s\beta s\alpha(\overrightarrow{PD}_{1,2})_y + s\beta c\alpha(\overrightarrow{PD}_{1,2})_z - (\overrightarrow{OA}_{1,2})_x \quad (5.9)$$

$$M = (\overrightarrow{OP})_y + c\alpha(\overrightarrow{PD}_{1,2})_x - s\alpha(\overrightarrow{PD}_{1,2})_z - (\overrightarrow{OA}_{1,2})_y \quad (5.10)$$

$$N = (\overrightarrow{OP})_z - s\beta(\overrightarrow{PD}_{1,2})_x + c\beta s\alpha(\overrightarrow{PD}_{1,2})_y + c\beta c\alpha(\overrightarrow{PD}_{1,2})_z - (\overrightarrow{OA}_{1,2})_z \quad (5.11)$$

The magnitude of vector $\overrightarrow{A_{1,2}D_{1,2}}$ is found by the calculation performed in Equation 5.12.

$$|\overrightarrow{A_{1,2}D_{1,2}}| = \sqrt{\begin{pmatrix} (\overrightarrow{A_{1,2}D_{1,2}})_x \\ (\overrightarrow{A_{1,2}D_{1,2}})_y \\ (\overrightarrow{A_{1,2}D_{1,2}})_z \end{pmatrix}^2} = \sqrt{(L)^2 + (M)^2 + (N)^2} \quad (5.12)$$

$|\overrightarrow{A_{1,2}D_{1,2}}|$ was carried forward into the inner vector loop analysis to solve the length of actuator 1.

5.3.3 Inverse Kinematic Relationships through the Inner Vector Loop Method

The inner vector loop equations were reduced to a Two-Dimensional (2D) analysis. Figure 5-3 shows a plane that actuators 1 and 2 lie along and illustrates the coplanar nature of the pair of legs. Figure 5-3a and Figure 5-3b shows different views of the pair of legs comprising of actuator 1 and 2. The arrangement of the revolute joints influences the coplanar nature of the actuators.

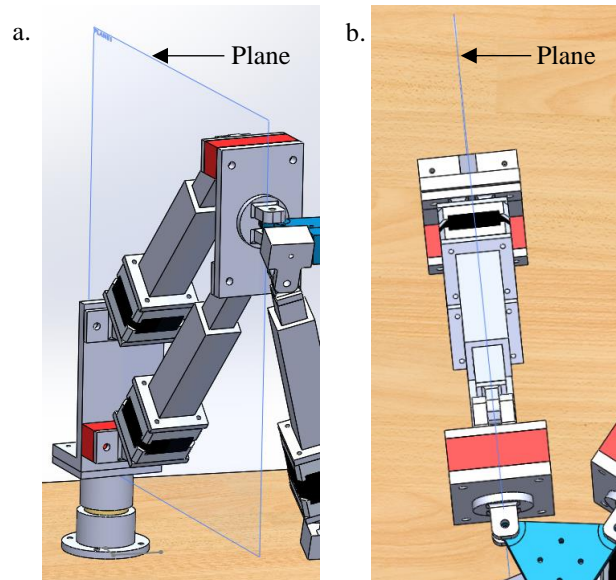


Figure 5-3: Two different views illustrating the coplanar nature of a pair of legs

- Isometric view of the plane.
- Top view of the PKM with the plane indicating the coplanar nature of the pair of legs.

Figure 5-4a and Figure 5-4b shows the vector loops for actuators 1 and 2 and for 5 and 6 respectively. Actuators 1 and 2 share joints at point A and point D , therefore, vector \overrightarrow{AD} was used in both inner vector loop equations. The inner vector loop equation was formed by taking two different paths from point A to point D . A local coordinate system was placed at point A , as shown in Figure 5-4. Vector \overrightarrow{AD} had to be reduced from a 3D vector into a 2D vector. Considering vector \overrightarrow{AD} along the 2D plane, the y value from vector \overrightarrow{AD} was omitted without losing vector integrity. The z value for vector \overrightarrow{AD} was retained from the outer vector loop calculation. The x value was calculated through the theorem of Pythagoras.

Once the 2D variation of vector \overrightarrow{AD} was calculated, the inner vector loop was established and solved. Vector \overrightarrow{AB} and vector \overrightarrow{CD} are machine parameters. Vector \overrightarrow{BC} was the only unknown vector which represented the length of the actuator. This method was repeated for the leg pair containing actuators 3 and 4 since they are identical to the arrangement of actuators 1 and 2. The approach was altered for solving leg lengths of actuator 5 and 6. The x value was omitted and the y value of vector \overrightarrow{AD} was retained from the outer vector loop calculation. The z value for vector \overrightarrow{AD} for leg pair 5 and 6 was calculated through the theorem of Pythagoras.

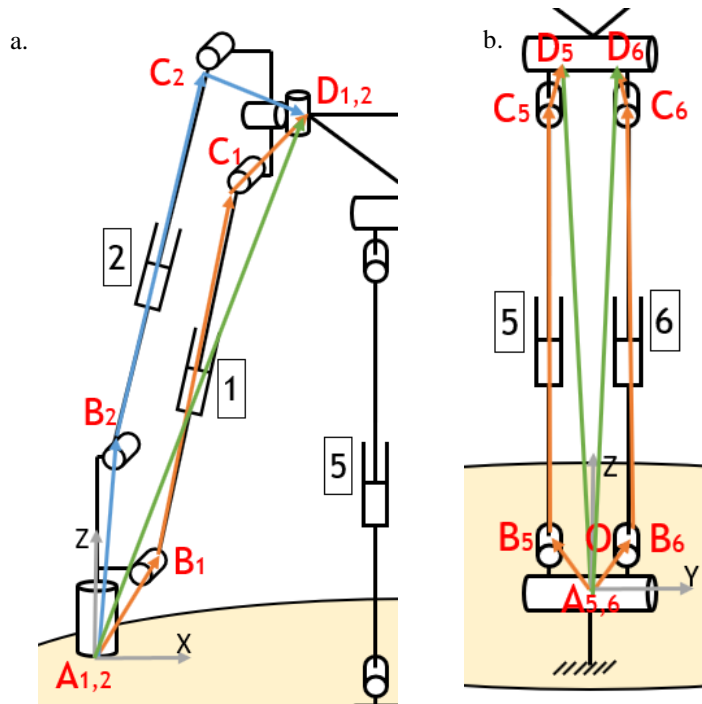


Figure 5-4: Inner vector loop for leg 1 and leg 2

- The inner vector loop for leg 1 and 2 which can be applied to leg 3 and 4.
- The inner vector loop for leg 5 and 6.

Equations 5.13 to 5.16 illustrate the inner vector loop equations.

$$\overrightarrow{B_i C_i} = \overrightarrow{A_{1,2} D_{1,2}} - \overrightarrow{A_{1,2} B_i} - \overrightarrow{C_i D_{1,2}} \quad (5.13)$$

Where $i = 1$ or 2

$$\overrightarrow{B_j C_j} = \overrightarrow{A_{3,4} D_{3,4}} - \overrightarrow{A_{3,4} B_j} - \overrightarrow{C_j D_{3,4}} \quad (5.14)$$

Where $j = 3$ or 4

$$\overrightarrow{B_5 C_5} = \overrightarrow{A_{5,6} D_5} - \overrightarrow{A_{5,6} B_5} - \overrightarrow{C_5 D_5} \quad (5.15)$$

$$\overrightarrow{B_6 C_6} = \overrightarrow{A_{5,6} D_6} - \overrightarrow{A_{5,6} B_6} - \overrightarrow{C_6 D_6} \quad (5.16)$$

Equation 5.13 is expanded into Equation 5.17 for actuators 1 and 2.

$$\begin{bmatrix} \overrightarrow{(B_i C_i)}_x \\ \overrightarrow{(B_i C_i)}_y \\ \overrightarrow{(B_i C_i)}_z \end{bmatrix} = \begin{bmatrix} \overrightarrow{(A_{1,2} D_{1,2})}_x \\ \overrightarrow{(A_{1,2} D_{1,2})}_y \\ \overrightarrow{(A_{1,2} D_{1,2})}_z \end{bmatrix} - \begin{bmatrix} \overrightarrow{(A_{1,2} B_i)}_x \\ \overrightarrow{(A_{1,2} B_i)}_y \\ \overrightarrow{(A_{1,2} B_i)}_z \end{bmatrix} - \begin{bmatrix} \overrightarrow{(C_i D_{1,2})}_x \\ \overrightarrow{(C_i D_{1,2})}_y \\ \overrightarrow{(C_i D_{1,2})}_z \end{bmatrix} \quad (5.17)$$

Since Equation 5.17 is in terms of the x-z plane, all y values were set to zero. Equation 5.17 was expanded into Equation 5.18 and 5.19.

$$\begin{bmatrix} \overrightarrow{(B_i C_i)}_x \\ 0 \\ \overrightarrow{(B_i C_i)}_z \end{bmatrix} = \begin{bmatrix} \sqrt{|\overrightarrow{A_{1,2} D_{1,2}}|^2 - (\overrightarrow{A_{1,2} D_{1,2}})_z^2} \\ 0 \\ \overrightarrow{(A_{1,2} D_{1,2})}_z \end{bmatrix} - \begin{bmatrix} \overrightarrow{(A_{1,2} B_i)}_x \\ 0 \\ \overrightarrow{(A_{1,2} B_i)}_z \end{bmatrix} - \begin{bmatrix} \overrightarrow{(C_i D_{1,2})}_x \\ 0 \\ \overrightarrow{(C_i D_{1,2})}_z \end{bmatrix} \quad (5.18)$$

$$\begin{bmatrix} \overrightarrow{(B_i C_i)}_x \\ 0 \\ \overrightarrow{(B_i C_i)}_z \end{bmatrix} = \begin{bmatrix} \sqrt{|\overrightarrow{A_{1,2} D_{1,2}}|^2 - (\overrightarrow{A_{1,2} D_{1,2}})_z^2} - \overrightarrow{(A_{1,2} B_i)}_x - \overrightarrow{(C_i D_{1,2})}_x \\ 0 \\ \overrightarrow{(A_{1,2} D_{1,2})}_z - \overrightarrow{(A_{1,2} B_i)}_z - \overrightarrow{(C_i D_{1,2})}_z \end{bmatrix} \quad (5.19)$$

Let the first row be represented by Equation 5.20.

$$Q = \sqrt{|\overrightarrow{A_{1,2} D_{1,2}}|^2 - (\overrightarrow{A_{1,2} D_{1,2}})_z^2} - \overrightarrow{(A_{1,2} B_i)}_x - \overrightarrow{(C_i D_{1,2})}_x \quad (5.20)$$

Let the third row be represented by Equation 5.21.

$$R = \overrightarrow{(A_{1,2} D_{1,2})}_z - \overrightarrow{(A_{1,2} B_i)}_z - \overrightarrow{(C_i D_{1,2})}_z \quad (5.21)$$

The magnitude of the vector $\overrightarrow{B_i C_i}$ is given by Equation 5.22.

$$|\overrightarrow{B_i C_i}| = \begin{bmatrix} \overrightarrow{(B_i C_i)}_x \\ 0 \\ \overrightarrow{(B_i C_i)}_z \end{bmatrix} = \sqrt{(Q)^2 + (R)^2} \quad (5.22)$$

All equations up to and including Equation 5.22 can be used to solve the position of the end effector for translation.

When the end effector performed an alpha or beta rotation, vector $\overrightarrow{C_i D_{1,2}}$ was altered. Figure 5-5 illustrates how

the x and z components of vector \overline{CD} was altered when the end effector performed rotation. Additional points of interest were used namely point $E_{1,2}$ and $F_{1,2}$. These points are colinear to $D_{1,2}$. The rotation matrix is also applied to the vectors \overline{PE} and \overline{PF} thus maintaining integrity of all calculations. The line joining points D, E and F is parallel to the vector component $(\overline{C_1D_{1,2}})_z$ and the mounting bracket. The gradient of the line EF was calculated which is equal to the gradient of $(\overline{C_1D_{1,2}})_z$ to the horizontal. Angle ψ_1 was then solved and the length of $(\overline{C_1D_{1,2}})_x'$ and $(\overline{C_1D_{1,2}})_z'$ was calculated through trigonometric calculations. The same procedure is used for other pairs of legs and the calculation varies slightly to accommodate for the mounting bracket either leaning forward or backward. A positive rotation refers to a positive gradient of the line EF . Appendix C.4 illustrates all other cases of the tilting mounting brackets and the associated calculations.

Leg 1 and 3 Positive Rotation

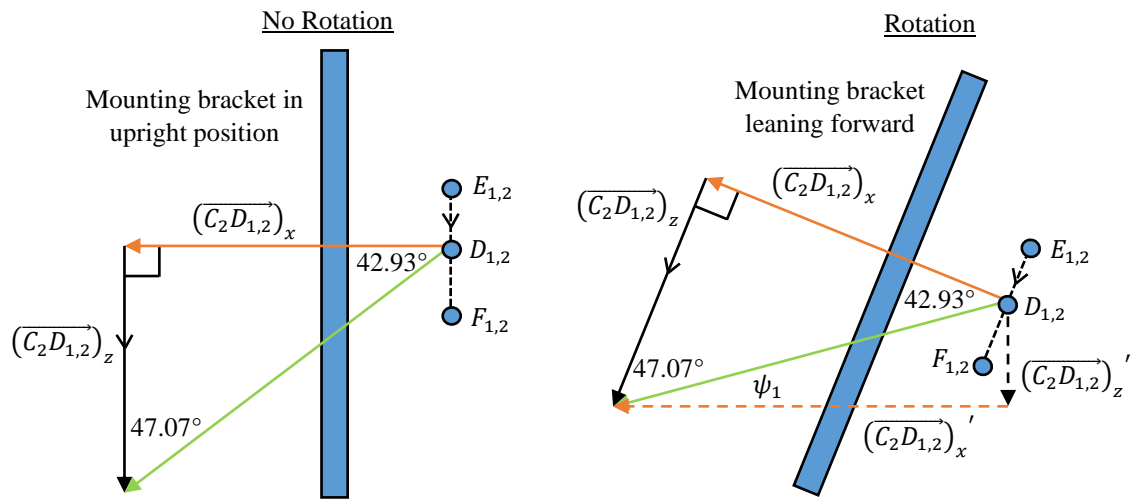


Figure 5-5: One of the cases of the x and z components of vector CD being altered

The rotational analysis for vector $\overline{C_1D_{1,2}}$ was examined for leg length 1. Equation 5.23 calculates the gradient of line EF and Equation 5.24 and 5.25 solves ψ_1 .

$$m_1 = \frac{\Delta z}{\Delta x} = \frac{(\overline{PE_{1,2}} - \overline{PF_{1,2}})_z}{(\overline{PE_{1,2}} - \overline{PF_{1,2}})_x} \quad (5.23)$$

$$\psi_1 + 47.07^\circ = \tan^{-1}(m_1) \quad (5.24)$$

$$\therefore \psi_1 = \tan^{-1}(m_1) - 47.07^\circ \quad (5.25)$$

Equation 5.26 and 5.27 solves the new x and z components of the vector $\overline{C_1D_{1,2}}$.

$$(\overline{C_1D_{1,2}})_x' = |\overline{C_1D_{1,2}}| \cos \psi_1 \quad (5.26)$$

$$(\overrightarrow{C_1D_{1,2}})_z' = |\overrightarrow{C_1D_{1,2}}| \sin \psi_1 \quad (5.27)$$

For rotation of the end effector, $(\overrightarrow{C_1D_{1,2}})_x$ and $(\overrightarrow{C_1D_{1,2}})_z$ were replaced in Equation 5.17 by $(\overrightarrow{C_1D_{1,2}})_x'$ and $(\overrightarrow{C_1D_{1,2}})_z'$ respectively. When alpha or beta rotation occurs, the mounting brackets can rotate in different combinations. The inverse kinematic solution accommodated 13 different cases excluding parasitic motion. The solution was based on the combination of translation and rotation of the end effector and the gradients of the mounting brackets for leg pair 1 and 2, leg pair 3 and 4 and the gradient of the joint from D5 to D6. Table 5-1 presents the cases of the inverse kinematic solution.

Table 5-1: The 13 different cases of inverse kinematic solutions

Orientation of end effector	Gradients of brackets and joints		
	Mounting bracket for leg pair 1 and 2	Mounting bracket for leg pair 3 and 4	Joint from D5 to D6
Only Translation (no rotation)	90°	90°	0°
Only Beta rotation and translation	Positive	Positive	0°
	Negative	Negative	0°
Only Alpha rotation and translation (Positive Alpha)	Negative	Positive	Positive
	Positive	Positive	Positive
	Negative	Negative	Positive
	90°	Positive	Positive
	Negative	90°	Positive
Only Alpha rotation and translation (Negative Alpha)	Positive	Negative	Negative
	Positive	Positive	Negative
	Negative	Negative	Negative
	90°	Negative	Negative
	Positive	90°	Negative

The inverse kinematic calculations were programmed in MATLAB® and the results of the simulations were documented in Section 8. Appendix B.1 presents the MATLAB® script files for the inverse kinematic analysis.

5.3.4 Inverse Kinematic Simulink Model

The inverse kinematics was also developed on Simulink. The purpose of developing a Simulink model was to validate the inverse kinematic equations and to allow future work to be carried out on Simulink. Figure 5-6 shows the top level of the Simulink model. The model flowed from left to right. The leftmost blocks were the constant blocks used as inputs for position and orientation of the end effector. The blue and orange blocks were machine parameters configured as matrices. The sequence of calculations was followed from Section 5.3.2 and Section 5.3.3. The various blocks used for the Simulink model are described in Table 5-2.

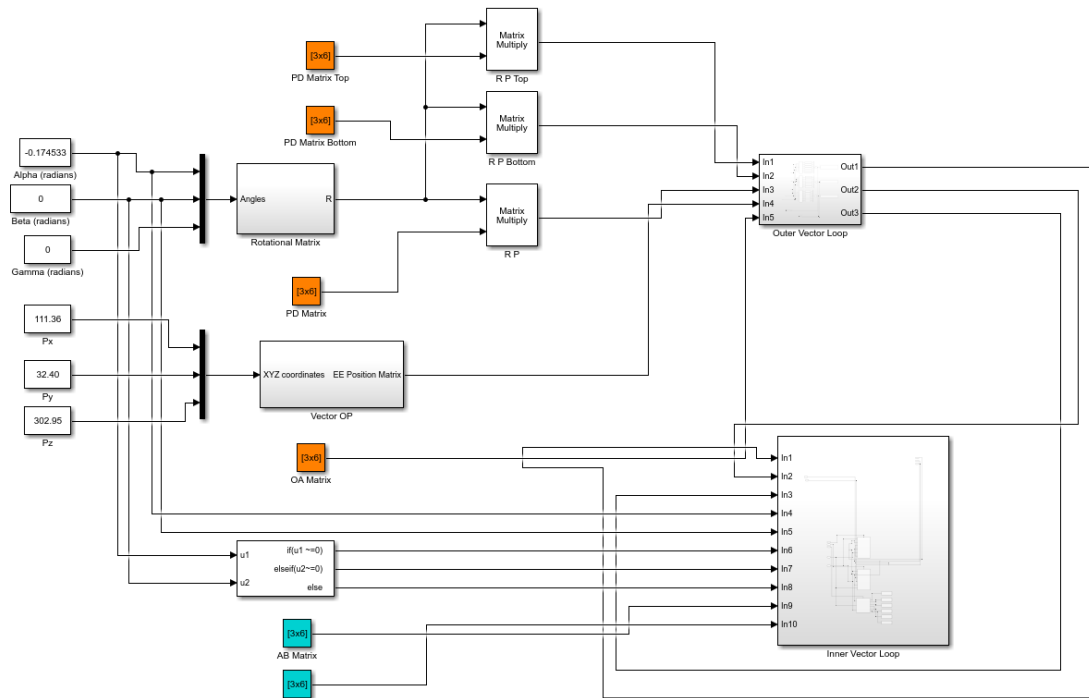
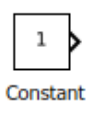
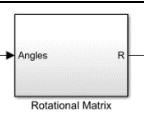
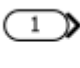
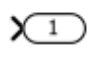


Figure 5-6: Simulink model for the inverse kinematics

Table 5-2: Description of Simulink function blocks used

Simulink Block	Symbol	Function and Application
Constant	 Constant	The constant block was used to input constants and matrices into the Simulink model.
Subsystem	 Rotational Matrix	The subsystem function was used to group multiple blocks together.
Inport	 In1	The inport block assisted in transferring data into subsystems.
Outport	 Out1	The outport block assisted in transferring data out of subsystems.


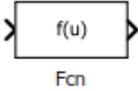
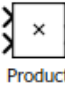





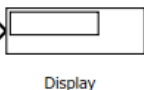
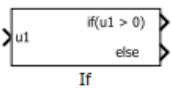
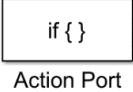
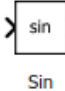
Simulink Block	Symbol	Function and Application
Mux		The mux was used to store more 2 or more signals or constants that were used in multiple equations. This reduced using numerous connectors.
Fcn		The Fcn block was used to read variables from the mux and used the values in symbolic equations created inside the Fcn block.
Product		The product block was used for simple straightforward and matrix multiplication.
Reshape		The reshape block was used to take signals from muxes and configure them into a matrix.
Add		The addition block was used to add matrices when performing the outer and inner loop calculations.
Dot product		The dot product was used to multiply constants by themselves.
Selector		The selector block was used to index different columns of vectors from matrices stored in constant and reshape blocks. Selector blocks condensed the Simulink model and was used frequently.
Square root		The square root function was used to solve the magnitudes of the vectors.
Display		Display blocks were useful for checking intermediate and final values. These blocks validated the accuracy of the Simulink model.
If		The If block was useful to replicate the inverse kinematic MATLAB® script file to accommodate for the 13 different cases of inverse kinematic solutions.
Action port		If action port was linked to the If block. This block was embedded into a subsystem block to account for the different If conditions.
Trigonometric Functions		Atan, sin and cos blocks were used. The trigonometric blocks have the same appearance.

Figure 5-7 illustrates an excerpt from the Simulink model representing vector \overline{AD} in Equation 5.18. Simulink blocks such as inport, selector, subsystem, dot product, add, square root, mux, constant and outport functions were used.

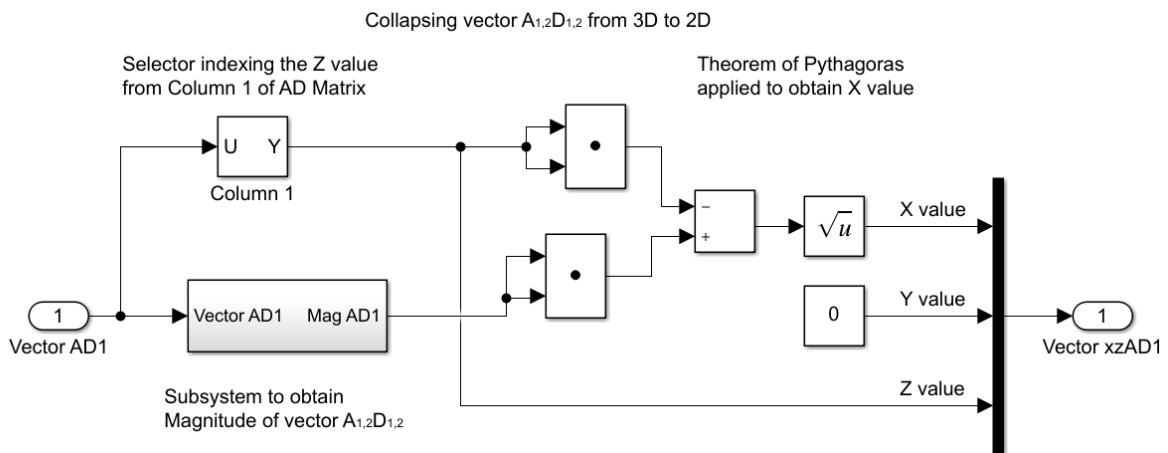


Figure 5-7: A close-up typical calculation using various blocks

5.4 Forward Kinematics

The forward kinematic equations are generally difficult to solve for PKMs due to multiple nonlinear equations. In a research performed by Borras [121], it was stated that the resolution of the forward kinematics is necessary for control, on-line simulation and for gauging the performance of a PKM. When the forward kinematics has a closed-form solution, this aids in providing fast and accurate computations as well as simplifies the error analysis. Nielsen and Roth stated that the three most useful techniques are a polynomial continuation, Grobner bases and the elimination method [122].

The polynomial continuation method is a numerical solution. This method is useful to solve actual numerical values by running experiments but its drawback lies in it not providing much assistance to general cases whereby symbolic parameters are used as metrics. The polynomial continuation method can find all possible solutions. The elimination method is an algebraic method that can eliminate large numbers of variables in one step and therefore can reduce nonlinear equations into a single polynomial containing one unknown. This method has proven to be useful when studying systems of equations on a symbolic level. Its disadvantage is that it requires more equation manipulation than continuation methods.

A method that proves to be useful in conjunction with the elimination method is the Grobner bases. This is an iterative approach that uses a variable-elimination technique. This method resembles a triangular set of equations based on Gaussian elimination techniques. The Grobner bases is useful in determining the upper bound of the possible number of solutions when legs of the robot share pivot points. The disadvantage of the Grobner bases is that there can be the generation of intermediate polynomials when carrying out the process. This leads to longer computational time and the complexity of a given problem is therefore unpredictable [122].

5.4.1 Newton Raphson Method

The NR method is a numerical iterative method that converges to a solution for a set of equations. This method possesses a local convergence property. The NR method converges quadratically. This method breaks down when the Jacobian is equal to zero. Figure 5-8 illustrates how convergence is achieved [123].

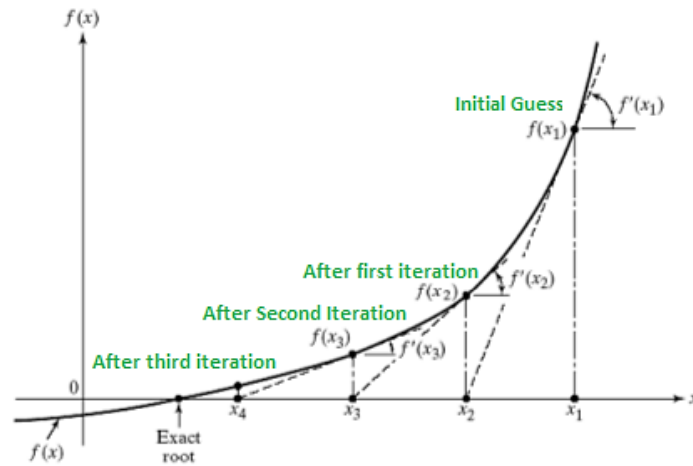


Figure 5-8: A graphical representation of the execution of the NR method

The NR method has been used by various researchers to solve the forward kinematics problem concerned with PKMs. Abo-Shanab [124] used the NR method to solve the forward kinematics for a 3RRR planar manipulator. Yang et al. [125] used a Global NR analysis on a 6 UPU PKM. This is a variation of the traditional NR method which applies a first-order Taylor Series expansion. The computational time was 0.0083 ms. Jacobovic and Budin [126] used various algorithms for the forward kinematics on a Stewart Platform inclusive of the NR approach which was found to be a successful optimization method. A hybrid strategy for the forward kinematic solution was investigated by Parikh and Lam [127]. This method employed the use of neural networks together with the NR method. Results based on a flight simulation showed that the position accuracy was close to 0.01 mm and the angular accuracy was close to 0.01° with an execution time of 0.02 s.

5.4.2 Derivation of the Constraint Equations

The equations can be expressed as functions of $(\overline{OP})_x$, $(\overline{OP})_y$, $(\overline{OP})_z$, α , β , θ_1 , θ_3 and θ_5 . The NR method makes use of the Jacobian matrix. It is preferred that the Jacobian matrix is a square matrix since it simplifies calculations which also aids in obtaining the determinant. The PKM developed possessed 6 actuators and possessed 5 DOFs with a parasitic rotation. The parasitic rotation was not investigated in this study.

Figure 5-9 depicts the virtual leg between actuator 5 and 6. The virtual leg, replacing actuators 5 and 6, is only used for the translation analysis and beta rotation with translation because the legs maintain equal length. $(\overline{OP})_x$, $(\overline{OP})_y$, $(\overline{OP})_z$, α and β were the unknown variables for translation. One actuator from each pair of legs was used for the forward kinematic analysis to eliminate the high similarity between equations and assist the computations of the Jacobian.

For translation, variables that needed to be solved were $(\overline{OP})_x$, $(\overline{OP})_y$ and $(\overline{OP})_z$. Additional equations were incorporated to account for the inner vector loop equations. The variables θ_1 , θ_3 and θ_5 were introduced as shown

in Figure 5-9. θ_1 , θ_3 and θ_5 represent the angles between the base and actuator 1, 3 and 5 respectively. Equation 5.28 to 5.36 presents the constraint equations for the translation case.

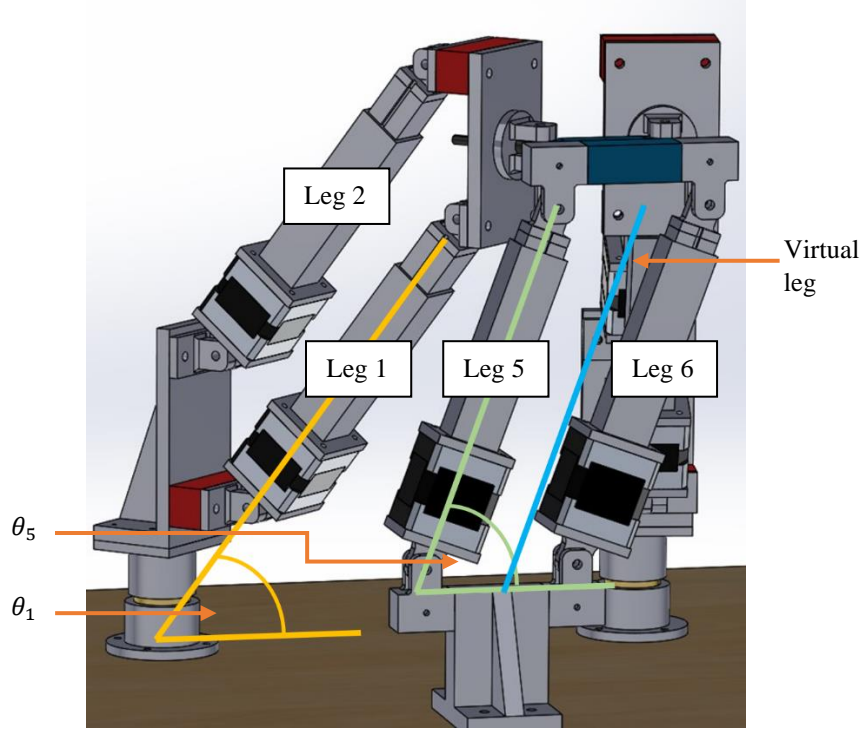


Figure 5-9: The location of theta 1 and theta 5

$$\begin{aligned}
 f_1 \left((\overline{OP})_x, (\overline{OP})_y, (\overline{OP})_z, \theta_1, \theta_3, \theta_5 \right) \\
 = \left((\overline{OP})_x + (\overline{PD}_{1,2})_x - (\overline{OA}_{1,2})_x \right)^2 + \left((\overline{OP})_y + (\overline{PD}_{1,2})_y - (\overline{OA}_{1,2})_y \right)^2 \\
 + \left((\overline{OP})_z + (\overline{PD}_{1,2})_z - (\overline{OA}_{1,2})_z \right)^2 - (\overline{A_{1,2}D_{1,2}})^2
 \end{aligned} \quad (5.28)$$

$$\text{Where } (\overline{A_{1,2}D_{1,2}})^2 = \left((\overline{A_{1,2}B_1})_x + \text{length1} \times \cos\theta_1 + (\overline{C_1D_{1,2}})_x \right)^2 + \left((\overline{A_{1,2}B_1})_y + \text{length1} \times \sin\theta_1 + (\overline{C_1D_{1,2}})_y \right)^2 + \left((\overline{A_{1,2}B_1})_z + \text{length1} \times \cos\theta_1 + (\overline{C_1D_{1,2}})_z \right)^2 \quad (5.29)$$

$$\begin{aligned}
 f_2 \left((\overline{OP})_x, (\overline{OP})_y, (\overline{OP})_z, \theta_1, \theta_3, \theta_5 \right) \\
 = \left((\overline{OP})_x + (\overline{PD}_{3,4})_x - (\overline{OA}_{3,4})_x \right)^2 + \left((\overline{OP})_y + (\overline{PD}_{3,4})_y - (\overline{OA}_{3,4})_y \right)^2 \\
 + \left((\overline{OP})_z + (\overline{PD}_{3,4})_z - (\overline{OA}_{3,4})_z \right)^2 - (\overline{A_{3,4}D_{3,4}})^2
 \end{aligned} \quad (5.30)$$

$$\text{Where } (\overline{A_{3,4}D_{3,4}})^2 = \left((\overline{A_{3,4}B_3})_x + \text{length3} \times \cos\theta_3 + (\overline{C_3D_{3,4}})_x \right)^2 + \left((\overline{A_{3,4}B_3})_y + \text{length3} \times \sin\theta_3 + (\overline{C_3D_{3,4}})_y \right)^2 + \left((\overline{A_{3,4}B_3})_z + \text{length3} \times \cos\theta_3 + (\overline{C_3D_{3,4}})_z \right)^2 \quad (5.31)$$

$$\begin{aligned}
 f_3 \left((\overline{OP})_x, (\overline{OP})_y, (\overline{OP})_z, \theta_1, \theta_3, \theta_5 \right) \\
 = \left((\overline{OP})_x + (\overline{PD}_5)_x - (\overline{OA}_{5,6})_x \right)^2 + \left((\overline{OP})_y + (\overline{PD}_5)_y - (\overline{OA}_{5,6})_y \right)^2 \\
 + \left((\overline{OP})_z + (\overline{PD}_5)_z - (\overline{OA}_{5,6})_z \right)^2 - (\overline{A_{5,6}D_5})^2
 \end{aligned} \quad (5.32)$$

$$\text{Where } (\overline{A_{5,6}D_6})^2 = \left((\overline{A_{5,6}B_5})_y + \text{length5} \times \cos\theta_5 + (\overline{C_5D_5})_y \right)^2 + \left((\overline{A_{5,6}B_5})_z + \text{length5} \times \sin\theta_5 + (\overline{C_5D_5})_z \right)^2 \quad (5.33)$$

$$f_4 \left((\overline{OP})_x, (\overline{OP})_y, (\overline{OP})_z, \theta_1, \theta_3, \theta_5 \right) = \overline{A_{1,2}B_1} + \text{length1} \times \sin\theta_1 + \overline{C_1D_{1,2}} - (\overline{OP})_z \quad (5.34)$$

$$f_5 \left((\overline{OP})_x, (\overline{OP})_y, (\overline{OP})_z, \theta_1, \theta_3, \theta_5 \right) = \overline{A_{3,4}B_3} + \text{length3} \times \sin\theta_3 + \overline{C_3D_{3,4}} - (\overline{OP})_z \quad (5.35)$$

$$f_6 \left((\overline{OP})_x, (\overline{OP})_y, (\overline{OP})_z, \theta_1, \theta_3, \theta_5 \right) = \overline{A_{5,6}B_5} + \text{length5} \times \cos\theta_5 + \overline{C_5D_5} - (\overline{OP})_y \quad (5.36)$$

The alpha and beta rotation cases were extensions of the equations from the translation case. For the isolated alpha rotation with translation, Equation 5.37 was added. The *gradient* variable was introduced to account for the α variable. The alpha rotation did not use the virtual leg since the actuation length for legs 5 and 6 are different for α rotation.

$$f_7 \left((\overline{OP})_x, (\overline{OP})_y, (\overline{OP})_z, \alpha, \theta_1, \theta_3, \theta_5 \right) = \text{gradient} - \tan(\alpha) \quad (5.37)$$

For the isolated beta rotation with translation, Equation 5.38 was introduced. The beta rotation made use of the virtual leg since the actuation length for leg 5 and 6 is the same for β rotation.

$$f_7 \left((\overline{OP})_x, (\overline{OP})_y, (\overline{OP})_z, \beta, \theta_1, \theta_3, \theta_5 \right) = \text{gradient} - \tan(\beta) \quad (5.38)$$

Equation 5.39 presents the Jacobian matrix for the case of isolated alpha rotation with translation. The Jacobian matrix was developed similarly when the calculations regarding translation and isolated beta rotation with translation were performed.

$$J_{\alpha \text{ and } T} \left((\overline{OP})_x, (\overline{OP})_y, (\overline{OP})_z, \alpha, \theta_1, \theta_3, \theta_5 \right) = \begin{bmatrix} \frac{\partial f_1}{\partial (\overline{OP})_x} & \frac{\partial f_1}{\partial (\overline{OP})_y} & \frac{\partial f_1}{\partial (\overline{OP})_z} & \frac{\partial f_1}{\partial \alpha} & \frac{\partial f_1}{\partial \theta_1} & \frac{\partial f_1}{\partial \theta_3} & \frac{\partial f_1}{\partial \theta_5} \\ \frac{\partial f_2}{\partial (\overline{OP})_x} & \frac{\partial f_2}{\partial (\overline{OP})_y} & \frac{\partial f_2}{\partial (\overline{OP})_z} & \frac{\partial f_2}{\partial \alpha} & \frac{\partial f_2}{\partial \theta_1} & \frac{\partial f_2}{\partial \theta_3} & \frac{\partial f_2}{\partial \theta_5} \\ \frac{\partial f_3}{\partial (\overline{OP})_x} & \frac{\partial f_3}{\partial (\overline{OP})_y} & \frac{\partial f_3}{\partial (\overline{OP})_z} & \frac{\partial f_3}{\partial \alpha} & \frac{\partial f_3}{\partial \theta_1} & \frac{\partial f_3}{\partial \theta_3} & \frac{\partial f_3}{\partial \theta_5} \\ \frac{\partial f_4}{\partial (\overline{OP})_x} & \frac{\partial f_4}{\partial (\overline{OP})_y} & \frac{\partial f_4}{\partial (\overline{OP})_z} & \frac{\partial f_4}{\partial \alpha} & \frac{\partial f_4}{\partial \theta_1} & \frac{\partial f_4}{\partial \theta_3} & \frac{\partial f_4}{\partial \theta_5} \\ \frac{\partial f_5}{\partial (\overline{OP})_x} & \frac{\partial f_5}{\partial (\overline{OP})_y} & \frac{\partial f_5}{\partial (\overline{OP})_z} & \frac{\partial f_5}{\partial \alpha} & \frac{\partial f_5}{\partial \theta_1} & \frac{\partial f_5}{\partial \theta_3} & \frac{\partial f_5}{\partial \theta_5} \\ \frac{\partial f_6}{\partial (\overline{OP})_x} & \frac{\partial f_6}{\partial (\overline{OP})_y} & \frac{\partial f_6}{\partial (\overline{OP})_z} & \frac{\partial f_6}{\partial \alpha} & \frac{\partial f_6}{\partial \theta_1} & \frac{\partial f_6}{\partial \theta_3} & \frac{\partial f_6}{\partial \theta_5} \\ \frac{\partial f_7}{\partial (\overline{OP})_x} & \frac{\partial f_7}{\partial (\overline{OP})_y} & \frac{\partial f_7}{\partial (\overline{OP})_z} & \frac{\partial f_7}{\partial \alpha} & \frac{\partial f_7}{\partial \theta_1} & \frac{\partial f_7}{\partial \theta_3} & \frac{\partial f_7}{\partial \theta_5} \end{bmatrix} \quad (5.39)$$

5.5 Chapter Summary

The concept of the inverse and forward kinematic analyses was introduced. The homogenous transformation matrix was discussed. The different methods of inverse kinematic analysis were stated and the geometric method was selected. The derivation of the inverse kinematic equations was documented and the novel extension to the geometric method was described. The inverse kinematic Simulink model and blocks used were discussed. The NR method was documented and the forward kinematic equations were derived. Simulations and data from physical testing are presented in Section 8. All MATLAB® script files are documented in Appendix B.

The succeeding chapter presents the singularity and workspace analysis. The different types of singularities are discussed. Three different types of singularity poses are presented for the PKM. Different types of workspace analyses are presented. The workspace was developed through the application of the Monte Carlo method which was used in conjunction with the inverse kinematic equations. Different types of workspace are presented for the PKM with a further investigation into the optimal workspace range for constant orientation of the end effector.

6. SINGULARITY AND WORKSPACE ANALYSIS

6.1 Introduction

This chapter presents the singularity and workspace analysis. The different types of singularities are presented. Singularities by observation are described. The different types of workspace and methods of solving the workspace are discussed. The Monte Carlo and surface wrapping methods are employed. Five different types of workspace are presented.

6.2 Singularity Analysis

When robotic manipulators reach or are in the neighbourhood of singular points, the behaviour of the robot becomes unstable and dangerous. Mathematically, the joint velocities of a robot need to be related to the end effector velocity. The mapping of joint space velocities to the end effector velocities is accomplished by formulating the Jacobian matrix. At certain points in a robot's workspace, the mapping between joint space and end effector space cannot be inverted and these are known as singular points [128].

Merlet [10] stated that it is essential to investigate singularities because the control system needs to accommodate uncontrolled DOFs. Moreover, the safety of humans in the vicinity of the robot is compromised when the robot reaches or is in the neighbourhood of a singular point. Singular points are hazardous because the robot could also attempt to perform unfeasible movements and potentially break. Various methods have been developed to avoid singularities. Some manufacturers overcome this by sending an error message when the robot is commanded to move dangerously [129]. Efficient path planning can avoid singular points. It is useful to generate an index that conveys the proximity of the end effector with respect to a singular point [10].

6.2.1 Types of Singularities

As indicated by Bruyninckx [130], there are two types of singularities. The first type of singularity is the architectural singularity. The architectural design causes the singularity and not a specific combination of actuator lengths or rotation. [131].

The second type of singularity, known as the configuration singularity, is caused by the combination of specific leg lengths of the robot. The Jacobian matrix can be divided into two matrices. One matrix is associated with the inverse kinematics and the other matrix is associated with the forward kinematics. Depending on which of the two matrices are singular, the robot could be in an inverse singularity, forward singularity and in some cases a combined singularity if both matrices are singular [8].

The Jacobian, J , relates the joint velocity to the end effector velocity. The vector q , is the actuated joint variables and the vector x , is the location of the end effector. Through derivations shown in [8], when Jx and/or Jq are singular, then a singularity is observed.

The inverse singularity occurs when the determinant of Jq is zero i.e. $\det(Jq) = 0$. Assuming that the null space of Jq is not empty, there exist some non-zero vectors \dot{q} which result in zero \dot{x} vectors. This means, for some joint velocity, there is no velocity of the end effector. In these poses, the robot can resist forces and torques in some directions with zero actuator forces or torques. The robot loses one or more DOFs. These types of singularities also occur at the workspace boundary of a robot. Figure 6-1 shows an example of a 3R serial robot at full extension

at the boundary point. When a force is applied from the right, the robot can passively resist this force without any actuator forces or torques.

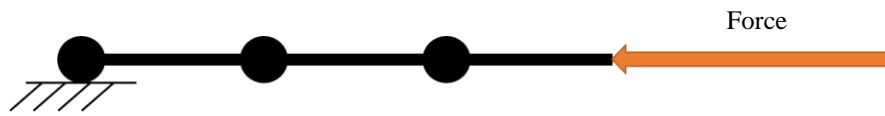


Figure 6-1: Mechanical resistance of a mechanism without the use of force or torque

Figure 6-2 depicts an ABB serial arm that loses the DOF manipulated by the wrist joint. For this particular pose, as the robot moves its wrist joint from Figure 6-2(a) to Figure 6-2 (c), the end effector is completely unaffected [128, 129].

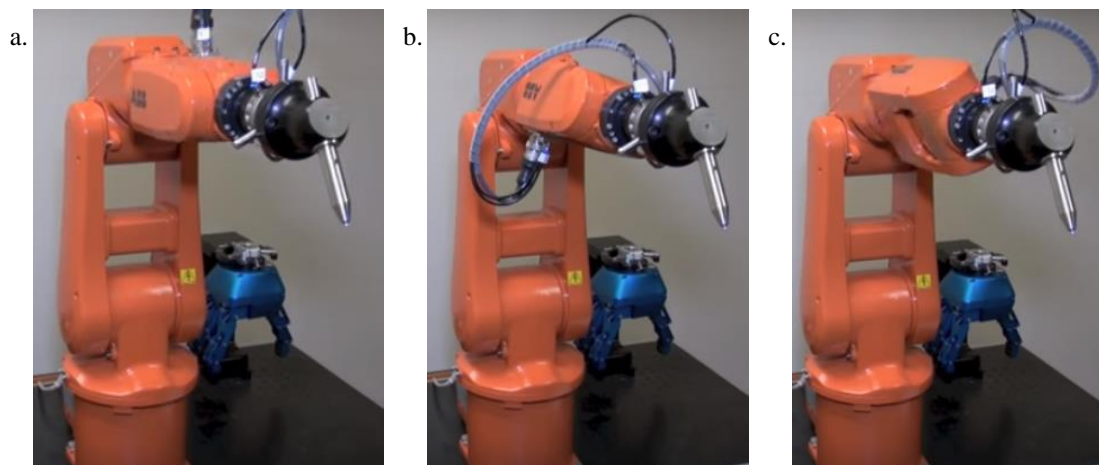


Figure 6-2: Loss of a DOF for a serial robot wrist [129]

- a. Initial position of the wrist joint
- b. Rotation of the wrist joint
- c. Final position of the wrist joint

The forward singularity occurs when the determinant of Jx is zero i.e. $\det(Jx) = 0$. In this case, assuming the null space of Jx is not empty, there exists nonzero \dot{x} vectors for the which there is zero \dot{q} vectors. This means, for some velocity of the end effector, there is no joint velocity. In this case, the robot has gained a DOF. The manipulator is unable to resist forces or torques in some directions and the robot loses its stiffness.

Figure 6-3 (a) shows a Stewart Platform in its home position. As it moved to a location, as shown in Figure 6-3 (b), the robot violently dropped to the position illustrated and could not move. Figure 6-3 (c) shows that the robotic platform could move while all actuators were locked. This indicated that a degree of freedom was gained (uncontrollable DOF). For this pose, the mathematical equations demand that the PKM needs to be infinitely stiff but that is not feasible in reality. The PKM cannot interpret the concept of infinity therefore a singularity was encountered. The actuator controller also has an infinite gain at this point [8, 129]

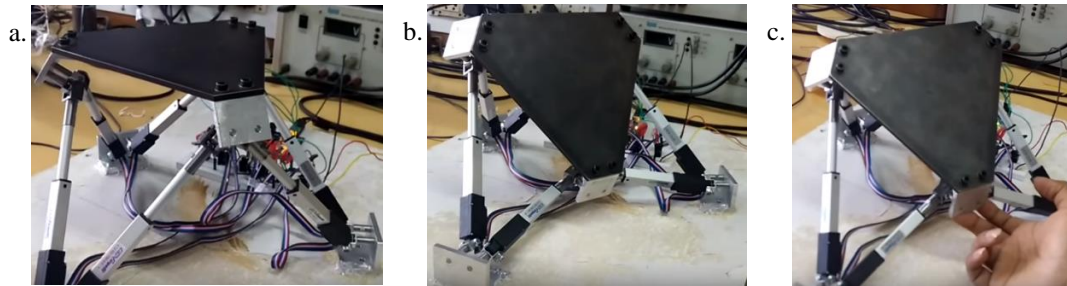


Figure 6-3: Sudden uncontrollable movement of the end effector and the gaining of a DOF[129]

- a. Initial position.
- b. Sudden collapse of the machine due to gaining a DOF.
- c. The end effector can still move even though all actuators locked.

6.2.2 Singularities of the 2R(Pa-IQ)RR, R(Pa-IQ)R PKM

Figure 6-4 depicts an example of the workspace boundary singularity of the PKM. This is classified under the inverse singularity type. Figure 6-5 (a) shows the PKM in a singularity pose under alpha rotation. If actuators 3 and 4 were actuated such that it produced a force along the direction shown, the end effector could either tilt up or down. This is an unstable position and the PKM loses the alpha rotational DOF. If the force acts in the opposite direction, the PKM would be able to resist the force along that direction without an opposing force or torque. The posture of the machine provides mechanical stiffness. Figure 6-5 (b) illustrates a singularity pose of the PKM under beta rotation. If actuator 1 to 4 exerts a force in the direction indicated, the end effector could tilt up or down in an unstable manner if there is any misalignment or inaccurate actuation. The same conditions apply as with Figure 6-5 (a) when a force is applied opposite to the direction indicated, the PKM can resist the force without any additional force or torque. Singularities of these types can occur at any point on the workspace boundary and for the same orientation of the end effector at different heights and also if the alpha rotation was reversed.

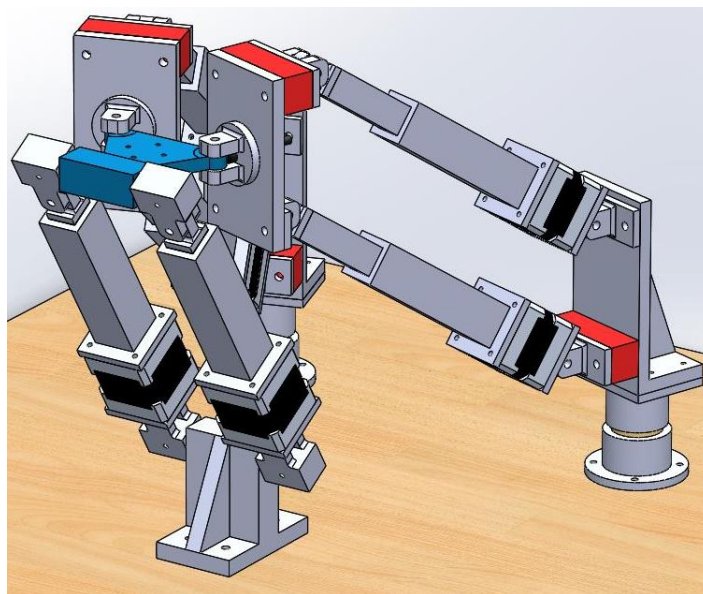


Figure 6-4: An example of a workspace boundary singularity

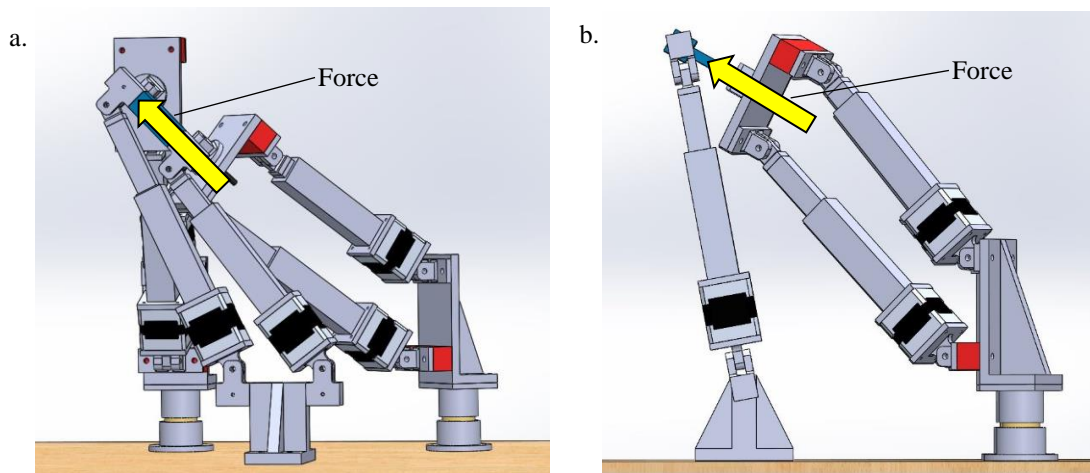


Figure 6-5: Singularity poses in which unpredictable motion could occur under certain conditions

- a. A singularity pose for alpha rotation
- b. A singularity pose for beta rotation

6.3 Workspace Analysis

The workspace of a parallel robot is dependent on factors such as mechanical limits on joint, stroke length of the actuators, singularities, self-collision between the legs of the machine and size of the end effector. According to Merlet [10], the following are the most common types of workspace:

- Constant orientation (translational) workspace which describes all possible locations that can be reached by the end effector with a constant orientation.
- Orientation workspace which defines all possible orientations that can be achieved by the end effector while in a fixed location.
- Maximal workspace is defined as all possible points that can be achieved with at least one orientation of the end effector.
- Inclusive orientation workspace describes all the possible locations that can be reached by the end effector with at least one orientation which is among a set defined by the ranges of the orientation angles. The maximal workspace is a case of the inclusive orientation workspace whereby the permitted angles range from 0 to 2π .
- Total orientation workspace involves all possible points that can be reached by the end effector in all possible orientations among a set of ranges of the orientation angles.
- Dextrous workspace is defined as all possible locations of the end effector for which all orientations are feasible. The dextrous workspace is a case of the total orientation workspace such that the range of angles is from 0 to 2π .
- Reduced total orientation workspace is all the possible locations that can be reached by the end effector with a subset of orientation angles whilst other orientation angles can be arbitrary. These angles can have any range of values. This analysis is applicable for tasks performed by the robot that does not require a particular DOF.

The orientation, total orientation, dextrous and reduced total orientation workspace was not addressed in this research.

6.3.1 Methods of Workspace Calculation

The architectural complexity and DOF influence the workspace calculation method. Geometric, discretisation and numerical methods may be used to compute the workspace.

The geometric method establishes a boundary using geometric characteristics. The method can be applied to many legs of the robot and the intersections of the volumes enveloped results in the robot's workspace. The geometric method is viable when the end effector possesses constant orientation. The merits of this method are that it is fast and accurate to employ and provides a minimal representation of the workspace. This method finds difficulty in considering all constraints and the minimal representation is not the most appropriate method of analysis for path planning [10]. Various authors have used the geometric method also to investigate volume, optimize PKM design for prescribed workspaces and to employ extensions of the geometric method for simplifying the workspace analysis [132-134].

The discretisation method establishes the workspace boundary by placing nodes on a uniform cartesian or polar coordinate grid. This is influenced by a PKM's pose parameters. Each node is verified to determine if it belongs to the workspace. The boundary nodes would then imply that it has one close neighbouring point that does not satisfy the workspace [135]. Authors such as Stan et al. [135] and Goa and Zhang [136] employed discretisation methods with the latter using this method in conjunction with the geometric method and inverse kinematics. Although this method is robust in considering all constraints, one of the drawbacks is that the accuracy of the boundary that creates the grid is largely affected by the sampling step size. Computational time is exponentially affected by changes in the step size. Another drawback is that the workspace model becomes problematic when voids exist.

A numerical method, known as the Monte Carlo Method, is used in mathematical analyses where random sampling is required. Random 3D points are generated and are passed through a set of constraints. If the constraints are satisfied, the random points are plotted and a 3D point cloud is generated [137]. Advantages of the Monte Carlo method include the ease of implementation, incorporation of joint limits and constraints, control of the number of sampling points by the designer and its use as an extension of the inverse kinematic solution [137, 138].

The disadvantages of the Monte Carlo are that it requires an additional step to calculate the volume and the accuracy of the point cloud volume is dependent on the number of points that satisfy the imposed constraints. Only an estimate of the theoretical volume can be achieved. The computational time increases exponentially with the number of valid points. The estimation error is dependent on the surface wrapped around the points. The randomness of the points is not always uniform but can be alleviated by a highly dense point cloud. Various authors have successfully used the Monte Carlo method [137-140].

The geometric and discretisation methods were not selected since the workspace was not intuitive considering that a novel PKM was developed. The Monte Carlo method was selected as it best suited the architectural complexity and DOFs. An extension to the Monte Carlo Method was carried out to enable a surface to be wrapped

around the point cloud. The workspace MATLAB® script was generated as an extension to the inverse kinematic code and is presented in Appendix B.4.

The convex hull function was chosen instead of the boundary function method to wrap a surface around the point cloud. The convex hull sweeps a surface that envelopes more volume as opposed to the boundary method. The boundary method wraps aggressively to points on the boundary thus necessary volume is sometimes not captured. Figure 6-6 depicts the comparison between the envelope created for the same set of points along the xz plane. A cylindrical volume was generated as a test. The convex hull method captured more volume.

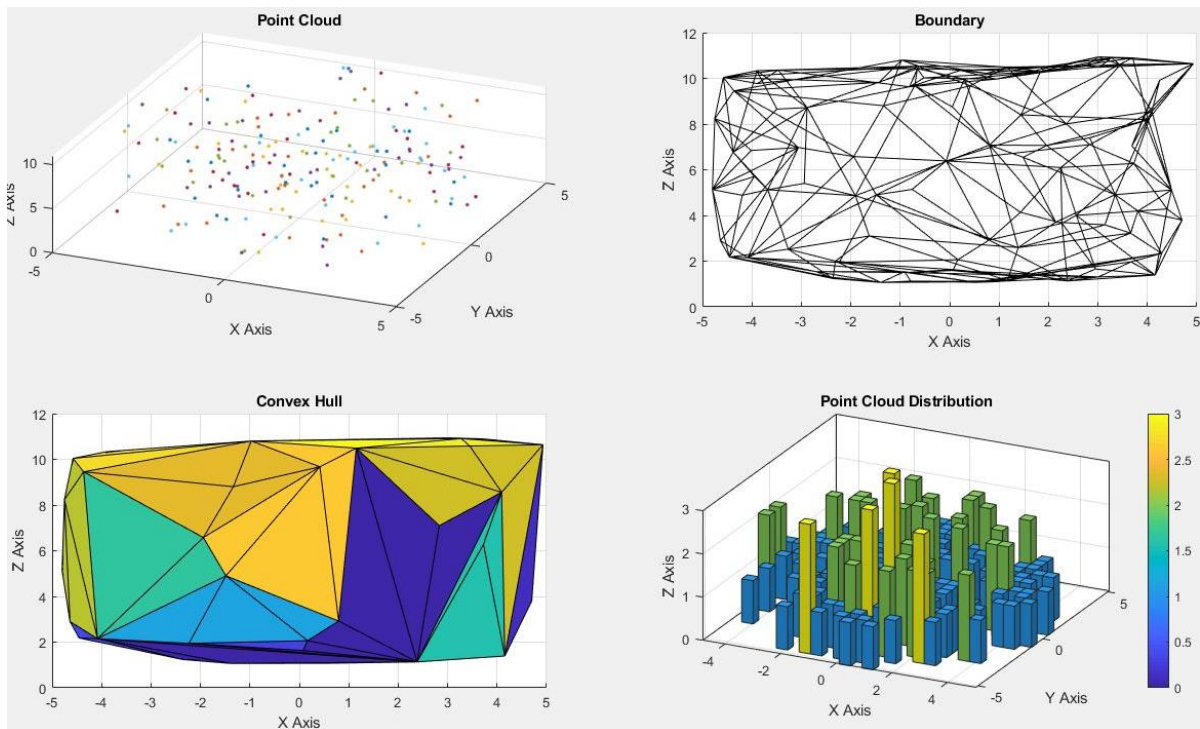


Figure 6-6: An example of a point cloud, surface wrap and point cloud distribution

Simulations were performed on the constant orientation workspace to determine a reasonable number of points required to be generated. Results showed that the volumetric difference between a point cloud of 10 000 points and 12 000 points was 0.13%. This indicated that either 10 000 or 12 000 points could be used to perform the simulations. Most of the points clouds were generated using 12 000 points.

The constant orientation, alpha rotation with translation, beta rotation with translation, maximal and inclusive orientation workspaces were investigated and is presented in the following sub-sections. The flowchart depicting the use of the Monte Carlo method is illustrated in Figure 6-7.

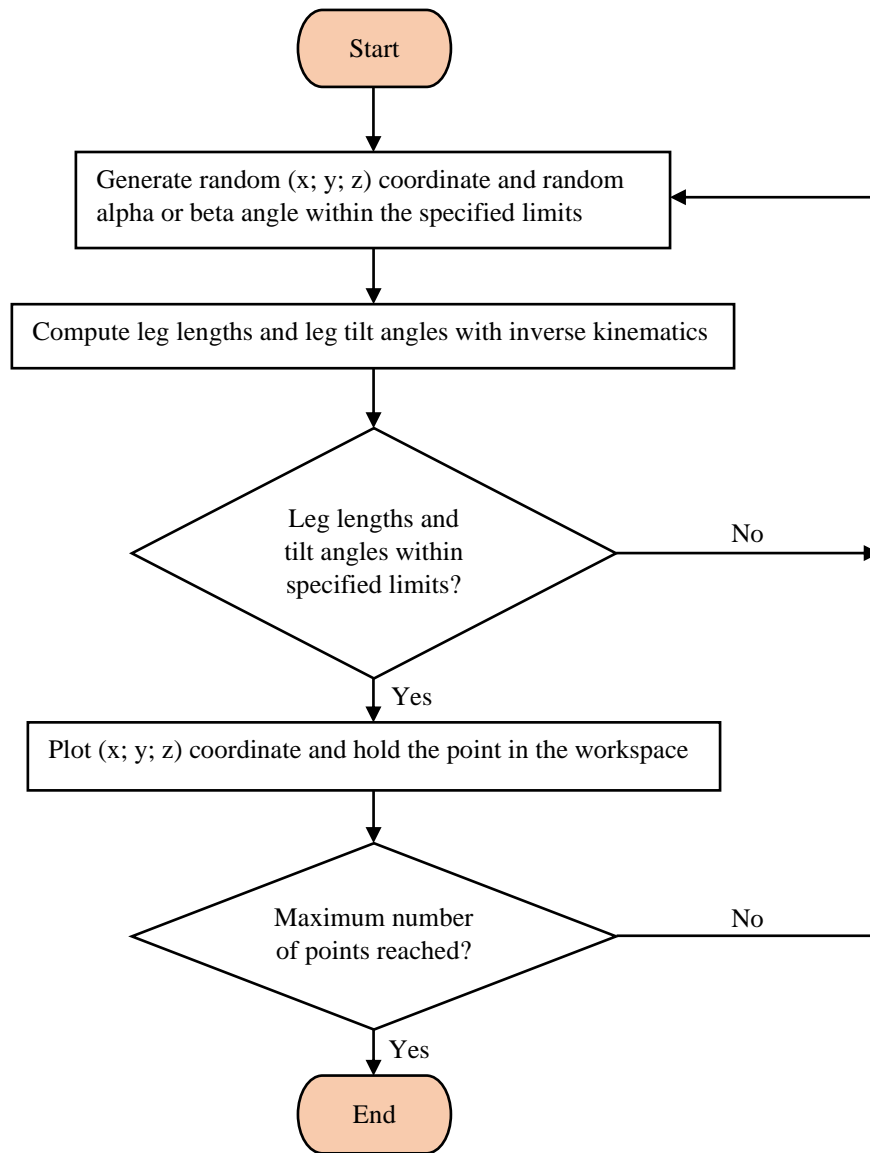


Figure 6-7: Flow chart for searching for the robot workspace

6.3.2 Constant Orientation (Translational) Workspace

The clash clearance was designed to be a minimum distance of 1mm between leg 1 and 2 and for leg 3 and 4. Table 6-1 presents the limits along the different axes for the constant orientation workspace.

Table 6-1: Summary of the workspace boundaries for constant orientation

Axes	Value (mm)	Reason for limitation
X minimum	46.50	Self-clashing.
X maximum	235.14	Maximum stroke length of actuator 1 – 4.
Y minimum	136.12	Maximum stroke length of actuator 3 and 4.
Y maximum	-136.12	Maximum stroke length of actuator 1 and 2.
Z minimum	262.08	Maximum stroke length for actuator 1 – 4.
Z maximum	356.68	Maximum stroke length of actuators.

Additional constraints were added to define the maximum and minimum tilt angles of the actuators. The maximum and minimum angle of tilt for leg 1 to 4 was 78.73° and 34.18° respectively. The maximum and minimum angle of tilt for leg 5 and 6 was 123.57° and 56.43° respectively.

The results of the constant orientation workspace are displayed in Figure 6-8. This was performed with 12 000 points and a volume of $1\,212\,900\text{ mm}^3$ was observed. The workspace was anisotropic and required a densely populated point cloud. This aided the accuracy of the estimated volume.

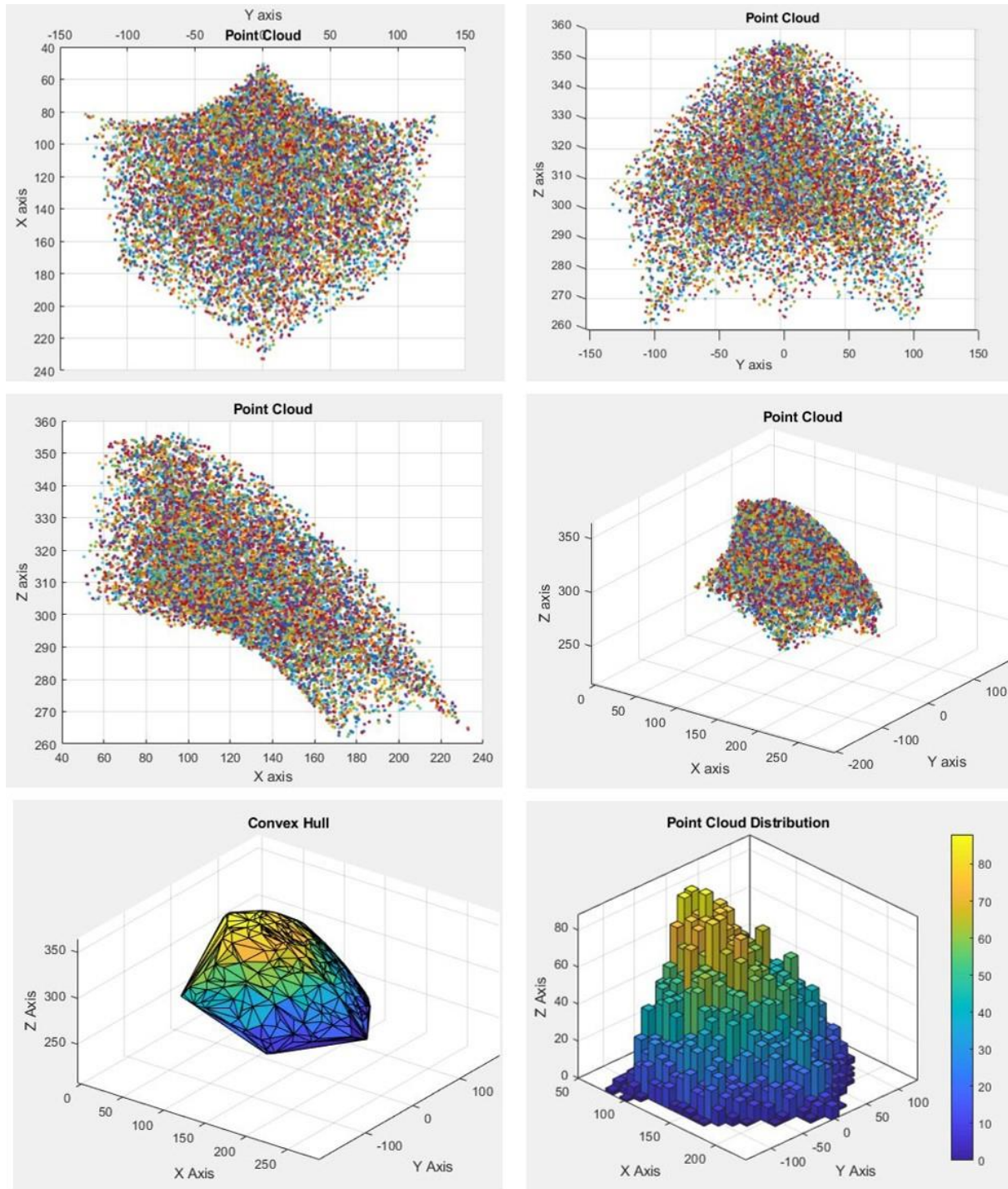


Figure 6-8: Results of the translation workspace analysis

Xiaolong et al. [90] designed a redundant actuated 5-DOF PKM which displayed a similar point cloud, shown in Figure 6-9. This served as a validation that the constraints imposed were correct.

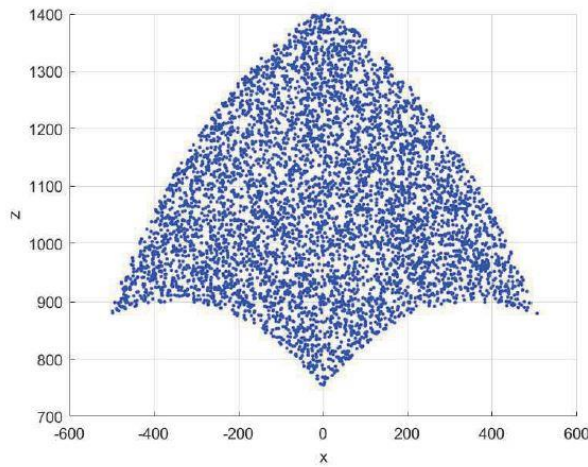


Figure 6-9: Workspace results that was obtained by Xiaolong et al. [90].

6.3.3 Alpha Rotation and Translational Workspace

The PKM constraints for alpha rotation with translation are shown in Table 6-2. The tilt angle constraints for the actuators are the same as for the constant orientation workspace. A noticeable difference for the alpha rotation with translation to the constant orientation workspace is that it loses a DOF along the x axis and the x value remained at 113.31 mm. This meant that the alpha rotation with translation only occurs about a plane. Poses and conditions depicting the alpha maximum and minimum angles of tilt is illustrated in Appendix G.1.

Table 6-2: PKM constraints for alpha rotation

Axes	Value	Reason for limitation
X value	111.31 mm	Translation along the x axis is lost.
Y minimum	136.12 mm	Maximum stroke length of actuator 3 and 4.
Y maximum	-136.12 mm	Maximum stroke length of actuator 1 and 2.
Z minimum	262.08 mm	Maximum stroke length for actuator 1 – 4.
Z maximum	356.68 mm	Maximum stroke length of actuators.
α minimum	-35.73°	Maximum stroke length of actuator 2 and actuator 5
α maximum	35.73°	Maximum stroke length of actuator 4 and actuator 6

The results of the alpha rotation with translation workspace is depicted in Figure 6-10. This was performed with 12 000 points and the resulting area was 18112 mm². The boundary function was used since the convex hull surface wrap is used for 3D volumes.

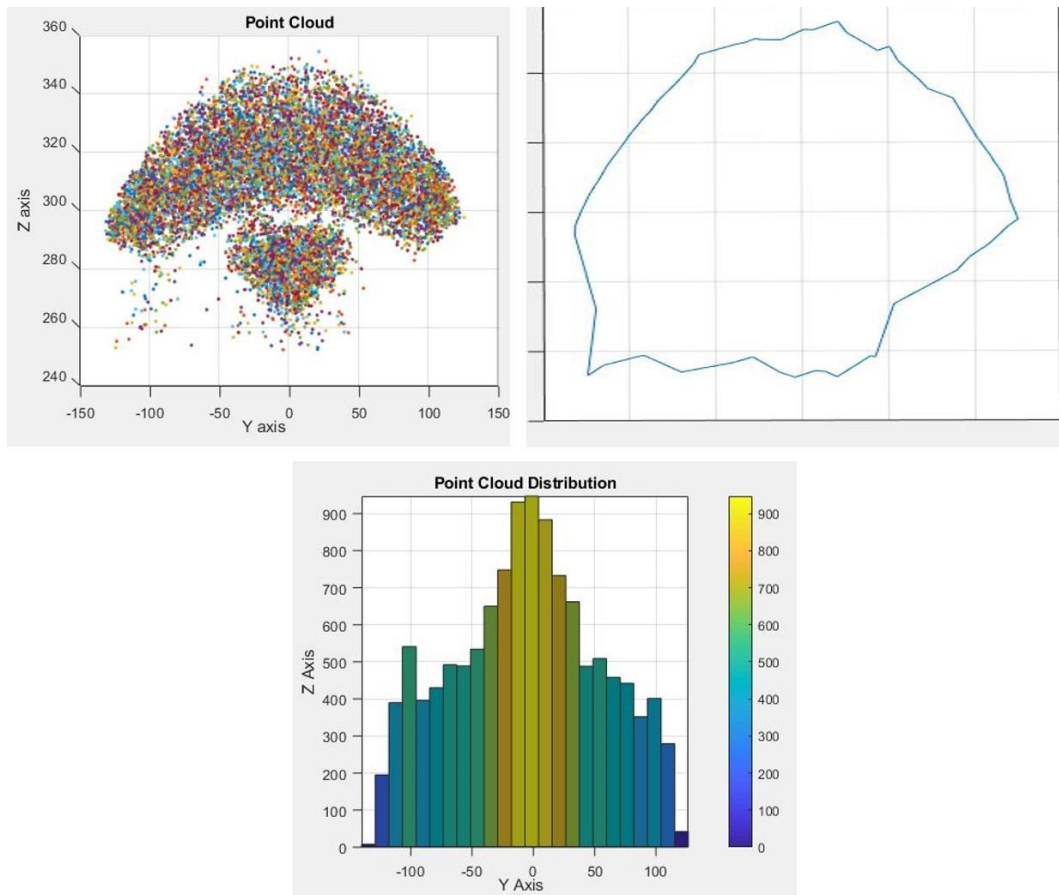


Figure 6-10: Alpha rotation and translational workspace

6.3.4 Beta Rotation and Translational Workspace

Table 6-3 presents the position and orientation limits of the end effector when undergoing beta rotation and with translation. The poses performing the maximum and minimum beta rotations are shown in Appendix G.2. The tilt angle constraints for the actuators are the same as for the constant orientation workspace.

Table 6-3: Limits for the beta workspace analysis

Axes	Value (mm)	Reason for limitation
X minimum	46.50	Self-clashing.
X maximum	239.50	Self-clashing.
Y minimum	136.12	Maximum stroke length of actuator 3 and 4.
Y maximum	-136.12	Maximum stroke length of actuator 1 and 2.
Z minimum	252.07	Self-clashing.
Z maximum	356.68	Maximum stroke length of actuators.
β minimum	-36.8°	Self-clashing.
β maximum	27.17°	Self-clashing.

Figure 6-11 displays the workspace of the end effector for beta rotation with translation. The simulation was performed with 12 000 points and a volume of 2 022 000 mm³ was obtained. The workspace volume was far greater than the workspace obtained for constant orientation and was therefore investigated for sources of errors.

The yellow portion highlighted on the xz plane indicates a region that the robot cannot physically move to due to self-clashing. An example of this is shown in Figure 6-12. The points were plotted due to MATLAB® not possessing a constraint equation to limit this movement. The limitation for this joint can be addressed in future research. To adequately understand the machine’s limits, the SolidWorks® model should be consulted and the PKM can be restrained through mates. Therefore, the problem can be solved through manipulation in a 3D CAD package. Translating the constraint mathematically should be addressed in future work. The volume generated is therefore an overestimation of the machine’s workspace for beta rotation with translation.

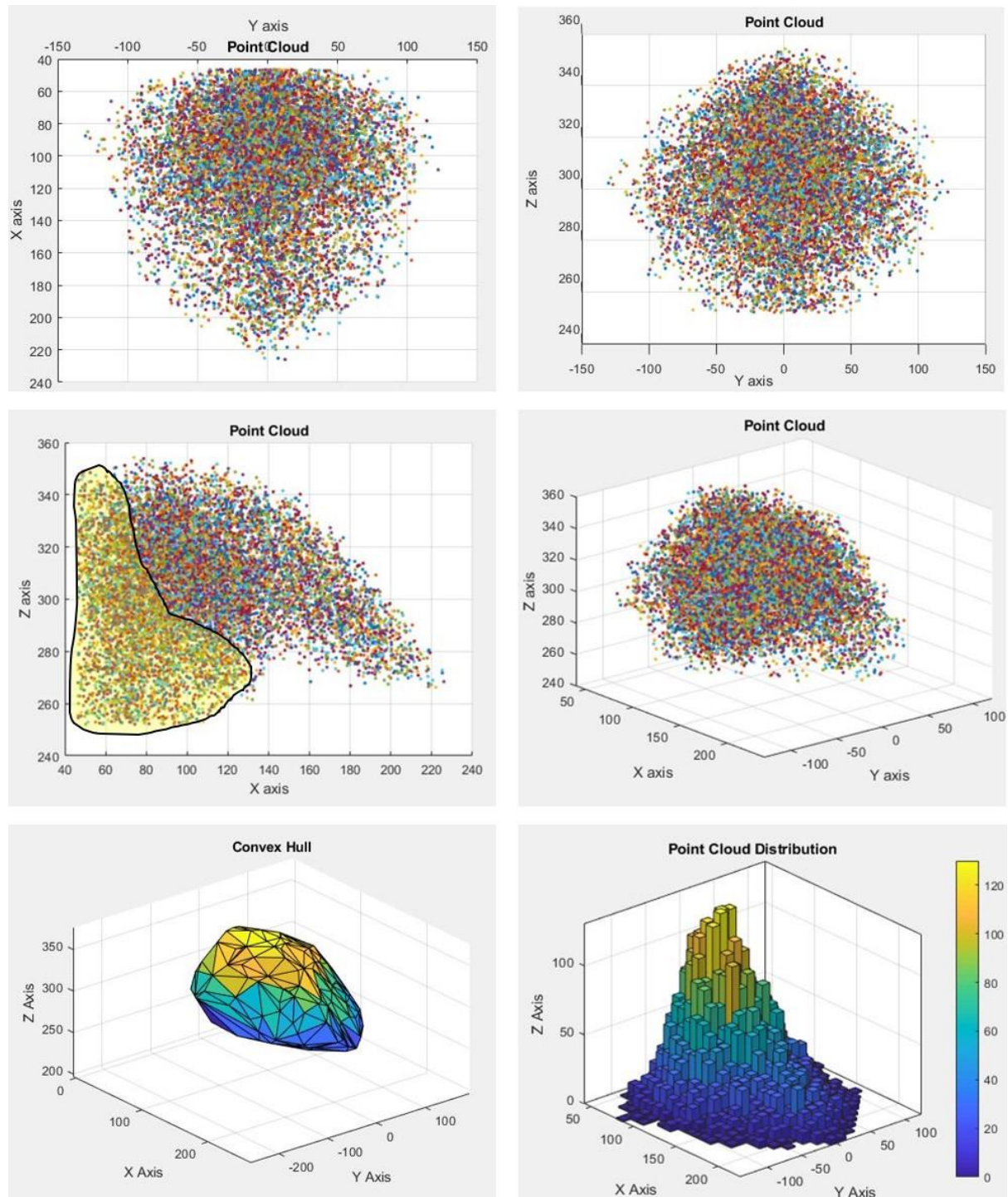


Figure 6-11: Beta rotation and translational workspace

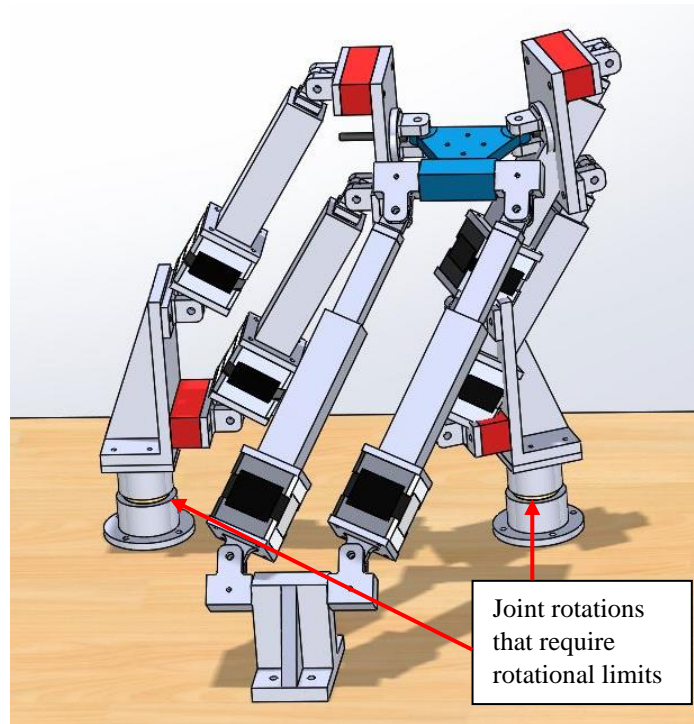


Figure 6-12: A physically impossible pose

6.3.5 Maximal Workspace Excluding Parasitic Motion

The maximal workspace considers all points that can be reached by the end effector in at least one orientation. Each of the workspace MATLAB® scripts (constant orientation, alpha rotation with translation and beta rotation with translation) were run with 4 000 points and were combined into a matrix. The points within the final matrix were then plotted as depicted in Figure 6-13. The overestimation of volume from the beta rotation with translation is present in this analysis as indicated on the xz plane with the yellow highlight. The volume produced from MATLAB® was 2 120 000 mm³. This result illustrates the correct employment of combining all valid points into a common matrix since the maximal workspace was the largest recorded workspace and is congruent with its definition.

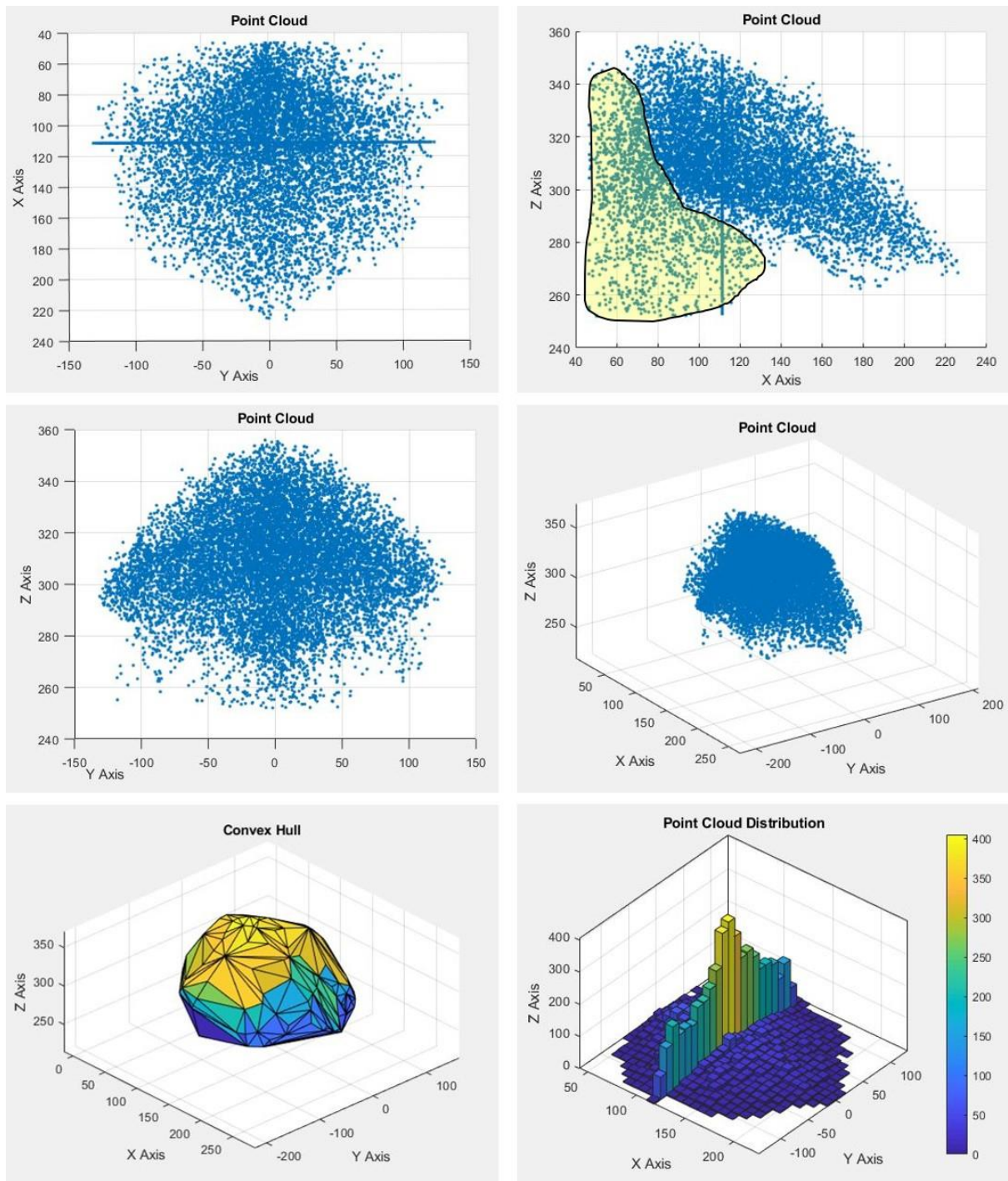


Figure 6-13: Maximal workspace of the PKM

6.3.6 Inclusive Orientation Workspace

For the inclusive orientation, the simulations were run for alpha and beta orientations that ranged from 8° up to and including 10° . The alpha rotation with translation and beta rotation with translation was plotted with 5 000 points each and all valid points were merged into a common matrix. The results of the inclusive orientation workspace are shown in Figure 6-14. The volume obtained was $804\,710\text{ mm}^3$. The inclusive orientation volume was the smallest volume obtained thus validates the approach.

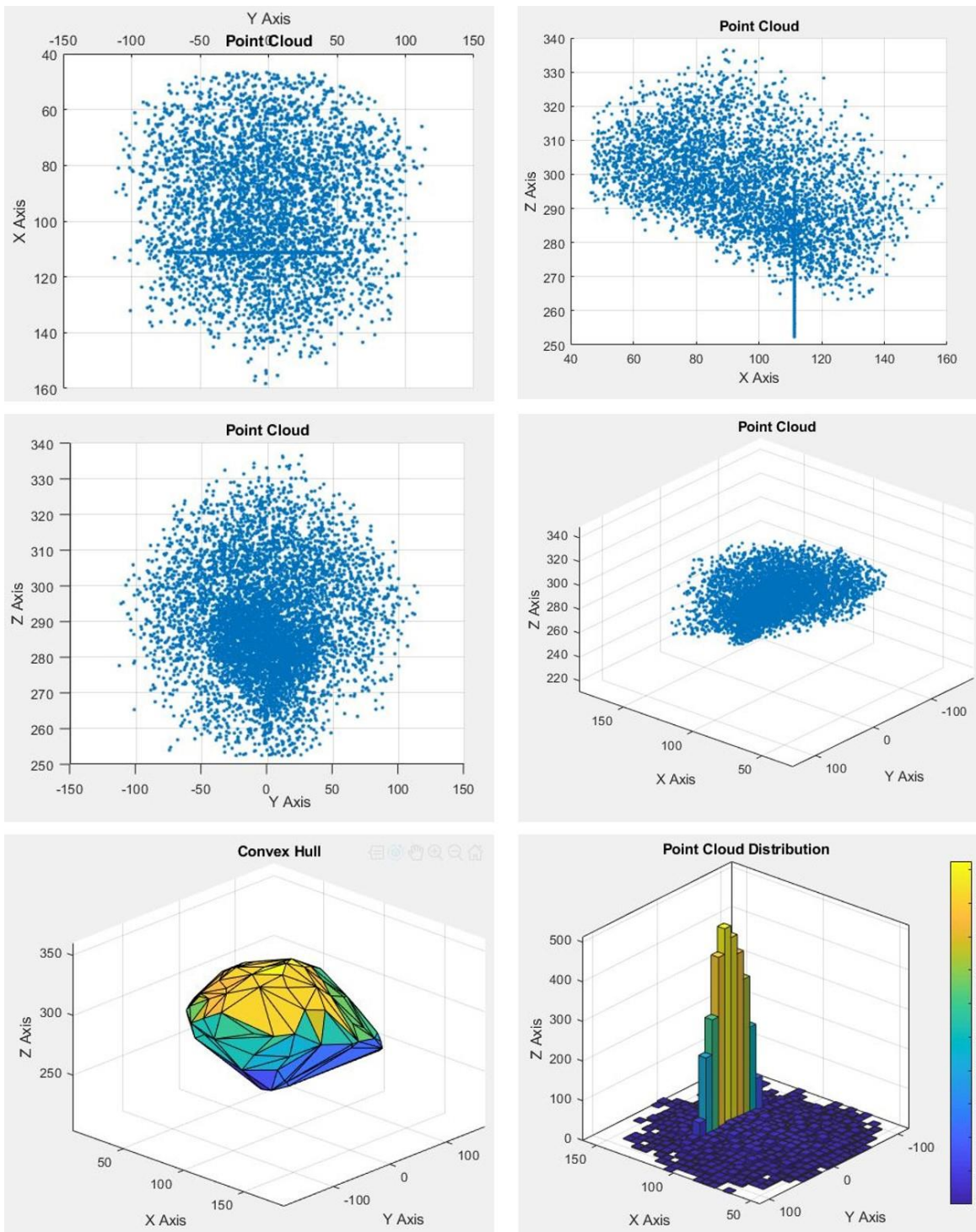


Figure 6-14: Inclusive orientation workspace for angles ranging from 8° up to and including 10°

6.3.7 Constant Orientation Workspace Height Investigation

The constant orientation workspace height was chosen to be investigated and this approach can be used for other workspaces. The height ranged from 262.08 mm up to and including 356.68 mm. The workspace was sliced at 263 mm and continued in 10 mm increments up to 353 mm. The last slice was taken at a height of 356 mm. Figure 6-15 depicts each of the planes but they are not displayed with the same scale. The height investigation was done for the purpose of presenting the change of shape of the workspace with a change in height. The correct scale of each slice is illustrated Figure 6-16. The following insights are deduced from Figure 6-15 and Figure 6-16:

- The optimal plane is observed at a height of 303 mm.
- The optimal working height range is from 303 mm up to 323 mm which is a band of 20 mm.
- The PKM doesn't possess a concave curve layout at 356 mm.
- The total height range does not suggest that the PKM can perform this length of movement in a straight line due to an anisotropic workspace layout.
- Considering applications:
 - Machining applications should occur between the height range of 303 mm and 323 mm for maximum energy saving and the allowance to machine material with larger surface areas. Machining could still occur at any height of the workspace and should match the machining requirements. Machining along large arcs is possible as shown in the available workspace along the xz plane in Figure 6-8.
 - Sorting and part handling can occur at most heights. The start and end point of the required movement should be first established and then an optimal path can be developed within the workspace. Sorting and part handling would generally require repetitive movements therefore the machine could be programmed to perform certain repetitive movements at specific ranges in its workspace.
 - General positioning can occur at any height and is dependent on the distance required to move the workpiece or load. Load bearing applications allows the most versatile use of the workspace as load bearing movements do not generally require extreme movements of the end effector.

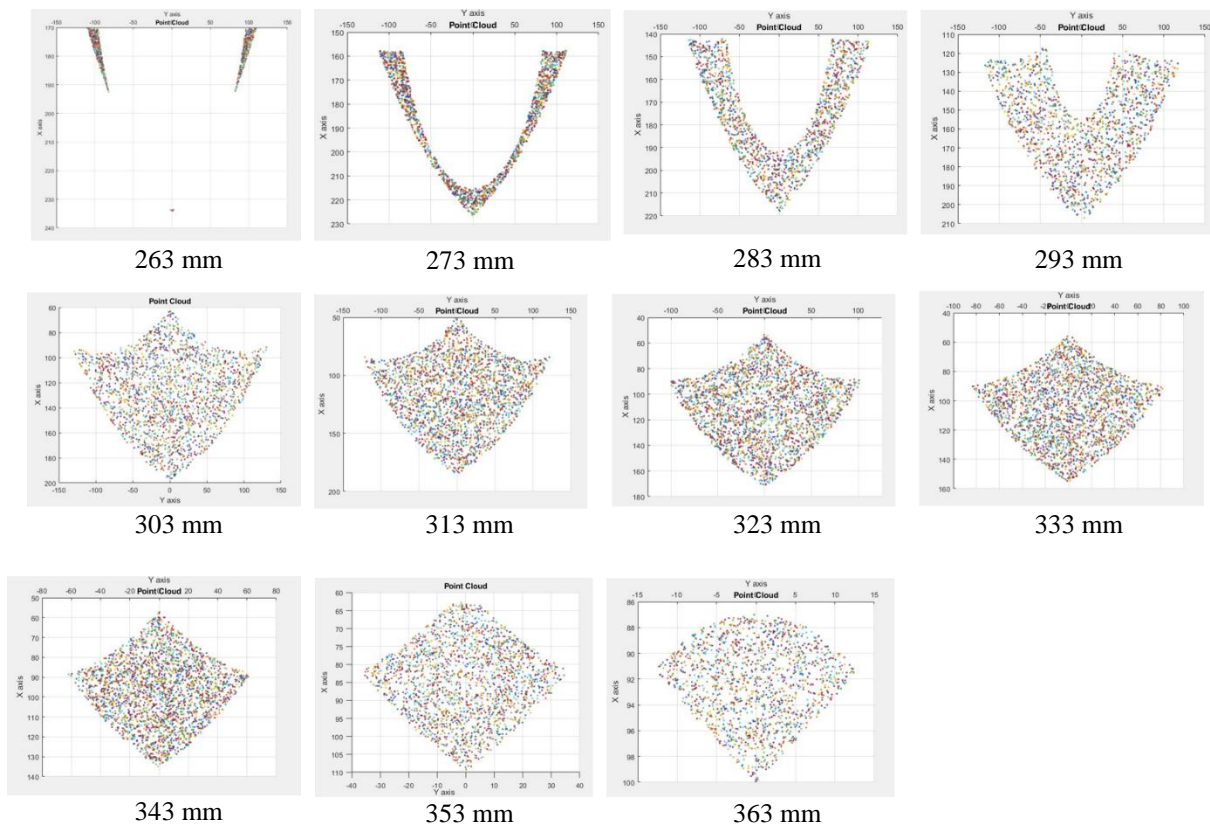


Figure 6-15: The xy view of the workspace at different heights for constant orientation

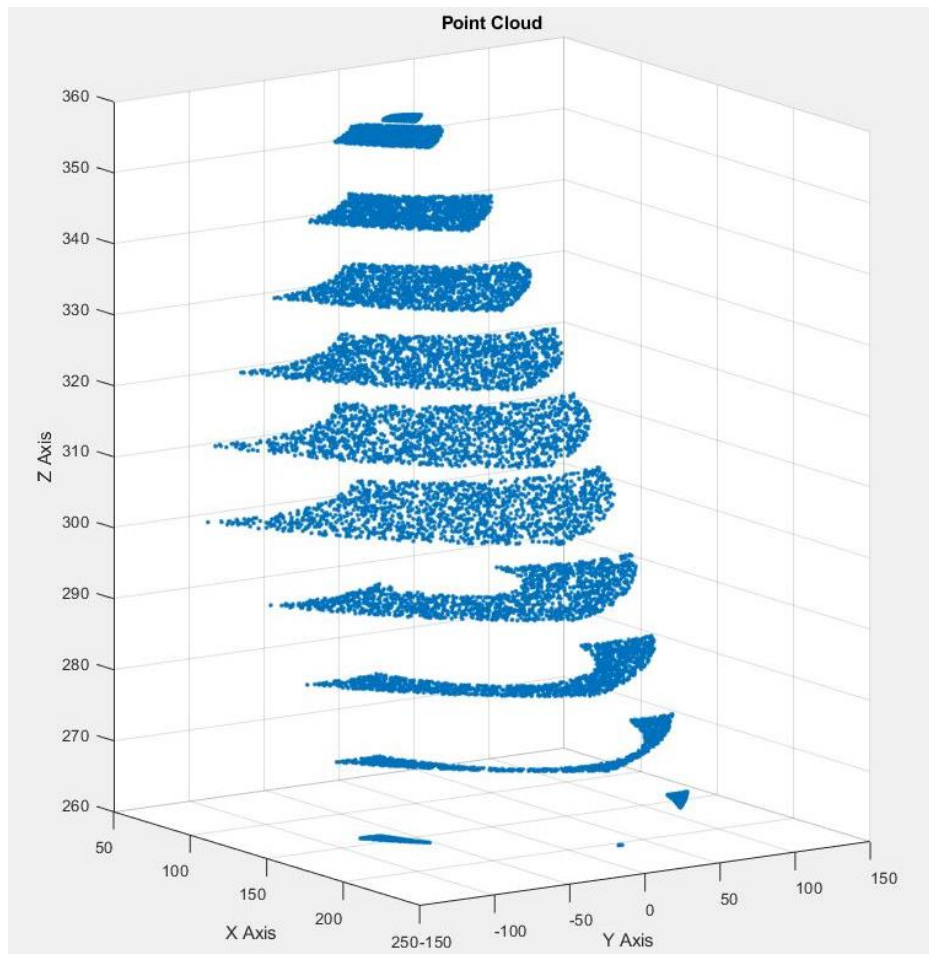


Figure 6-16: Isometric view of slices of the constant orientation workspace at different heights

6.4 Chapter Summary

This chapter described the singularities and workspace analysis. The different types of singularities were discussed and 3 singularity poses were discovered by observation. The different types of workspace were discussed. The Monte Carlo method, convex hull and point cloud distributions using histograms were generated through MATLAB®. The workspace analysis was an extension the inverse kinematic analysis documented in Section 5. The following workspace volumes were achieved:

- Constant orientation: 1 212 900 mm³
- Alpha rotation with translation 18112 mm² (area)
- Beta rotation with translation 2 022 000 mm³
- Maximal workspace excluding parasitic motion 2 120 000 mm³
- Inclusive orientation workspace 804 710 mm³

The following chapter presents the electronic and software system. The selected components are discussed and wiring diagrams are presented. The development of a control box is documented. The software system used to automate the prototype is presented and a flow diagram of the integration of the electronic and software system with the prototype is documented.

7. ELECTRONIC AND SOFTWARE SYSTEM

7.1 Introduction

An electronic and software system was designed to automate the motion of the PKM and considered the following design aspects:

- **Low cost:** The research aimed to produce a low-cost desktop prototype through AM.
- **Mobile:** Electronic hardware must be portable.
- **Compact:** The electronic hardware must be enclosed in a control box with the allowance for airflow through the control box to allow for cooling of the electronic hardware.
- **Aesthetic:** The control box must be aesthetically pleasing.

7.2 Flow Diagram of System

Figure 7-1 shows the flow diagram for the electronic hardware. The diagram only represents the connection to one actuator for simplicity. Appendix E presents the cost of the electronic components.

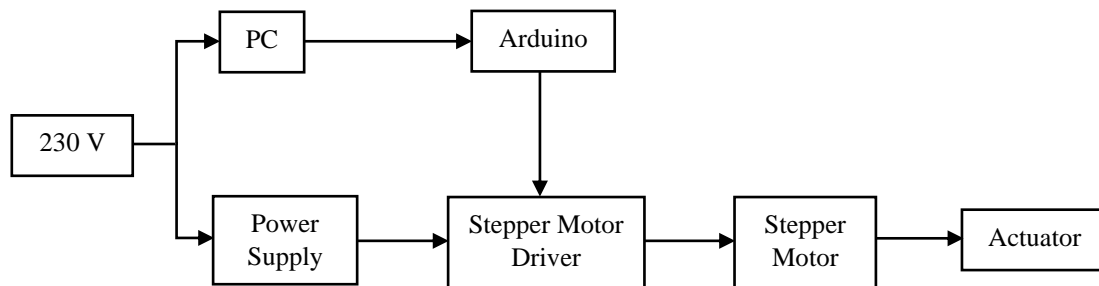


Figure 7-1: Flow Diagram of Electronic Hardware

7.3 Description of Selected Components

7.3.1 Motor Selection

Stepper motors were selected in the development of the prototype due to their high positioning capability and range of motion. The disadvantage of the stepper motor was its application as an open loop system. NEMA 11, 17, and 23 stepper motors were applicable. The NEMA 17 stepper motor was the most cost effective from the available stepper motors. The NEMA 17 stepper motors were more compact than the NEMA 23 stepper motors therefore aiding the development of a compact prototype. The torque capability of the stepper motors did not influence the selection of the stepper motors since the prototype was aimed to demonstrate the potential use in machining, part handling, sorting and general positioning applications. The payload test in Section 8.7 demonstrated the payload capability although the PKM was not designed toward a payload specification and was tested until failure.

NEMA 17 Stepper motors were selected. Four 42BYGHW609 stepper motors and two 42BYGHM809 stepper motors were used and possessed 1.8 degrees/step and 0.9 degrees/step, respectively. The motors had a 1.7A rating. A test was carried out to determine which wires of the stepper motors belonged to the same coil. A multimeter was used to test the resistances between the various wires. The value of 1 represents a finite resistance measured between the two wires suggesting they belong to the same coil. The value of 0 represents an infinite resistance

(no connection) between the two wires meaning they do not belong to the same coil. Pulse Width Modulation (PWM) energizes the coils with signals sent from the microcontroller and stepper motor driver. Table 7-1 displays the pairs of wires that belong to the same coil. All six stepper motors displayed the same results shown in Table 7-1. Open Impulse and Longway Motor [141-143] provides the technical specifications of the stepper motors.

Table 7-1: Determining the wire pairs for the stepper motors

	Green	Blue	Black	Red
Green	-	0	1	0
Blue	0	-	0	1
Black	1	0	-	0
Red	0	1	0	-

7.3.2 Stepper Motor Drivers

Stepper motors can be controlled by a range of stepper motor drivers. The M860H, DM542, TB6600 and TB6560 stepper motors drivers were considered. The TB6560 was selected as it was the most cost-effective and compact. A disadvantage of the TB6560 is that it not as robust as other stepper motor drivers but the TB6560 was designed to be housed within a control box as presented in Section 7.5. The TB6560 has 14 different amperage outputs, which are set using switches *SW1, SW2, SW3* and *S1*. The decay setting is set with switch *S2* and refers to the amperage delivered when the motors static. The driver can accomplish microstepping with switch *S3* and *S4*. The decay setting relates to how the stepper motor is switched off. The switches *S5* and *S6* control the decay setting and this determines how fast the motor decelerates to a stop. Fast decay refers to a fast deceleration of the motor and is applicable for low speeds and vice versa. Figure 7-2 displays the TB6560 stepper driver. DIY Electronics [144] provided the technical specifications of the TB6560 stepper motor.

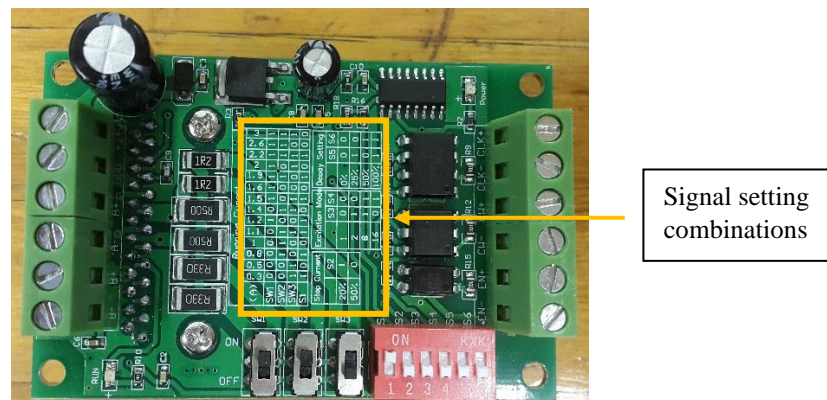


Figure 7-2: The TB6560 stepper motor driver

7.3.3 Microcontroller Board Layout and Selection

The operating voltage of the Arduino Mega 2560 is 5V. The Arduino Mega was more cost-effective than the Arduino Due and it does not have interfacing challenges with peripheral components as faced by the Arduino Due. The Arduino Mega was selected and had at least 12 PWM ports, which was sufficient for this research. The Arduino Uno was more cost-effective and compact but only possessed 6 PWM ports which hindered its use. Figure 7-3 [145] depicts the schematic diagram of the Arduino Mega indicating the PWM ports. Mantech [146] provided the technical specifications of the Arduino Mega 2560.

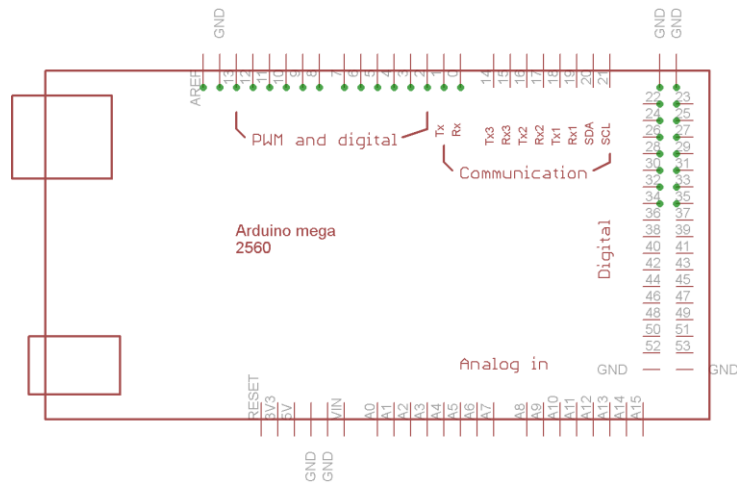


Figure 7-3: Schematic Diagram of the Arduino Mega [145]

7.3.4 Power Supply

Two Mean Well S-320-24-D power supplies were chosen to power the TB6560 stepper motor drivers. The motor drivers required 10V to 35V to be powered thus a 24V power supply was selected. The motor drivers required 3A each thus, one power supply unit could supply 3 motor drivers with current since it is rated at 12.5A. An attractive feature was the built-in cooling fan which aided in its selection. Figure 7-4 depicts the power supply. The power supply is powered by 230V from a wall socket. Mouser Electronics [147] provided the technical specifications of the power supplies.

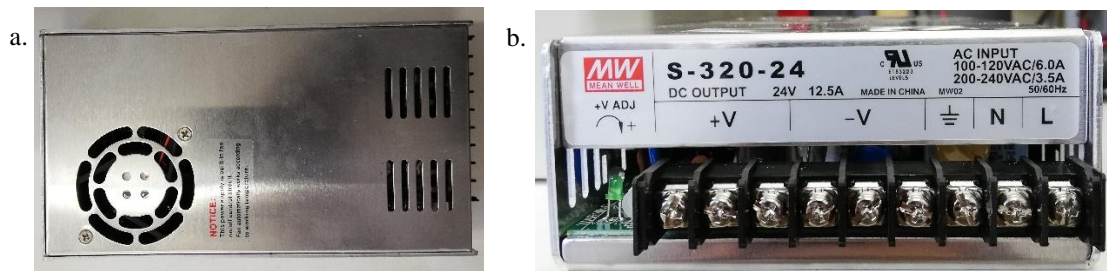


Figure 7-4: Mean Well S-320-24

7.3.5 Sensor Selection

This research used the OCM as a low-cost displacement sensor. One of the advantages of the optical mouse is that it is readily interfaced with the computer and is cost effective. Some of the disadvantages are that the mouse needs to translate along a plane or flat surface to avoid errors. The user needs to test the mouse experimentally to obtain an acceptable resolution. Laser and draw wire sensors were considered with data acquisition hardware and software. Laser and draw wire sensors possess advantages such as high-resolution measuring capabilities, ease of data acquisition and data analysis. However, the laser and draw wire sensors are high in cost especially when multiple sensors are required. The data acquisition hardware and software units are expensive and generally cannot be easily interfaced with sensors from other suppliers hence the selection of the OCM sensor. Other cost-effective sensors such as infrared and ultrasonic sensors possessed low-resolution measuring capabilities and were not suitable for this research.

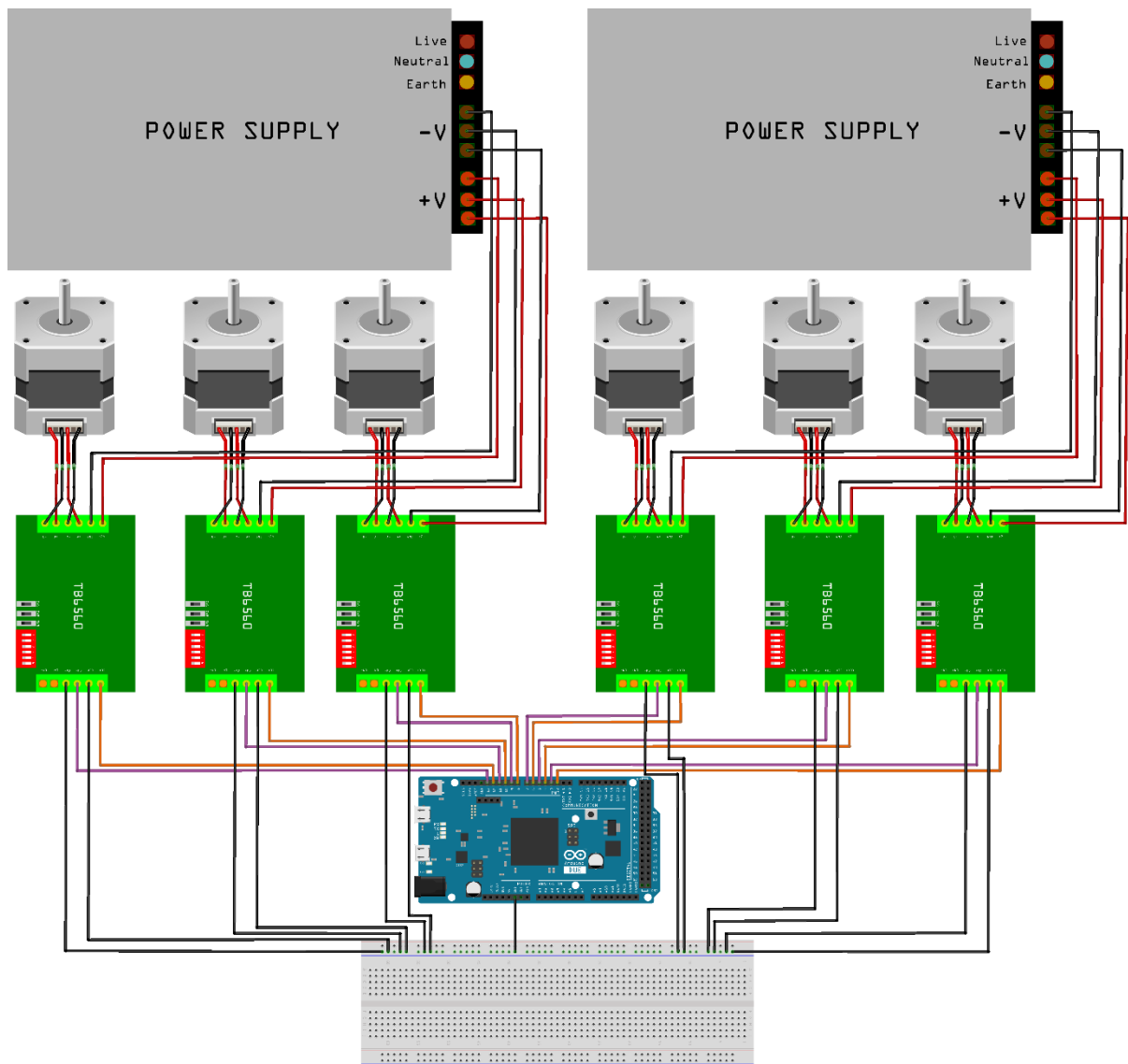
Bachraty and Zalman [148] investigated using the optical mouse as a 2D position sensor. The ADNS6010 sensor was tested and noted that parameters such as the interacting surface, sensor acceleration and sampling rate affects the accuracy of the mouse. Bonarini et al. [149] used a pair of optical mouse sensors for dead reckoning of mobile robots. Ng [150] used the mouse sensor as a 2D displacement sensor to measure the viscoelastic elongation of polyethylene. The mouse could not operate if the distance between the object and itself was larger than 1.25 mm. Wang [151] used a mouse sensor for tactile sensing in conjunction with MATLAB®. The mouse produced accurate measurements with sub-millimeter resolution for slow displacements. Figure 7-5 depicts an HP M-UAE96 mouse. The optical mouse was used in conjunction with MATLAB®.



Figure 7-5: The optical mouse sensor selected

7.4 Wiring Diagrams

Figure 7-6 shows the wiring scheme used for the electronic system. Figure 7-7 shows a close-up view of the wiring scheme for one stepper motor.



fritzing

Figure 7-6: Wiring diagram of the electronic system

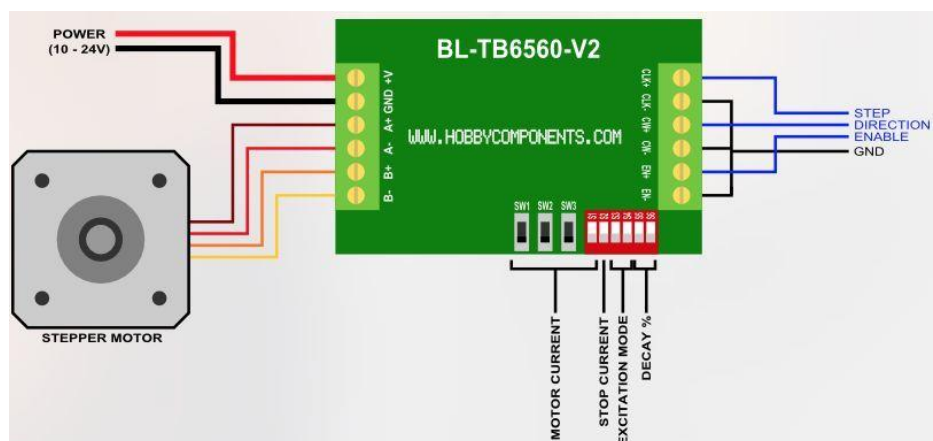


Figure 7-7: Close-up wiring diagram of a stepper motor to a TB6560 Stepper motor driver [152]

7.5 Control Box

Figure 7-8 shows the SolidWorks® assembly and the physical construction of the control box. The stepper motors were connected to microphone 5-P-in-line sockets with matching plugs. The power supplies were mounted on its side and the motor drivers were mounted upright into an additive manufactured casing. Spacing strips were produced through AM to stabilise and mount the power supplies to the control box. The advantages of this arrangement are that the motor drivers are positioned ideally such that air flows through the fins and the row of motor drivers was positioned close to the fan. The power supply fans exhaust air inward towards the box and the suction fan draws out the heat generated. This arrangement also allowed more space for wiring and facilitated the removal of electrical hardware without disconnecting many components. The disadvantages were that wiring was a challenge for motor drivers furthest away from the power supply outputs.

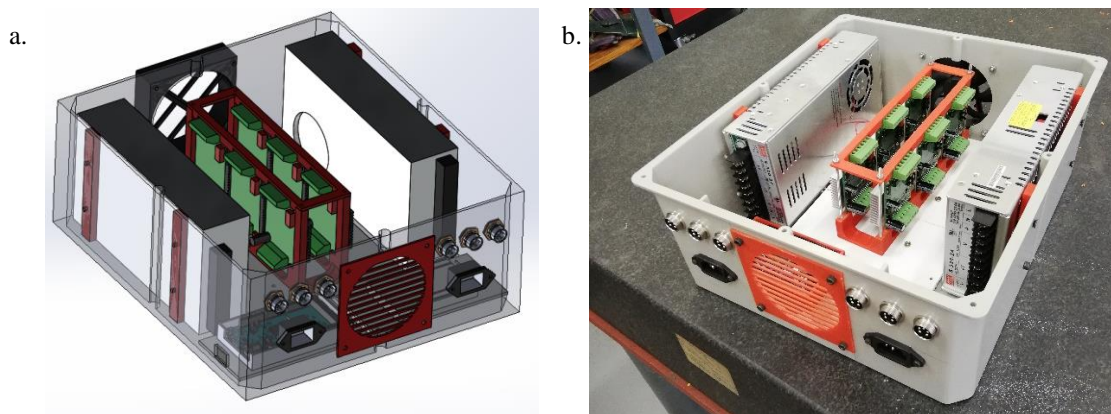


Figure 7-8: The SolidWorks® model and fully assembled control box

- a. The SolidWorks® Assembly.
- b. The control box fully assembled.

7.6 Software System

SolidWorks® provided reference points for the inverse and forward kinematic analyses for MATLAB®. All mathematical analyses were performed using MATLAB®. Simulink was used to create the inverse kinematic block diagram and verify the MATLAB® scripts which performed the inverse kinematic calculations.

Arduino Integrated Developmental Environment (IDE) software served as the platform to program the stepper motors. All steppers were moved simultaneously by using the AccelStepper and MultiStepper libraries. The MultiStepper code was sensitive to the pin specification. Figure 7-9 illustrates how different software and electronic system are related to each other and other aspects of the project.

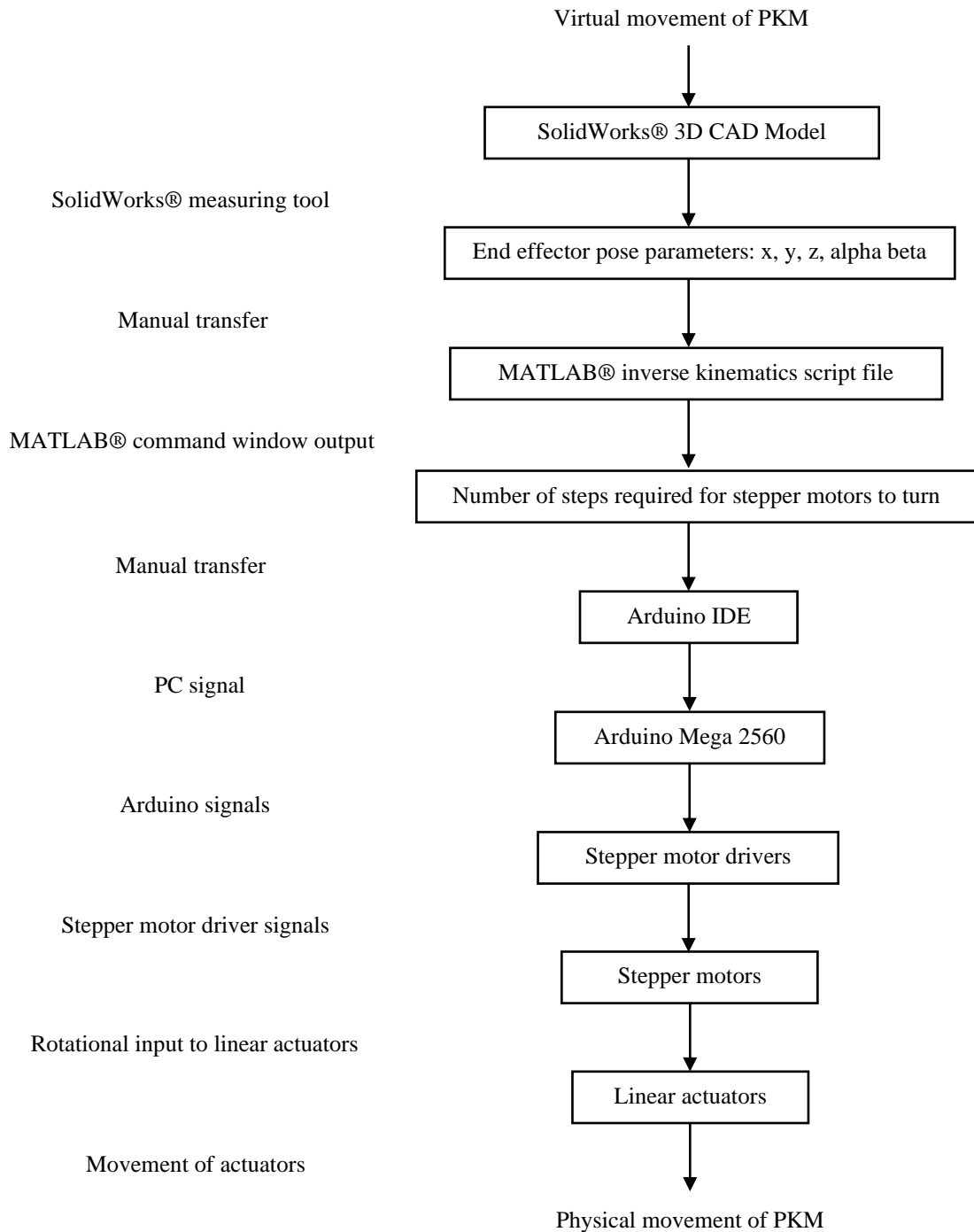


Figure 7-9: The integration of the electronic and software system with the prototype

Simulink can be used to send pulses to the stepper motor as an alternative to the Arduino IDE software. Figure 7-10 displays the Simulink model used to test the connection between Simulink and the Arduino board. The Arduino IDE software was preferred.

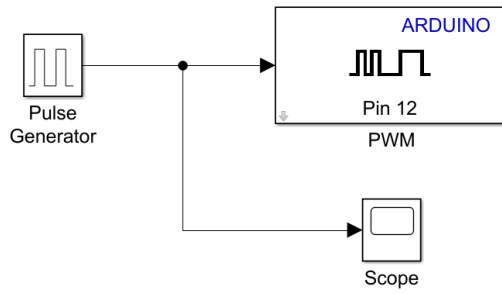


Figure 7-10: A typical Simulink model that can be used communicate with an Arduino board

7.7 Chapter Summary

This chapter described the design requirements for the electronic and software design. A flow diagram was developed to indicate the relationship between the different electronic hardware. The components of the electronic system were described and the use of an optical mouse as a low-cost position sensor was presented. The control box was documented. The chapter concluded with a description of the software system.

The following chapter presents the system performance and testing. Simulations and physical testing were conducted on the prototype. Physical tests such linear actuator accuracy and repeatability, PKM accuracy and repeatability and payload tests are presented. Simulations were carried out on the inverse and forward kinematic analyses using SolidWorks® and MATLAB®.

8. SYSTEM PERFORMANCE AND TESTING

8.1 Introduction

This chapter documents the simulations and physical testing. The linear actuators were tested to determine the accuracy and repeatability of each of them. This was conducted to determine sources of error. Simulations were conducted on the inverse kinematics to validate the inverse kinematic equations developed with MATLAB® script files with reference to the SolidWorks® model. Testing was conducted on the physical model to investigate accuracy and repeatability in terms of the inverse kinematics. The inverse kinematic analysis was used to perform payload testing on the PKM to investigate the relationship between load and leg actuation accuracy and to determine the maximum payload that the PKM could lift. Simulations were conducted to determine the accuracy of the forward kinematic equations developed with MATLAB® script files with reference to the SolidWorks® model. Further simulations were conducted to determine if the guess deviations influenced the number of iterations in accordance with the NR method. Another aim of this experiment was to determine the sensitivity of each variable to guess deviations and convergence.

8.2 Testing System

The testing system was designed to measure the accuracy and repeatability. The OCM was investigated and used as a low-cost displacement sensor with an advantage of being readily interfaced with a computer. MATLAB® was used to acquire data. PG 30 aluminium profile was used to build a frame around the PKM for the mounting of sensors and shaft supports. 90° angled supports were used to mount the aluminium profiles to the wooden base. Wooden inserts were fixed into the wooden base, which allowed the 90° support brackets to be fastened to the base. Appendix E shows the cost of the materials and components.

8.2.1 Translation Testing System

Figure 8-1 (a) depicts the testing system to test the translational movement of the end effector. Two computer mice were used. One mouse was mounted vertically (z-direction measurement) and the other mouse was mounted to the end effector (x and y-direction measurement) with a connecting bracket shown in Figure 8-2 (c). The mouse tracking z-direction movements were mounted onto a wooden platform, using the component shown in Figure 8-2 (b) and both OCM sensors were mounted within the brackets illustrated in Figure 8-2 (a). The wooden platform moved vertically along stainless-steel shafts with linear bearings. The specifications for the linear bearings are provided by Precision Bearing House [153].

The OCM needed to move along a flat surface to output readings. The reverse side of a mirror was used because it possessed a matte finish allowing the OCM to log accurate data. A mirror was also used since it has a smooth surface and the mirror would not bend. The vertical OCM moved passively as the wooden platform is pushed up or lowered by the end effector.

The OCM is sensitive to inconsistent movements and could output inaccurate readings therefore the wooden platform was designed to run along linear shafts with linear bearings. The linear shafts were fastened with shaft supports to the aluminium profiles. The mirror was fastened onto two pairs of linearly adjustable brackets. The pairs of adjustable brackets allowed the mirror to be positioned to make the appropriate contact with the OCM.

8.2.2 Rotation Testing System

The OCM could not measure tilt and the testing system was altered and is shown in Figure 8-1 (b). The component is shown in Figure 8-2 (d) was attached to the end effector. A mirror was also attached to the top of the component to replicated the tilt angle of the end effector. A digital Vernier calliper was used to measure the angle of tilt through the gradient formula. A horizontal level (layer) was designed such that a measuring bracket could be mounted onto it. The horizontal level assisted in recording z displacements from the same height consistently and the measuring bracket was designed with predefined hole spacings.

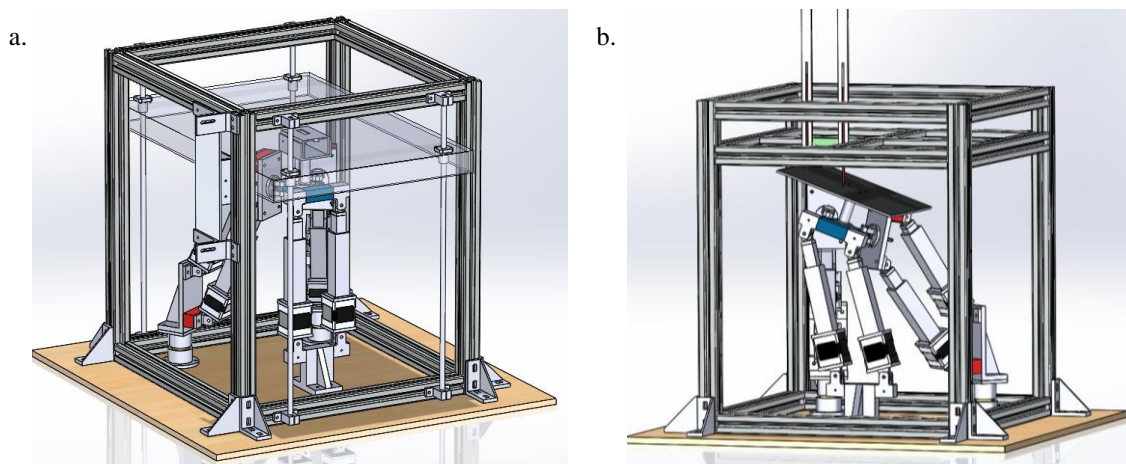


Figure 8-1: Testing system designs for translation and rotation

- a. Testing system for translational testing
- b. Testing system for rotational testing

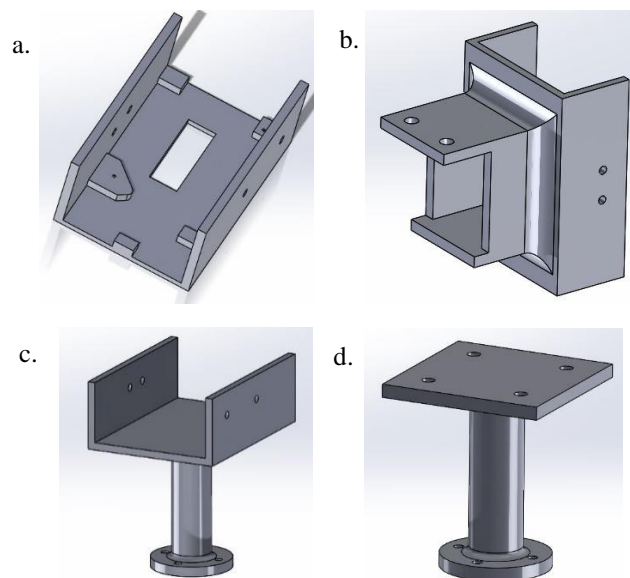


Figure 8-2: Mouse and end effector attachments

- a. The OCM mounting bracket
- b. Bracket connecting the OCM to the wooden platform
- c. Component connecting the end effector to the OCM mounting bracket
- d. Component connecting the mirror to the end effector

8.3 Method of Calibration

The PKM was calibrated before every test. The stroke length of each actuator influenced the position and orientation of the end effector. A manual method was used to calibrate the PKM, whereby the stroke length of the actuator was measured with a digital Vernier calliper. The difference between the measured stroke length and a stroke length of 5 mm was converted into steps for the stepper motor. The signal was sent to the stepper motor and then the linear actuator was calibrated. This was done for each actuator. Figure 8-3 shows the method of measuring the stroke length of an actuator.

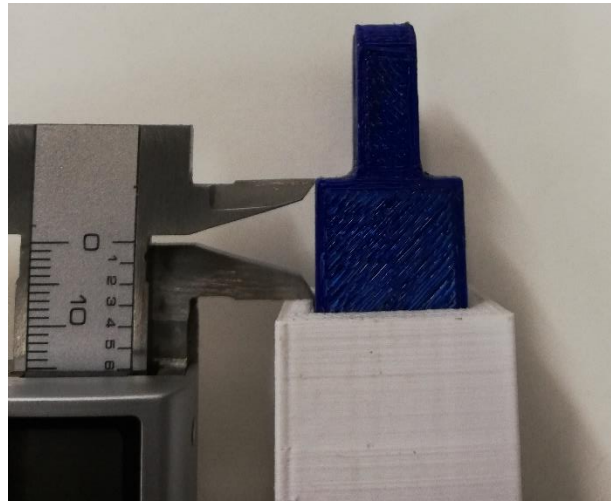


Figure 8-3 Calibration of an actuator

8.4 Linear Actuator Accuracy and Repeatability

8.4.1 Aim

This experiment aimed to determine the accuracy and repeatability of each linear actuator.

8.4.2 Apparatus

- Digital depth gauge Vernier Calliper
- Aluminium extruded profiles
- Desktop computer
- Arduino IDE software
- Linear actuators

8.4.3 Methodology

The test followed the steps below:

1. Remove all revolute joints from the back of the motors.
2. Mount a horizontal beam (aluminium profile) across one side of the testing frame as displayed in Figure 8-5 (a).
3. Place all actuators underneath the aluminium horizontal beam as shown in Figure 8-5 (a).
4. Calibrate the digital depth gauge Vernier calliper using a flat granite table, as illustrated in Figure 8-4.

5. Place the digital depth gauge Vernier calliper onto the horizontal beam and record the initial distance to the top of the actuators.
6. Switch on the actuators using the Arduino IDE and set each actuator to move 10 mm.
7. Record the final distance to the top of the actuators, as depicted in Figure 8-5 (b).
8. Repeat steps 5 to 7 until 10 readings are obtained for an actuation distance of 10 mm.
9. Repeat steps 5 to 8 for actuation distances of 20 mm, 30 mm, 40 mm and 50 mm.



Figure 8-4: Calibration of the digital depth gauge Vernier Calliper

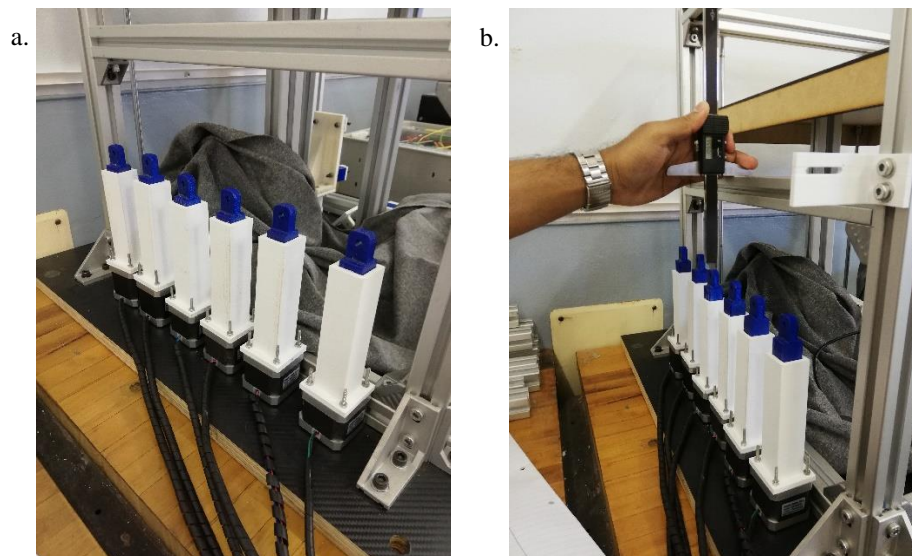


Figure 8-5: Set-up and measurement of actuator lengths

- a. The set-up of the linear actuators under the horizontal aluminium profile.
- b. Placement of the Vernier calliper on the horizontal aluminium profile and measuring the distance to the top of the actuators.

8.4.4 Results

The repeatability and accuracy of the linear actuators were calculated using the formulae for robot accuracy and repeatability, as described by Groover [154]. Control Resolution (CR) is defined as the smallest possible addressable point that can be manipulated over a range of motion. The CR is dependent on the electromechanical

components and the controller of the robot. This research used electromechanical *CR* and is calculated in Equation 8.1. Other related calculations are presented in Appendix C.2.

$$CR = \frac{\text{pitch of threaded rod}}{\text{steps/rev of stepper motor}} = \frac{1.25 \text{ mm}}{200} = 0.00625 \text{ mm/step} \quad (8.1)$$

The *CR* for actuator 1 to 4 was 0.00625 mm/step. Actuators 5 and 6 used stepper motors that performed 400 steps/revolution; therefore, the *CR* for these actuators was 0.003125 mm/step.

The accuracy and repeatability formulae are noted below in Equation 8.2 and 8.3 [154].

$$\text{Repeatability} = \pm 3\sigma \quad (8.2)$$

$$\text{Accuracy} = \frac{CR}{2} + 3\sigma \quad (8.3)$$

Table 8-1 summarises the accuracy and repeatability of all the actuators. This was conducted to find sources of error when the PKM is tested with all actuators moving simultaneously. Figure 8-6 depicts the relationship between the actuation distance and standard deviation. The data obtained from testing is presented in Appendix A.1.

Table 8-1: Accuracy and repeatability of actuator 1 to 6

Actuator	Repeatability (mm)	Accuracy (mm)
1	0.18	0.19
2	0.12	0.12
3	0.13	0.13
4	0.14	0.14
5	0.12	0.12
6	0.20	0.20

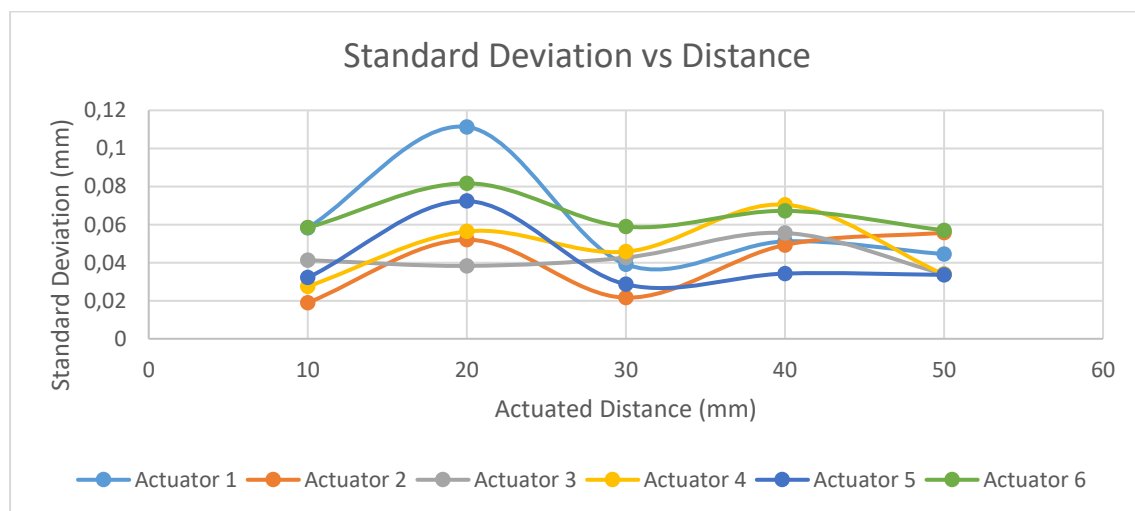


Figure 8-6: Graph of standard deviation versus actuation length

8.4.5 Analysis

The linear actuators, though constructed mainly through AM, exhibits readings that were accurate to a tenth of a millimeter in most cases. The accuracy and repeatability, calculated from the formulae given by Equation 8.1 to 8.3, showed that sub-millimeter movements could be attained. The accuracy and repeatability are acceptable since the target specification for accuracy and repeatability was set to 2 mm. The values in Table 8-1 are well below the target value therefore the actuators were permitted to be used for further testing. The graph of standard deviation vs. actuation length showed that there is no pattern between the two variables. The actuator maintains its accuracy and repeatability over different distances affirming its viability. The advantages of the conducted methodology were the use of cost-effective equipment and short set-up time. One of the disadvantages of the employed methodology was the repetitive manual measuring and data logging which was time-consuming. Another disadvantage was the additional attention that was required to ensure the effective and accurate use of a digital depth gauge Vernier calliper for reliable results. This process was also time-consuming.

8.4.6 Conclusion

The linear actuators proved to be suitable concerning accuracy and repeatability, with the most significant value for both parameters being approximately 0.2 mm. The additive manufactured components were found to be relatively accurate as a low-cost actuator and this validates the use of AM for prototyping. The linear actuators were acceptable to be used for the position and orientation testing of the end effector.

8.5 Inverse Kinematic Analysis Simulations

8.5.1 Aim

To determine the accuracy of the inverse kinematic equations developed with MATLAB® script files with respect to the SolidWorks® model.

8.5.2 Apparatus

- Desktop computer
- MATLAB® Software
- SolidWorks® Software

8.5.3 Methodology

The PKM was designed and developed in SolidWorks® and could, therefore, be used as a reference to validate the kinematic equations. MATLAB® script files were developed to theoretically calculate the length of each leg for a particular position and orientation of the end effector. This approach was also used by Xu et al. [102] and Zhang and Jing [155]. The region for testing points was divided into 5 regions as shown in Figure 8-7. Regions are 55 mm in width along the y-axis. Table 8-2 summarizes the regions for sampling points to eliminate bias sampling of randomly selected points.

Table 8-2: Regions for sampling testing points

Region	Range of y values (mm)
1	$-137.5 \leq y < -82.5$
2	$-82.5 \leq y < -27.5$
3	$-27.5 \leq y \leq 27.5$
4	$27.5 < y \leq 82.5$
5	$82.5 < y \leq 137.5$

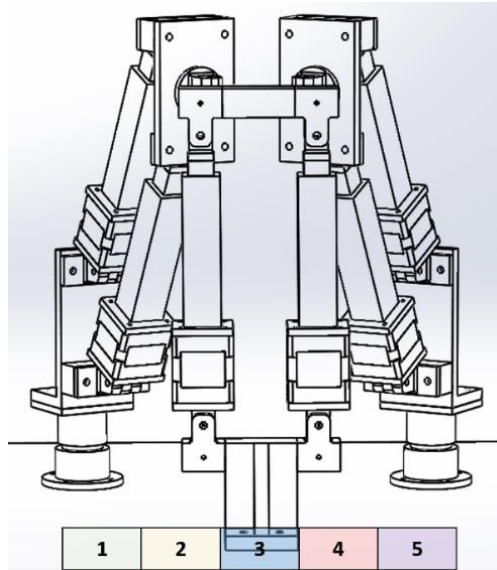


Figure 8-7: The region of testing points. The regions are equally spaced along the y-axis

The methodology that was employed is listed:

1. Move the PKM in SolidWorks®
2. Record the position and orientation of the end effector
3. Record the leg length values from the virtual sensors in SolidWorks® for all six legs
4. Enter the end effector position and orientation values in the MATLAB® script file
5. Run the MATLAB® script file and record the calculated leg length values
6. Enter the end effector position and orientation values in Simulink
7. Run the Simulink model and record the calculated leg length values
8. Compare the values obtained from SolidWorks® to the values obtained from the MATLAB® script file and Simulink.

8.5.4 Results

Ten points were tested in each region for the cases of translation, alpha rotation with translation and beta rotation with translation. The results showed the largest deviation of 0.01 mm between the MATLAB® script file and SolidWorks®. The errors between Simulink and SolidWorks® were the same as the errors observed in the MATLAB® script file and SolidWorks®. Random points were selected in each region. The simulation results are presented in Appendix A.2.

8.5.5 Analysis

The methodology employed to test the accuracy of the equations was time-consuming to transfer points between SolidWorks® and MATLAB®. The errors observed are negligible and are due to rounding off errors. The spread of points shows that the data used is unbiased and also proves that the machine's theoretical position and orientation are unaffected by its position in a specific region of its workspace. The advantage of the employed methodology was that the kinematic equations could be verified before physical testing. This enabled the movements of the prototype to be programmed as discussed in Section 8.6.

8.5.6 Conclusion

The method of validating the inverse kinematic equations was successful. The test also proved that the kinematic equations were accurate. The errors observed were acceptable.

8.6 PKM Accuracy and Repeatability

8.6.1 Aim

This experiment aimed to investigate the accuracy and repeatability of the PKM.

8.6.2 Apparatus

- A digital Vernier calliper
- 2 Desktop computers
- Arduino IDE software
- MATLAB® software
- SolidWorks® software
- 2 OCM

8.6.3 Methodology

The test for the translational movement of the end effector followed the steps below:

1. Move the PKM in SolidWorks®.
2. Enter the coordinates of the end effector in MATLAB® to obtain the number of steps that the stepper motor shaft needs to turn.
3. Enter the number of steps for the stepper motors in the Arduino IDE software.
4. Run the MATLAB® script file to track the position of the mouse on both computers and record the initial pixel reading.
5. Upload the Arduino code to the Arduino microcontroller.
6. Record the final pixel readings from each computer when the PKM stops.
7. Reverse the sign of the steps that the stepper motors were required to execute to move it back to its home position.
8. Upload the Arduino code to the Arduino microcontroller.
9. Repeat steps 3 to 8 until 10 movements are carried out to the same point.
10. Repeat steps 1 to 9 until 15 different points in the robot's workspace have been tested.

The tests for the alpha and beta rotations of the end effector followed the steps below.

1. Move the PKM in SolidWorks®.
2. Enter the coordinates of the end effector in MATLAB® to obtain the number of steps that the stepper motor shaft is to turn.
3. Enter the number of steps for the stepper motor to move in the Arduino IDE software.
4. Upload the Arduino code to the Arduino microcontroller.
5. Use the digital Vernier calliper to measure the depth at two different points using the measuring bracket.
6. Reverse the sign of the steps that the stepper motors were required to execute to move it back to its home position.
7. Upload the Arduino code to the Arduino microcontroller.
8. Repeat steps 3 to 7 until 10 movements are carried out to the same point.
9. Repeat steps 1 to 8 until 15 different points in the robot's workspace have been tested.

Figure 8-8 depicts the PKM performing translational motion. Figure 8-9 illustrates how two different depths were measured to calculate the tilt of the end effector. Figure 8-10 shows the end effector performing a positive alpha rotation. When the mirror was mounted onto the end effector with all actuators locked, the end effector could still move due to the relatively large tolerances from additive manufactured plastic components. This allowed the end effector to exhibit a tilt bias of -4° and this was accounted for when analysing the data for the beta rotation. Figure 8-11 shows the PKM with a tilt bias.

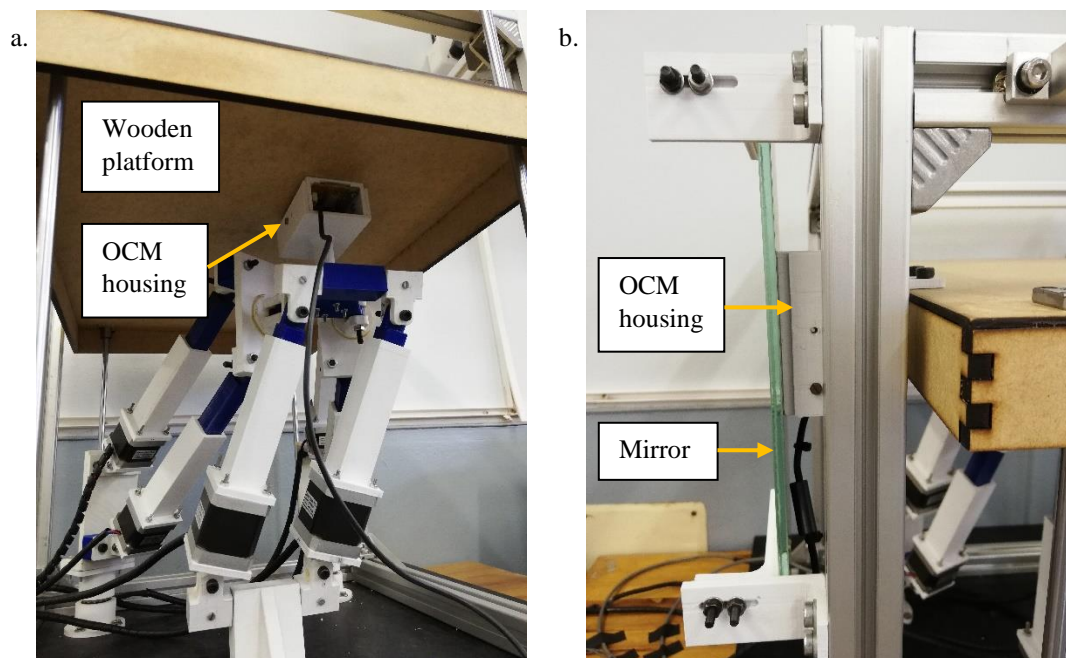


Figure 8-8: Testing the translational motion of the end effector.

- a. The mouse tracking the x and y displacements of the end effector.
- b. The mouse tracking the z displacement of the end effector.

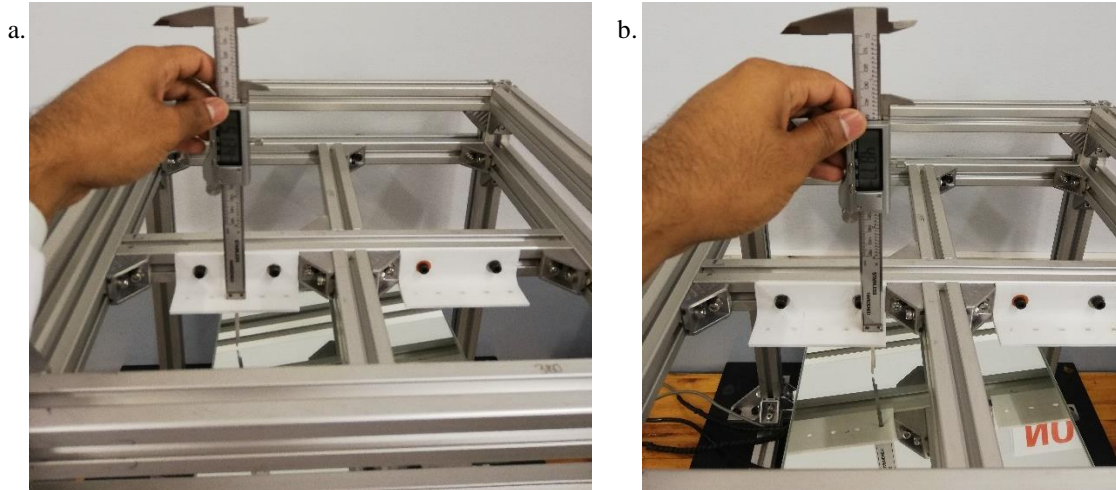


Figure 8-9: Measuring the angle of tilt for an alpha rotation.

- a. Measuring depth 1 from the white bracket to the mirror
- b. Measuring depth 2 from the white bracket to the mirror

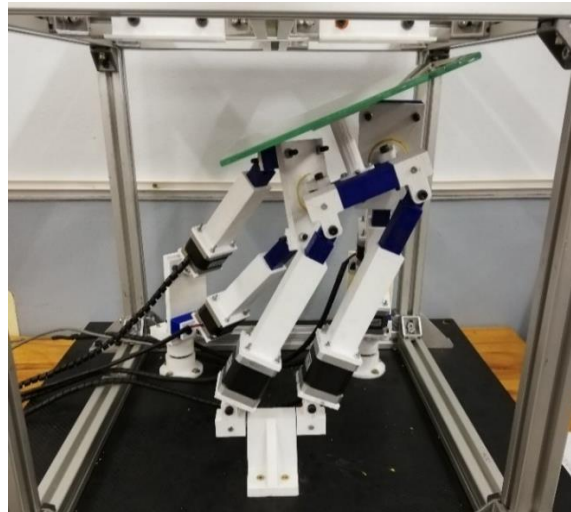


Figure 8-10: The PKM performing a positive alpha rotation.

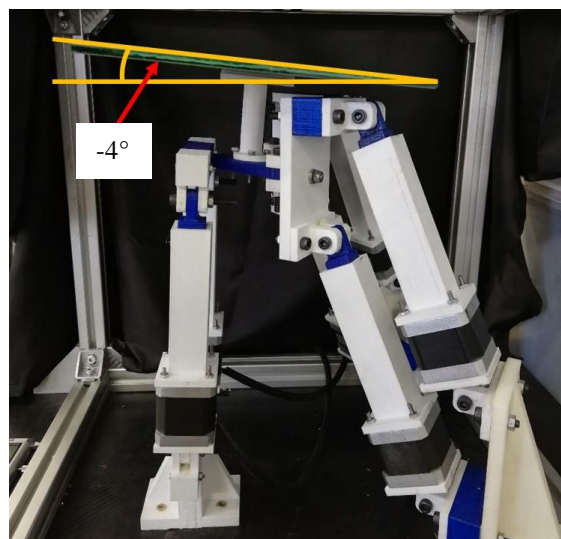


Figure 8-11: The tilt bias of the end effector when the mirror was placed on the end effector.

Figure 8-12 depicts the SolidWorks® message that was displayed when all actuators were locked and the end effector was attempted to be moved. The message confirmed that the end effector could not be moved theoretically.

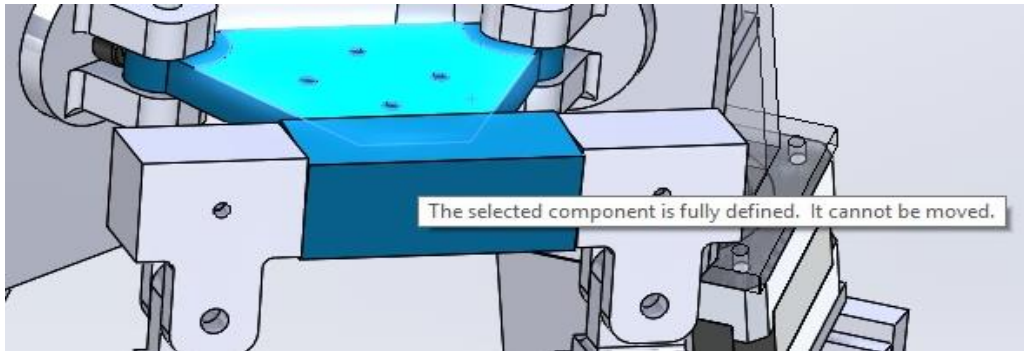


Figure 8-12: SolidWorks confirmation of no PKM movement when all actuators are locked.

8.6.4 Results

Accuracy and repeatability formulae used in the research were used by Zhao et al. [156] for the metrological evaluation of a novel medical PKM developed. Other authors have used the formulae for accuracy and repeatability analysis [157, 158]. The formulae are linked to ISO 9283: 1998 and are presented below. The Position Accuracy (AP) is given by:

$$AP = \sqrt{AP_x^2 + AP_y^2 + AP_z^2} \quad (8.4)$$

$$AP_x = \bar{x} - x_c \quad (8.5)$$

$$AP_y = \bar{y} - y_c \quad (8.6)$$

$$AP_z = \bar{z} - z_c \quad (8.7)$$

Where $(\bar{x}, \bar{y}, \bar{z})$ is the mean values or barycentre and (x_c, y_c, z_c) is the commanded position.

$$\bar{x} = \frac{1}{n} \sum_{j=1}^n (x_j) \quad (8.8)$$

$$\bar{y} = \frac{1}{n} \sum_{j=1}^n (y_j) \quad (8.9)$$

$$\bar{z} = \frac{1}{n} \sum_{j=1}^n (z_j) \quad (8.10)$$

Where (x_j, y_j, z_j) is the coordinates of the reached point.

The Position Repeatability (RP) is given by:

$$RP = \bar{l} + 3S_l \quad (8.11)$$

$$\bar{l} = \frac{1}{n} \sum_{j=1}^n (l_j) \quad (8.12)$$

Where \bar{l} is the mean value with respect to the deviations between the j^{th} reached positions.

$$S_l = \sqrt{\frac{1}{n-1} \sum_{j=1}^n (l_j - \bar{l})^2} \quad (8.14)$$

Where S_l is the standard deviation of the sample.

Table 8-3 and Table 8-4 presents the accuracy and repeatability results for translation. The tests were conducted 10 times for each point and a total of 15 different sample points were used. 3 points were used in each region. The data obtained from testing is presented in Appendix A.3. The data obtained from the OCM testing is presented in Appendix A.7. Appendix B.2 presents the Arduino code used for accuracy and repeatability testing.

Table 8-3: Accuracy results for translational motion.

Region - Point	Accuracy			
	Entire PKM (mm)	X axis (mm)	Y axis (mm)	Z axis (mm)
1-1	1.63	1.13	0.81	0.86
1-2	1.82	1.09	0.79	1.22
1-3	1.51	0.97	0.84	0.79
2-1	1.49	0.89	0.92	0.77
2-2	1.34	0.59	0.91	0.79
2-3	1.53	0.83	0.97	0.85
3-1	1.17	0.74	0.27	0.87
3-2	1.38	0.72	0.77	0.89
3-3	1.33	0.92	0.74	0.61
4-1	1.63	0.94	1.08	0.78
4-2	1.78	1.07	1.03	0.98
4-3	1.77	0.95	1.02	1.09
5-1	1.91	1.06	1.13	1.11
5-2	1.71	1.1	1.12	0.69
5-3	1.83	1.02	1.25	0.87

Table 8-4: Repeatability results for translational motion.

Region - Point	Repeatability			
	Entire PKM (mm)	X axis (mm)	Y axis (mm)	Z axis (mm)
1-1	2.71	2.16	1.92	1.73
1-2	2.29	2.02	1.61	1.11
1-3	1.56	0.78	1.54	0.82
2-1	1.96	1.61	1.42	0.72
2-2	2.51	2.01	1.81	1.17
2-3	1.62	1.49	0.62	1.33
3-1	2.51	2.64	0.46	1.67
3-2	2.67	1.85	0.76	2.42
3-3	2.56	2.43	2.09	1.03
4-1	1.78	1.69	1.37	0.8
4-2	2.2	1.8	1.84	1.66
4-3	2.33	1.69	1.7	1.05
5-1	2.05	1.53	1.49	1.33
5-2	1.67	0.75	1.53	0.6
5-3	2.48	1.87	2.45	1.02

Figure 8-13 shows a graphical representation of the results documented in Table 8-3 and Table 8-4.

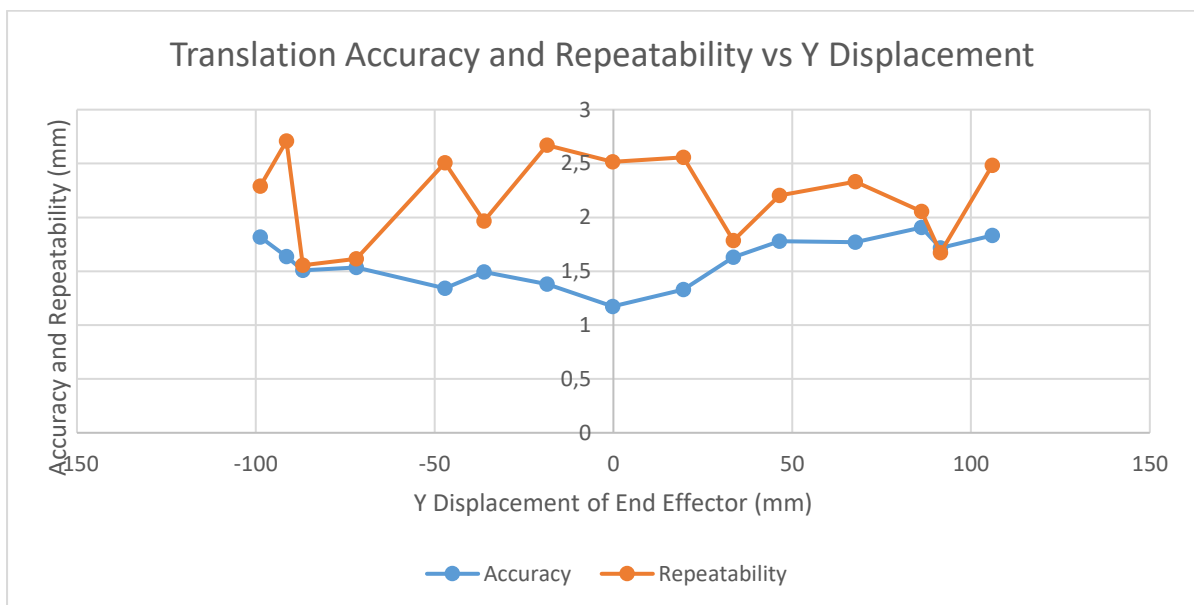


Figure 8-13: Translational Accuracy and Repeatability vs. Y Displacement.

The same sample size was used to test rotational performance. The graph of alpha rotation accuracy and repeatability vs. alpha angle is given by Figure 8-14. Figure 8-15 shows the relationship between the alpha rotation accuracy and repeatability and the y displacement.

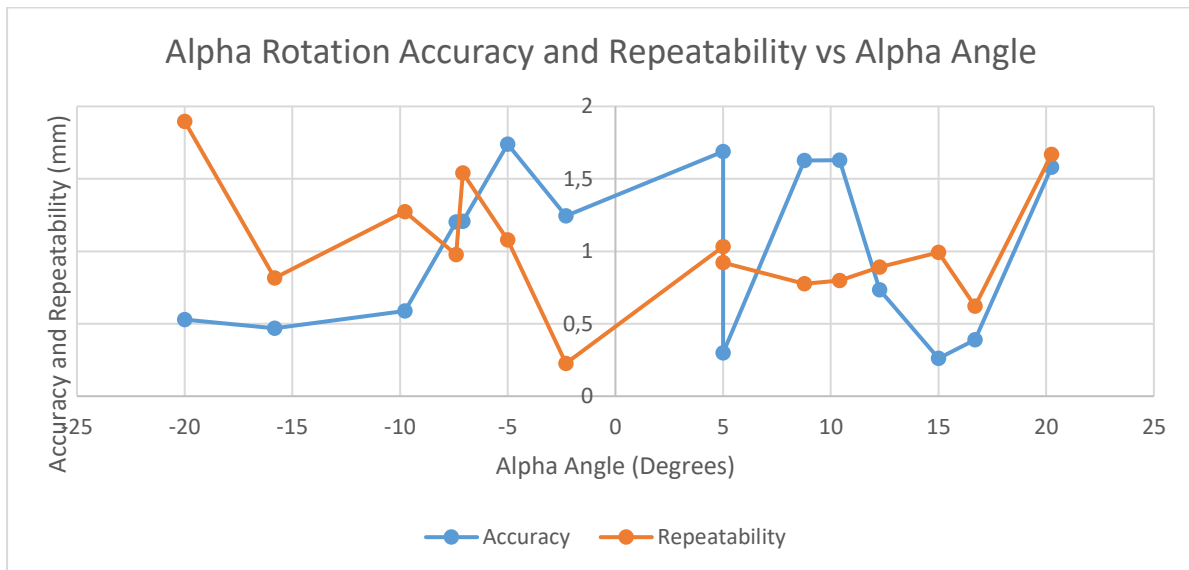


Figure 8-14: Alpha Rotation Accuracy and Repeatability vs. Alpha Angle

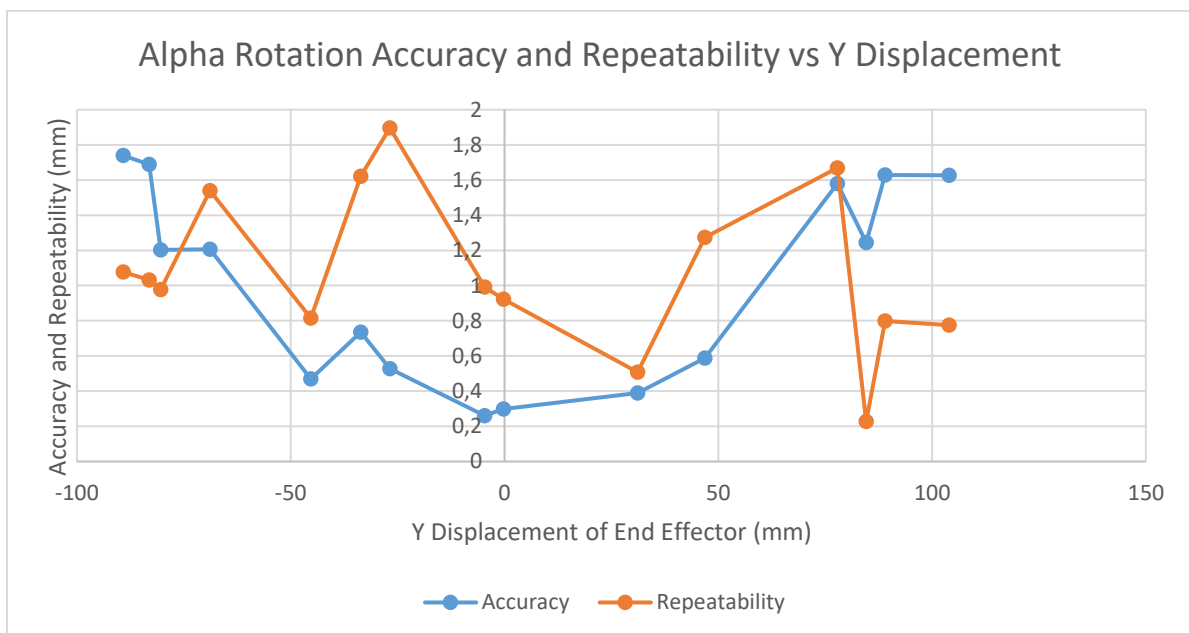


Figure 8-15: Alpha Rotation Accuracy and Repeatability vs. Y Displacement

The graph of beta rotation accuracy and repeatability vs. beta angle is given by Figure 8-16. Figure 8-17 shows the relationship between the beta rotation accuracy and repeatability and the y displacement of the end effector.

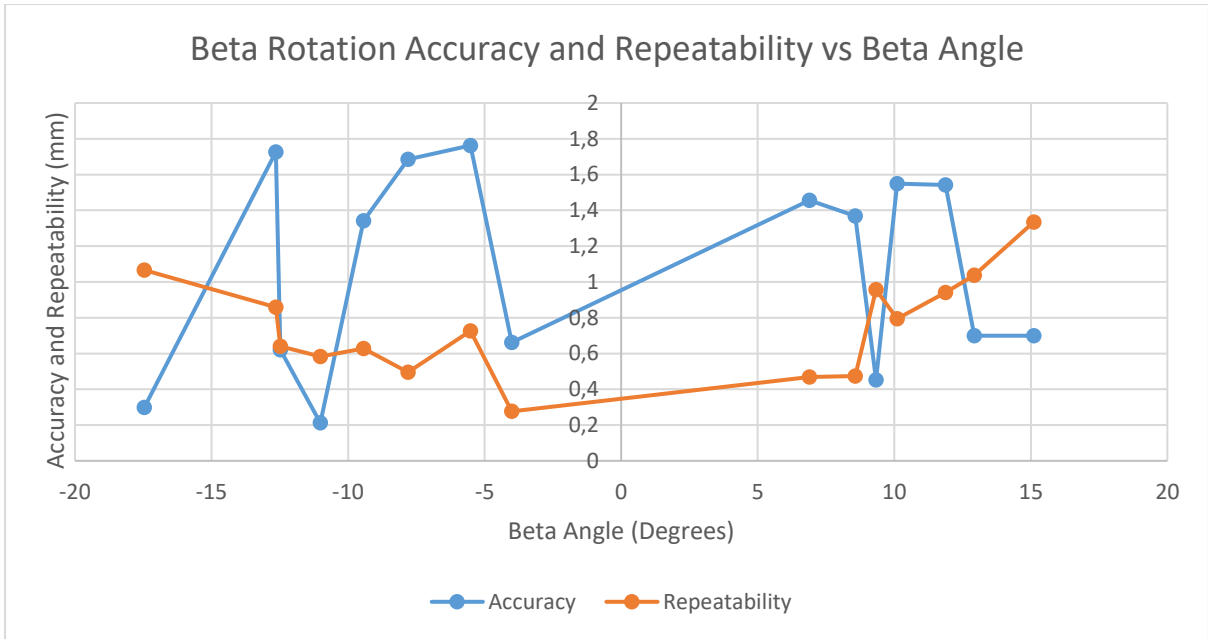


Figure 8-16: Beta Rotation Accuracy and Repeatability vs. Beta Angle

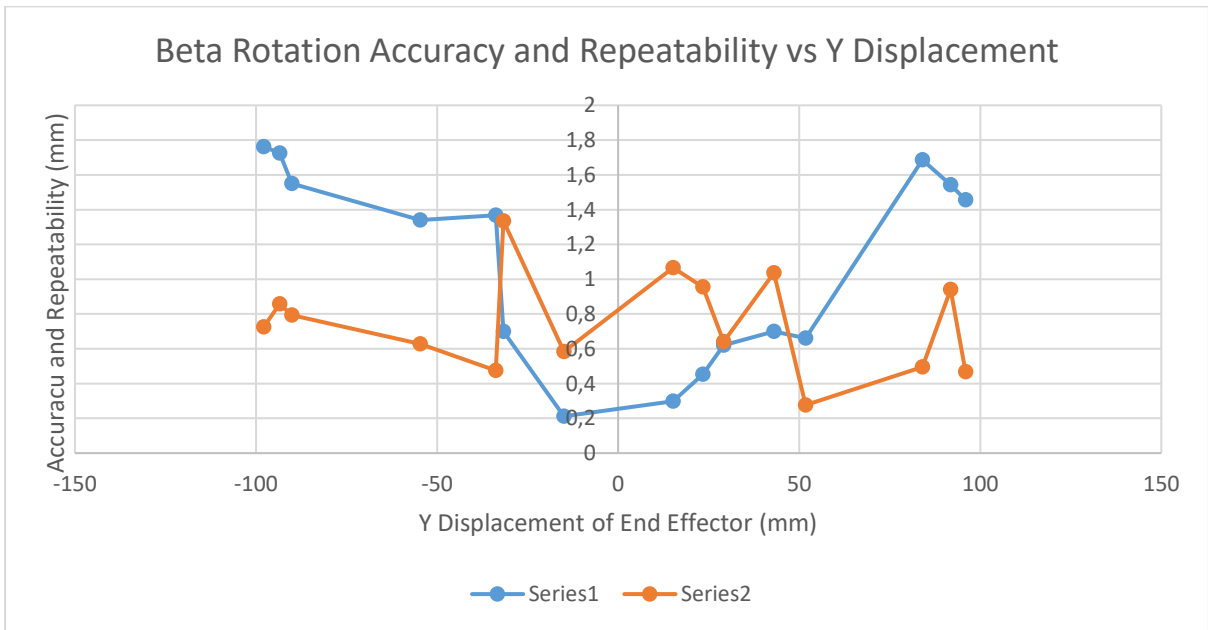


Figure 8-17: Beta Rotation Accuracy and Repeatability vs. Y Displacement

8.6.5 Analysis

Figure 8-13 shows a relationship between the translation accuracy and the y-direction. This indicates that accuracy is anisotropic. The PKM is most accurate when the y-displacement is low and loses accuracy as the y displacement increases. The accuracy deviations are magnified through the use of an additive manufactured desktop model. The tolerances of plastic joints are not as high nor as rigid as metal mechanical joints. The accuracy ranged from 1.17 mm to 1.91 mm. This is acceptable and was below the target specification of 2 mm.

The results of the translational repeatability did not show any relationship to the displacement along the y-direction. The repeatability results were erratic, as shown in Figure 8-13. This is due to the high sensitivity OCM sensors and it encountering noise since it was used on a robotic system that vibrates. The repeatability of the translational movement ranged from 1.56 mm to 2.71 mm. This indicates the large variances encountered when using OCM sensors as low-cost displacement sensors. The formulae used to calculate repeatability included a standard deviation calculation which resulted in the repeatability values being sensitive to variance in pixel measurements. The pixel data obtained from the measurements contained a few outliers which produced relatively high repeatability values. The OCM sensors provide more accurate results when many iterations of the movement to the same point are conducted due to the relatively high variance observed. For this reason, 10 iterations were conducted per point. Most of the repeatability values were more than 2 mm which exceeded the target specification of 2 mm. The repeatability was therefore larger than the accuracy due to the high sensitivity of the OCM sensors and outliers in the pixel measurements.

For the rotational analysis, the accuracy and repeatability were measured against the angle of rotation and the y displacement. The alpha accuracy displayed a similar pattern as to the translational accuracy. The accuracy was high for small y displacements but the PKM lost accuracy as it moved further along the y-direction. The weight of the PKM itself tends to magnify the loss of accuracy as the machine moves towards extreme points along the y-direction. The accuracy ranged from 0.26° to 1.74° . This was acceptable as it is lower than the target specification of 2° . There was no evident relationship between accuracy and rotation angle. The repeatability of the alpha rotation showed a relationship with the angle of rotation. The larger the angle of rotation, the poorer the repeatability. The repeatability ranged from 0.23° to 1.9° which was below the target specification of 2° . There was no correlation found between the alpha rotation repeatability and y displacement. Figure 8-14 and Figure 8-15 illustrate the insights.

The beta rotation results illustrated the same patterns as the alpha rotations. The beta rotation accuracy was dependent on the y displacement of the end effector whereby the larger the y displacement, the poorer the accuracy. The accuracy ranged from 0.21° to 1.76° . The repeatability was dependant on the angle of rotation such that high repeatability was observed for small angles of rotation. The repeatability ranged from 0.28° to 1.33° . Both the accuracy and repeatability observed were smaller than the target specification. Figure 8-16 and Figure 8-17 illustrates the described relationships.

The methodology was time-consuming. Many machine movements were conducted which was tiresome through manual measurements and data logging. Another disadvantage was that 3 software programs were required to conduct each movement. Advantages of the methodology were the cost-effective equipment that were used and no additional software was required from the institution to conduct the tests except for the Arduino IDE which was free.

8.6.6 Conclusion

The accuracy and repeatability of the PKM were smaller than the target specifications of 2 mm and 2° . The only exception was repeatability of the translational movement which showed most of the repeatability results to have exceeded 2 mm. The use of a digital Vernier calliper produced better results in terms of the variance observed as opposed to the OCM sensors. The tolerances in the plastic joints allow movement of the end effector when all

actuators are locked. The PKM also incurred a tilt bias about the y-axis when the mirror was attached to the end effector.

8.7 Payload Testing

8.7.1 Aim

This experiment aimed to investigate the relationship between load and leg actuation accuracy and to determine the maximum payload that the PKM could lift.

8.7.2 Apparatus

- Digital scale
- Digital Vernier Calliper
- Calibrated weights
- Desktop computer
- Arduino IDE software

8.7.3 Methodology

The test followed the steps below:

1. Validate the mass of each calibrated disc with the digital scale.
2. Position the PKM in SolidWorks® such that the end effector does not move in the x and y directions, thus only performing the vertical motion.
3. Set the corresponding number of steps to turn for each stepper motor.
4. Load the PKM.
5. Run the Arduino code such that the end effector moves vertically upward.
6. When the PKM stops, measure all actuator legs using the Vernier Calliper.
7. Return the PKM to its home position.
8. Repeat steps 4 to 7 for different weights.

Figure 8-18 shows the validation of a 1-pound mass. All weighted discs were placed on the scale and validated before loading the PKM with the various weights.



Figure 8-18: Mass validation of calibrated weights

8.7.4 Results

The leg lengths were measured with a digital Vernier calliper after each test under when the PKM was subjected to various loads. Table 8-5 displays the largest actuation error recorded for each leg and the weight under which the largest actuation error occurred. The results of this test can be found in Appendix A.4. Figure 8-19 depicts the graph of mass versus leg actuation error. The results were plotted for each measured leg length for each load that the PKM elevated. Figure 8-20 shows the PKM lifting various loads by a vertical distance of 50.42 mm.

Table 8-5: Summary of leg actuation errors as a function of load

	Leg 1	Leg 2	Leg 3	Leg 4	Leg 5	Leg 6
Largest error (mm)	0.21	0.29	0.27	0.28	0.2	0.18
Load occurrence (kg)	7.09	7.09	7.09	12.07	8.44	5.27

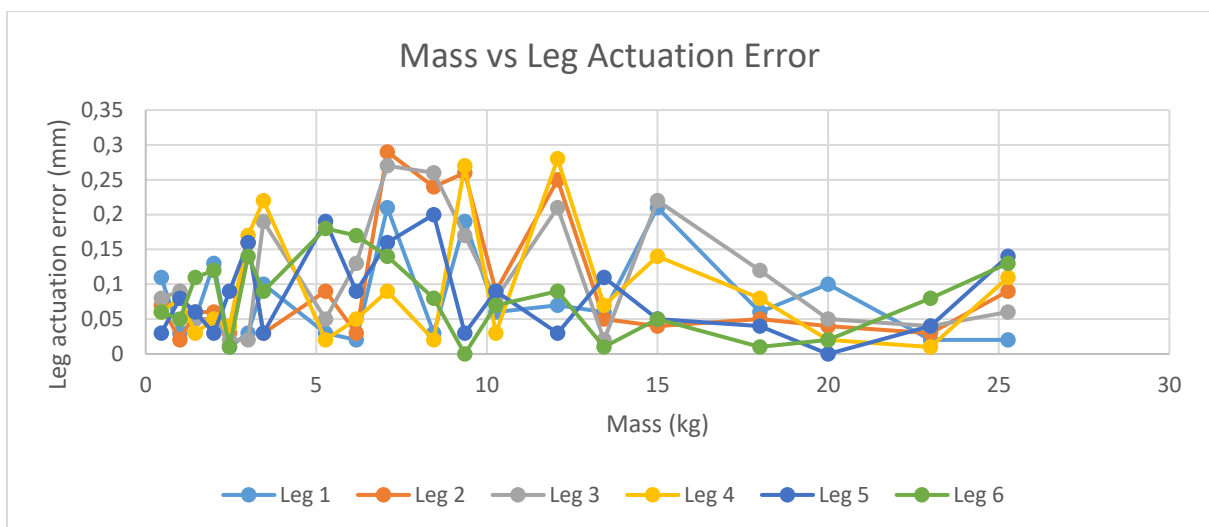


Figure 8-19: Graph of Mass vs. Leg Actuation Error

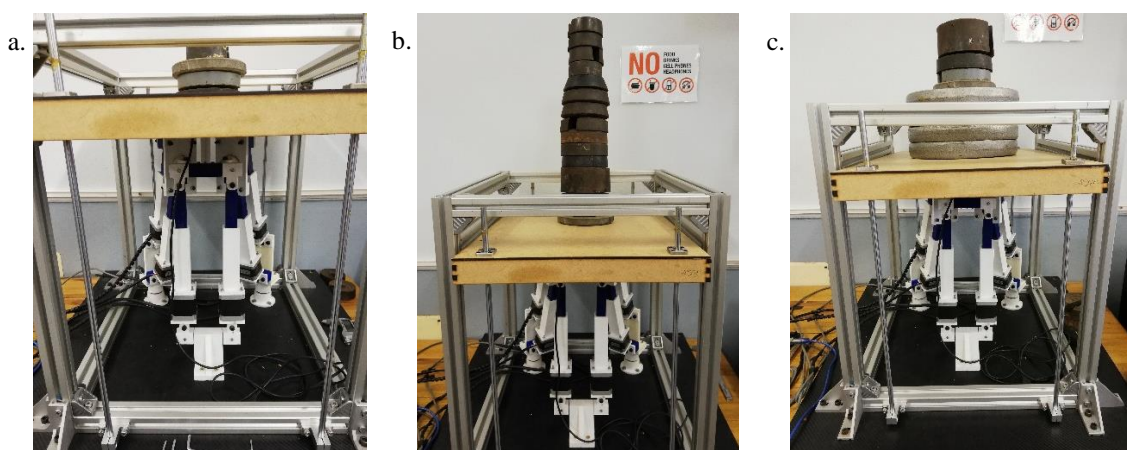


Figure 8-20: The PKM lifting various weights vertically by 50.42 mm

- The PKM lifting a load of 5.27 kg
- The PKM lifting a load of 13.43 kg
- The PKM lifting its maximum load of 25.23 kg

Figure 8-21 illustrates the components that failed. The PKM lifted a load of 25.23 kg. Upon reloading, at 25kg, the mouse bracket and end effector failed.

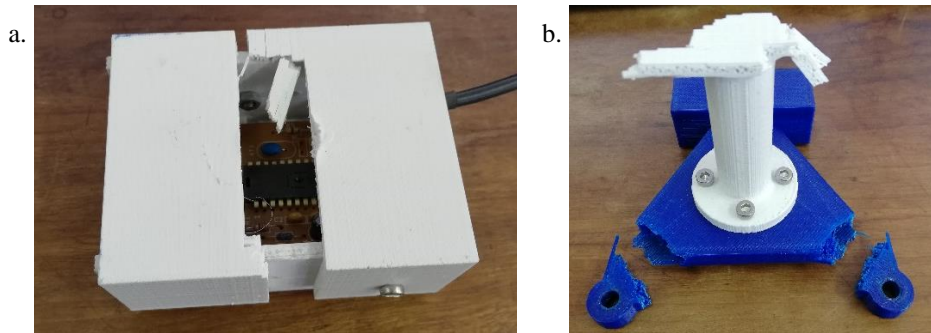


Figure 8-21: Failed components after lifting a 25.23 kg load

- a. Failure of the mouse bracket
- b. Failure of the end effector

8.7.5 Analysis

The results from Table 8-5 shows the largest error of 0.29 mm at a load of 7.09 kg. The PKM lifted a mass of 25.23 kg at which the actuation error was smaller than 0.29 mm. Figure 8-19 shows that the actuation error and mass have no relationship suggesting that the accuracy is independent of mass. The errors observed are accepted. The errors obtained could also be attributed to human errors when using the digital Vernier calliper. Figure 8-20 shows that the load was placed directly above the PKM and not spread around the wooden platform for the purpose of consistency of results and to replicate a point load as accurately as possible.

Figure 8-22 illustrates the joint at which failure occurred. The weakest point is at the revolute joints of the end effector. This suggests that the additive manufactured components failed before the stepper motors could not push a heavier load. Based on the power screw calculations and buckling calculations presented in Appendix C.1 and C.3 respectively, the weakest element was the additive manufactured components. The advantage of the methodology was that it was cost-effective with a short set up time. One of the disadvantages of the use of a Vernier calliper and manual data logging was that the test was time-consuming. Manual loading and unloading of weights could cause harm if not carried out appropriately. The point of failure of components caused the weights to fall which could be dangerous if not carried out cautiously.

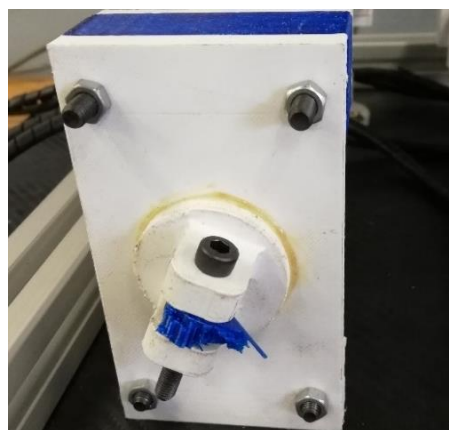


Figure 8-22: The weakest point of the PKM where the failure occurred.

8.7.6 Conclusion

The results proved that leg actuation accuracy is independent of load. The PKM lifted the various loads with the largest leg actuation error found to be 0.29 mm. This was acceptable. The PKM was able to lift a load of 25.23 kg. Improvements could be made to the design of the end effector to withstand a higher load. The weakest point was found to exist at the actuator revolute joints linked to leg pair 1 and leg pair 2.

8.8 Forward Kinematic Simulations for Repeatability – MATLAB® and SolidWorks®

8.8.1 Aim

To determine the accuracy of the forward kinematic equations developed with MATLAB® script files with respect to the SolidWorks® model.

8.8.2 Apparatus

- Desktop computer
- MATLAB® Software
- SolidWorks® Software

8.8.3 Methodology

The test followed the steps below:

1. Set the mates that allow the end effector to move in translation only.
2. Move the end effector in SolidWorks®.
3. Record the end effector, theta and leg length values.
4. Input leg length data and relevant data into the forward kinematic script code in MATLAB®.
5. Record the converged values and the number of iterations.
6. Repeat steps 1 to 4 until 5 values are obtained from each region.
7. Repeat steps 1 to 5 for alpha rotation with translation and for beta rotation with translation.

8.8.4 Results

Points were taken from each region to eliminate the possibility of a biased data set. 25 points were obtained for each of the cases tested. The results are presented in Table A.4 to Table A.6 in Appendix A.5.

8.8.5 Analysis

The greatest number of iterations observed for converged solutions was 8. Large initial guess deviations were made in numerous cases and a solution was obtained. In certain instances, large initial guesses deviations caused divergence. There were also cases when convergence occurred but not an incorrect value. This relates to the unfeasible poses.

Concerning translation, the maximum initial guesses from the true position and orientation were 168.29 mm and 44.55° respectively. The largest convergence errors for position and orientation were 0.025 mm and 0.68 degrees respectively. The alpha rotation with translation maximum initial guesses from the true position and orientation was 101.31 mm and 43.79° respectively. The largest convergence errors for position and orientation were 0.04 mm and 0.09° respectively. The beta rotation with translation maximum initial guesses from the true position and

orientation was 167.33 mm and 73.57° respectively. The largest convergence errors for position and orientation were 0.07 mm and 1.13° respectively.

The convergence errors are in the region of hundredths of a millimeter for translation. The orientation errors are generally in the region of a tenth of a millimeter. There was an outlier observed of 1.13 mm orientation error. The results showed a consistency of high accuracy irrespective of theoretical position.

The disadvantage of the methodology was that it was time-consuming due to the number of points tested and manually transferring information across from SolidWorks® to MATLAB®. The methodology was advantageous such that the forward kinematic equations could be verified through simulations before physical testing of the prototype.

8.8.6 Conclusion

The NR method was successfully employed with high convergence accuracy for translation, alpha rotation with translation and beta rotation with translation. The accuracy of the NR method is independent of position and orientation. When convergence was observed, the number of iterations did not exceed 8 iterations.

8.9 Forward Kinematic Simulations – Guess Deviations Analysis

8.9.1 Aim

This investigation aimed to determine the sensitivity of each variable with respect to guess deviations from the true value of the variable and convergence.

8.9.2 Apparatus

- Desktop computer
- MATLAB® Software
- SolidWorks® Software

8.9.3 Methodology

The test followed the steps below:

1. Set the mates that allow the end effector to move in translation only.
2. Move the end effector in SolidWorks®.
3. Record the end effector coordinates and the theta and leg length values.
4. Input leg length data and relevant data into the forward kinematic script code in MATLAB®.
5. Guess values close to the actual value and record the number of iterations.
6. Manipulate each variable by increasing the guess deviation of one variable at a time while holding all other values to the values used in step 5. Record the number of iterations and check for convergence.
7. Repeat steps 1 to 6 for alpha rotation with translation and beta rotation with translation.

8.9.4 Results

The results of translation, alpha rotation with translation and beta rotation with translation have been split up into graphs for position and for orientation because the guess deviation values used for the position have a larger range than for rotation. The graphs for translation are illustrated in Figure 8-23 and Figure 8-24. Figure 8-25 and Figure

8-26 depict the results of alpha rotation with translation and finally Figure 8-27 and Figure 8-28 depict the results of beta rotation with translation. Appendix A.6 presents the simulation results.

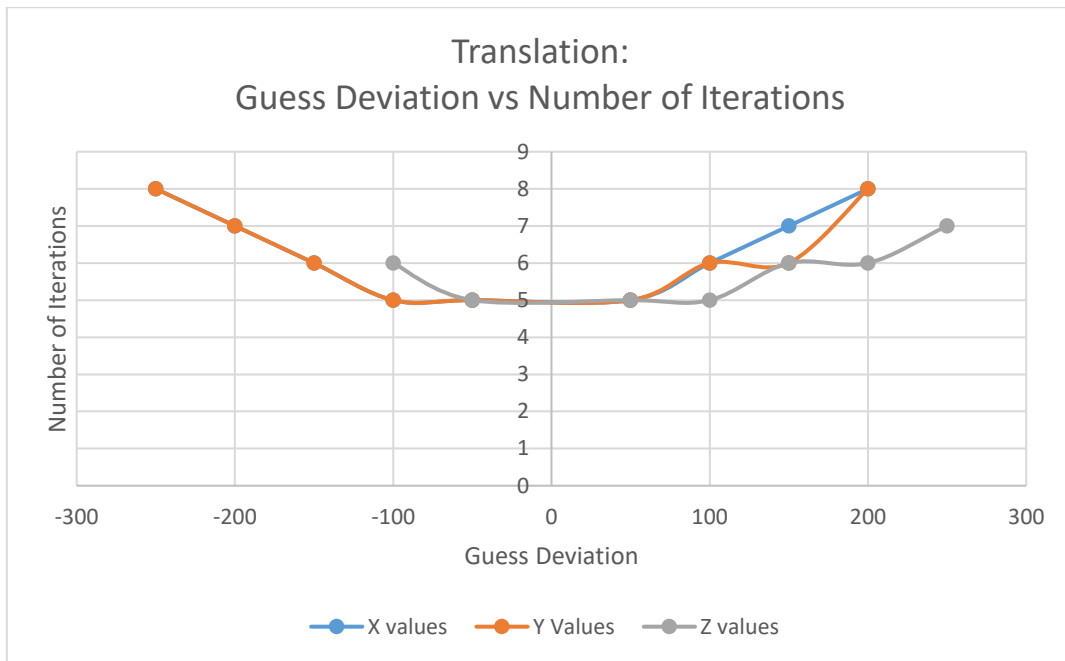


Figure 8-23: Translation Guess Deviation vs. Number of Iterations for position

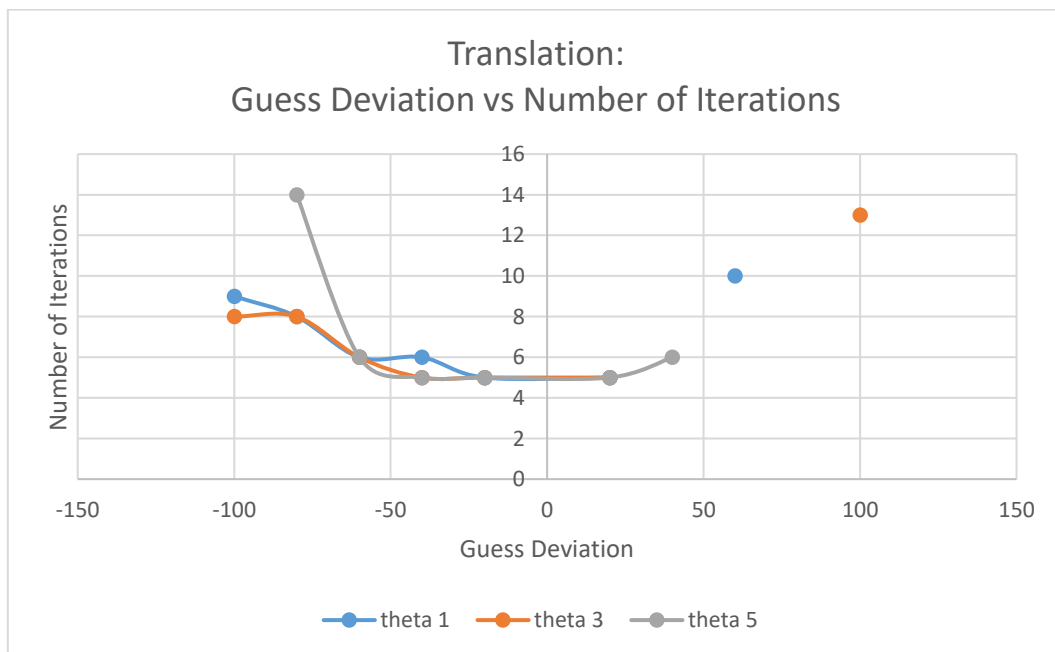


Figure 8-24: Translation Guess Deviation vs. Number of Iterations for angular values

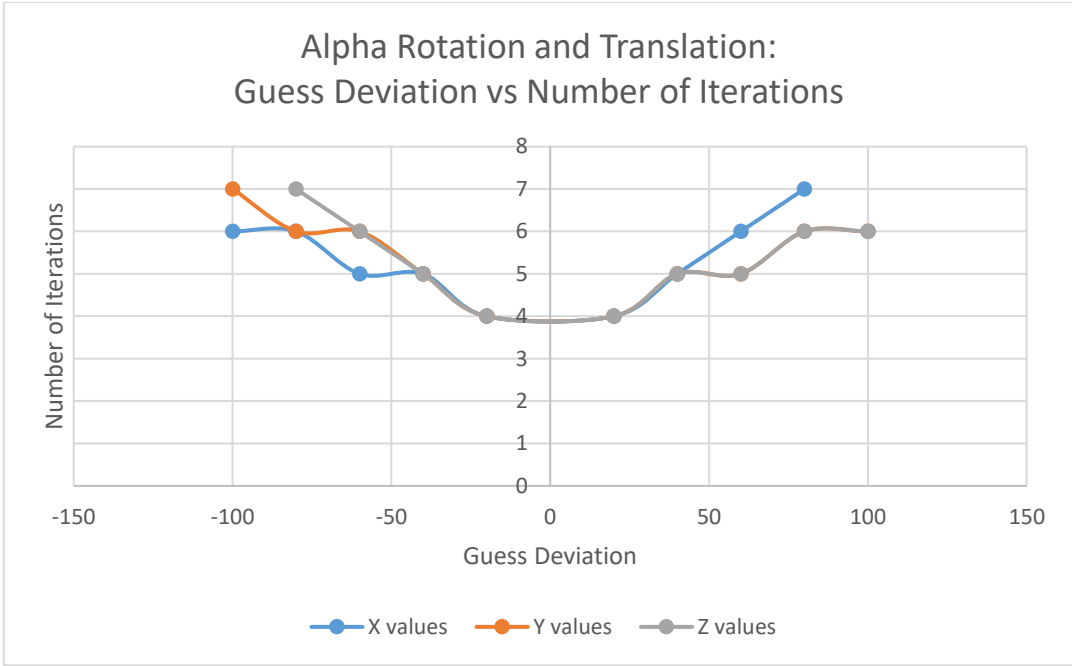


Figure 8-25: Guess deviation results for alpha rotation with translation – position

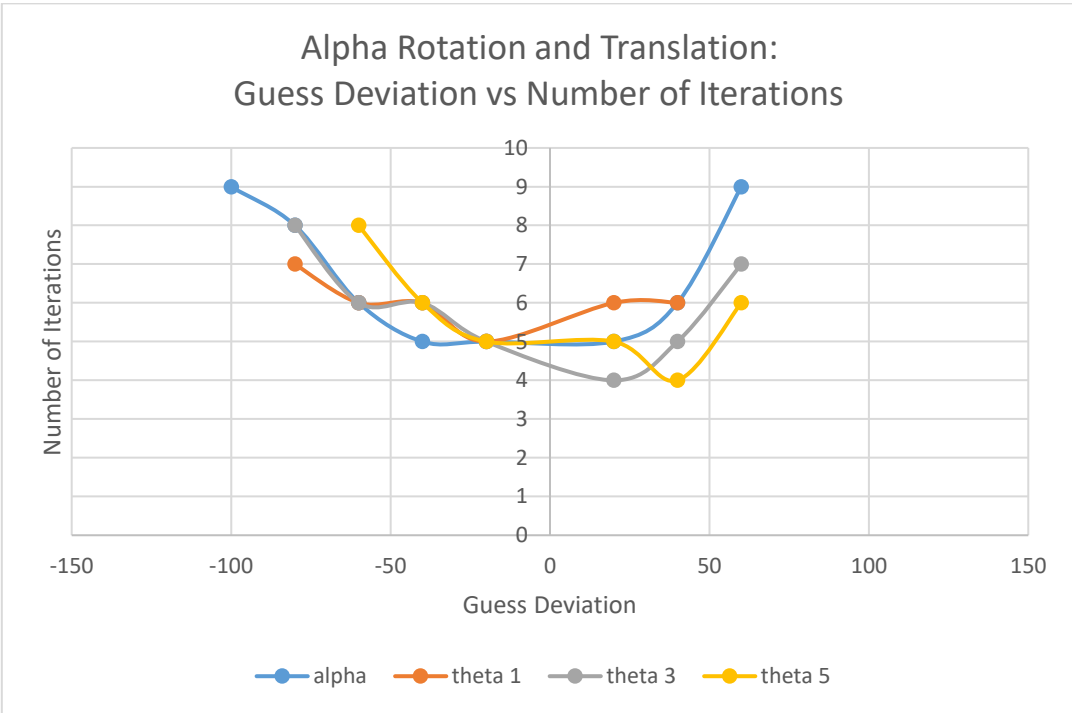


Figure 8-26: Guess deviation results for alpha rotation with translation - angles

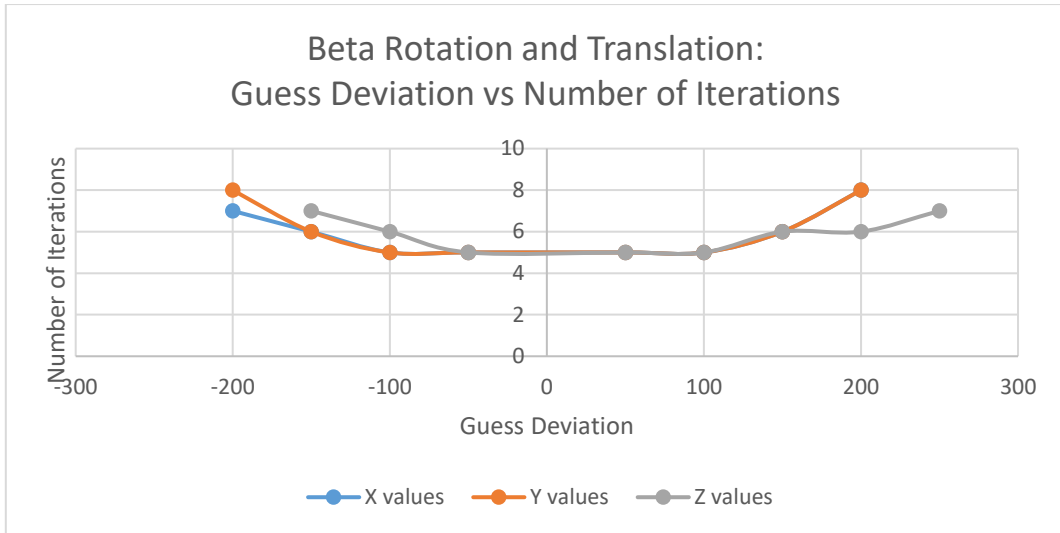


Figure 8-27: Guess deviation results for beta rotation with translation – position

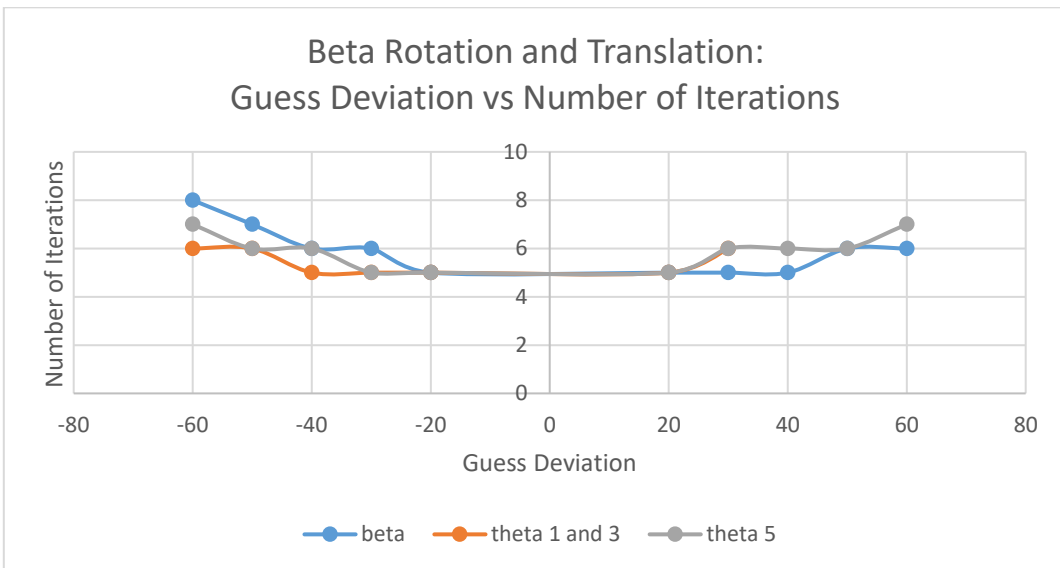


Figure 8-28: Guess deviation results for beta rotation with translation - angles

8.9.5 Analysis

All graphs illustrate that as the guess deviation increases further away from the actual value, the solution undergoes more iterations to converge. For translation, Figure 8-23 shows convergence for deviations up to 250 mm away from the actual value. The z value failed to converge and sometimes converged to an incorrect solution when guesses were made between 150 mm and 250 mm lower than the true value. The z value was more sensitive to deviations than the x and y values. The angular guesses for translation showed difficulty in convergence for angular guesses greater than 20° from the true value but showed convergence for angles up to 100° less than the actual value of the variables. Convergence also occurred in some cases where preceding guesses did not. These observations show that reasonable guesses for the NR method are not symmetrical nor does it follow a predictable pattern for a reasonable guess.

The graphs relating to the alpha rotation with translation, illustrate that the position range for deviation was lower than the translational case. Most iterations occurred with 4, 5 and 6 iterations. The angular guesses showed convergence for the alpha guesses up to 100° less than the true value and guesses up to 60° greater than the actual value. Other angular guesses showed convergence up to 80° less than the actual value and up to 60° greater than the actual value. The theta 1 and theta 5 values are the most sensitive since the least number of convergence cases occurred for these variables.

The graphs relating to the beta rotation with translation, Figure 8-27, show that most calculations were performed in 5 iterations and z value is more sensitive to guesses less than the real value in comparison to the x and y values. Concerning the angular guesses, most of the convergences also occurred with 5 iterations. The theta 1 and 3 variables were found to be most sensitive since convergence occurred the least number of times from the guess deviation range. The beta and theta 5 variables displayed good convergence characteristics as convergence occurred for all guess deviations ranging from 100° less and greater than the actual value.

The disadvantage of the test was that it required large amounts manual data logging and the transference of data from SolidWorks to MATLAB® for each position and orientation of the end effector. The advantage of the test was that it provided another validation of the forward kinematic equations and the effective use of the NR method.

8.9.6 Conclusion

Results showed that the number of iterations was dependent on guess deviation. This was observed for all cases of the end effector's movement and for all variables within each case. The result also showed that some variables are more sensitive to guess deviation than to others. The range of the guess deviation is dependent on the type of movement of the end effector. Convergence patterns are not symmetrical and sometimes convergence can occur whilst preceding guess deviations do not bring about convergence. This suggests the unpredictability of a convergence pattern in certain regions of a guess deviation.

8.10 Chapter Summary

Physical testing and simulations were conducted on various aspects, mainly centered around repeatability and accuracy. Each of the individual tests documents the findings and conclusions drawn from each of the tests. The key observations include:

- The novel inverse kinematic method consistently produced accurate results with errors in the range of hundredths of a millimeter, mostly attributed to rounding off errors.
- The forward kinematic simulations yielded accurate results and conformed to the general patterns of the NR method.
- A computer mouse can be used as a low-cost displacement sensor in conjunction with MATLAB® yielding a resolution of 0.2 mm per pixel. The drawback is that it has a tolerance of 1.06 mm and produced a large variance in pixels measured.
- The linear actuators, although produced through AM, possessed good accuracy and repeatability with both parameters approximately 0.2 mm.

- The PKM produced acceptable accuracy and repeatability for translation, translation with alpha rotation and translation with beta rotation. All results for accuracy and repeatability were smaller 2 mm and 2° except for one case.
- The PKM loses accuracy as it moves further along in the positive or negative y-direction.
- Repeatability is dependent on the angle of rotation of the end effector.
- The PKM lifted a load of 25.23 kg. The failure occurred due to the strength of the additive manufactured components.

The succeeding chapter presents the discussion for the conducted research. The research question, findings, observations, performance and insights are discussed. The concept overview, justification and literature are discussed. A discussion concerning the synthesis, design, singularities and workspace is presented. Physical testing and performance of the PKM are discussed. The chapter also documents the implication of the PKM.

9. DISCUSSION

9.1 Chapter Introduction

The research question from Section 1.5 was: Can a novel PKM be developed for 3 translational and 2 rotational DOFs to validate part handling, sorting, general positioning and robotic machining capabilities? This chapter summarises the dissertation with the findings, observations, performance, and insights of the research while addressing the research question. The implications of the novel PKM in the manufacturing sector are discussed.

9.2 Concept Overview, Justification and Literature

The growing inflation rate, weaker Rand and higher interest rates in South Africa inhibits entrepreneurship. South Africa needs to remain technologically competitive and produce goods at a low cost and high quality. The BRICS index of industrial production showed that South Africa has not significantly increased its industrial progress since 2014 [2]. Stats SA [7] showed that the manufacturing, mining and trade sectors underperformed for the first 3 months of 2019 with a contraction of 3.2%. South African Market Insights [159] revealed that the South African manufacturing underutilisation had reached its highest percentage in 4 years with a value of 19.7%. This is due mainly to insufficient demand suggested by a weak economy or increased imports. This identifies the need that manufacturing machinery should be designed and produced within South Africa as opposed to being imported which, in turn, creates job opportunities.

Researchers are exploring robotic platforms to perform tasks that were thought to be only possible with CNC machines [15]. The drawbacks of CNC machines are that they are large, heavy and expensive [16, 17]. The relatively low capital investment of robotic manipulators, reusability and flexibility, making them a suitable alternative to CNC machines [18]. Robotic platforms have the potential to replace CNC machines for specific tasks. PKM possesses a high payload to weight ratio, high stiffness and the errors of the joints are averaged. PKMs, however, suffer from a relatively small workspace in comparison to serial manipulators. The selection of the correct robotic platform is application-dependent. The workspace of a PKM can be designed to suit the needs of the end-user [19]. PKMs have the potential to be designed, manufactured and implemented to assist the South African economy.

PKMs that have been commercialised for dedicated machining tasks are large and heavy [8]. Other PKMs have been commercialised but still, do not have the industrial presence as serial robots [11]. This establishes the need for affordable robotic platforms. Industry 4.0 paradigms can be applied to robotic platforms to make them technological relevant in the context of Industry 4.0.

Literature suggests that 2-DOF PKMs can perform either translational or rotational motion. Although possessing more straightforward mathematical analyses, they lack the mechanical rigidity in comparison to PKMs with more actuators. 2-DOF PKMs are designed for specific tasks that require a limited range of planar or spatial movements. 3-DOF can possess 2 translation and 1 rotation, 1 translation and 2 rotations, pure translations or pure rotations. These motion capabilities produce a variety of architectural designs. The delta and spatial architectural type have industrial presence. 3-DOF PKMs possessing pure rotations have not been adopted by industry as mainstream mechanisms and lack mechanical rigidity.

Concerning 4-DOF PKMs, research suggests that the delta architectural type is the most commonly researched and adopted by industry. The delta structure possesses low inertia since the motors are positioned at its footpoints which enables high-speed pick and place applications. Many delta PKMs have been commercialised for pick and place and AM applications. 4-DOF PKMs possess a larger workspace in comparison to 5-DOF and 6-DOF PKMs.

5-DOF PKMs have numerous architectural designs and unique machine structures in comparison to other DOF PKMs. The most common motion combination is 3 rotational and 2 translational DOFs. It is uncommon for a 5-DOF PKM to possess 2 rotational and 3 translational DOFs. The category of 5-DOF PKMs have received lesser attention relative to 3-DOF, 4-DOF and 6-DOF PKMs, therefore, presenting a research gap. Researchers have produced functional 3D CAD models with fully solved kinematic analyses and some producing prototypes but have not been made commercially available. The most common type of 5-DOF platforms with PKM architectures are hybrid structures. Some of these platforms are commercially available. The kinematic analysis of hybrid architectures is challenging [8].

6-DOF PKMs possess better mechanical rigidity in comparison to other DOF PKMs and due to these PKMs possessing 6 legs. This imparts better high stiffness characteristics leading to better mechanical rigidity. 6-DOF PKMs find its niche applications in machining, high vibrations applications and general positioning. These applications have made 6-DOF PKMs an attractive study and much research has gone into optimising their characteristics. More 6-DOF PKMs have been commercialised relative to 5-DOF PKMs. The rotational ranges of 5 DOF PKMs are, however, higher than that of 6-DOF PKMs and can, therefore, be used for large rotation applications. The Pentapod PKM developed by Metrom is an example of a 5-DOF PKM with large rotation ranges [94].

The hexapod-type layout for 5-DOF and 6-DOF PKMs employs prismatic joints as the source of actuation. In this configuration, the PKM possesses high inertia due to large moving masses (actuators) and is better suited to low-speed applications hence its adoption and research for machining and positioning tasks. These platforms can still, however, be used for short-distance pick and place and sorting applications. There is a trade-off between large workspaces and mechanical rigidity. The workspace of the robot can be altered to suit the application, but the singularity analysis needs to be conducted.

This research explored the concept of a 5-DOF PKM. To perform machining applications, at least 3-DOFs were required. This inherently disqualified 2-DOF PKMs. The PKMs was intended to perform rotations which then disqualified 3-DOF PKMs and 4-DOF PKMs. The validation of PKM movement for machining applications was intended thus 4-DOF PKMs were further disqualified. Since machining applications do not require the rotational DOF about the axis normal to the workpiece, a 6-DOF PKM was not researched. The research gap for a 5-DOF PKM was discovered. This research was an exploratory study intended to lay the groundwork for further research and also explored the concept of exclusive use of revolute and prismatic joint to synthesise a novel architectural design. The review of PKM robotic platforms supported the exploration of a 5-DOF platform.

9.3 Synthesis and Design of a Novel PKM

The adopted synthesis methodology was presented by Pandilov and Dukovski, and Weck [40, 94]. The work done by Chablat and Wenger [58] and Qiu et al. [89] influenced the development of a novel actuated parallelogram joint, shown in Figure 3-5. The prismatic type, depicted in Table 3-1, was selected as the architectural type due to its mechanical rigidity. The research performed by Liu and Kim [60] was used to establish the structure and joint layout of the end effector. The research presented by Liu and Kim [60], Xiaolong et al. [90] and Zhu et al. [91] provided insight into the arrangement of the leg layout. The arrangement of revolute joints possesses the ability to restrict a DOF or convert an independent motion to a dependent motion. The mounting pattern of the joints on the base was chosen to lie in a circular arrangement spaced at 120° apart. The symmetric arrangement of joints increases the isotropic behaviour. The direction of the applied force was along the length of the linear actuators and the global and local z-axes were normal to the base and end effector respectively.

Revolute joints were preferred instead of universal joints to provide additional stiffness, tighter machine tolerances and higher ranges of motion. The disadvantage is that the design required twice as many revolute joints as universal joints. The PKM was classified as an over-constrained mechanism based on the Grubler Kutzbach criterion with a DOF value of -4. This is per the theory presented by Merlet [10]. The DOFs were identified through observations and measurements conducted in SolidWorks® and is presented in Appendix G.

A characteristic of the novel Pa-IQ joint was the parallelogram structure exhibited when both legs are actuated to the same distance and an irregular quadrilateral structure exhibited when a leg pair accomplish different stroke lengths. Each pair of legs are coplanar which aided the kinematic calculations. The differences between then the 2R(Pa-IQ)RR, R(Pa-IQ)R PKM and the Hexapod are listed in Table 3-2. A distinct difference between the two platforms is that the 2R(Pa-IQ)RR, R(Pa-IQ)R PKM possesses some actuators that can entirely move spatially while Hexapod structures do not allow the bottom of its actuators to move relative to its base.

The QFD analysis provided target specifications for the prototype as per Table 3-3. Potential customer requirements were related to engineering metrics. Engineering metrics were related to each other to establish supportive or conflicting relationships. The rotation about the x and y axes had the highest number of strong relationships with engineering metrics. The rotational capability is the most affected by changes to engineering parameters. The stroke length of the linear actuators possessed the highest number of strong relationships with customer requirements and was ranked with the highest importance. This metric affected many customer requirements. The second-highest ranked engineering parameters were accuracy and repeatability. These parameters required more design and investigation.

The accuracy, repeatability and singularity parameters were ranked as the most challenging target specifications to reach due to their high level of dependency on other engineering parameters. This suggests that these parameters are simpler to optimise once a prototype has been finalised and assembled. Simulations and physical testing investigated accuracy and repeatability, shown in Section 8.

The QFD allowed a competitive analysis to be conducted between industrial PKMs and the PKM developed. The PKM was ranked the best concerning weight, cost, modularity and portability. The PKM was ranked the least favourable concerning translation along the x, y and z axes, durability, high precision and use for different applications. The extreme nature of the rankings was due AM. AM allows the PKM to be lightweight but

possessed the drawback of relatively large joint tolerances in comparison to industrial robotic joints. The relatively large joint clearances also caused the PKM to be the least durable however, AM allowed the PKM to be produced at low-cost. A desktop prototype was aimed to be produced therefore its translational characteristic did not score as high as industrial PKMs. The lightweight nature of the PKM allowed it to be modular and portable. The PKM was also ranked the lowest for use in different applications. All other PKMs compared were also capable of performing multiple tasks. The PKM developed was not aimed to perform industrial tasks such as milling but could still be used to validate the movement of those tasks since it was mostly constructed from additive manufactured components. The QFD competitive analysis was not a true reflection of performance as it compared customer requirements and not engineering ratios such as actuator stroke length to workspace and others. In this instance, the size of the robotic platform determined many machine characteristics hence, performance and engineering ratios are better suited as a method of comparison.

The Metrom Pentapod P800 and the FANUC F-200iB served as the best PKM platforms for benchmarking. The Metrom Pentapod P800 was the most favourable on three instances and least favourable only once. The FANUC F-200iB was the least favourable and most favourable only once. The FANUC F-200iB was competitive against other industrial PKMs. The PKM developed was aimed to be produced with large rotational capability whilst still being as portable as the FANUC F-200iB. The larger PKMs generally possessed higher accuracy and repeatability but possessed drawbacks of poor portability, high costs and are extremely heavy. The PKM developed was ranked the most favourable on 4 instances and indicated that AM could be used to compliment designs used on an industrial scale. The PKM proved that it possessed enough favourable characteristics to be used as a prototype. More accurate comparisons can be conducted should the PKM be built on a large scale with the aim to maintain its favourable characteristics.

The prototype was manufactured with PLA plastic. PLA filament was selected due mainly to its lower print and bed temperature which resulted in faster production of components. PLA possessed a higher tensile strength and bending strength than ABS filament. ABS printed components were more susceptible to warpage hence the selection of PLA as the manufacturing material. The PKM was compact, portable and low-cost. Appendix E presents the project costs. General component thicknesses ranged from 2 to 8 mm depending on the application. An infill of 80% and a layer height of 0.2 mm ensured fair component strength, faster print times and an aesthetic finish. Some thin-walled components were printed with 100% infill due to unexpected shorter production time. The shorter production time was due to the minimal nozzle movement. Additive manufactured joint tolerances were established in Section 4. The linear actuator had a stroke length of 66 mm and was designed mainly with additive manufactured components which aided the development of a low-cost prototype. A testing frame was designed to test the translations and rotations of the end effector. Laser tracking and point-to-point laser displacement sensors were not available and were high in cost therefore an OCM and Vernier calliper were used to perform measurements that were accounted for during the design process.

The final design showed that the end effector possessed a rotation range of $71.46^\circ (\pm 35.73^\circ)$ for the α rotation about the x-axis and a rotation range of $63.97^\circ (-36.8^\circ \text{ to } 27.17^\circ)$ for the β rotation about the y-axis. The new architecture provided a higher rotational range than similar architectural 5-DOF and 6-DOF PKMs [94]. Other final PKM specifications are presented in Table 4-2. The PKM also possessed parasitic rotation which was induced when alpha and beta rotations occurred simultaneously. The parasitic rotation was not investigated in this study.

9.4 Singularity and Workspace Analysis

Singularities were identified through observation. Three types of singularities were discovered. The first type of singularity was when the PKM reached its workspace boundary, shown in Figure 6-4. At the boundary, the PKM can exhibit unstable motion and resist forces solely with its mechanical structure. A pose with alpha rotation and a pose with beta rotation were discovered as singular points as depicted by Figure 6-5. The singularity poses concerning the rotation of the end effector shows that the end effector can resist forces in certain directions without having to counteract these forces with a force or torque (resistance by the mechanical structure).

Merlet [10] described the various workspace analyses that could be conducted, shown in Section 6.3. Five workspaces were investigated in this research, namely the constant orientation, alpha rotation with translation, beta rotation with translation, maximal excluding parasitic motion and inclusive orientation workspace. Other workspaces were beyond the scope of this research. The Monte Carlo method was used to produce the workspace with a point cloud and a surface was wrapped around the point cloud in MATLAB®. The advantages of this method are described in Section 6.3 and various authors [137, 138]. This method was used since a novel PKM was designed and the shape of the workspace was not intuitive. The convex hull was selected as the triangulation surface wrapping method. The geometric and discretisation methods were not selected due to the complex shape of the workspace which, as mentioned, was not intuitive. The Monte Carlo method was best suited for the architectural complexity of the PKM.

Simulations for the constant orientation showed that the difference between a point cloud of 10 000 points and 12 000 points was 0.13%. This indicated that either 10 000 or 12 000 points could be used. 12 000 points were used for most of the point clouds. All point clouds, volumes and point cloud distributions are presented in Section 6.3. The constant orientation workspace was 1 212 900 mm³ while the beta rotation with translation 2 022 000 mm³. The workspaces were asymmetrical due to the architectural design. The shape of the constant orientation workspace was validated by the shape of the workspace produced by Xiaolong et al. [90] for a redundant actuated 5-DOF PKM. The curves that form the boundary of the constant orientation workspace and the beta rotation with translation workspace are not intuitive and require other numerical methods to determine the equations of the curves to accurately determine the workspace.

The use of the Monte Carlo method is justified as it is a more straightforward approach. The volume of the beta rotation with translation was larger than the constant orientation workspace as expected due to the additional volume that can be reached by the tilt of the end effector. The increase in volume was 67%, which was unexpectedly high. The beta rotation with translation required an additional constraint, which can be addressed as future work. This was the reason for the large increase in volume. The additional volume range is indicated with a yellow highlight in Figure 6-11. The additional constraint required by the beta rotation with translation is shown in Figure 6-12. The point cloud distribution for the constant orientation workspace and the beta rotation with translation was concentrated at the center since it is easier to satisfy the constraints of the workspace at the center than at the boundaries.

The maximal workspace, excluding parasitic motion, produced a volume of 2 120 000 mm³ and the inclusive orientation workspace 804 710 mm³. The maximal workspace volume was the largest, which was coherent with its definition. Figure 6-13 shows the maximal workspace as a merge of constant orientation, alpha rotation with

translation and beta rotation with translation workspace. The point distribution for the maximal workspace was more densely populated at the center of the workspace but not as densely as the constant orientation and beta rotation with translation. This was due to 4000 points from the constant orientation, alpha rotation with translation and beta rotation with translation conditions being used to generate the cloud. A third of the points are concentrated along the plane of the alpha rotation with translation. The maximal workspace also has an overestimation of the workspace as indicated with a yellow highlight in Figure 6-13.

The inclusive orientation workspace produced the smallest volume as expected since it was constrained to generate valid end effector positions for angles of rotation ranging from 8° up to and including 10° for alpha and beta. The inclusive orientation workspace produced a similar point cloud distribution to the maximal workspace. Different ranges of angles can be used, but the range of angles was randomly selected for proof-of-concept. The PKM loses the translational DOF along the x-axis when performing alpha rotation with translation. The workspace was confined to a plane with an area of 18112 mm^2 . A boundary wrapping function wrapped the plane of points.

All PKM workspaces were asymmetric. It was only symmetric about the x-axis. The distribution of the points was highly concentrated in the central regions of the workspace. This was congruent with what was predicted. The random distribution of the point cloud was indicated by histograms. Various authors have successfully used the Monte Carlo method for PKM workspace generation. These PKMs ranged from 3-DOFs up to and including 6-DOFs. The shapes of the workspaces generated were similar in shape to those found in literature with a resemblance to some boundary curves that are not intuitive [90, 138, 139, 160].

9.5 Physical Testing and Performance

9.5.1 Inverse Kinematics

The accuracy and repeatability of each linear actuator were tested to evaluate the design of the actuators and identify sources of error when the PKM was tested for accuracy and repeatability. The accuracy and repeatability of actuators were both calculated to be approximately 0.2 mm. The graph of standard deviation vs actuation length, shown in Figure 8-6, indicated that there was no relationship between the accuracy and repeatability with respect to actuation distance. Since the accuracy and repeatability were approximately 0.2 mm, this proved that the actuators were suitable for further testing since the target accuracy and repeatability of the entire PKM was 2 mm. Section 8.4. presents the details of this test. The test employed a Vernier calliper which was low-cost but resulted in manual measurements and data logging. The time taken for data acquisition and data analyses could be reduced by data acquisition hardware and software but such equipment is high in cost.

Simulations were conducted to verify the inverse kinematic equations and the MATLAB® script files performing the inverse kinematic calculations. The inverse kinematic simulations were verified with SolidWorks®. The results showed errors in the sub-millimeter range with the largest error of 0.01 mm observed for the actuation length of the actuators. This can be attributed to rounding off errors. This test proved that the novel extension to the geometric method was successful and the inverse kinematic equations were correct and accurate. Section 8.5. presents the details of this test. Xu et al. [102] and Zhang and Jing [155] used SolidWorks® to develop novel architectures with the former and latter using it in conjunction with MATLAB® and ADAMS® respectively. Since novel PKMs were investigated in both cases which produced satisfactory results, this validated the approach used to verify the inverse kinematic equations. The manual data transferring from SolidWorks® to MATLAB®

was time consuming. The advantage of this method allowed the PKM's kinematic equations to be validated before physical testing.

Research showed that laser displacement sensors in combination with their data acquisition units cost more than R25 000.00 [161]. This research presented the use of an OCM to be used as a low-cost displacement sensor which costs R100.00. From the tests conducted, presented in Appendix A.7, the resolution obtained was 0.2 mm per pixel for the x and y direction movements using a mouse speed 4. This proved that the OCM was capable of sub-millimeter resolution and was suitable to be employed for accuracy and repeatability testing. The tolerance of the mouse was found to be approximately 1.06 mm for 3 standard deviations. This test was documented in Appendix A.7.

The PKM was tested for accuracy and repeatability. For the translation of the end effector, a relationship between y displacement and accuracy was observed. There was no relationship observed between the y displacement and repeatability as these results were erratic. The change in the accuracy along the y-axis shows that the robotic platform exhibits anisotropic mechanical strength. The accuracy for translation in the different regions did not exceed 2 mm and ranged from 1.17 mm to 1.91 mm. The repeatability ranged from 1.56 mm to 2.71 mm. Most of the repeatability values obtained for translation were over 2 mm but still close to 2 mm.

Repeatability calculations included a standard deviation calculation which resulted in the repeatability values being sensitive to variance in pixel measurements. The pixel data obtained from the measurements contained a few outliers which produced relatively high repeatability values which were larger than values obtained for accuracy. Laser displacement sensors and data acquisition hardware and software could aid in more accurate measurements.

For the rotational and translational movement of the end effector, accuracy and repeatability were measured against y displacement and angle of rotation. The angular accuracy showed a relationship to the y displacements in which PKM loses accuracy as it moves further along the y-axis. This was observed irrespective of direction along the y-axis. The repeatability of the angular movements showed a dependency on the angle of rotation such that the larger the angle of rotation, the poorer the repeatability. For alpha rotation with translation, the accuracy ranged from 0.26° to 1.74° and the repeatability ranged from 0.23° to 1.9° . For the beta rotation with translation, the accuracy ranged from 0.21° to 1.76° , and the repeatability ranged from 0.28° to 1.33° . When the mirror was mounted onto the end effector, an unexpected tilt bias of -4° was observed and is shown in Figure 8-11. This was due to the relatively large tolerances used for additive manufactured components and the flexible couplings behaving as springs under the weight of the PKM. Manual data logging was cost-effective but the time incurred due to manual data logging could be shortened with laser displacement sensors and data acquisition hardware and software.

The results from the accuracy and repeatability tests proved that the accuracy and repeatability were acceptable and validated the design and experimental setup. Errors could have resulted from human error through measurement with the Vernier calliper. Other sources of error could have resulted in the calibration procedure which was also conducted with a Vernier calliper. The additive manufactured joints were lightly filed for smoother motion, the thrust bearing revolute joints were able to tilt slightly due to AM tolerances and the weight of the machine. The linear actuator also possessed small error which could have added to the errors observed. The tests

were performed using the inverse kinematic MATLAB script files®. Section 8.6. presents the details of this test. Various authors have used specialised measurement equipment such as laser tracking sensors to investigate accuracy and repeatability of PKMs. The results were in the sub-millimeter range [156, 162, 163]. The accuracy and repeatability found in this research was not as high as those found in literature and this was due to specialised measurement equipment not being accessible.

The PKM payload characteristics were tested to investigate the relationship between payload and actuator stroke accuracy and PKM payload capacity. The PKM lifted a maximum mass of 25.23 kg (247.51 N) before the mouse sensor housing bracket and end effector failed. The largest actuator stroke length errors ranged from 0.18 mm to 0.29 mm. These errors occurred at various weights. No relationship was observed between payload and stroke length accuracy. The failure occurred due to the failure of the additive manufactured components. This is congruent with the calculations documented in Appendix C. The power screw calculations showed each actuator could lift a load of 260.1 N. The buckling calculations revealed that the threaded rod would buckle under a load of 16.8 kN. The additive manufactured components possessed the least mechanical strength. The test was performed using the inverse kinematic MATLAB script files®. Section 8.7. presents the details of this test.

Manually loading and unloading weights was cost-effective with a short set up time but was time-consuming could cause harm if not carried out appropriately. The point of failure of components caused the weights to fall which could be dangerous if not carried out cautiously. The employment of a load cell with data acquisition hardware and software would increase efficiency and safety.

9.5.2 Forward Kinematics

The forward kinematic equations were validated through simulations on MATLAB® and SolidWorks. The largest errors observed for translation was in the range of hundredths of a millimeter. Errors concerned with rotation and translation of the end effector were in the range of a tenth of a millimeter. The errors observed are acceptable since a numerical method was employed and most errors were attributed to rounding off errors. The results displayed are Appendix A.5 The NR method was successfully employed and validated the forward kinematic equations. When guesses converged to incorrect values it indicated a convergence to an unfeasible machine pose. The divergence of the solution occurred when the guesses deviated too far from the actual value or many zeroes were made as guesses. The NR method was robust and converged within a maximum of 8 iterations. Section 8.8. presents the details of this test.

The forward kinematic equations were also tested to determine the sensitivity of each variable with respect to guess deviations and convergence. A graphical representation of the number of iterations vs. guess deviations is shown from Figure 8-23 to Figure 8-28. For the guesses of end effector position, convergence occurred for deviations up to and including 250 mm. Angular guesses resulted in convergence for guesses that deviated of up to 100°.

For alpha rotation with translation, the theta 1 and theta 5 values were the most sensitive since the least number of convergence cases occurred for these variables. For beta rotation with translation, the theta 1 and 3 variables were the most sensitive variables. The NR method is not symmetric such that guesses made greater than or less than the actual value doesn't exhibit the same number of iterations. Most solutions took 4 to 6 iterations to

converge with high accuracy. This proved that the NR method was a suitable solution for the forward kinematic analysis and was robust. Section 8.9. presents the details of this test.

The NR method was used by various researchers to solve the forward kinematics [124-127]. The results of the literature showed that a maximum of 3 iterations was recorded for convergence. Accuracy of the NR and hybrid NR methods were in the sub-millimeter range with errors ranging from 9×10^{-15} m to 0.01 mm. The highest angular error was 0.01° . For this research, 5 iterations were generally required to observe convergence. The number of iterations can be decreased through hybrid strategies. When 5 iterations were observed, the positional errors were generally 0.01 mm due to rounding off errors. These results are comparable to results from literature. The angular errors observed were in the range of tenths of a millimeter. The angular errors observed were larger than those found in literature. Alteration of the termination criterion can improve angular accuracy. Transferring data points from SolidWorks® to MATLAB® was time consuming. This method, however, allowed the forward kinematic equations to be tested without the influence of other variables incurred through physical testing and experimentation.

9.6 Implications of the Research

The design and investigation of a novel 5-DOF PKM was proposed to validate part handing, sorting, general positioning and robotic machining capabilities. The PKM was synthesised according to the method presented by Pandilov and Dukovski, and Weck [40, 94]. The method was useful and can be used to synthesise novel PKMs. The PKM explicitly follows the synthesis methodology and serves as an example for authors aiming to develop novel PKMs.

The study showed that the development of a new joint and using offsets in the architectural layout could permit higher ranges of rotation while converting an independent DOF to a dependent (parasitic) DOF. The research validates that the category of 5-DOF PKMs still has the potential for further research. Machine architecture can also be exploited to formulate new methods of analysis, as observed with the extension of the geometric method. Researchers can use the extension of the geometric method. The exploitation of machine architecture serves as an example of the exploitation that could be adopted for PKMs that are similar to realise higher ranges of tilt.

The accuracy and repeatability results, shown in Section 8.6, revealed that the upper limits of the ranges for all cases were close to 2 mm and 2° . This suggests that for prototyping of the architecture design, validating kinematic equations and basic movements, AM is viable but will need to be constructed with stronger material and high precision mechanical components such as bearings. This will result in higher accuracy and repeatability and will position the research to accomplish industry applications.

An OCM can be used as a low-cost position sensor. This is useful for research and development that require point-to-point measurements in the millimeter and sub-millimeter range. The OCM presents a cost-saving for low-budget research or when access to displacement measuring equipment is not possible.

Concerning potential applications, the PKM is not aimed to replace CNC machines completely but can instead be used to accomplish some tasks of a CNC machine or perform pre- or post-machining of a part. The PKM can be used for general positioning applications in assembly lines, the medical environment, the energy sector for solar

panels and the entertainment sector for movable seats. Sorting and pick and place applications that do not require high-speed movements can use the PKM to perform these tasks should the machine workspace be sufficient.

Disadvantages of the employment of the PKM being adopted in industry could include factories investing in new equipment, staff and training for operating new machinery and maintenance costs. The implementation of PKM technology would also require restructuring in manufacturing lines and the shop floors. The restructuring could lead to downtime and reduce the efficiency of the production line during this period.

9.7 Chapter Summary

This chapter presented the research question, findings, observations, performance and insights of the research. The concept overview, justification and literature were discussed. A discussion of the synthesis, design, singularities and workspace was presented. Findings and observations from simulations and testing were discussed in terms of the forward and inverse kinematics. The chapter concluded with the implications of the PKM. The concept of the adoption of PKMs in industry is viable and this research sufficiently addressed the research question it set out to solve. The following chapter concludes the research with discussions addressing the fulfilment of the aim and objectives, research contribution, insights of the novel PKM and limitations of the research. Future work and recommendations are suggested.

10. CONCLUSION

10.1 Introduction

This chapter concludes the findings and insights of the research measured against the aims and objectives. The contribution of the research is documented together with insights, limitations and future work. The aim and objectives of the research were presented in Section 1.3. The aim was met whereby the PKM was validated for its kinematic equations and physical movements. The discussion, Section 9, validates that all objectives were met. The fourth objective concerning workspace and singularities was most challenging when identifying singularities.

10.2 Research Contribution

The research set out to achieve 4 research contributions, as seen in Section 1.5. This research proposed a novel 5-DOF PKM with a higher range of rotation than most 5-DOF and 6-DOF PKMs. This was accomplished through literature validating the research gap and serving as a basis to innovate on existing PKMs and produce a novel architectural design inclusive of a new joint.

A novel inverse kinematic analysis was developed, which is an extension of the existing geometric (vector) method. The novel inverse kinematic analysis exploited the unique architectural layout and was used to develop the forward kinematic equations and was extended to accomplish the workspace analyses. The results discussed in Section 9 validate the accuracy of the novel inverse kinematic model.

A computer mouse was used as a low-cost displacement sensor in conjunction with MATLAB®. The computer mouse possessed a resolution of 0.2 mm/pixel and tolerance of 1.06 mm. The tolerance of the mouse was 1.06 mm due to the pixel deviations observed when testing was performed. The mouse was successfully implemented.

The insights on the kinematics, workspace and isotropic characteristics are described in Section 10.3.

10.3 Insights of the Novel PKM

The PKM possessed 5 DOFs and a parasitic rotation. The trade-off concerning the parasitic motion was realised through higher ranges of tilt than most 5-DOF and 6-DOF PKMs found in literature. The parasitic rotation was induced when alpha and beta rotations occurred simultaneously.

The PKM displayed anisotropic motion characteristics. The accuracy and repeatability were dependent on machine pose. This suggested that the PKM possessed anisotropic mechanical strength in different directions.

The mechanical weight of the PKM was not considered as it is beyond the scope of kinematic analyses. However, mechanical weight must be compensated for because the machine leans toward forward toward actuators 5 and 6. This needs to be accounted for when performing the dynamic study.

Actuators 1 to 4 can move completely spatially which increases the moving mass but could also add stability to the PKM under different poses. The thrust bearing revolute joint needs to be designed with high mechanical strength as it can induce a cantilever effect if not designed appropriately.

The PKM produces anisotropic workspaces that are symmetric about the x-axis. The shape of the workspace changes significantly in shape and size vertically as shown in Section 6.3.7. A point cloud was implemented since the curves of the workspace cannot be interpreted intuitively for all types of end effector movements.

The initial Jacobian matrix was sensitive to the equations developed directly of the inverse kinematic equations because of the outer loop being common to both inner loops for a leg pair. The similarity between equations produced a badly scaled Jacobian therefore new equations were developed.

The machine possesses a broad scope for modularity and reconfigurability to be explored.

10.4 Limitations of the Research

High-resolution displacement measuring equipment and calibration equipment were not available during this study. The budget of the research did not allow the purchase of this equipment. This impacted the accuracy and repeatability of results and required the design of a testing frame. This also resulted in the investigation of using an OCM as a low-cost displacement sensor and its calibration.

Some academic websites containing relevant research papers were not accessible during the research. This was due to the university not obtaining a subscription to the academic websites. This inhibited the progress of the literature review and PKM synthesis.

Limited mechanical testing was performed on the PKM. The PKM was produced through AM and could not undergo mechanical tests. This could be overcome in this research as this served as a desktop prototype for proof-of-concept. This limited the range of tests that were performed on the physical platform.

10.5 Recommendations

The selection and implementation of the sequence of rotations of the end effector should be made more explicit in literature. The method to obtain values for each angle could be described for compound rotations of the end effector. This will assist researchers in expanding simulations and physical testing on prototypes. Current methods involve the use of 3D CAD modelling software to calculate the individual angles of rotation and but requires the 3D CAD models to be configured appropriately.

Many opportunities exist for the design and investigation of architectures for 5-DOF PKMs. Different machine configurations can be explored. The variety in the novelty observed from literature in Section 2.3.4 suggests that there is more scope for novelty. Many 5-DOF PKMs are still in the research phase and these serve as avenues for extension of existing research with further technical analyses or commercialisation of these platforms.

10.6 Future Work

The inverse kinematic analysis could be investigated using screw theory which can aid in the generation of a simpler Jacobian. The inverse kinematic analysis could also investigate the parasitic rotation. The forward kinematic analysis could be explored with other numerical techniques such as the method least squares regression and particle swarming.

Dynamic characteristics due to the directional dependence of mechanical strength can be investigated. The mechanical strength is anisotropic. Machine stiffness can also be an avenue for research linked to the anisotropic machine properties. Joint mounting patterns on the base and other joint arrangements can be investigated to aid isotropic properties and reduce machine self-clashing. Workspace optimisation can be researched in relation to modularity and reconfigurability and produce specific workspace volumes for dedicated tasks.

Calibration techniques can be explored using calibration equipment and generating a calibration procedure for robotic platforms. This can lead to a study of the effects of calibration on accuracy and repeatability. Future work can pursue producing a minimum viable, marketable PKM. This research could be expanded on or an entirely new PKM can be investigated

10.7 Chapter Summary

This chapter briefly discussed the fulfilment of the aim and objectives. The research contributions were described and insights of the reach were presented. Limitations of the research were noted and recommendations were suggested. The chapter concluded with scope for suggested areas for future work. The post-conclusion sections of the dissertation present the references and appendices. The appendices document the system performance and testing results, software code, calculations and the QFD. The appendices also include the project costs, linear actuator concepts, poses illustrating the different DOFs and engineering drawings.

REFERENCES

- [1] BRICS. "What is BRICS?" <http://brics2019.itamaraty.gov.br/en/about-brics/what-is-brics> (accessed Feb. 2, 2019).
- [2] BRICS. "Joint Statistical Publication." Statistics South Africa. <https://www.statssa.gov.za/wp-content/uploads/2018/11/BRICS-JSP-2018.pdf> (accessed Feb. 2, 2019).
- [3] OrbisResearch. "Global Manufacturing Analytics Market 2018 by Manufacturers, Countries, Type and Application, Forecast to 2023." <https://www.orbisresearch.com/reports/index/global-manufacturing-analytics-market-2018-by-manufacturers-countries-type-and-application-forecast-to-2023> (accessed Sept. 20, 2018).
- [4] OrbisResearch. "2012-2022 Report on Global Robotics (Industrial Robot And Service Robots) Market Competition, Status and Forecast, Market Size by Players, Regions, Type, Application." <https://www.orbisresearch.com/reports/index/2012-2022-report-on-global-robotics-industrial-robot-and-service-robots-market-competition-status-and-forecast-market-size-by-players-regions-type-application> (accessed May 22, 2018).
- [5] OrbisResearch. "2013-2028 Report on Global CNC Machine (CNC Machine Tools) Market by Player, Region, Type, Application and Sales Channel." <https://www.orbisresearch.com/reports/index/2013-2028-report-on-global-cnc-machine-cnc-machine-tools-market-by-player-region-type-application-and-sales-channel> (accessed July 30, 2019).
- [6] Statssa. "Manufacturing: winner and losers of 2018." <http://www.statssa.gov.za/?p=11890> (accessed Mar. 5, 2019).
- [7] Statssa. "Stats Biz - May 2019." <http://www.statssa.gov.za/?p=12208> (accessed June 6, 2019).
- [8] Z. Pandilov and V. Dukovski, "Comparison of the characteristics between serial and parallel robots," *Acta Technica Corviniensis-Bulletin of Engineering*, vol. 7, no. 1, pp. 143-160, Jan. 2014.
- [9] L.-W. Tsai, *Robot analysis: the mechanics of serial and parallel manipulators*, 1st ed. New York: John Wiley & Sons, 1999.
- [10] J.-P. Merlet, *Parallel Robots*, 2nd ed. Dordrecht: Springer Science & Business Media, 2006.
- [11] J. D. Barnfather, M. J. Goodfellow, and T. Abram, "Positional capability of a hexapod robot for machining applications," *The International Journal of Advanced Manufacturing Technology*, vol. 89, no. 1, pp. 1103-1111, Mar. 2017, doi: 10.1007/s00170-016-9051-0.
- [12] A. Changela and K. Hirpara, "Geometric Approach For Inverse Kinematics Solution: 3-PSU Parallel Kinematic Manipulator," *International Journal of Engineering Research & Technology (IJERT)*, vol. 2, no. 4, pp. 324-327, Apr. 2013.
- [13] J. Wang, H. Zhang, and T. Fuhlbrigge, "Improving machining accuracy with robot deformation compensation," in *2009 IEEE/RSJ International Conference on Intelligent Robots and Systems*, St. Louis, USA, 2009, pp. 3826-3831, doi: 10.1109/IROS.2009.5353988.
- [14] U. Schneider, M. Drust, J. Diaz Posada, and A. Verl, "Position control of an industrial robot using an optical measurement system for machining purposes," in *Proceedings of the 11th International Conference on Manufacturing Research (ICMR2013)*, Cranfield University, UK, 2013, pp. 307-312.

- [15] Y. Chen and F. Dong, "Robot machining: recent development and future research issues," *The International Journal of Advanced Manufacturing Technology*, vol. 66, no. 9, pp. 1489-1497, June 2013, doi: 10.1007/s00170-012-4433-4.
- [16] T. Daun, "Iterative Learning Control for Milling with Industrial Robots in Advanced Manufacturing," MSc. dissertation, Dept. Autom. Control, Lund Univ., Lund, Scania, 2014.
- [17] A. Karim and A. Verl, "Challenges and obstacles in robot-machining," in *IEEE International Symposium on Robotics (ISR) 2013*, Seoul, 2013, pp. 1-4, doi: 10.1109/ISR.2013.6695731.
- [18] J. Brüning, B. Denkena, M. A. Dittrich, and H. S. Park, "Simulation Based Planning of Machining Processes with Industrial Robots," *Procedia Manufacturing*, vol. 6, pp. 17-24, 2016, doi: 10.1016/j.promfg.2016.11.003.
- [19] A. Olarra, J. M. Allen, and D. A. Axinte, "Experimental evaluation of a special purpose miniature machine tool with parallel kinematics architecture: Free leg hexapod," *Precision Engineering*, vol. 38, no. 3, pp. 589-604, July 2014, doi: 10.1016/j.precisioneng.2014.02.009.
- [20] S. M. Sackey and A. Bester, "Industrial Engineering Curriculum in Industry 4.0 in a South African Context," *South African Journal of Industrial Engineering*, vol. 27, no. 4, pp. 101-114, Dec. 2016, doi: 10.7166/27-4-1579.
- [21] M. Hermann, T. Pentek, and B. Otto, "Design Principles for Industrie 4.0 Scenarios," in *2016 49th Hawaii International Conference on System Sciences (HICSS)*, Koloa, HI, 2016, pp. 3928-3937, doi: 10.1109/HICSS.2016.488.
- [22] R. Drath and A. Horch, "Industrie 4.0: Hit or Hype? [Industry Forum]," *IEEE Industrial Electronics Magazine*, vol. 8, no. 2, pp. 56-58, June 2014, doi: 10.1109/MIE.2014.2312079.
- [23] X. Yao and Y. Lin, "Emerging manufacturing paradigm shifts for the incoming industrial revolution," *The International Journal of Advanced Manufacturing Technology*, vol. 85, no. 5-8, pp. 1665-1676, Nov. 2015, doi: 10.1007/s00170-015-8076-0.
- [24] J. Lee, B. Bagheri, and H.-A. Kao, "A Cyber-Physical Systems architecture for Industry 4.0-based manufacturing systems," *Manufacturing Letters*, vol. 3, pp. 18-23, Jan. 2015, doi: 10.1016/j.mfglet.2014.12.001.
- [25] N. J. Raj, K. Iyer, and A. K. Dash, "Design, fabrication, kinematic analysis and control of a 3-DOF serial manipulator," in *2016 International Conference on Next Generation Intelligent Systems (ICNGIS)*, Kottayam, 2016, pp. 1-6, doi: 10.1109/ICNGIS.2016.7854020.
- [26] FANUC Corporation. "FANUC Robot iSeries." http://www.fanucsa.co.za/Data/R-2000_2.pdf (accessed May 22, 2017).
- [27] U. Schneider, J. R. D. Posada, M. Drust, A. Verl, and J. v. d. Zwaag, "Combining holistic programming with kinematic parameter optimisation for robot machining," in *ISR/Robotik 2014; 41st International Symposium on Robotics*, Munich, Germany, 2014, pp. 1-7.
- [28] F. Domroes, M. Rieger, and B. Kuhlenkoetter, "Towards Autonomous Robot Machining," in *ISR/Robotik 2014; 41st International Symposium on Robotics*, Munich, Germany, 2014, pp. 1-6.
- [29] T. Kubela, A. Pochyly, and V. Singule, "Assessment of industrial robots accuracy in relation to accuracy improvement in machining processes," in *2016 IEEE International Power Electronics and Motion Control Conference (PEPMC)*, Varna, 2016, pp. 720-725, doi: 10.1109/EPEPMC.2016.7752083.

- [30] A. Klimchik, A. Ambiehl, S. Garnier, B. Furet, and A. Pashkevich, "Efficiency evaluation of robots in machining applications using industrial performance measure," *Robotics and Computer-Integrated Manufacturing*, vol. 48, pp. 12-29, Dec. 2017, doi: 10.1016/j.rcim.2016.12.005.
- [31] C. Dumas, S. Caro, S. Garnier, and B. Furet, "Joint stiffness identification of six-revolute industrial serial robots," *Robotics and Computer-Integrated Manufacturing*, vol. 27, no. 4, pp. 881-888, Aug. 2011, doi: 10.1016/j.rcim.2011.02.003.
- [32] S. H. H. Zargarbashi, W. Khan, and J. Angeles, "Posture optimization in robot-assisted machining operations," *Mechanism and Machine Theory*, vol. 51, pp. 74-86, May 2012, doi: 10.1016/j.mechmachtheory.2011.11.017.
- [33] Y. Lin, H. Zhao, and H. Ding, "Posture optimization methodology of 6R industrial robots for machining using performance evaluation indexes," *Robotics and Computer-Integrated Manufacturing*, vol. 48, pp. 59-72, Dec. 2017, doi: 10.1016/j.rcim.2017.02.002.
- [34] E. Uhlmann, S. Reinkober, and T. Hollerbach, "Energy Efficient Usage of Industrial Robots for Machining Processes," *Procedia CIRP*, vol. 48, pp. 206-211, 2016, doi: 10.1016/j.procir.2016.03.241.
- [35] X. Wang, L. Baron, and G. Cloutier, "Topology of serial and parallel manipulators and topological diagrams," *Mechanism and Machine Theory*, vol. 43, no. 6, pp. 754-770, June 2008, doi: 10.1016/j.mechmachtheory.2007.05.005.
- [36] N. Plitea, D. Lese, D. Pisla, and C. Vaida, "Structural design and kinematics of a new parallel reconfigurable robot," *Robotics and Computer-Integrated Manufacturing*, vol. 29, no. 1, pp. 219-235, Feb. 2013, doi: 10.1016/j.rcim.2012.06.001.
- [37] A. A. Shaik, "Sensor system for flex-picker and Multi-axis automated machines," MSc. dissertation, Dept. of Mech. Eng., Univ. of KwaZulu-Natal, KZN, Durban, 2006.
- [38] T. Brogårdh, "Design of high performance parallel arm robots for industrial applications," in *Proceedings of a Symposium Commemorating the Legacy, Works, and Life of Sir Robert Ball Upon the 100th Anniversary of A Treatise on the Theory of Screws*, University of Cambridge, Trinity College, 2000, pp. 9-11.
- [39] M. Glavonjic, D. Milutinovic, S. Zivanovic, Z. Dimic, and V. Kvrjic, "Desktop 3-axis parallel kinematic milling machine," *The International Journal of Advanced Manufacturing Technology*, vol. 46, no. 1, pp. 51-60, Jan. 2010, doi: 10.1007/s00170-009-2070-3.
- [40] Z. Pandilov and K. Rall, "Parallel kinematics machine tools: History, present, future," *Mechanical Engineering - Scientific Journal*, vol. 25, no. 1, pp. 3-20, 2006.
- [41] Robolution. "FANUC F-200iB robot." <http://robolution.eu/robot/f-200ib> (accessed June 5, 2017).
- [42] J. Borràs and F. Thomas, "Singularity-invariant leg substitutions in pentapods," in *2010 IEEE/RSJ International Conference on Intelligent Robots and Systems*, Taipei, 2010, pp. 2766-2771, doi: 10.1109/IROS.2010.5652202.
- [43] A. Campos, C. Budde, and J. Hesselbach, "A type synthesis method for hybrid robot structures," *Mechanism and Machine Theory*, vol. 43, no. 8, pp. 984-995, Aug. 2008, doi: 10.1016/j.mechmachtheory.2007.07.006.
- [44] V. Poppeova, J. Uricek, V. Bulej, and P. Šindler, "Development of Simulation Software and Control System for Mechanism with Hybrid Kinematic Structure," in *ISR 2010 (41st International Symposium*

- on Robotics) and ROBOTIK 2010 (6th German Conference on Robotics), Munich, Germany, 2010, pp. 1-6.
- [45] Y. Y. Wang, T. Huang, X. M. Zhao, J. P. Mei, D. G. Chetwynd, and S. J. Hu, "Finite Element Analysis and Comparison of Two Hybrid Robots-the Tricept and the TriVariant," in *2006 IEEE/RSJ International Conference on Intelligent Robots and Systems*, Beijing, 2006, pp. 490-495, doi: 10.1109/IROS.2006.282522.
- [46] K. H. Harib, K. A. Moustafa, A. S. Ullah, and S. Zenieh, "Parallel, serial and hybrid machine tools and robotics structures: comparative study on optimum kinematic designs," in *Serial and Parallel Robot Manipulators-Kinematics, Dynamics, Control and Optimization*, S. Küçük Ed. Rijeka, Croatia: InTech, 2012, ch. 6, pp. 109-124.
- [47] Z. M. Bi, "Kinetostatic modeling of Exechon parallel kinematic machine for stiffness analysis," *The International Journal of Advanced Manufacturing Technology*, vol. 71, no. 1, pp. 325-335, Mar. 2014, doi: 10.1007/s00170-013-5482-z.
- [48] Z. M. Bi and Y. Jin, "Kinematic modeling of Exechon parallel kinematic machine," *Robotics and Computer-Integrated Manufacturing*, vol. 27, no. 1, pp. 186-193, Feb. 2011, doi: 10.1016/j.rcim.2010.07.006.
- [49] D. Kanaan, P. Wenger, and D. Chablat, "Kinematic analysis of a serial-parallel machine tool: The VERNE machine," *Mechanism and Machine Theory*, vol. 44, no. 2, pp. 487-498, Feb. 2009, doi: 10.1016/j.mechmachtheory.2008.03.002.
- [50] X. Duan, Y. Yang, and B. Cheng, "Modeling and Analysis of a 2-DOF Spherical Parallel Manipulator," *Sensors*, vol. 16, no. 9, 1485, Sept. 2016, doi: 10.3390/s16091485.
- [51] J. Qu, W. Chen, J. Zhang, and W. Chen, "A piezo-driven 2-DOF compliant micropositioning stage with remote center of motion," *Sensors and Actuators A: Physical*, vol. 239, pp. 114-126, Mar. 2016, doi: 10.1016/j.sna.2016.01.025.
- [52] E. R. J. Bozorgi, I. Yahyapour, A. Karimi, M. T. Masouleh, and M. Yazdani, "Design, development, dynamic analysis and control of a 2-DOF spherical parallel mechanism," in *2014 Second RSI/ISM International Conference on Robotics and Mechatronics (ICRoM)*, Tehran, 2014, pp. 445-450, doi: 10.1109/ICRoM.2014.6990942.
- [53] X. Kong, "Reconfiguration Analysis of a 2-DOF 3-4R Parallel Manipulator with Orthogonal Base and Platform," in *Advances in Reconfigurable Mechanisms and Robots II*, X. Ding, X. Kong, and J. S. Dai Eds. Cham: Springer International Publishing, 2016, pp. 235-245.
- [54] X. Yang *et al.*, "Modified Robust Dynamic Control for a Diamond Parallel Robot," *IEEE/ASME Transactions on Mechatronics*, vol. 24, no. 3, pp. 959-968, June 2019, doi: 10.1109/TMECH.2019.2914165.
- [55] G. Niu, B. Pan, F. Zhang, H. Feng, and Y. Fu, "Kinematic analysis of a novel uncoupled and isotropic 2-degree-of-freedom parallel mechanism," *Advances in Mechanical Engineering*, vol. 8, no. 3, pp. 1-17, Mar. 2016, doi: 10.1177/16878140166638040.
- [56] Y. Bang, J. K. Paik, B. Shin, and C. Lee, "A three-degree-of-freedom anthropomorphic oculomotor simulator," *International Journal of Control Automation and Systems*, vol. 4, no. 2, pp. 227-235, Apr. 2006.

- [57] K. Al-Widyan, X. Q. Ma, and J. Angeles, "The robust design of parallel spherical robots," *Mechanism and Machine Theory*, vol. 46, no. 3, pp. 335-343, Mar. 2011, doi: 10.1016/j.mechmachtheory.2010.11.002.
- [58] D. Chablat and P. Wenger, "Architecture optimization of a 3-DOF translational parallel mechanism for machining applications, the orthoglide," *IEEE Transactions on Robotics and Automation*, vol. 19, no. 3, pp. 403-410, June 2003, doi: 10.1109/TRA.2003.810242.
- [59] R. Dahmouche, N. Andreff, Y. Mezouar, and P. Martinet, "Efficient high-speed vision-based computed torque control of the orthoglide parallel robot," in *2010 IEEE International Conference on Robotics and Automation*, Anchorage, AK, 2010, pp. 644-649, doi: 10.1109/ROBOT.2010.5509394.
- [60] L. Xin-Jun and K. Jongwon, "A new spatial three-DoF parallel manipulator with high rotational capability," *IEEE/ASME Transactions on Mechatronics*, vol. 10, no. 5, pp. 502-512, Oct. 2005, doi: 10.1109/TMECH.2005.856219.
- [61] L. Carbonari, D. Corinaldi, G. Palmieri, and M. Palpacelli, "Kinematics of a Novel 3-URU Reconfigurable Parallel Robot," in *2018 International Conference on Reconfigurable Mechanisms and Robots (ReMAR)*, Delft, 2018, pp. 1-7, doi: 10.1109/REMAR.2018.8449898.
- [62] L. Nurahmi and D. Gan, "Operation Mode and Workspace of a 3-rRPS Metamorphic Parallel Mechanism with a Reconfigurable Revolute Joint," in *2018 International Conference on Reconfigurable Mechanisms and Robots (ReMAR)*, Delft, 2018, pp. 1-9, doi: 10.1109/REMAR.2018.8449879.
- [63] S. Ahangar, M. V. Mehrabani, A. P. Shorijeh, and M. T. Masouleh, "Design a 3-DOF Delta Parallel Robot by One Degree Redundancy along the Conveyor Axis, A Novel Automation Approach," in *2019 5th Conference on Knowledge Based Engineering and Innovation (KBEI)*, Tehran, 2019, pp. 413-418, doi: 10.1109/KBEI.2019.8734975.
- [64] I. Al-Naimi, A. Taeim, and N. Alajdah, "Fully-Automated Parallel-Kinematic Robot for Multitask Industrial Operations," in *2018 15th International Multi-Conference on Systems, Signals & Devices (SSD)*, Hammamet, 2018, pp. 390-395, doi: 10.1109/SSD.2018.8570552.
- [65] P. Ataei, Z. Anvari, and M. T. Masouleh, "Kinetostatic Performance and Collision-free Workspace Analysis of a 3-DOF Delta Parallel Robot," in *2017 5th RSI International Conference on Robotics and Mechatronics (ICRoM)*, Tehran, 2017, pp. 576-581, doi: 10.1109/ICRoM.2017.8466178.
- [66] X. Han, Z. Ge, K. Zhang, and Z. Wang, "Design and analysis of a single-input three-DOF parallel manipulator," in *2017 IEEE 3rd Information Technology and Mechatronics Engineering Conference (ITOEC)*, Chongqing, 2017, pp. 324-328, doi: 10.1109/ITOEC.2017.8122308.
- [67] B. Mehrafrooz, M. Mohammadi, and M. T. Masouleh, "Kinematic Sensitivity Evaluation of Revolute and Prismatic 3-DOF Delta Robots," in *2017 5th RSI International Conference on Robotics and Mechatronics (ICRoM)*, Tehran, 2017, pp. 225-231, doi: 10.1109/ICRoM.2017.8466159.
- [68] R. Nowell, B. Shirinzadeh, L. Lai, J. Smith, and Z. Yongmin, "Design of a 3-DOF parallel mechanism for the enhancement of endonasal surgery," in *2017 IEEE International Conference on Advanced Intelligent Mechatronics (AIM)*, Munich, 2017, pp. 749-754, doi: 10.1109/AIM.2017.8014107.
- [69] A. Arian, B. Danaei, M. T. Masouleh, and A. Kalhor, "Dynamic Modeling and Base Inertial Parameters Determination of 3- DoF Planar Parallel Manipulator," in *2017 5th RSI International Conference on Robotics and Mechatronics (ICRoM)*, Tehran, 2017, pp. 546-551, doi: 10.1109/ICRoM.2017.8466186.

- [70] F. Pierrot, V. Nabat, O. Company, S. Krut, and P. Poignet, "Optimal Design of a 4-DOF Parallel Manipulator: From Academia to Industry," *IEEE Transactions on Robotics*, vol. 25, no. 2, pp. 213-224, Apr. 2009, doi: 10.1109/TRO.2008.2011412.
- [71] A. Rasoulzadeh and M. T. Masouleh, "Singularity configurations analysis of a 4-DOF parallel mechanisms using Grassmann-Cayley Algebra," in *2016 4th International Conference on Robotics and Mechatronics (ICROM)*, Tehran, 2016, pp. 222-227, doi: 10.1109/ICRoM.2016.7886850.
- [72] L. Kang, W. Kim, and B. J. Yi, "Kinematic modeling, analysis, and load distribution algorithm for a redundantly actuated 4-DOF parallel mechanism," in *2016 IEEE/RSJ International Conference on Intelligent Robots and Systems (IROS)*, Daejeon, 2016, pp. 356-361, doi: 10.1109/IROS.2016.7759079.
- [73] A. Khalifa, M. Fanni, and A. M. Mohamed, "Singularity Analysis of a Novel 4-DOF Surgical Robot," in *2016 3rd International Conference on Information Science and Control Engineering (ICISCE)*, Beijing, 2016, pp. 1126-1130, doi: 10.1109/ICISCE.2016.242.
- [74] M. Mohammadi, B. Mehrafrouz, and M. T. Masouleh, "Weighted kinematic sensitivity of a 4-DOF robot," in *2016 4th International Conference on Robotics and Mechatronics (ICROM)*, Tehran, 2016, pp. 536-541, doi: 10.1109/ICRoM.2016.7886799.
- [75] M. Azmoun, A. Rouhollahi, M. T. Masouleh, and A. Kalhor, "Kinematics and Control of a 4-DOF Delta Parallel Manipulator," in *2018 6th RSI International Conference on Robotics and Mechatronics (ICRoM)*, Tehran, 2018, pp. 494-500, doi: 10.1109/ICRoM.2018.8657618.
- [76] S. Akhbari, A. Z. Jond, and M. Mahboubkhah, "Kinematic and workspace analyses of a novel 4-dof parallel mechanism," in *2018 6th RSI International Conference on Robotics and Mechatronics (ICRoM)*, Tehran, 2018, pp. 280-285, doi: 10.1109/ICRoM.2018.8657564.
- [77] T. C. Apostolescu, G. Ionaşcu, D. Duminiţă, L. A. Cartal, and L. Bogatu, "Design and Programming of a New 4-DOF Parallel Robot," in *9th International Conference on Electronics, Computers and Artificial Intelligence (ECAI)*, Targoviste, 2017, pp. 1-6, doi: 10.1109/ECAI.2017.8166404.
- [78] A. Rouhollahi, M. Azmoun, and M. T. Masouleh, "Experimental study on the visual servoing of a 4-DOF parallel robot for pick-and-place purpose," in *2018 6th Iranian Joint Congress on Fuzzy and Intelligent Systems (CFIS)*, Kerman, 2018, pp. 27-30, doi: 10.1109/CFIS.2018.8336617.
- [79] Y. Fang and L.-W. Tsai, "Structure Synthesis of a Class of 4-DoF and 5-DoF Parallel Manipulators with Identical Limb Structures," *The International Journal of Robotics Research*, vol. 21, no. 9, pp. 799-810, Sept. 2002, doi: 10.1177/0278364902021009314.
- [80] F. Hairong, F. Yuefa, and H. Bin, "Preparation Structure Synthesis of 5-DOF Symmetrical Parallel Manipulator," in *2006 International Conference on Mechatronics and Automation*, Luoyang, Henan, 2006, pp. 2336-2340, doi: 10.1109/ICMA.2006.257696.
- [81] L. Qinchuan, H. Zhen, and J. M. Herve, "Type synthesis of 3R2T 5-DOF parallel mechanisms using the Lie group of displacements," *IEEE Transactions on Robotics and Automation*, vol. 20, no. 2, pp. 173-180, Apr. 2004, doi: 10.1109/TRA.2004.824650.
- [82] E. Fiore, H. Giberti, and L. Sbaglia, "Dimensional synthesis of a 5-DOF parallel kinematic manipulator for a 3d printer," in *2015 16th International Conference on Research and Education in Mechatronics (REM)*, Bochum, 2015, pp. 41-48, doi: 10.1109/REM.2015.7380372.

- [83] J. Guo, G. Li, B. Li, and S. Wang, "A ship active vibration isolation system based on a novel 5-DOF parallel mechanism," in *2014 IEEE International Conference on Information and Automation (ICIA)*, Hailar, 2014, pp. 800-805, doi: 10.1109/ICInfA.2014.6932761.
- [84] K.-J. Zheng, J.-S. Gao, and Y.-S. Zhao, "Path control algorithms of a novel 5-DOF parallel machine tool," in *IEEE International Conference Mechatronics and Automation, 2005*, Niagara Falls, Ont., 2005, vol. 3, pp. 1381-1385 Vol. 3, doi: 10.1109/ICMA.2005.1626755.
- [85] L. Cheng, Y. Zhao, and Y. Zhao, "Motion control algorithm of a 5-DOF parallel machine tool," in *2007 IEEE International Conference on Robotics and Biomimetics (ROBIO)*, Sanya, 2007, pp. 2194-2199, doi: 10.1109/ROBIO.2007.4522510.
- [86] O. Ersoy, M. C. Yildirim, A. Ahmad, O. D. Yirmibesoglu, N. Koroglu, and O. Bebek, "Design and Kinematics of a 5-DOF Parallel Robot for Beating Heart Surgery," in *2019 IEEE 4th International Conference on Advanced Robotics and Mechatronics (ICARM)*, Toyonaka, Japan, 2019, pp. 274-279, doi: 10.1109/ICARM.2019.8833632.
- [87] Y. Song, B. Lian, T. Sun, G. Dong, Y. qi, and H. Gao, "A Novel Five-Degree-of-Freedom Parallel Manipulator and Its Kinematic Optimization," *Journal of Mechanisms and Robotics*, vol. 6, no. 4, p. 041008 (9 pages), Nov. 2014, doi: 10.1115/1.4027742.
- [88] T. Sun, B. Lian, Y. Song, and L. Feng, "Elastodynamic Optimization of a 5-DoF Parallel Kinematic Machine Considering Parameter Uncertainty," *IEEE/ASME Transactions on Mechatronics*, vol. 24, no. 1, pp. 315-325, Feb. 2019, doi: 10.1109/TMECH.2019.2891355.
- [89] Y. Qiu, Z. Wei, W. Li, and L. Sun, "Simulation and Study on 5-DOF Parallel Mechanism," in *2010 International Conference on Multimedia Technology*, Ningbo, 2010, pp. 1-3, doi: 10.1109/ICMULT.2010.5631251.
- [90] Y. Xiaolong, L. Bin, and Z. Xinhua, "Kinematic Analysis of a Redundant Actuated Five Degrees of Freedom Parallel Mechanism," in *2018 IEEE International Conference on Robotics and Biomimetics (ROBIO)*, Kuala Lumpur, Malaysia, 2018, pp. 2031-2037, doi: 10.1109/ROBIO.2018.8665338.
- [91] S. Zhu, Z. Huang, and M. Zhao, "Singularity Analysis for a 5-DoF Fully-Symmetrical Parallel Manipulator 5-RRR(RR)," in *Proceedings 2007 IEEE International Conference on Robotics and Automation*, Roma, 2007, pp. 1189-1194, doi: 10.1109/ROBOT.2007.363146.
- [92] X. Liu, Z. Xie, F. Xie, and J. Wang, "Design and Development of a Portable Machining Robot with Parallel Kinematics*," in *2019 16th International Conference on Ubiquitous Robots (UR)*, Jeju, Korea (South), 2019, pp. 133-136, doi: 10.1109/URAI.2019.8768593.
- [93] J. Huang, X. Wang, D. Zhao, H. Guo, Y. San, and S. Hou, "Kinematic analysis of a novel 5-DOF parallel mechanism," in *2017 IEEE 2nd Advanced Information Technology, Electronic and Automation Control Conference (IAEAC)*, Chongqing, 2017, pp. 941-945, doi: 10.1109/IAEAC.2017.8054152.
- [94] M. Weck and D. Staimer, "Parallel Kinematic Machine Tools – Current State and Future Potentials," *CIRP Annals*, vol. 51, no. 2, pp. 671-683, 2002, doi: 10.1016/S0007-8506(07)61706-5.
- [95] C. M. McCann and A. M. Dollar, "Design of a stewart platform-inspired dexterous hand for 6-DOF within-hand manipulation," in *2017 IEEE/RSJ International Conference on Intelligent Robots and Systems (IROS)*, Vancouver, BC, 2017, pp. 1158-1163, doi: 10.1109/IROS.2017.8202287.

- [96] D. J. Gonzalez and H. H. Asada, "Design and Analysis of 6-DOF Triple Scissor Extender Robots With Applications in Aircraft Assembly," *IEEE Robotics and Automation Letters*, vol. 2, no. 3, pp. 1420-1427, July 2017, doi: 10.1109/LRA.2017.2671366.
- [97] T. Stenzel, M. Sajkowski, and J. Hetmańczyk, "Application of 6-DOF parallel manipulator for simulation of selected manoeuvres of emergency vehicles," in *2016 21st International Conference on Methods and Models in Automation and Robotics (MMAR)*, Miedzyzdroje, 2016, pp. 251-255, doi: 10.1109/MMAR.2016.7575142.
- [98] M. Becerra-Vargas, A. M. Bueno, O. D. Vargas, and J. M. Balthazar, "Robust joint space control of a 6 DOF parallel robot," in *2016 IEEE Conference on Control Applications (CCA)*, Buenos Aires, 2016, pp. 1404-1407, doi: 10.1109/CCA.2016.7588003.
- [99] E. H. Hasnaa and B. Mohammed, "Planning a trajectory of a 6-DOF parallel robot «HEXA»," in *2016 International Conference on Electrical and Information Technologies (ICEIT)*, Tangiers, 2016, pp. 300-305, doi: 10.1109/EITech.2016.7519610.
- [100] J. Ding, J. Li, Y. Yao, C. Xu, and H. Jing, "A forward kinematics based statistical method for the pose errors of a 6-dof parallel manipulator," in *2013 IEEE International Symposium on Assembly and Manufacturing (ISAM)*, Xi'an, 2013, pp. 248-251, doi: 10.1109/ISAM.2013.6643538.
- [101] L. Ghorbani and V. E. Omurlu, "Forward Kinematics of a 6x6 UPU Parallel Mechanism by ANFIS Method," in *2018 6th International Conference on Control Engineering & Information Technology (CEIT)*, Istanbul, Turkey, 2018, pp. 1-6, doi: 10.1109/CEIT.2018.8751887.
- [102] W. Xu, Y. Li, and X. Xiao, "Kinematics and workspace analysis for a novel 6-PSS parallel manipulator," in *2013 IEEE International Conference on Robotics and Biomimetics (ROBIO)*, Shenzhen, 2013, pp. 1869-1874, doi: 10.1109/ROBIO.2013.6739740.
- [103] T. Harada and J. Angeles, "From the McGill pepper-mill carrier to the Kindai ATARIGI Carrier: A novel two limbs six-dof parallel robot with kinematic and actuation redundancy," in *2017 IEEE International Conference on Robotics and Biomimetics (ROBIO)*, Macau, 2017, pp. 1328-1333, doi: 10.1109/ROBIO.2017.8324601.
- [104] S. Ibaraki, T. Yokawa, Y. Kakino, M. Nakagawa, and T. Matsushita, "Kinematic calibration on a parallel kinematic machine tool of the Stewart platform by circular tests," in *Proceedings of the 2004 American Control Conference*, Boston, MA, USA, 2004, pp. 1394-1399 vol.2, doi: 10.23919/ACC.2004.1386770.
- [105] OKUMA. "PM-600." <https://www.scribd.com/doc/210600538/Okuma-PM-600-pdf> (accessed Aug. 7, 2017).
- [106] I. Bonev. "Gallery of Existing Parallel Mechanisms." <https://www.parallemic.org/WhosWho/Gallery.html#> (accessed May 14, 2020).
- [107] Mikrolar. "P1500 Hexapod." <http://mikrolar.com/plite.html> (accessed Oct. 10, 2018).
- [108] Mikrolar. "P3000 Hexapod." <http://mikrolar.com/p3000.html> (accessed Oct. 10, 2018).
- [109] MetromMechatronischeMaschinenGmbH. "Optimum solution - Icosaeder structure + Pentapod kinematics." https://www.gefertec.de/wp-content/uploads/2018/06/3DMP_Forum_2018_Marcus_Witt_Metrom_GmbH.pdf (accessed Apr. 5, 2019).

- [110] T. Kai, "A model predictive control approach to attitude stabilization and trajectory tracking control of a 3D universal joint space robot with an initial angular momentum," in *2011 50th IEEE Conference on Decision and Control and European Control Conference*, Orlando, FL, 2011, pp. 3547-3552, doi: 10.1109/CDC.2011.6160342.
- [111] Y. Yu, Z.-b. Xu, Q.-w. Wu, P. Yu, S. He, and G.-q. Wang, "Kinematic analysis and testing of a 6-RRRPRR parallel manipulator," *Proceedings of the Institution of Mechanical Engineers, Part C: Journal of Mechanical Engineering Science*, vol. 231, no. 13, pp. 2515-2527, July 2017, doi: 10.1177/0954406216633034.
- [112] Y. Koseki, T. Arai, K. Sugimoto, T. Takatuji, and M. Goto, "Design and accuracy evaluation of high-speed and high precision parallel mechanism," in *1998 IEEE International Conference on Robotics and Automation Proceedings (Cat. No.98CH36146)*, Leuven, Belgium, 1998, vol. 2, pp. 1340-1345, doi: 10.1109/ROBOT.1998.677291.
- [113] R. Lin, W. Guo, and F. Gao, "On Parasitic Motion of Parallel Mechanisms," in *Proceedings of the ASME 2016 International Design Engineering Technical Conferences and Computers and Information in Engineering Conference. Volume 5B: 40th Mechanisms and Robotics Conference*, Charlotte, North Carolina, USA, 2016, p. 13 pages, doi: 10.1115/DETC2016-59859.
- [114] A. Pashkevich, D. Chablat, and P. Wenger, "Stiffness analysis of overconstrained parallel manipulators," *Mechanism and Machine Theory*, vol. 44, no. 5, pp. 966-982, May 2009, doi: 10.1016/j.mechmachtheory.2008.05.017.
- [115] J. R. Hauser, A. Griffin, R. L. Klein, G. M. Katz, and S. P. Gaskin, "Quality Function Deployment (QFD)," in *Wiley International Encyclopedia of Marketing*, J. Sheth and N. Malhotra Eds.: John Wiley & Sons, Ltd, 2010, ch. Part 5. Product Innovation and Management.
- [116] J.-P. Merlet, "Optimal design of robots," in *Robotics: Science and systems*, MIT, 2005, p. (8 pages), doi: inria-00000473, version 1.
- [117] eSun. "ESUN ABS FILAMENT - 3MM WHITE." DIY Electronics. <https://www.diyelectronics.co.za/store/abs/718-esun-abs-filament-3mm-white.html> (accessed Nov. 1, 2019).
- [118] 3DPrintingStore. "BEARING 608ZZ." <http://www.3dprintingstore.co.za/mechanics/bearing-608zz/> (accessed Nov. 1, 2019).
- [119] RSComponents. "17mm Thrust Ball Bearing 30mm O.D." https://za.rs-online.com/web/p/products/4090861?cm_mmc=ZA-PLA-DS3A_-google_-PLA_ZA_EN_Pneumatics_And_Hydraulics_And_Power_Transmission_-Power_Transmission_Rotary_Bearings%7CBall_Bearings_-PRODUCT_GROUP&matchtype=&aud-386562756216:pla-394904215358&gclid=EAIaIQobChMIvaj-ie7I5QIVirTtCh1YpwtdeAYYAiABEGIc-PD_BwE&gclsrc=aw.ds (accessed Nov. 1, 2019).
- [120] M. M. Dalvand, B. Shirinzadeh, and S. Nahavandi, "Inverse kinematics Analysis of 6-RRRPRR parallel manipulators," in *2013 IEEE/ASME International Conference on Advanced Intelligent Mechatronics*, Wollongong, NSW, 2013, pp. 644-648, doi: 10.1109/AIM.2013.6584165.
- [121] J. Borràs, "Singularity-Invariant Leg Rearrangements in Stewart-Gough Platforms," PhD thesis, Institut de Robòtica i Informàtica Industrial, Polytechnic Univ. of Catalonia, Barcelona, 2011.

- [122] J. Nielsen and B. Roth, "On the Kinematic Analysis of Robotic Mechanisms," *The International Journal of Robotics Research*, vol. 18, no. 12, pp. 1147-1160, Dec. 1999, doi: 10.1177/02783649922067771.
- [123] GeeksforGeeks. "Program for Newton Raphson Method." <https://www.geeksforgeeks.org/program-for-newton-raphson-method/> (accessed Aug. 7, 2018).
- [124] R. F. Abo-Shanab, "An Efficient Method for Solving the Direct Kinematics of Parallel Manipulators Following a Trajectory," *Journal of Automation and Control Engineering Vol*, vol. 2, no. 3, pp. 228-233, Sept. 2014, doi: 10.12720/joace.2.3.228-233.
- [125] C. Yang, Q. Huang, P. O. Ogbobe, and J. Han, "Forward Kinematics Analysis of Parallel Robots Using Global Newton-Raphson Method," in *2009 Second International Conference on Intelligent Computation Technology and Automation*, Changsha, Hunan, 2009, vol. 3, pp. 407-410, doi: 10.1109/ICICTA.2009.564.
- [126] D. Jakobović and L. Budin, "Forward kinematics of a Stewart platform mechanism," *Faculty of Electrical Engineering and Computing, Unska, Zagreb, Croatia*, 2002.
- [127] P. J. Parikh and S. S. Y. Lam, "A hybrid strategy to solve the forward kinematics problem in parallel manipulators," *IEEE Transactions on Robotics*, vol. 21, no. 1, pp. 18-25, Feb. 2005, doi: 10.1109/TRO.2004.833801.
- [128] J. J. Craig, *Introduction to Robotics: Mechanics and Control*, 3rd ed. Upper Saddle River: Pearson Prentice Hall, 2005, p. 408.
- [129] A. Owen-Hill and R. Inc. "3 types of robot singularities and how to avoid them." <https://robohub.org/3-types-of-robot-singularities-and-how-to-avoid-them/> (accessed Apr. 4, 2019).
- [130] H. Bruyninckx, "Parallel robots," *The Robotics WEBook*, 2005.
- [131] T. Charters, R. Enguica, and P. Freitas, "Detecting singularities of stewart platforms," *Mathematics-in-Industry Case Studies Journal*, vol. 1, pp. 66-80, 2009.
- [132] S. Ay, A. Hacioglu, and E. Vatandas, "A novel geometrical approach to determining the workspace of 6-3 Stewart Platform Mechanism," in *Proceedings of 5th International Conference on Recent Advances in Space Technologies - RAST2011*, Istanbul, 2011, pp. 95-100, doi: 10.1109/RAST.2011.5966982.
- [133] H. N. Le and X. H. Le, "Geometrical Design of a RUU Type Delta Robot Based on the Predescribed Workspace," in *2018 4th International Conference on Green Technology and Sustainable Development (GTSD)*, Ho Chi Minh City, 2018, pp. 359-364, doi: 10.1109/GTSD.2018.8595674.
- [134] L. Moldovan, "Geometrical Method for Description of the 6-PGK Parallel Robot's Workspace," in *2008 First International Conference on Complexity and Intelligence of the Artificial and Natural Complex Systems. Medical Applications of the Complex Systems. Biomedical Computing*, Targu Mures, Mures, 2008, pp. 45-51, doi: 10.1109/CANS.2008.13.
- [135] S.-D. Stan, M. Manic, C. Szep, and R. Balan, "Performance analysis of 3 DOF Delta parallel robot," in *2011 4th International Conference on Human System Interactions (HSI)*, Yokohama, 2011, pp. 215-220, doi: 10.1109/HSI.2011.5937369.
- [136] Z. Gao and D. Zhang, "Workspace Representation and Optimization of a Novel Parallel Mechanism with Three-Degrees-of-Freedom," *Sustainability*, vol. 3, no. 11, pp. 2217-2228, Nov. 2011, doi: 10.3390/su3112217.

- [137] Y. Cao, K. Lu, X. Li, and Y. Zang, "Accurate numerical methods for computing 2d and 3d robot workspace," *International Journal of Advanced Robotic Systems*, vol. 8, no. 6, p. 76, Jan. 2011, doi: doi.org/10.5772/45686.
- [138] A. Chaudhury and A. Ghosal, "Determination of Workspace Volume of Parallel Manipulators Using Monte Carlo Method," in *Computational Kinematics. Mechanisms and Machine Science*, vol. 50, S. Zeghloul, L. Romdhane, and M. Laribi Eds. Cham: Springer, 2018, pp. 323-330.
- [139] E. Kuznetcova, V. Titov, E. Smirnov, I. Dalyaev, and A. Truts, "DESIGN AND SIMULATION ANALYSIS OF HAPTIC DEVICE WITH PARALLEL KINEMATIC," in *Proceedings of the 29th DAAAM International Symposium*, Vienna, Austria, 2018, pp. 636-644, doi: 10.2507/29th.daaam.proceedings.092.
- [140] R. Y. Abdolmalaki, "Development of direct kinematics and workspace representation for smokie robot manipulator & the barret WAM," in *5th International Conference on Robotics and Mechatronics (ICROM)*, Tehran, 2017, p. (7 pages), doi: abs/1707.04820.
- [141] OpenImpulse. "42BYGHW609." https://www.openimpulse.com/blog/document-viewer/?pdf_file=42BYGHW609-Stepper-Motor-Datasheet1.pdf (accessed Nov. 1, 2019).
- [142] OpenImpulse. "42BYGHM809 Stepper Motor (1.68 A, 4.2 kg-cm)." <https://www.openimpulse.com/blog/products-page/product-category/42byghm809-stepper-motor-1-68-4-2-kg%E2%8B%85cm/> (accessed Nov. 1, 2019).
- [143] LongwayMotor. "Hybrid Stepping Motor " <http://longwaymotor.en.hisupplier.com/product-233806-Hybrid-Stepping-Motor.html> (accessed Nov. 8, 2019).
- [144] DIYElectronics. "TB6560 STEPPER MOTOR DRIVER." <https://www.diyelectronics.co.za/store/stepper-motor-drivers/1393-tb6560-stepper-motor-driver.html> (accessed Nov. 1, 2019).
- [145] C. Lee. "How to make schematic drawings for Arduino." <http://www.music.chrblee.net/arduinoeagle/index.html> (accessed Dec. 2, 2018).
- [146] Mantech. "Product Information." <https://www.mantech.co.za/ProductInfo.aspx?Item=14M4531> (accessed Nov. 1, 2019).
- [147] MouserElectronics. "S-320-24." <https://www.mouser.co.za/ProductDetail/MEAN-WELL/S-320-24?qs=moO%2F8p2K0t%252B2QRvG%2F65Ryg==> (accessed Nov.1 2019).
- [148] M. Bachratý and M. Žalman, "2D Position Measurement with optical laser mouse sensor," in *NSSS Slovakia*, Bratislava, 2010.
- [149] A. Bonarini, M. Matteucci, and M. Restelli, "Dead Reckoning for Mobile Robots Using Two Optical Mice," in *ICINCO 2004, Proceedings of the First International Conference on Informatics in Control, Automation and Robotics*, Setúbal, Portugal, 2004, pp. 87-94.
- [150] T. W. Ng, "The optical mouse as a two-dimensional displacement sensor," *Sensors and Actuators A: Physical*, vol. 107, no. 1, pp. 21-25, Oct. 2003, doi: 10.1016/S0924-4247(03)00256-5.
- [151] X. Wang, "Tactile Sensing with Optical Mouse Sensor," PhD dissertation, Dept. of Adv. Syst. Control Eng., Saga University, Honjomachi, Saga, 2008.

- [152] Instructables. "Using a Single-Axis TB6560 Stepper Driver With GRBL/RAMPS." <https://www.instructables.com/id/Using-a-Single-Axis-TB6560-Stepper-Driver-With-GRB/> (accessed June 5, 2018).
- [153] P. B. House. "LMK8UU." <https://pbh.in/index.php/linear-bearing/lmk/lmk-8uu.html> (accessed Nov. 1, 2019).
- [154] M. P. Groover, *Automation, Production Systems, and Computer-Integrated Manufacturing*, 3rd ed. Prentice Hall Press, 2007, p. 840.
- [155] Y. Zhang and X. Jing, "Kinematics analysis and simulation of a novel spatial translational parallel manipulator," in *2017 2nd International Conference on Robotics and Automation Engineering (ICRAE)*, Shanghai, 2017, pp. 131-135, doi: 10.1109/ICRAE.2017.8291367.
- [156] L. Zhao, A. Joubair, P. Bigras, and I. A. Bonev, "Metrological Evaluation of a Novel Medical Robot and Its Kinematic Calibration," *International Journal of Advanced Robotic Systems*, vol. 12, no. 9, p. 126 (13 pages), Jan. 2015, doi: 10.5772/60881.
- [157] M. Placzek and Ł. Piszczek, "Testing of an industrial robot's accuracy and repeatability in off and online environment," *Eksploatacja i Niezawodność - Maintenance and Reliability*, vol. 20, no. 3, pp. 455-464, June 2018, doi: 10.17531/ein.2018.3.15.
- [158] D. Kumičáková, V. Tlach, and M. Cisar, "Testing the Performance Characteristics of Manipulating Industrial Robots," *Transactions of the VŠB - Technical University of Ostrava, Mechanical Series*, vol. 62, no. 1, pp. 39-50, Sept. 2016, doi: 10.22223/tr.2016-1/2009.
- [159] SouthAfricanMI. "South Africa's Manufacturing Industry." <https://www.southafricanmi.com/south-africas-manufacturing-industry.html> (accessed Nov. 10, 2019).
- [160] Y. Cao, "An engineering-oriented method for the three dimensional workspace generation of robot manipulator," *Journal of Information and Computational Science*, vol. 8, no. 1, pp. 51–61, 2011.
- [161] MicroEpsilon. "Smart laser triangulation displacement sensor." https://www.micro-epsilon.com/displacement-position-sensors/laser-sensor/optoNCDT_1420_basic/ (accessed Aug. 5, 2019).
- [162] M. Shang and J. Butterfield, "The experimental test and FEA of a PKM (Exechon) in a flexible fixture application for aircraft wing assembly," in *2011 IEEE International Conference on Mechatronics and Automation*, Beijing, 2011, pp. 1225-1230, doi: 10.1109/ICMA.2011.5985836.
- [163] Y. Jiang, T. Li, L. Wang, and F. Chen, "Kinematic Accuracy Improvement of a Novel Smart Structure-Based Parallel Kinematic Machine," *IEEE/ASME Transactions on Mechatronics*, vol. 23, no. 1, pp. 469-481, Feb. 2018, doi: 10.1109/TMECH.2017.2756348.
- [164] Guillaume. "How to get the real-time position of mouse outside matlab." <https://www.mathworks.com/matlabcentral/answers/331746-how-to-get-the-real-time-position-of-mouse-outside-matlab> (accessed Aug. 5, 2018).
- [165] J. E. Shigley, *Shigley's mechanical engineering design*, 8th ed. Tata McGraw-Hill Education, 2011, p. 1059.
- [166] J. Padayachee, "Design methods Formulae: Graphs and Tables," 2017, pp. 1-8.

APPENDICES

Appendix A – Testing Results

A.1 Linear Actuator Accuracy and Repeatability

Table A.1 to Table A.7 displays the results of the accuracy and repeatability of the linear actuators.

Table A.1: Data from Actuator 1

	Theoretical distance (mm)				
	10	20	30	40	50
Experimental Distance (mm)	10.05	20.01	29.86	39.84	49.92
	10	20.01	29.84	39.94	49.94
	9.92	20.03	29.88	39.82	49.82
	9.93	19.95	29.83	39.99	49.94
	10.07	19.75	29.89	39.87	49.85
	10	19.74	29.85	39.94	49.86
	9.92	19.78	29.8	39.9	49.83
	10.07	19.89	29.93	39.88	49.9
	9.98	19.88	29.9	39.93	49.89
	9.97	19.97	29.9	39.91	49.92

Table A.2: Data from Actuator 2

	Theoretical distance (mm)				
	10	20	30	40	50
Experimental Distance (mm)	10.03	20.06	30.03	40.06	49.9
	10.05	20.09	29.98	40	49.91
	10.02	20.08	30.03	40.08	49.94
	10.05	20.07	29.99	40.07	50.01
	10.05	19.96	29.99	39.93	50.03
	10.08	20	30.03	40.02	49.96
	10.02	19.98	30	39.99	50.01
	10.03	19.98	30.03	39.97	50.04
	10.05	20.08	29.99	39.98	50.03
	10.06	19.98	30.03	40.05	50.05

Table A.3: Data from Actuator 3

	Theoretical distance (mm)				
	10	20	30	40	50
Experimental Distance (mm)	9.9	19.85	29.93	39.98	50.07
	9.9	19.89	29.93	40.08	50.02
	9.95	19.9	30.02	40.07	50.09
	9.98	19.95	30.02	40.1	50.03
	9.94	19.96	30	39.99	50.09
	9.94	19.94	29.98	39.95	50.07
	9.84	19.97	30.04	40.11	50.08
	9.95	19.94	30.01	40.01	50.03
	9.94	19.89	30.01	40.08	50.07
	9.88	19.94	30.06	40.03	49.99

Table A.4: Data from Actuator 4

	Theoretical distance (mm)				
	10	20	30	40	50
Experimental Distance (mm)	10.03	20.02	29.94	40.07	49.99
	9.99	20.05	30.04	40.11	49.96
	10.04	20.08	29.99	39.93	50.02
	10.03	19.97	29.96	40.03	50.05
	9.97	19.88	29.94	39.93	50.01
	10.01	19.95	30.04	40.05	49.98
	10.02	20	29.89	39.91	50.03
	10	20.02	29.98	40	50.07
	9.98	19.96	29.97	39.92	49.99
	9.96	20	29.99	40.01	49.99

Table A.5: Data from Actuator 5

	Theoretical distance (mm)				
	10	20	30	40	50
Experimental Distance (mm)	9.94	19.97	29.87	39.79	49.84
	9.98	19.98	29.82	39.87	49.83
	9.97	19.95	29.89	39.83	49.84
	9.97	19.89	29.89	39.82	49.94
	9.92	19.83	29.82	39.83	49.84
	9.89	19.79	29.83	39.86	49.83
	9.9	19.84	29.87	39.9	49.85
	9.92	19.82	29.86	39.81	49.85
	9.93	19.85	29.89	39.88	49.84
	9.97	19.79	29.84	39.83	49.82

Table A.6: Data from Actuator 6

	Theoretical distance (mm)				
	10	20	30	40	50
Experimental Distance (mm)	10.05	20.01	30.1	39.97	49.92
	10.05	19.96	30	39.93	49.91
	9.98	20.11	29.96	39.95	50.02
	9.96	19.86	29.96	39.97	49.99
	10.01	19.94	30.05	40.02	49.96
	10.06	19.85	30.09	40.13	50.09
	9.94	20.04	30.09	40.1	49.98
	9.94	19.95	30.05	39.95	50.03
	10.08	19.92	29.95	39.97	49.93
	9.92	19.89	29.99	39.97	49.94

Table A.7: Standard deviations vs Actuated Distance

	Actuator Standard deviations					
Distance	1	2	3	4	5	6
10 mm	0.06	0.02	0.04	0.03	0.03	0.06
20 mm	0.11	0.05	0.04	0.06	0.07	0.08
30 mm	0.04	0.02	0.04	0.05	0.03	0.06
40 mm	0.05	0.05	0.06	0.07	0.03	0.07
50 mm	0.04	0.06	0.03	0.03	0.03	0.06

A.2 Inverse Kinematic Simulations – MATLAB® and SolidWorks®

Table A.8 to Table A.10 presents the data obtained from the inverse kinematic simulations conducted on MATLAB® and SolidWorks® for verification of the inverse kinematic equations.

Table A.8: Testing of translation of the end effector

Region 1				
End effector position (mm)			Largest error among the six legs (mm)	
x	y	z	MATLAB Script Error	Simulink Error
148.97	-114.54	278.54	0	0
147.59	-109.37	281.74	0.01	0.01
148.97	-99.44	282.38	0	0
160.14	-92.11	287.48	0.01	0.01
129.08	-84.62	300.76	0.01	0.01
130.69	-91.17	298.5	0	0
161.24	-86.62	270.51	0	0
134.32	-95.17	297.52	0.01	0.01
89.91	-132.26	303.31	0	0
87.57	-133.08	303.82	0	0
Region 2				
End effector position (mm)			Largest error among the six legs (mm)	
x	y	z	MATLAB Script Error	Simulink Error
136.92	-70.03	308.22	0	0
113.35	-67.81	330.76	0	0
122.41	-56.32	331.43	0.01	0.01
128.65	-47.15	332.04	0.01	0.01
157.68	-28.35	304.34	0.01	0.01
159.16	-34.78	293.95	0.01	0.01
155.99	-39.59	292.26	0	0
158.61	-48.41	285.9	0.01	0.01
150.46	-55.85	287.61	0.01	0.01
146.94	-61.13	285.81	0	0
Region 3				
End effector position (mm)			Largest error among the six legs (mm)	
x	y	z	MATLAB Script Error	Simulink Error
164.76	-21.49	298.54	0	0
170.05	-14.48	296.26	0	0
175.67	-6.54	294.69	0.01	0.01
169.44	-0.03	321.15	0	0

Region 3				
End effector position (mm)			Largest error among the six legs (mm)	
x	y	z	MATLAB Script Error	Simulink Error
165.76	0	326.91	0	0
145.76	-21.37	332.22	0.01	0.01
160.43	21.33	323.72	0.01	0.01
168.4	23.97	312.15	0	0
167.57	17.15	312.15	0	0
163.73	8.35	314.56	0	0
Region 4				
End effector position (mm)			Largest error among the six legs (mm)	
x	y	z	MATLAB Script Error	Simulink Error
164.94	64.03	300.97	0.01	0.01
181.1	79.03	271.22	0.01	0.01
187.86	43.58	281.71	0.01	0.01
138.52	63.88	308.87	0.01	0.01
85.34	72.76	304.17	0	0
156.5	69.49	279.38	0	0
177.78	64.07	279.83	0.01	0.01
172.24	82.01	277.96	0	0
215.64	28.35	270.45	0.01	0.01
204.59	54.48	269.26	0.01	0.01
Region 5				
End effector position (mm)			Largest error among the six legs (mm)	
x	y	z	MATLAB Script Error	Simulink Error
144.13	115.76	281.83	0	0
124.98	120.98	291.74	0.01	0.01
139.4	112.89	284.78	0.01	0.01
150.25	94.8	278.53	0	0
152.61	90.03	276.93	0.01	0.01
155	83.27	275.36	0	0
158.17	83.65	272.72	0.01	0.01
150.19	85.64	293.46	0.01	0.01
148.12	86.36	298.96	0.01	0.01
132.1	105.79	298.64	0	0

Table A.9: Testing of translation and alpha rotation of the end effector

Region 1					
End effector position and orientation				Largest error among the six legs (mm)	
x (mm)	y (mm)	z (mm)	alpha (deg)	MATLAB Script Error	Simulink Error
111.31	-95.52	312.28	17.6	0.01	0.01
111.31	-95.51	303.26	14.7	0	0
111.31	-124.39	281.2	-9.47	0	0
111.31	-127.91	276.8	-13.17	0.01	0.01
111.31	-136.1	274.14	-26.47	0	0
111.31	-132.5	287.35	-23.2	0	0
111.31	-137	288.2	-27.33	0.01	0.01
111.31	-83.2	310.18	14.24	0	0
111.31	-99.3	296.79	10.03	0	0
111.31	-103.58	291.69	4.59	0	0
Region 2					
End effector position and orientation				Largest error among the six legs (mm)	
x (mm)	y (mm)	z (mm)	alpha (deg)	MATLAB Script Error	Simulink Error
111.31	-55.66	310.27	23.08	0	0
111.31	-48.88	311.43	20.09	0.01	0.01
111.31	-61.66	296.01	7.97	0	0
111.31	-72.34	292.99	5.7	0.01	0.01
111.31	-80.53	293.2	3.47	0	0
111.31	-77.71	297.02	-9.09	0.01	0.01
111.31	-53.11	306.11	-7.3	0.01	0.01
111.31	-51.18	316.62	-13.65	0.01	0.01
111.31	-38.81	326.94	-18.27	0	0
111.31	-41.52	319.78	-23.59	0	0
Region 3					
End effector position and orientation				Largest error among the six legs (mm)	
x (mm)	y (mm)	z (mm)	alpha (deg)	MATLAB Script Error	Simulink Error
111.31	-5.05	318.5	-9.49	0.01	0.01

Region 3					
End effector position and orientation				Largest error among the six legs (mm)	
x (mm)	y (mm)	z (mm)	alpha (deg)	MATLAB Script Error	Simulink Error
111.31	10.58	321.54	-14.49	0	0
111.31	19.38	315.73	-20.98	0	0
111.31	26.36	313.45	-14.33	0.01	0.01
111.31	14.3	317.72	-15.7	0.01	0.01
111.31	13.51	333.27	9.28	0	0
111.31	-25.87	316.7	12.21	0.01	0.01
111.31	-21.81	315.45	23.84	0.01	0.01
111.31	9.68	311.57	18.5	0	0
111.31	13.02	332.24	16.77	0	0
Region 4					
End effector position and orientation				Largest error among the six legs (mm)	
x (mm)	y (mm)	z (mm)	alpha (deg)	MATLAB Script Error	Simulink Error
111.31	48.04	336.95	13.37	0	0
111.31	58.71	325.55	8.22	0.01	0.01
111.31	79.97	317.08	22.07	0	0
111.31	66	324.13	30.36	0.01	0.01
111.31	30.14	315.06	10.71	0	0
111.31	46.1	307.93	-18.5	0	0
111.31	32.78	310.15	-20.57	0	0
111.31	56.34	304.9	-15.87	0.01	0.01
111.31	67.52	302.91	-16.9	0.01	0.01
111.31	60.81	313.75	-22.7	0.01	0.01
Region 5					
End effector position and orientation				Largest error among the six legs (mm)	
x (mm)	y (mm)	z (mm)	alpha (deg)	MATLAB Script Error	Simulink Error
111.31	85.08	298.26	-18.22	0.01	0.01
111.31	92.57	299.83	-22.23	0.01	0.01
111.31	96.44	288.07	-15.59	0.01	0.01
111.31	86.15	295.5	-20.99	0.01	0.01

Region 5					
End effector position and orientation				Largest error among the six legs (mm)	
x (mm)	y (mm)	z (mm)	alpha (deg)	MATLAB Script Error	Simulink Error
111.31	96.42	282.39	-12.62	0	0
111.31	85.49	313.16	7.61	0	0
111.31	89.29	303.22	13.3	0	0
111.31	110.42	300.47	26.66	0	0
111.31	112.58	284.92	31.34	0	0
111.31	125.08	303.95	22.18	0.01	0.01

Table A.10: Testing of translation and beta rotation of the end effector

Region 1					
End effector position and orientation				Largest error among the six legs (mm)	
x (mm)	y (mm)	z (mm)	beta (deg)	MATLAB Script Error	Simulink Error
169.32	-95.78	278.21	-6.96	0.01	0.01
177.57	-87.67	290.85	-16.06	0	0
167.71	-93.86	298.91	-17.24	0.01	0.01
173.24	-84.1	288.35	-8.88	0.01	0.01
174.74	-91.09	285.73	-6.77	0	0
114.75	-103.19	286.65	15.47	0	0
116.57	-106.44	284.7	18.56	0.01	0.01
114.77	-117.2	273.76	16.77	0	0
109.27	-124.83	275.92	19.13	0	0
129.67	-123.89	273.1	13.43	0	0
Region 2					
End effector position and orientation				Largest error among the six legs (mm)	
x (mm)	y (mm)	z (mm)	beta (deg)	MATLAB Script Error	Simulink Error
136.69	-78.46	282.92	4.51	0	0
118.01	-69.31	315.82	3.9	0.01	0.01
105.04	-56.96	330.49	-9.24	0	0
87.63	-29.67	312.22	15.43	0	0

Region 2					
End effector position and orientation				Largest error among the six legs (mm)	
x (mm)	y (mm)	z (mm)	beta (deg)	MATLAB Script Error	Simulink Error
89.05	-50	313.75	13.22	0.01	0.01
74.79	-32.86	320.49	-19.3	0	0
74.89	-28.15	333.17	-19.77	0	0
84.68	-51.78	329.98	-25.19	0	0
104.96	-32.74	324.21	18.37	0	0
111.7	-30.72	315.42	-14.41	0	0
Region 3					
End effector position and orientation				Largest error among the six legs (mm)	
x (mm)	y (mm)	z (mm)	beta (deg)	MATLAB Script Error	Simulink Error
112.18	12.33	319.06	-13.86	0	0
111.96	27.29	329.44	-20.27	0	0
110.47	25.81	311.94	20.18	0.01	0.01
135.62	-26.63	310.7	15.46	0.01	0.01
137.68	-8.73	314.89	13.36	0.01	0.01
113.89	-14	325.31	-12.12	0.01	0.01
105.57	-7.03	329.67	-17.61	0	0
107.08	5.78	336.18	-20.7	0	0
96.55	11.29	315.62	10.95	0	0
85.11	27.12	317.28	12.36	0	0
Region 4					
End effector position and orientation				Largest error among the six legs (mm)	
x (mm)	y (mm)	z (mm)	beta (deg)	MATLAB Script Error	Simulink Error
82.25	50.87	316.73	15.62	0.01	0.01
115.72	55.22	302.85	19.29	0	0
87.87	31.1	327.35	-17.77	0	0
123.93	34.77	324.32	-6.33	0.01	0.01
131.36	30.24	320.84	-2.81	0	0
129.8	70.98	322.11	2.62	0.01	0.01
131.49	81.71	323.51	2.63	0	0

Region 4					
End effector position and orientation				Largest error among the six legs (mm)	
x (mm)	y (mm)	z (mm)	beta (deg)	MATLAB Script Error	Simulink Error
128.28	49.13	308.65	-13.66	0	0
115.95	28.64	307.89	-19.38	0	0
118.43	25.69	318.92	19.52	0	0
Region 5					
End effector position and orientation				Largest error among the six legs (mm)	
x (mm)	y (mm)	z (mm)	beta (deg)	MATLAB Script Error	Simulink Error
138.66	90.27	301.95	0.34	0	0
141.28	93.12	305.74	-7.95	0.01	0.01
117.85	115.26	299.62	-5.68	0	0
103.53	109.48	298.23	10.43	0.01	0.01
86.07	112.07	310.08	-3.98	0.01	0.01
89.97	83.43	317.48	15.41	0.01	0.01
144.81	91.86	297.63	2.08	0	0
143	109.68	304.28	-12.74	0	0
142.16	82.55	302.64	-13.86	0.01	0.01
106.86	83.55	314.62	13.14	0	0

A.3 PKM Accuracy and Repeatability

Table A.11 to A.13 presents the accuracy and repeatability of the PKM.

Table A.11: List of coordinates used for the translation accuracy and repeatability analysis

Region-point	X value (mm)	Y value (mm)	Z value (mm)
1-1	170.67	-91.43	268.83
1-2	171.83	-98.75	264.29
1-3	163.49	-86.82	275.46
2-1	167.59	-36.14	293.74
2-2	174.87	-47.07	293.64
2-3	151.93	-71.93	292.72
3-1	110.52	-0.19	305.5
3-2	99.12	-18.53	345.4
3-3	177.3	19.54	294.36
4-1	139.28	33.52	312.11
4-2	142.83	46.43	302.21
4-3	145.77	67.62	304.64
5-1	160.7	86.19	281.34
5-2	130.6	91.48	297.3
5-3	130.06	105.95	292.9

Table A.12: Summary of the accuracy and repeatability results for alpha rotation testing

Region-point	X value (mm)	Y value (mm)	Z value (mm)	α (degrees)	Accuracy (mm)	Repeatability (mm)
1-1	111.31	-80.44	311.76	-7.39	1.2	0.98
1-2	111.31	-89.17	296.29	-5	1.74	1.08
1-3	111.31	-83.08	302.83	5	1.69	1.03
2-1	111.31	-45.29	310.77	-15.82	0.47	0.82
2-2	111.31	-33.65	309.97	12.26	0.73	0.89
2-3	111.31	-68.9	299.1	-7.09	1.21	1.12
3-1	111.31	-4.66	310.83	15	0.26	0.99
3-2	111.31	-26.81	311.43	-20	0.53	1.9
3-3	111.31	-0.26	311.09	5	0.3	0.92
4-1	111.31	31.15	317.07	16.7	0.39	0.62
4-2	111.31	77.88	304.67	20.25	1.58	1.67
4-3	111.31	46.86	309.34	-9.78	0.59	1.27
5-1	111.31	89.04	305.48	10.41	1.63	0.8

Region-point	X value (mm)	Y value (mm)	Z value (mm)	α (degrees)	Accuracy (mm)	Repeatability (mm)
5-2	111.31	103.97	299.41	8.78	1.63	0.78
5-3	111.31	84.59	306.17	-2.3	1.25	0.23

Table A.13: Summary of the accuracy and repeatability results for beta rotation testing

Region-point	X value (mm)	Y value (mm)	Z value (mm)	β (degrees)	Accuracy (mm)	Repeatability (mm)
1-1	124.47	-90.11	287.16	10.11	1.55	0.79
1-2	101.57	-97.88	314.82	-5.52	1.76	0.73
1-3	105.16	-93.48	322.4	-12.64	1.73	0.86
2-1	105.45	-33.76	317.56	8.57	1.37	0.47
2-2	113.84	-31.64	308.17	15.11	0.7	1.34
2-3	97.84	-54.65	322.13	-9.43	1.34	0.63
3-1	164.34	-15	305.66	-11.02	0.21	0.58
3-2	164.48	15.15	296.16	-17.46	0.3	1.07
3-3	138.51	23.44	304.56	9.33	0.45	0.96
4-1	111.03	43.04	308.45	12.93	0.7	1.04
4-2	135.94	29.14	319.64	-12.48	0.62	0.64
4-3	137.56	51.8	315.32	-4	0.66	0.28
5-1	123.69	91.82	287.49	11.87	1.54	0.94
5-2	151.61	95.94	273.93	6.89	1.46	0.47
5-3	142.28	84.02	301.35	-7.8	1.69	0.5

A.4 Payload Tests

Table A.14 presents the data for the load vs. leg actuation error investigation.

Table A.14: Load vs. Leg Actuation Error

Load (kg)	Error (mm)					
	Leg 1	Leg 2	Leg 3	Leg 4	Leg 5	Leg 6
0.45	0.11	0.07	0.08	0.06	0.03	0.06
1	0.03	0.02	0.09	0.08	0.08	0.05
1.45	0.05	0.06	0.05	0.03	0.06	0.11
2	0.13	0.06	0.05	0.05	0.03	0.12
2.45	0.01	0.03	0.02	0.04	0.09	0.01
3	0.03	0.16	0.02	0.17	0.16	0.14
3.45	0.1	0.03	0.19	0.22	0.03	0.09
5.27	0.03	0.09	0.05	0.02	0.19	0.18
6.18	0.02	0.03	0.13	0.05	0.09	0.17
7.08	0.21	0.29	0.27	0.09	0.16	0.14
8.44	0.03	0.24	0.26	0.02	0.2	0.08
9.35	0.19	0.26	0.17	0.27	0.03	0
10.26	0.06	0.09	0.08	0.03	0.09	0.07
12.07	0.07	0.25	0.21	0.28	0.03	0.09
13.43	0.06	0.05	0.02	0.07	0.11	0.01
15	0.21	0.04	0.22	0.14	0.05	0.05
18	0.06	0.05	0.12	0.08	0.04	0.01
20	0.1	0.04	0.05	0.02	0	0.02
23	0.02	0.03	0.04	0.01	0.04	0.08
25.23	0.02	0.09	0.06	0.11	0.14	0.13

A.5 Forward Kinematic Simulations – MATLAB® and SolidWorks®

Table A.15 to Table A.17 displays the results obtained from the simulations of the forward kinematic analysis performed with MATLAB® and SolidWorks®.

Table A.15: Forward kinematic results for translation

Region 1	mm			degrees		
	x	y	z	θ_1	θ_3	θ_5
True value	126.98	-120.41	290.84	64.33	42.82	122.78
Guess	150	-150	350	57.3	57.3	108.86
Converged value	126.98	-120.4	290.84	64.33	42.82	122.87
Absolute error	0	0.01	0	0	0	0.09
Iterations	5					
True value	99.96	-113.57	311.91	74.44	50	118.7
Guess	150	-70	350	51.57	40.11	108.86
Converged value	99.96	-113.57	311.9	74.43	50	118.73
Absolute error	0	0	0.01	0.01	0	0.03
Iterations	5					
True value	149.04	-87.7	280.25	57.12	42.27	115.77
Guess	220	-10	220	63.03	34.38	103.13
Converged value	149.05	-87.69	280.25	57.11	42.27	116.17
Absolute error	0.01	0.01	0	0.01	0	0.4
Iterations	7					
True value	155.94	-100.29	274.59	54.39	39.05	119.25
Guess	100	-70	350	68.75	45.84	120.32
Converged value	155.94	-100.3	274.6	54.39	39.05	119.93
Absolute error	0	0.01	0.01	0	0	0.68
Iterations	5					
True value	146.93	-104.65	288.73	59.03	42.15	118.92
Guess	0	0	0	0	0	0
Converged value	146.92	-104.66	288.72	59.03	42.15	119.3
Absolute error	0.01	0.01	0.01	0	0	0.38
Iterations	6					
Region 2	mm			degrees		
	x	y	z	θ_1	θ_3	θ_5
True value	145.09	-77.8	293.73	60.08	46.29	111.91

Region 2	mm			degrees		
	x	y	z	θ_1	θ_3	θ_5
Guess	100	-20	150	45.84	57.3	126.05
Converged value	145.08	-77.8	293.74	60.08	46.29	112.15
Absolute error	0.01	0	0.01	0	0	0.24
Iterations	6					
True value	133.25	-68.42	320.35	66.12	53.19	107.49
Guess	180	-20	380	44.12	36.1	114.59
Converged value	133.24	-68.42	320.35	66.13	53.19	107.56
Absolute error	0.01	0	0	0.01	0	0.07
Iterations	5					
True value	137.97	-44.46	315.41	63.25	54.68	101.79
Guess	80	0	260	45.84	57.3	114.59
Converged value	137.95	-44.46	315.42	63.25	54.68	101.85
Absolute error	0.02	0	0.01	0	0	0.06
Iterations	6					
True value	138.09	-33.61	315.04	62.44	55.87	98.98
Guess	200	20	354	50.42	35.52	54.43
Converged value	138.08	-33.61	315.03	62.45	55.87	99.03
Absolute error	0.01	0	0.01	0.01	0	0.05
Iterations	6					
True value	116.55	-28.84	343.58	69.78	63.61	96.89
Guess	200	-50	400	57.3	68.75	111.73
Converged value	116.54	-28.84	343.59	69.79	63.62	96.89
Absolute error	0.01	0	0.01	0.01	0.01	0
Iterations	7					
Region 3	mm			degrees		
	x	y	z	θ_1	θ_3	θ_5
True value	119.65	-13.31	346.52	68	65.21	93.15
Guess	19	-50	400	74.48	57.3	106.57
Converged value	119.65	-13.32	346.51	68	65.21	93.16
Absolute error	0	0.01	0.01	0	0	0.01
Iterations	6					
True value	115.85	3.48	342.62	66.64	67.41	89.16

Region 3	mm			degrees		
	x	y	z	θ_1	θ_3	θ_5
Guess	30	80	400	74.48	74.48	101.99
Converged value	115.85	3.48	342.62	66.65	67.4	89.16
Absolute error	0	0	0	0.01	0.01	0
Iterations	6					
True value	116.39	13.59	341.55	65.28	68.24	86.71
Guess	74	87	450	51.57	50.42	102.56
Converged value	116.4	13.6	341.54	65.29	68.23	86.65
Absolute error	0.01	0.01	0.01	0.01	0.01	0.06
Iterations	6					
True value	186.11	0	312.8	50.32	50.32	90
Guess	220	42	366	57.3	63.03	74.48
Converged value	186.1	0	312.81	50.33	50.33	90
Absolute error	0.01	0	0.01	0.01	0.01	0
Iterations	5					
True value	181.31	24.99	307.68	48.48	51.95	83.54
Guess	142	78	400	57.3	44.12	94.54
Converged value	181.3	24.99	307.68	48.48	51.95	83.29
Absolute error	0.01	0	0	0	0	0.25
Iterations	5					
Region 4	mm			degrees		
	x	y	z	θ_1	θ_3	θ_5
True value	172.03	64.7	295.64	44.37	53.69	72.52
Guess	115	96	333	35.52	37.24	80.21
Converged value	172.02	64.69	295.64	44.38	53.69	71.93
Absolute error	0.01	0.01	0	0.01	0	0.59
Iterations	5					
True value	153.5	73.67	304.68	47.43	59.49	70.38
Guess	90	133	450	54.43	50.42	82.51
Converged value	153.5	73.68	304.68	47.42	59.49	70.08
Absolute error	0	0.01	0	0.01	0	0.3
Iterations	6					
True value	103.86	69.1	333.17	58.94	74.6	73.17

Region 4	mm			degrees		
	x	y	z	θ_1	θ_3	θ_5
Guess	33	155	488	42.97	63.03	49.27
Converged value	103.84	69.08	333.18	58.95	74.6	73.16
Absolute error	0.02	0.02	0.01	0.01	0	0.01
Iterations	6					
True value	93.15	81.96	332.6	58.39	77.77	70.29
Guess	201	33	469	50.99	65.32	89.38
Converged value	93.15	81.98	332.6	58.38	77.77	70.24
Absolute error	0	0.02	0	0.01	0	0.05
Iterations	8					
True value	91.6	32.76	351.24	68.01	76.12	82.46
Guess	244	-10	462	34.38	45.84	91.67
Converged value	91.61	32.77	351.24	68	76.11	82.44
Absolute error	0.01	0.01	0	0.01	0.01	0.02
Iterations	6					
Region 5	mm			degrees		
	x	y	z	θ_1	θ_3	θ_5
True value	88.58	86.16	332.63	58.32	79.07	69.42
Guess	256	10	488	31.51	55.58	46.98
Converged value	88.57	86.16	332.64	58.32	79.07	69.35
Absolute error	0.01	0	0.01	0	0	0.07
Iterations	7					
True value	111.71	109.13	297.75	47.1	69.86	60.48
Guess	280	222	350	34.38	45.84	44.12
Converged value	111.71	109.13	297.75	47.1	69.86	60.48
Absolute error	0	0	0	0	0	0
Iterations	7					
True value	140.21	116.77	284.1	40.7	59.85	57.47
Guess	193	88	201	37.82	44.69	74.48
Converged value	140.21	116.77	284.1	40.7	59.85	57.16
Absolute error	0	0	0	0	0	0.31
Iterations	6					
True value	156.25	86.16	285.71	42.53	56.18	65.55

Region 5	mm			degrees		
	x	y	z	θ_1	θ_3	θ_5
Guess	220	30	350	0	28.65	28.65
Converged value	156.25	86.16	285.7	42.53	56.18	65.04
Absolute error	0	0	0.01	0	0	0.51
Iterations	6					
True value	80.56	135.59	305.19	47.6	78.32	56.44
Guess	120	100	450	37.82	63.03	74.48
Converged value	80.55	135.59	305.19	47.6	78.32	56.14
Absolute error	0.01	0	0	0	0	0.3
Iterations	6					

Table A.16: Forward kinematic results for alpha rotation and translation

Region 1	mm			degrees			
	x	y	z	α	θ_1	θ_3	θ_5
True value	111.31	-126.79	297.78	-12.41	69.51	41.02	122.91
Guess	150	-100	350	-17.19	80.21	57.3	108.29
Converged value	111.29	-126.78	297.79	-12.4	69.52	41.02	122.91
Absolute error	0.02	0.01	0.01	0.01	0.01	0	0
Iterations	5						
True value	111.31	-109.59	303.08	6.78	70.27	49.79	118.86
Guess	80	-50	289	11.46	80.21	37.82	120.32
Converged value	111.32	-109.6	303.07	6.78	70.26	49.79	118.87
Absolute error	0.01	0.01	0.01	0	0.01	0	0.01
Iterations	5						
True value	111.31	-85.7	331.42	-10.8	73.71	52.55	110.84
Guess	145	-10	300	14.32	57.3	57.3	85.94
Converged value	111.31	-85.7	331.43	-10.81	73.71	52.55	110.84
Absolute error	0	0	0.01	0.01	0	0	0
Iterations	6						
True value	111.31	-96.78	297.23	12.21	69.27	52.08	116.31
Guess	95	-133	220	18.91	57.3	45.84	74.48
Converged value	111.33	-96.79	297.22	12.22	69.26	52.08	116.32
Absolute error	0.02	0.01	0.01	0.01	0.01	0	0.01

Region 1	mm			degrees			
	x	y	z	α	θ_1	θ_3	θ_5
Iterations	6						
True value	111.31	-121.99	296.16	-21	69.88	38.61	121.61
Guess	100	-60	350	-22.92	74.48	45.84	126.05
Converged value	111.3	-122	296.17	-21	69.97	38.63	121.6
Absolute error	0.01	0.01	0.01	0	0.09	0.02	0.01
Iterations	6						
Region 2	mm			degrees			
	x	y	z	α	θ_1	θ_3	θ_5
True value	111.31	-76.73	296.83	-16.95	71.23	46.35	111.74
Guess	120	-60	300	-28.65	85.94	68.75	85.94
Converged value	111.32	-76.73	296.82	-16.95	71.22	46.34	111.74
Absolute error	0.01	0	0.01	0	0.01	0.01	0
Iterations	6						
True value	111.31	-37.14	323.67	-26.69	73.06	53.91	100.19
Guess	80	-80	300	-28.65	80.21	63.03	85.94
Converged value	111.3	-37.1	323.67	-26.68	73.05	53.91	100.19
Absolute error	0.01	0.04	0	0.01	0.01	0	0
Iterations	5						
True value	111.31	-28.61	316.81	23.87	63.85	66.03	94.66
Guess	100	0	300	28.65	51.57	51.57	74.48
Converged value	111.3	-28.59	316.81	23.88	63.85	66.03	94.65
Absolute error	0.02	0.02	0	0.01	0	0	0.01
Iterations	5						
True value	111.31	-67.4	304.31	9.53	69	56.61	108.11
Guess	99	-30	390	12.61	45.84	57.3	101.99
Converged value	111.32	-67.43	304.3	9.51	69	56.6	108.12
Absolute error	0.01	0.03	0.01	0.02	0	0.01	0.01
Iterations	5						
True value	111.31	-41.35	326.51	20.74	67.32	64.93	98.39
Guess	10	-20	365	5.73	57.3	57.3	95.11
Converged value	111.33	-41.37	326.5	20.74	67.32	64.92	98.39
Absolute error	0.02	0.02	0.01	0	0	0.01	0

Region 2	mm			degrees			
	x	y	z	α	θ_1	θ_3	θ_5
Iterations	6						
Region 3	mm			degrees			
	x	y	z	α	θ_1	θ_3	θ_5
True value	111.31	0.69	320.1	14.32	62.47	68.18	87.92
Guess	48	50	330	5.73	51.57	45.84	91.67
Converged value	111.28	0.73	320.1	14.33	62.48	68.19	87.9
Absolute error	0.03	0.04	0	0.01	0.01	0.01	0.02
Iterations	5						
True value	111.31	-26.92	332.84	-20.87	72.44	58.59	97.56
Guess	62	10	341	22.92	74.48	68.75	108.86
Converged value	111.29	-26.92	332.85	-20.86	72.44	58.59	97.56
Absolute error	0.02	0	0.01	0.01	0	0	0
Iterations	6						
True value	111.31	19.34	329.02	-27.56	68.71	63.19	86.85
Guess	12	61	280	-34.38	74.48	68.75	103.13
Converged value	111.32	19.36	329.02	-27.57	68.71	63.19	86.85
Absolute error	0.01	0.02	0	0.01	0	0	0
Iterations	7						
True value	111.31	-11.39	314.44	13.97	63.5	66.21	91.37
Guess	30	-60	320	17.19	74.48	77.92	92.82
Converged value	111.33	-11.41	314.44	13.97	63.5	66.22	91.41
Absolute error	0.02	0.02	0	0	0	0.01	0.04
Iterations	6						
True value	111.31	16.67	322.14	29.02	56.17	71.79	80.77
Guess	80	30	300	34.38	57.3	57.3	74.48
Converged value	111.3	16.68	322.14	29.03	56.17	71.8	80.76
Absolute error	0.01	0.01	0	0.01	0	0.01	0.01
Iterations	5						
Region 4	mm			degrees			
	x	y	z	α	θ_1	θ_3	θ_5
True value	111.31	72.62	293.73	9.23	48.93	70.13	67.2
Guess	60	60	233	13.18	56.72	45.84	51.57
Converged value	111.32	72.61	293.72	9.23	48.93	70.12	67.2

Region 4	mm			degrees			
	x	y	z	α	θ_1	θ_3	θ_5
Absolute error	0.01	0.01	0.01	0	0	0.01	0
Iterations	6						
True value	111.31	79.99	307.43	13.71	48.79	71.95	65.93
Guess	31	2	300	17.19	51.57	57.3	45.84
Converged value	111.32	79.98	307.43	13.71	48.8	71.95	65.94
Absolute error	0.01	0.01	0	0	0.01	0	0.01
Iterations	6						
True value	111.31	29.97	314.49	8.16	59.03	69.56	80.66
Guess	10	66	358	5.16	68.75	57.3	65.89
Converged value	111.3	29.97	314.49	8.16	59.03	69.56	80.66
Absolute error	0.01	0	0	0	0	0	0
Iterations	6						
True value	111.31	30.11	317.09	-14.77	64.34	66.06	83.43
Guess	10	90	285	-22.92	74.48	80.21	108.86
Converged value	111.31	30.13	317.08	-14.77	64.34	66.06	83.42
Absolute error	0	0.02	0.01	0	0	0	0.01
Iterations	7						
True value	111.31	69.59	320.08	-25.99	61.53	68.75	74.81
Guess	55	20	289	-34.38	68.75	68.75	85.94
Converged value	111.3	69.63	320.07	-25.98	61.52	68.74	74.8
Absolute error	0.01	0.04	0.01	0.01	0.01	0.01	0.01
Iterations	6						
Region 5	mm			degrees			
	x	y	z	α	θ_1	θ_3	θ_5
True value	111.31	122.76	303.03	10.49	43.06	70.27	56.29
Guess	20	60	260	14.9	57.3	57.3	57.3
Converged value	111.3	122.76	303.03	10.49	43.06	70.27	56.29
Absolute error	0.01	0	0	0	0	0	0
Iterations	6						
True value	111.31	104.07	286.88	26.66	37.2	70.33	54.55
Guess	150	120	222	32.09	42.4	85.94	40.11
Converged value	111.3	104.08	286.87	26.67	37.19	70.34	54.55

Region 5	mm			degrees			
	x	y	z	α	θ_1	θ_3	θ_5
Absolute error	0.01	0.01	0.01	0.01	0.01	0.01	0
Iterations	5						
True value	111.31	64.05	296.11	10.35	50.3	70.21	69.54
Guess	160	50	320	17.19	68.75	80.21	57.3
Converged value	111.31	64.05	296.11	10.35	50.31	70.21	69.55
Absolute error	0	0	0	0	0.01	0	0.01
Iterations	5						
True value	111.31	90.24	290.95	-7.7	50.87	68.72	65.42
Guess	148	78	369	-11.46	57.3	74.48	80.21
Converged value	111.31	90.23	290.96	-7.7	50.87	68.72	65.43
Absolute error	0	0.01	0.01	0	0	0	0.01
Iterations	6						
True value	111.31	97.23	289.98	-17.08	52.13	68.05	64.95
Guess	85	60	350	-18.33	68.75	74.48	80.21
Converged value	111.31	97.24	290	-17.09	52.13	68.04	64.95
Absolute error	0	0.01	0.02	0.01	0	0.01	0
Iterations	6						

Table A.17: Forward kinematic results for beta rotation and translation

Region 1	mm			degrees			
	x	y	z	β	θ_1	θ_3	θ_5
True value	133.68	-99.6	280.91	15.38	66.26	46.4	120.69
Guess	180	-55	354	5.73	5.61	35.52	105.42
Converged value	133.67	-99.6	280.91	15.38	66.26	46.4	120.86
Absolute error	0.02	0	0	0	0	0	0.17
Iterations	7						
True value	164.5	-85.91	282.78	12.68	57.78	44.08	115.28
Guess	200	-40	230	5.73	50.42	51.57	97.4
Converged value	164.46	-85.92	282.79	12.69	57.79	44.09	116.08
Absolute error	0.04	0.01	0.01	0.01	0.01	0.01	0.8
Iterations	6						

Region 1	mm			degrees			
	x	y	z	β	θ_1	θ_3	θ_5
True value	177.17	-94.51	280.85	-6.44	48.22	36.84	115.37
Guess	230	-10	360	11.46	51.57	25.78	95.11
Converged value	177.16	-94.5	280.86	-6.44	48.23	36.85	116.5
Absolute error	0.01	0.01	0.01	0	0.01	0.01	1.13
Iterations	6						
True value	141.4	-104.53	308.05	-9.91	59.83	43.79	116.12
Guess	100	-70	369	-5.73	44.69	25.78	127.2
Converged value	141.38	-104.54	308.05	-9.91	59.83	43.8	116.31
Absolute error	0.02	0.01	0	0	0	0.01	0.19
Iterations	5						
True value	140.14	-113.51	316.79	-15.87	59.15	43.08	116.75
Guess	200	-70	250	8.59	45.84	37.82	89.95
Converged value	140.12	-113.51	316.79	-15.87	59.15	43.08	116.89
Absolute error	0.02	0	0	0	0	0	0.14
Iterations	6						
Region 2	mm			degrees			
	x	y	z	β	θ_1	θ_3	θ_5
True value	159.84	-58.84	304.91	-15.24	52.48	44.18	105.08
Guess	220	-12	400	8.59	48.13	34.38	31.51
Converged value	159.81	-58.85	304.92	-15.22	52.49	44.19	105.35
Absolute error	0.03	0.01	0.01	0.02	0.01	0.01	0.27
Iterations	5						
True value	147.3	-55.31	327.04	-16.5	58.02	49.56	103.13
Guess	200	0	350	45.84	35.52	88.81	88.81
Converged value	147.32	-55.3	327.02	-16.51	58.01	49.56	103.24
Absolute error	0.02	0.01	0.02	0.01	0.01	0	0.11
Iterations	8						
True value	128.17	-71.14	307.24	-8.02	63.38	49.69	108.83
Guess	200	-10	399	-22.92	51.57	57.3	114.59
Converged value	128.16	-71.15	307.24	-8.02	63.39	49.69	108.86
Absolute error	0.01	0.01	0	0	0.01	0	0.03
Iterations	6						

Region 2	mm			degrees			
	x	y	z	β	θ_1	θ_3	θ_5
True value	149.18	-31.59	317.32	6.91	62.02	56.22	98.44
Guess	180	-60	350	8.02	68.75	68.75	91.67
Converged value	149.17	-31.6	317.32	6.92	62.02	56.22	98.54
Absolute error	0.01	0.01	0	0.01	0	0	0.1
Iterations	7						
True value	147.35	-28.99	316.28	7.99	62.37	56.93	97.84
Guess	150	-10	320	5.73	51.57	45.84	91.67
Converged value	147.34	-29	316.28	7.99	62.38	56.92	97.92
Absolute error	0.01	0.01	0	0	0.01	0.01	0.08
Iterations	5						
Region 3	mm			degrees			
	x	y	z	β	θ_1	θ_3	θ_5
True value	152.56	-4.41	297.08	-8.14	51.86	51.1	91.24
Guess	100	-50	200	-17.19	71.62	74.48	70.47
Converged value	152.56	-4.39	297.07	-8.14	51.86	51.1	91.25
Absolute error	0	0.02	0.01	0	0	0	0.01
Iterations	7						
True value	161.27	0.78	297.98	-19.62	46.21	46.32	89.79
Guess	82	36	369	25.78	34.38	31.51	75.63
Converged value	161.27	0.77	297.97	-19.64	46.21	46.32	89.79
Absolute error	0	0.01	0.01	0.02	0	0	0
Iterations	6						
True value	167.33	16.03	311.93	-24.02	45.24	47.26	86.05
Guess	0	50	295	-28.65	34.38	40.11	72.19
Converged value	167.35	16.04	311.91	-24.04	45.24	47.26	85.94
Absolute error	0.02	0.01	0.02	0.02	0	0	0.11
Iterations	6						
True value	119.78	25.1	305.46	11.34	61.7	67.81	82.59
Guess	150	0	260	11.46	51.57	51.57	74.48
Converged value	119.85	25.09	305.44	11.31	61.68	67.79	82.59
Absolute error	0.07	0.01	0.02	0.03	0.02	0.02	0
Iterations	5						

Region 3	mm			degrees			
	x	y	z	β	θ_1	θ_3	θ_5
True value	117.27	26.1	312	19.41	64.45	70.75	82.35
Guess	185	-10	280	22.92	57.3	57.3	68.75
Converged value	117.28	26.07	312	19.41	64.45	70.75	82.35
Absolute error	0.01	0.03	0	0	0	0	0
Iterations	6						
Region 4	mm			degrees			
	x	y	z	β	θ_1	θ_3	θ_5
True value	159.9	50.99	296.7	3.96	48.66	57.25	75.59
Guess	120	6	312	5.73	57.3	68.75	88.81
Converged value	159.87	50.99	296.72	3.98	48.67	57.26	75.28
Absolute error	0.03	0	0.02	0.02	0.01	0.01	0.31
Iterations	5						
True value	145.35	60.79	293.44	6.45	49.83	61.44	72.15
Guess	100	100	350	18.91	57.3	71.62	82.51
Converged value	145.38	60.78	293.43	6.44	49.82	61.43	71.96
Absolute error	0.03	0.01	0.01	0.01	0.01	0.01	0.19
Iterations	5						
True value	120.8	68.1	319.23	-12.08	52	65.29	72.99
Guess	196	30	387	-20.05	63.03	48.7	77.92
Converged value	120.83	68.1	319.22	-12.09	52	65.28	72.98
Absolute error	0.03	0	0.01	0.01	0	0.01	0.01
Iterations	5						
True value	125.83	73.89	329.36	-21.08	49.88	62.34	72.8
Guess	80	130	355	-34.38	68.75	63.03	76.2
Converged value	125.82	73.9	329.35	-21.08	49.88	62.34	72.79
Absolute error	0.01	0.01	0.01	0	0	0	0.01
Iterations	5						
True value	115.02	51.64	323.2	-7.95	56.62	67.73	77
Guess	35	20	266	-28.65	63.03	74.48	85.94
Converged value	114.99	51.66	323.21	-7.94	56.63	67.74	76.99
Absolute error	0.03	0.02	0.01	0.01	0.01	0.01	0.01
Iterations	6						

Region 5	mm			degrees			
	x	y	z	β	θ_1	θ_3	θ_5
True value	100.93	94.37	294.47	3.87	50.83	74.09	63.26
Guess	22	49	320	6.3	57.3	57.3	45.84
Converged value	100.92	94.38	294.47	3.87	50.83	74.09	63.23
Absolute error	0.01	0.01	0	0	0	0	0.03
Iterations	5						
True value	101.02	103.8	314.55	-4.79	50.73	73.14	64.04
Guess	166	150	277	2.86	68.75	80.21	50.42
Converged value	101.06	103.78	314.54	-4.81	50.73	73.13	64.02
Absolute error	0.04	0.02	0.01	0.02	0	0.01	0.02
Iterations	5						
True value	81.94	121.76	308.99	-5.86	49.09	77.4	60.08
Guess	174	66	266	-20.63	68.75	85.94	42.4
Converged value	81.95	121.77	308.99	-5.87	49.09	77.4	59.85
Absolute error	0.01	0.01	0	0.01	0	0	0.23
Iterations	6						
True value	105.77	113.46	282.27	10.39	46.69	73.01	56.36
Guess	221	80	250	0	57.3	57.3	44.12
Converged value	105.75	113.47	282.27	10.4	46.69	73.02	56.34
Absolute error	0.02	0.01	0	0.01	0	0.01	0.02
Iterations	7						
True value	125.16	118.16	299.55	-4.15	43.88	64.64	59.19
Guess	130	90	350	-51.57	51.57	57.3	45.84
Converged value	125.15	118.17	299.55	-4.15	43.88	64.64	59.13
Absolute error	0.01	0.01	0	0	0	0	0.06
Iterations	8						

A.6 Forward Kinematic Simulations – Guess Deviations Analysis

Table A.18 to Table A.23 presents the data obtained from the guess deviation analysis and was used to generate the graphs shown in Section 8.9.

Table A.18: Guess deviations and number of iterations for x, y and z values for translation

Guess deviation (mm)	Number of iterations		
	x	y	z
-250	8	8	Incorrect convergence
-200	7	7	Diverges
-150	6	6	Incorrect convergence
-100	5	5	6
-50	5	5	5
50	5	5	5
100	6	6	5
150	7	6	6
200	8	8	6
250	Incorrect convergence	Diverges	7

Table A.19: Guess deviations and number of iterations for θ_1 , θ_3 and θ_5 values for translation

Guess deviation (degrees)	Number of iterations		
	θ_1	θ_3	θ_5
-100	9	8	Diverges
-80	8	8	14
-60	6	6	6
-40	6	5	5
-20	5	5	5
20	5	5	5
40	Diverges	Diverges	6
60	10	Diverges	Incorrect convergence
80	Diverges	Diverges	Diverges
100	Diverges	13	Incorrect convergence

Table A.20: Guess deviations and number of iterations for x, y and z values for α rotation and translation

Guess deviation (mm)	Number of iterations		
	x	y	z
-100	6	7	Diverges
-80	6	6	7
-60	5	6	6
-40	5	5	5
-20	4	4	4
20	4	4	4
40	5	5	5
60	6	5	5
80	7	6	6
100	Diverges	6	6

Table A.21: Guess deviations and number of iterations for α , θ_1 , θ_3 and θ_5 values for α rotation and translation

Guess deviation (degrees)	Number of iterations			
	α	θ_1	θ_3	θ_5
-100	9	Incorrect convergence	Diverges	Diverges
-80	8	7	8	Incorrect convergence
-60	6	6	6	8
-40	5	6	6	6
-20	5	5	5	5
20	5	6	4	5
40	6	6	5	4
60	9	Diverges	7	6
80	Incorrect convergence	Incorrect convergence	Incorrect convergence	Incorrect convergence
100	Incorrect convergence	Incorrect convergence	Diverges	Incorrect convergence

Table A.22: Guess deviations and number of iterations for x, y and z values for β rotation and translation

Guess deviation (mm)	Number of iterations		
	x	y	z
-250	Incorrect convergence	Incorrect convergence	Diverges
-200	7	8	Incorrect convergence
-150	6	6	7
-100	5	5	6
-50	5	5	5
50	5	5	5
100	5	5	5
150	6	6	6
200	8	8	6
250	Diverges	Incorrect convergence	7

Table A.23: Guess deviations and number of iterations for β , θ_1 , θ_3 and θ_5 values for β rotation and translation

Guess deviation (degrees)	Number of iterations		
	β	θ_1 and θ_3	θ_5
-60	8	6	7
-50	7	6	6
-40	6	5	6
-30	6	5	5
-20	5	5	5
20	5	5	5
30	5	6	6
40	5	Incorrect convergence	6
50	6	Incorrect convergence	6
60	6	Diverges	7

A.7 Mouse Resolution

A.7.1 Aim

To determine the resolution and tolerance of using an OCM in conjunction with MATLAB® as a low-cost displacement sensor.

A.7.2 Apparatus

- Desktop computer
- MATLAB® software
- Arduino IDE software
- Linear displacement platform module
- OCM
- OCM mounting bracket

A.7.3 Methodology

A Dell U2413f computer monitor was used to track the location of the mouse cursor. A MATLAB® script printed mouse coordinates in terms of x and y positions at a specified sampling rate [164]. By using a linear displacement platform module, the distance was converted into millimeter per pixel values

The “Enhance pointer precision” option was turned off, as shown in Figure A.1, to eliminate mouse acceleration and produce more accurate results.

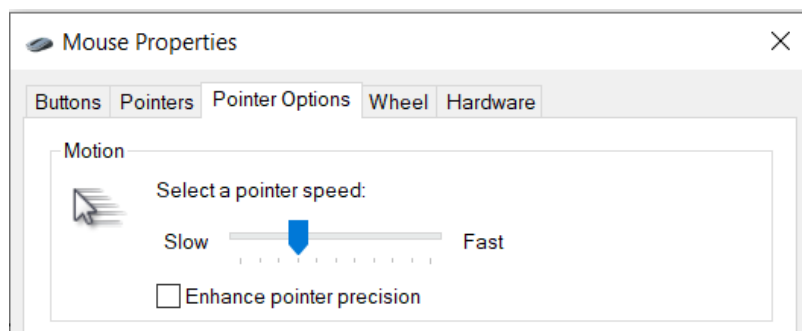


Figure A.1: The enhanced pointer precision option turned off

The steps below outline the procedure conducted.

1. Mount the OCM into the bracket to be attached to the linear displacement platform module.
2. Mount the optical mouse onto the linear displacement platform module in the configuration to test the y-axis movement.
3. Select various mouse speeds and move the mouse sensor over various distances with the linear displacement platform module. Record pixels traversed by the mouse.
4. Establish the resolutions at different speeds.
5. Repeat steps 2 to 4 now for the measurements along the x-axis.
6. Determine the optimum mouse speed.

A.7.4 Results

The pitch of the ball screw shaft was 5 mm therefore the stepper motor was programmed to perform a specific number of revolutions to meet the required linear displacements. Figure A.2. illustrates the different mounting orientations of the OCM and the linear displacement platform module.

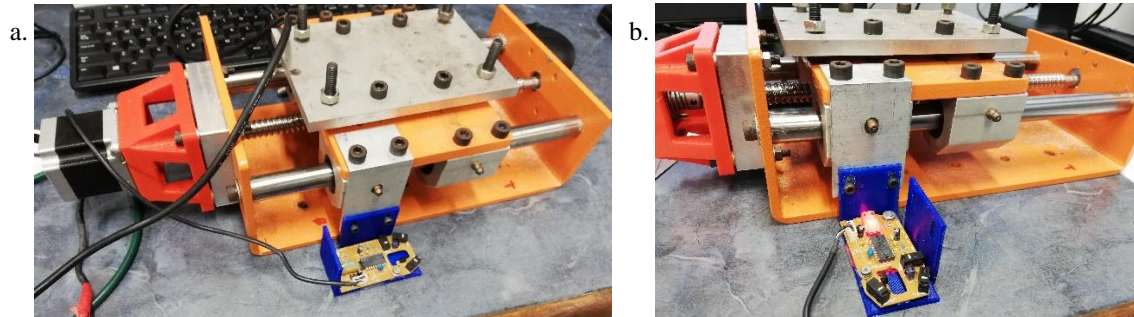


Figure A.2: Testing the OCM along the x and y axes

- a. Resolution testing along the y-axis
- b. Resolution testing along the x-axis

Table A.24 displays the summarised results of the OCM pixel resolution testing. Table A.25 shows the standard deviations from the mean pixels recorded.

Table A.24: A summary of results for the OCM pixel resolution testing

Mouse Speed	Direction	Average resolution (mm/pixel)	Average of X and Y average resolution
2	X	1.63	1.64
2	Y	1.64	
3	X	0.79	0.81
3	Y	0.82	
4	X	0.2	0.2
4	Y	0.2	
5	X	0.1	0.1
5	Y	0.1	
6	X	0.07	0.07
6	Y	0.07	

Table A.25: Standard deviations from the mean pixels recorded

Speed 2		
Distance (mm)	3 standard deviations X axis (pixels)	3 standard deviations Y axis (pixels)
5	0	1
10	1.06	1.92
15	1.45	1
20	1.57	1.21
40	2.26	2.66
Speed 3		
Distance (mm)	3 standard deviations X axis (pixels)	3 standard deviations Y axis (pixels)
5	0.97	0.9
10	1.54	1.73
15	1.13	0.95
20	0.9	2.12
40	2.12	1.22
Speed 4		
Distance (mm)	3 standard deviations X axis (pixels)	3 standard deviations Y axis (pixels)
5	2.15	1.78
10	3.17	3.42
15	5.41	3.09
20	4.53	2.12
40	5.32	5.07
Speed 5		
Distance (mm)	3 standard deviations X axis (pixels)	3 standard deviations Y axis (pixels)
5	3.44	3.36
10	6.81	3.56
15	8.05	4.11
20	10.3	4.7
40	8.9	8.61
Speed 6		
Distance (mm)	3 standard deviations X axis (pixels)	3 standard deviations Y axis (pixels)
5	7.61	4.3
10	12.21	4.9
15	17.54	9.48
20	17.89	7.72
40	15.7	13.18

A.7.5 Analysis

The mouse speed 2 was not considered because it did not yield a sub-millimeter resolution. Mouse speed 3 was not used because it produced a resolution of 0.81mm/pixel, which was close to 1 mm. Mouse speed 5 and 6 yielded sub-millimeter resolutions but the high sensitivity setting of the mouse required more monitor pixels than what was available and was therefore not used. Moreover, the standard deviations increase with mouse speed, as displayed in Table A.25. The three standard deviations from the mean showed a difference of approximately 5 pixels between speed 4 and speed 5 and showed a difference of approximately 12.5 pixels between speed 4 and speed 6. Speed 4 is the best trade-off between resolution and monitor size and between resolution and 3 standard deviations.

Three standard deviations from the mean for speed 4 is has a maximum number of 5.32 pixels at a travel distance of 40 mm. In perspective, this relates to a tolerance of 1.06 mm from the mean. The three standard deviations from the mean increases with distances therefore at distances travelled greater than 40 mm the deviation from the predicted value of the PKM's position may vary slightly more than 1.06 mm.

The advantages of using an OCM as a displacement sensor was that it was cost-effective and could easily interface with the computer. The OCM is readily available with short lead times to obtain one. One of the disadvantages was that it could only be used to measure translation of the end effector and not rotation. Another disadvantage was that brackets had to be specifically designed to house the sensor to test the resolution of the mouse and for the translation testing of the PKM. A linear displacement platform module was required to test the mouse resolution which is not freely available to all researchers. Another challenge using an OCM as a displacement sensor was that it only functioned appropriately when moving along a flat surface which required additional designs to the testing system to accommodate this.

A.7.6 Conclusion

The OCM proved to be a viable low-cost displacement sensor when used with MATLAB®. Speed 4 was the best speed setting and the pointer precision enhancement was turned off. A resolution of 0.2mm/pixel was obtained. A tolerance of 1.06 mm was carried forward for physical testing.

A.7.7 Testing Data for Mouse Resolution Testing

Table A.26 to Table A.35 presents the pixels obtained and resulting resolution from testing the OCM. The mouse was moved in increments of 5, 10, 15, 20 and 40 mm. The pixel position was recorded at the start of each movement and the pixel difference between incremental movements was recorded. The mouse was moved accurately in reality by the specified increments through the use of the linear displacement platform module.

Table A.26: Y-axis pixel displacements for Mouse Speed 2

5 mm	Δ Pixel	10 mm	Δ Pixel	15 mm	Δ Pixel	20 mm	Δ Pixel	40 mm	Δ Pixel
700	N/A	433	N/A	983	N/A	858	N/A	93	N/A
703	3	426	7	974	9	846	12	118	25
706	3	420	6	965	9	833	13		
709	3	414	6	956	9	821	12	904	N/A

5 mm	Δ Pixel	10 mm	Δ Pixel	15 mm	Δ Pixel	20 mm	Δ Pixel	40 mm	Δ Pixel
712	3			946	10	809	12	881	23
715	3	239	N/A	937	9			856	25
719	4	246	7			147	N/A		
722	3	251	5	40	N/A	159	12	38	N/A
725	3	257	6	49	9	172	13	63	25
728	3	263	6	58	9	184	12		
		269	6	67	9			1055	N/A
				76	9	1019	N/A	1031	24
						1007	12	1007	24
						995	12		
						983	12	21	N/A
						971	12	46	25
								69	23
Average	3.11		6.13		9.11		12.18		24.25
Resolution	1.61		1.63		1.65		1.64		1.65
Average Resolution	1.64								

Table A.27: Y-axis pixel displacements for Mouse Speed 3

5 mm	Δ Pixel	10 mm	Δ Pixel	15 mm	Δ Pixel	20 mm	Δ Pixel	40 mm	Δ Pixel
981	N/A	28	N/A	124	N/A	45	N/A	1075	N/A
975	6	41	13	142	18	69	24	1026	49
969	6	54	13	160	18	94	25		
963	6	66	12	178	18	117	23	181	N/A
957	6	78	12	196	18	142	25	230	49
950	7	90	12						
944	6	102	12	1104	N/A	1097	N/A	1065	N/A
938	6	114	12	1086	18	1073	24	1016	49
932	6	126	12	1068	18	1049	24	966	50
926	6			1050	18	1024	25		
920	6	1049	N/A	1032	18	1000	24	54	N/A
914	6	1037	12	1013	19	975	25	103	49
		1025	12	995	18			152	49
		1014	11						

5 mm	Δ Pixel	10 mm	Δ Pixel	15 mm	Δ Pixel	20 mm	Δ Pixel	40 mm	Δ Pixel
		1002	12						
		991	11						
Average	6.1		12		18.1		24.33		49.17
Resolution	0.82		0.83		0.83		0.82		0.81
Average Resolution	0.82								

Table A.28: Y-axis pixel displacements for Mouse Speed 4

5 mm	Δ Pixel	10 mm	Δ Pixel	15 mm	Δ Pixel	20 mm	Δ Pixel	40 mm	Δ Pixel
951	N/A	10	N/A	156	N/A	172	N/A	250	N/A
926	25	60	50	230	74	271	99	448	198
902	24	110	50	305	75	371	100		
877	25	161	51	379	74	470	99	105	N/A
853	24	210	49	453	74	568	98	304	199
829	24	259	49	527	74			497	193
805	24	308	49	600	73	1068	N/A		
780	25	355	47			969	99	1120	N/A
756	24	404	49	1066	N/A	871	98	923	197
731	25	453	49	992	74	773	98	726	197
706	25			918	74	674	99		
682	24	840	N/A	843	75	576	98	101	N/A
657	25	793	47	768	75			299	198
633	24	745	48	696	72			496	197
608	25	697	48	624	72				
584	24	648	49					973	N/A
560	24	599	49					777	196
537	23	551	48					580	197
513	24	504	47						
Average	24.33		48.69		73.83		98.67		196.89
Resolution	0.21		0.21		0.21		0.20		0.20
Average Resolution	0.20								

Table A.29: Y-axis pixel displacements for Mouse Speed 5

5 mm	Δ Pixel	10 mm	Δ Pixel	15 mm	Δ Pixel	20 mm	Δ Pixel	40 mm	Δ Pixel
1062	N/A	72	N/A	13	N/A	202	N/A	1061	N/A
1012	50	170	98	158	145	397	195	662	399
964	48	269	99	306	148	595	198	269	393
915	49	368	99	454	148	792	197		
866	49	466	98	600	146			388	
817	49	564	98	746	146	1115	N/A	785	397
768	49	663	99			921	194		
721	47	759	96	1082	N/A	723	198	995	N/A
673	48	856	97	933	149	526	197	603	392
624	49			785	148	330	196	207	396
578	46	966	N/A	638	147				
529	49	868	98			429	N/A	129	N/A
482	47	772	96	796	N/A	627	198	524	395
434	48	675	97	649	147	821	194	915	391
385	49	579	96	504	145	1017	196		
338	47	480	99						
288	50	381	99						
239	49	282	99						
Average	48.41		97.87		146.9		196.3		394.71
Resolution	0.10		0.10		0.10		0.10		0.10
Average Resolution	0.10								

Table A.30: Y-axis pixel displacements for Mouse Speed 6

5 mm	Δ Pixel	10 mm	Δ Pixel	15 mm	Δ Pixel	20 mm	Δ Pixel	40 mm	Δ Pixel
983	N/A	107	N/A	245	N/A	132	N/A	279	N/A
912	71	254	147	473	228	426	294	868	589
839	73	402	148	696	223	717	291		
765	74	550	148	920	224	1014	297	872	N/A
691	74	698	148	1144	224			273	599
615	76	846	148			906	N/A		
541	74	992	146	953	N/A	609	297	161	N/A
467	74	1137	145	731	222	316	293	749	588

5 mm	Δ Pixel	10 mm	Δ Pixel	15 mm	Δ Pixel	20 mm	Δ Pixel	40 mm	Δ Pixel
				510	221	24	292		
323	N/A	894	N/A	292	218			882	N/A
250	73	748	146	73	219	998	N/A	292	590
176	74	597	151			707	291		
105	71	450	147					1170	N/A
32	73	301	149					578	592
Average	73.36		147.55		222.38		293.57		591.6
Resolution	0.07		0.07		0.07		0.07		0.07
Average Resolution	0.07								

Table A.31: X-axis pixel displacements for Mouse Speed 2

5 mm	Δ Pixel	10 mm	Δ Pixel	15 mm	Δ Pixel	20 mm	Δ Pixel	40 mm	Δ Pixel
50	N/A	214	N/A	-1788	N/A	965	N/A	-935	N/A
53	3	220	6	-1797	9	952	13	-961	26
56	3	226	6	-1806	9	940	12		
59	3	232	6	-1816	10	927	13	-1101	N/A
62	3	239	7	-1825	9	914	13	-1076	25
65	3	245	6	-1835	10	902	12	-1052	24
68	3	251	6	-1844	9				
71	3	257	6			-783	N/A	-1145	N/A
74	3	263	6	719	N/A	-771	12	-1170	25
77	3	269	6	728	9	-759	12		
80	3					-747	12	-870	N/A
83	3			756	N/A	-734	13	-846	24
86	3			765	9	-722	12	-821	25
89	3			775	10	-709	13		
92	3			784	9				
Average	3		6.13		9.3		12.45		24.83
Resolution	1.67		1.63		1.61		1.61		1.61
Average Resolution	1.63								

Table A.32: X-axis pixel displacements for Mouse Speed 3

5 mm	Δ Pixel	10 mm	Δ Pixel	15 mm	Δ Pixel	20 mm	Δ Pixel	40 mm	Δ Pixel
-763	N/A	793	N/A	-877	N/A	-1162	N/A	1029	N/A
-769	6	781	12	-895	18	-1187	25	979	50
-775	6	768	13	-914	19	-1212	25	929	50
-781	6	755	13	-933	19	-1237	25		
-787	6	743	12	-952	19	-1262	25	943	N/A
-793	6	730	13	-971	19			993	50
-799	6	717	13	-990	19	959	N/A	1043	50
-805	6	705	12	-1009	19	983	24	1093	50
-812	7	692	13			1008	25		
-818	6	680	12	-912	N/A	1033	25	897	N/A
-824	6	667	13	-894	18	1058	25	848	49
-830	6			-875	19	1033	25	797	51
-836	6	920	N/A	-856	19	1058	25		
-843	7	932	12	-837	19	1083	25	1044	N/A
-849	6	944	12	-818	19			1093	49
-855	6	957	13	-799	19			1144	51
-861	6	970	13						
-867	6	982	12						
-873	6	995	13						
Average	6.11		12.56		18.84		24.91		50
Resolution	0.82		0.80		0.80		0.80		0.80
Average Resolution	0.80								

Table A.33: X-axis pixel displacements for Mouse Speed 4

5 mm	Δ Pixel	10 mm	Δ Pixel	15 mm	Δ Pixel	20 mm	Δ Pixel	40 mm	Δ Pixel
965	N/A	991	N/A	1432	N/A	1226	N/A	1053	N/A
941	24	1040	49	1505	73	1326	100	1256	203
916	25	1091	51	1580	75	1427	101	1456	200
892	24	1141	50			1529	102		
867	25	1192	51	805	N/A	1628	99	672	N/A
843	24	1243	51	733	72			469	203
819	24	1293	50	657	76	833	N/A	267	202

5 mm	Δ Pixel	10 mm	Δ Pixel	15 mm	Δ Pixel	20 mm	Δ Pixel	40 mm	Δ Pixel
794	25	1342	49	581	76	735	98		
770	24	1391	49	506	75	632	103	1129	N/A
745	25	1440	49	428	78	531	101	1331	202
720	25			352	76	431	100		
695	25	947	N/A	278	74	331	100	667	N/A
670	25	898	49					467	200
644	26	849	49					262	205
619	25	799	50						
594	25	748	51						
568	26	696	52						
544	24	646	50						
518	26	594	52						
493	25	544	50						
467	26	495	49						
Average	24.9		50.06		75		100.4 4		202.14
Resolution	0.20		0.20		0.20		0.20		0.20
Average Resolution	0.20								

Table A.34: X-axis pixel displacements for Mouse Speed 5

5 mm	Δ Pixel	10 mm	Δ Pixel	15 mm	Δ Pixel	20 mm	Δ Pixel	40 mm	Δ Pixel
832	N/A	767	N/A	272	N/A	27	N/A	309	N/A
881	49	670	97	125	147	-174	201	-87	396
930	49	572	98	-24	149	-377	203	-490	403
979	49	472	100	-178	154	-580	203		
1028	49	368	104	-328	150	-779	199	587	N/A
1078	50	267	101	-479	151	-976	197	989	402
1128	50	165	102	-629	150			1388	399
1177	49	62	103	-779	150	399	N/A		
1229	52	-39	101			596	197	1718	N/A
1280	51	-140	101	377	N/A	798	202	1316	402
1332	52	-236	96	522	145	1005	207	912	404
1382	50			675	153	1209	204		

5 mm	Δ Pixel	10 mm	Δ Pixel	15 mm	Δ Pixel	20 mm	Δ Pixel	40 mm	Δ Pixel
1432	50	314	N/A	824	149	1406	197		
1482	50	411	97	977	153				
1532	50	511	100	1126	149				
1584	52	609	98	1273	147				
1635	51	711	102	1419	146				
1684	49	812	101						
1733	49	915	103						
1783	50	1015	100						
1831	48	1116	101						
Average	49.95		100.28		149.5		201		401
Resolution	0.10		0.10		0.10		0.10		0.10
Average Resolution	0.10								

Table A.35: X-axis pixel displacements for Mouse Speed 6

5 mm	Δ Pixel	10 mm	Δ Pixel	15 mm	Δ Pixel	20 mm	Δ Pixel	40 mm	Δ Pixel
-57	N/A	532	N/A	282	N/A	145	N/A	1807	N/A
-128	71	676	144	477	195	436	291	1215	592
-199	71	816	140	681	204	730	294	625	590
-272	73	950	134	892	211	1015	285		
-344	72	1086	136	1098	206	1305	290	387	N/A
-413	69	1222	136	1310	212	1596	291	992	605
-483	70	1357	135	1517	207			1597	605
-553	70					1595	N/A		
-623	70	-261	N/A	1800	N/A	1300	295	-434	N/A
-697	74	-401	140	1589	211	1003	297	-1035	601
-769	72	-541	140	1377	212	700	303		
-842	73	-677	136	1166	211	401	299	189	N/A
-912	70	-818	141	951	215			795	606
-978	66	-963	145	739	212	1530	N/A	1392	597
-1044	66	-1107	144	540	199	1232	298		
-1110	66	-1243	136	328	212	930	302	1351	N/A
-1179	69	-1375	132			625	305	749	602
-1246	67					323	302	146	603

5 mm	Δ Pixel	10 mm	Δ Pixel	15 mm	Δ Pixel	20 mm	Δ Pixel	40 mm	Δ Pixel
								133	N/A
								733	600
								1332	599
Average	69.94		138.5		208.2 3077		296.3 0769		600
Resolution	0.07		0.07		0.07		0.07		0.07
Average Resolution	0.071								

Figure A.3 to Figure A.7 presents the 3 standard deviations of pixel measurements versus distance travelled.

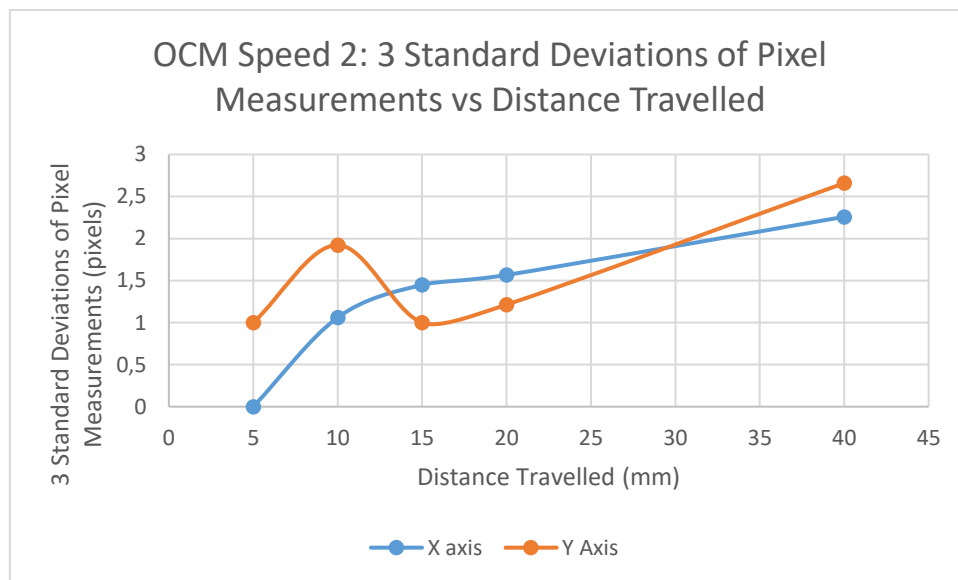


Figure A.3: Graph of OCM Speed 2: 3 Standard Deviations of Pixel Measurements vs. Distance Travelled

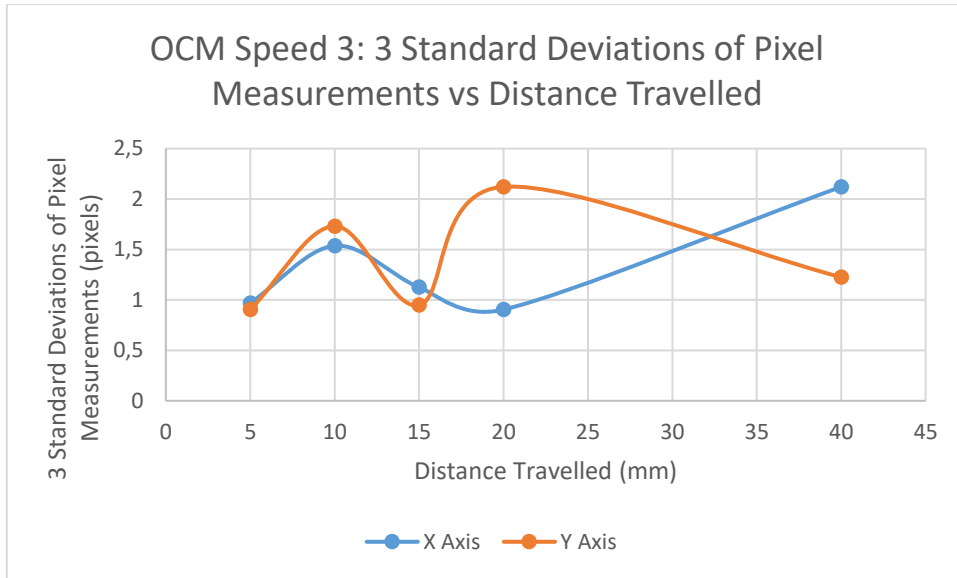


Figure A.4: Graph of OCM Speed 3: 3 Standard Deviations of Pixel Measurements vs. Distance Travelled

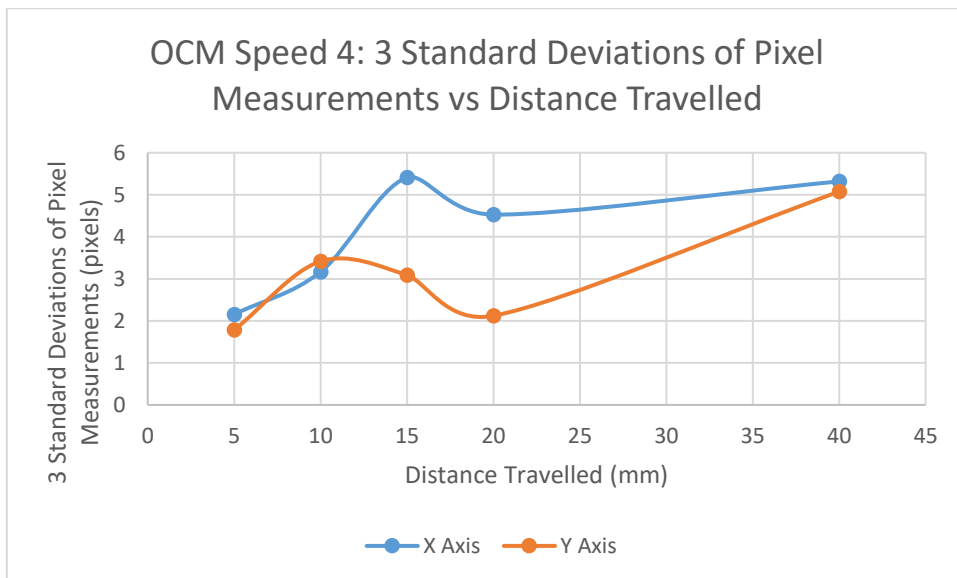


Figure A.5: Graph of OCM Speed 4: 3 Standard Deviations of Pixel Measurements vs. Distance Travelled

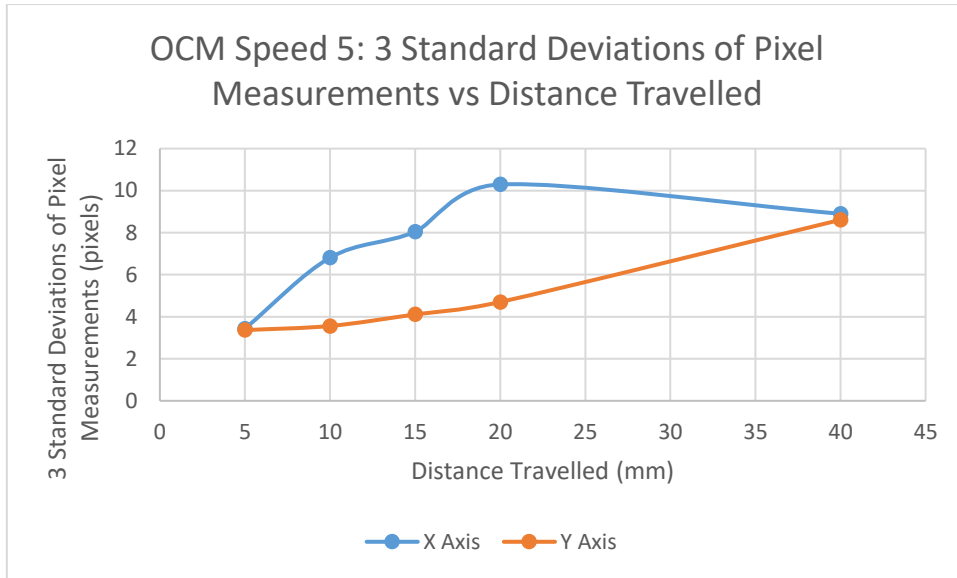


Figure A.6: Graph of OCM Speed 5: 3 Standard Deviations of Pixel Measurements vs. Distance Travelled

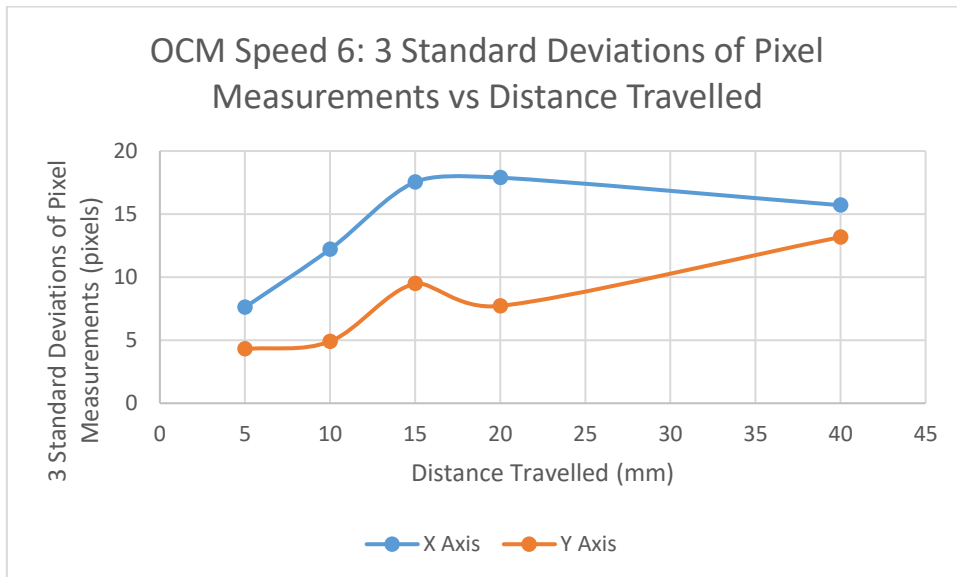


Figure A.7: Graph of OCM Speed 6: 3 Standard Deviations of Pixel Measurements vs. Distance Travelled

Appendix B – Code from Software

B.1 Inverse Kinematics: MATLAB® Code

B.1.1 Main script file

```
%Inverse kinematics of the 5 DOF PKM

%Inputs
d2r=pi/180;

alpha=20*d2r;
beta=0*d2r;
gamma=0*d2r;

xf=111.36;
yf=-53.27;
zf=311.04;

%End Effector inputs ('f' = final)
OPPORG=[xf; yf; zf];

ROP=RotationalMatrix(alpha,beta,gamma);

%Machine parameters
%Leg 1
PPDORG1=[-19.34; -33.50; 0];
OPAORG1=[-75; -129.9; 0];
AB1=[61.5; 0; 85]; %thrust bearing measurements
DC1=[43; 0; 40];
PPDORG1top=[-19.34; -33.50; 12];
PPDORG1bottom=[-19.34; -33.50; -12];

%Leg 2
PPDORG2=PPDORG1;
OPAORG2=OPAORG1;
AB2=[41.5; 0; 165]; % thrust bearing measurements
DC2=[63; 0; -40];
PPDORG2top=PPDORG1top;
PPDORG2bottom=PPDORG1bottom;

%Leg 3
PPDORG3=[-19.34; 33.50; 0];
OPAORG3=[-75; 129.9; 0];
AB3=AB1;
DC3=DC1;
PPDORG3top=[-19.34; 33.50; 12];
PPDORG3bottom=[-19.34; 33.50; -12];

%Leg 4
PPDORG4=PPDORG3;
OPAORG4=OPAORG3;
AB4=AB2;
DC4=DC2;
PPDORG4top=PPDORG3top;
PPDORG4bottom=PPDORG3bottom;

%Leg 5
PPDORG5=[38.69; -25; 0];
```

```

OPAORG5=[150; 0; 60];
AB5=[0; -40; 22.5];
DC5=[0; 15; 22.5];

%Leg 6
PPDORG6=[38.69; 25; 0];
OPAORG6=OPAORG5;
AB6=[0; 40; 22.5];
DC6=[0; -15; 22.5];

%%%%%%%%%%%%%%%%%%%%%%%%%%%%%%%%%%%%%%%%%%%%%%%%%%%%%%%%%%%%%%%%%%%%%%%%
%General Actuator 1 Calculations
%AD1 Calculation
AD1=OPPORG+(ROP*PPDORG1)-OPAORG1;
MagAD1=norm(AD1);

AD1top=OPPORG+(ROP*PPDORG1top)-OPAORG1;
MagAD1top=norm(AD1top);

AD1bottom=OPPORG+(ROP*PPDORG1bottom)-OPAORG1;
MagAD1bottom=norm(AD1bottom);

%Location of point D
xA1=sqrt((MagAD1^2)-(AD1(3,1))^2);
xzAD1=[xA1; 0; AD1(3,1)];

xA1top=sqrt((MagAD1top^2)-(AD1top(3,1))^2);
xzAD1top=[xA1top; 0; AD1top(3,1)];

xA1bottom=sqrt((MagAD1bottom^2)-(AD1bottom(3,1))^2);
xzAD1bottom=[xA1bottom; 0; AD1bottom(3,1)];

%General Actuator 2 Calculations
%AD2 Calculation
AD2=AD1;
AD2top=AD1top;
AD2bottom=AD1bottom;

MagAD2=MagAD1;
MagAD2top=MagAD1top;
MagAD2bottom=MagAD1bottom;

%Location of point D
xA2=xA1;
xzAD2=xzAD1;

xA2top=xA1top;
xzAD2top=xzAD1top;

xA2bottom=xA1bottom;
xzAD2bottom=xzAD1bottom;

%General Actuator 3 Calculations
%AD3 Calculation
AD3=OPPORG+(ROP*PPDORG3)-OPAORG3;
MagAD3=norm(AD3);

```

```

AD3top=OPPORG+ (ROP*PPDORG3top) -OPAORG3;
MagAD3top=norm (AD3top);

AD3bottom=OPPORG+ (ROP*PPDORG3bottom) -OPAORG3;
MagAD3bottom=norm (AD3bottom);

%Location of point D
xA3=sqrt ( (MagAD3^2) - (AD3 (3,1)) ^2);
xzAD3=[xA3; 0; AD3 (3,1)];

xA3top=sqrt ( (MagAD3top^2) - (AD3top (3,1)) ^2);
xzAD3top=[xA3top; 0; AD3top (3,1)];

xA3bottom=sqrt ( (MagAD3bottom^2) - (AD3bottom (3,1)) ^2);
xzAD3bottom=[xA3bottom; 0; AD3bottom (3,1)];

%General Actuator 4 Calculations
%AD3 Calculation
AD4=AD3;
AD4top=AD3top;
AD4bottom=AD3bottom;

MagAD4=MagAD3;
MagAD4top=MagAD3top;
MagAD4bottom=MagAD3bottom;

%Location of point D
xA4=xA3;
xzAD4=xzAD3;

xA4top=xA3top;
xzAD4top=xzAD3top;

xA4bottom=xA3bottom;
xzAD4bottom=xzAD3bottom;

%General Actuator 5 Calculations
%AD5 Calculation
AD5=OPPORG+ (ROP*PPDORG5) -OPAORG5;
MagAD5=norm (AD5);

%Location of point D
zA5=sqrt ( (MagAD5^2) - (AD5 (2,1)) ^2);
yzAD5=[0; AD5 (2,1); zA5];

%General Actuator 6 Calculations
%AD6 Calculation
AD6=OPPORG+ (ROP*PPDORG6) -OPAORG6;
MagAD6=norm (AD6);

%Location of point D
zA6=sqrt ( (MagAD6^2) - (AD6 (2,1)) ^2);
yzAD6=[0; AD6 (2,1); zA6];

%%%%%%%%%%%%%%%%%%%%%%%%%%%%%%%%%%%%%%%%%%%%%%%%%%%%%%%%%%%%%%%%%%%%%%%%
%Leg lengths by Cases
if beta>0 %12bracket leans Forward and 34bracket leans Forward

```

```

[Length1,Length2]=PosGrad12(d2r,xzAD1top,xzAD1bottom,DC1,xzAD1,AB1,DC2,xzAD
2,AB2);

[Length3,Length4]=PosGrad34(d2r,xzAD3top,xzAD3bottom,DC3,xzAD3,AB3,DC4,xzAD
4,AB4);

    BC5=yzAD5-AB5-DC5;
    Length5=norm(BC5);

    BC6=yzAD6-AB6-DC6;
    Length6=norm(BC6);

elseif beta <0 %12bracket leans Backward and 34bracket leans Backward

[Length1,Length2]=NegGrad12(d2r,xzAD1top,xzAD1bottom,DC1,xzAD1,AB1,DC2,xzAD
2,AB2);

[Length3,Length4]=NegGrad34(d2r,xzAD3top,xzAD3bottom,DC3,xzAD3,AB3,DC4,xzAD
4,AB4);

    BC5=yzAD5-AB5-DC5;
    Length5=norm(BC5);

    BC6=yzAD6-AB6-DC6;
    Length6=norm(BC6);

elseif alpha >0
    gradient12=(xzAD1top(3,1)-xzAD1bottom(3,1))/(xzAD1top(1,1)-
xzAD1bottom(1,1));
    gradient34=(xzAD3top(3,1)-xzAD3bottom(3,1))/(xzAD3top(1,1)-
xzAD3bottom(1,1));

    [Length5,Length6]=PosGrad56(alpha,d2r,DC5,yzAD5,AB5,DC6,yzAD6,AB6);

    if gradient12>0 && gradient34>0 %12bracket leans Forward and 34bracket
leans Forward

[Length1,Length2]=PosGrad12(d2r,xzAD1top,xzAD1bottom,DC1,xzAD1,AB1,DC2,xzAD
2,AB2);

[Length3,Length4]=PosGrad34(d2r,xzAD3top,xzAD3bottom,DC3,xzAD3,AB3,DC4,xzAD
4,AB4);

        elseif gradient12<0 && gradient34>0 %12bracket leans Backward and
34bracket leans Forward

[Length1,Length2]=NegGrad12(d2r,xzAD1top,xzAD1bottom,DC1,xzAD1,AB1,DC2,xzAD
2,AB2);

[Length3,Length4]=PosGrad34(d2r,xzAD3top,xzAD3bottom,DC3,xzAD3,AB3,DC4,xzAD
4,AB4);

        elseif gradient12<0 && gradient34<0 %12bracket leans Backward and
34bracket leans Backward

[Length1,Length2]=NegGrad12(d2r,xzAD1top,xzAD1bottom,DC1,xzAD1,AB1,DC2,xzAD
2,AB2);

```

```
[Length3,Length4]=NegGrad34 (d2r,xzAD3top,xzAD3bottom,DC3,xzAD3,AB3,DC4,xzAD4,AB4);
```

```
elseif xzAD1top(1,1) == xzAD1bottom(1,1) %12bracket stands Upright and 34bracket leans Forward
```

```
BC1=xzAD1-AB1-DC1;
Length1=norm(BC1);
```

```
BC2=xzAD2-AB2-DC2;
Length2=norm(BC2);
```

```
[Length3,Length4]=PosGrad34 (d2r,xzAD3top,xzAD3bottom,DC3,xzAD3,AB3,DC4,xzAD4,AB4);
```

```
elseif xzAD3top(1,1) == xzAD3bottom(1,1) %12bracket leans Backward and 34bracket stands Upright
```

```
[Length1,Length2]=NegGrad12 (d2r,xzAD1top,xzAD1bottom,DC1,xzAD1,AB1,DC2,xzAD2,AB2);
```

```
BC3=xzAD3-AB3-DC3;
Length3=norm(BC3);
```

```
BC4=xzAD4-AB4-DC4;
Length4=norm(BC4);
```

```
end
```

```
elseif alpha<0
```

```
gradient12=(xzAD1top(3,1)-xzAD1bottom(3,1))/(xzAD1top(1,1)-xzAD1bottom(1,1));
```

```
gradient34=(xzAD3top(3,1)-xzAD3bottom(3,1))/(xzAD3top(1,1)-xzAD3bottom(1,1));
```

```
[Length5,Length6]=NegGrad56 (alpha,d2r,DC5,yzAD5,AB5,DC6,yzAD6,AB6);
```

```
if gradient12>0 && gradient34<0 %12bracket leans Forward and 34bracket leans Backward
```

```
[Length1,Length2]=PosGrad12 (d2r,xzAD1top,xzAD1bottom,DC1,xzAD1,AB1,DC2,xzAD2,AB2);
```

```
[Length3,Length4]=NegGrad34 (d2r,xzAD3top,xzAD3bottom,DC3,xzAD3,AB3,DC4,xzAD4,AB4);
```

```
elseif gradient12>0 && gradient34>0 %12bracket leans Forward and 34bracket leans Forward
```

```
[Length1,Length2]=PosGrad12 (d2r,xzAD1top,xzAD1bottom,DC1,xzAD1,AB1,DC2,xzAD2,AB2);
```

```
[Length3,Length4]=PosGrad34 (d2r,xzAD3top,xzAD3bottom,DC3,xzAD3,AB3,DC4,xzAD4,AB4);
```

```
elseif gradient12<0 && gradient34<0 %12bracket leans Backward and 34bracket leans Backward
```

```
[Length1,Length2]=NegGrad12(d2r,xzAD1top,xzAD1bottom,DC1,xzAD1,AB1,DC2,xzAD2,AB2);
```

```
[Length3,Length4]=NegGrad34(d2r,xzAD3top,xzAD3bottom,DC3,xzAD3,AB3,DC4,xzAD4,AB4);
```

```
elseif xzAD1top(1,1) == xzAD1bottom(1,1) %12bracket stands Upright and 34bracket leans Backward
```

```
    %Length1
    BC1=xzAD1-AB1-DC1;
    Length1=norm(BC1);
```

```
    %Length2
    BC2=xzAD2-AB2-DC2;
    Length2=norm(BC2);
```

```
[Length3,Length4]=NegGrad34(d2r,xzAD3top,xzAD3bottom,DC3,xzAD3,AB3,DC4,xzAD4,AB4);
```

```
elseif xzAD3top(1,1) == xzAD3bottom(1,1) %12bracket leans Forward and 34bracket stands Upright
```

```
[Length1,Length2]=PosGrad12(d2r,xzAD1top,xzAD1bottom,DC1,xzAD1,AB1,DC2,xzAD2,AB2);
```

```
    BC3=xzAD3-AB3-DC3;
    Length3=norm(BC3);
```

```
    BC4=xzAD4-AB4-DC4;
    Length4=norm(BC4);
```

```
end
```

```
elseif beta==0 && alpha==0
```

```
    %Inner Vector loops
```

```
    %Length1
    BC1=xzAD1-AB1-DC1;
    Length1=norm(BC1);
```

```
    %Length2
    BC2=xzAD2-AB2-DC2;
    Length2=norm(BC2);
```

```
    %Length3
    BC3=xzAD3-AB3-DC3;
    Length3=norm(BC3);
```

```
    %Length4
    BC4=xzAD4-AB4-DC4;
    Length4=norm(BC4);
```

```
    %Length5
    BC5=yzAD5-AB5-DC5;
    Length5=norm(BC5);
```

```
    %Length6
    BC6=yzAD6-AB6-DC6;
    Length6=norm(BC6);
```

```
end
```

B.1.2 Function file – Rotational Matrix

```
function [ROP]=RotationalMatrix(alpha,beta,gamma)
ROP=[cos(gamma)*cos(beta) (cos(gamma)*sin(beta)*sin(alpha))-
(sin(gamma)*cos(alpha))
(cos(gamma)*sin(beta)*cos(alpha))+(sin(gamma)*sin(alpha));...
sin(gamma)*cos(beta)
(sin(gamma)*sin(beta)*sin(alpha))+(cos(gamma)*cos(alpha))
(sin(gamma)*sin(beta)*cos(alpha))-(cos(gamma)*sin(alpha));...
-sin(beta) cos(beta)*sin(alpha) cos(beta)*cos(alpha)];
end
```

B.1.3 Function file – Negative gradient of the Joint D bracket for leg 1 and 2

```
function
[Length1,Length2]=NegGrad12(d2r,xzAD1top,xzAD1bottom,DC1,xzAD1,AB1,DC2,xzAD
2,AB2)
    %Length1
    gradient12=(xzAD1top(3,1)-xzAD1bottom(3,1))/(xzAD1top(1,1)-
xzAD1bottom(1,1));
    radgradient12=atan(gradient12);
    deggradient12=radgradient12/d2r+180;

    MagDC1 = sqrt((DC1(1,1)^2)+(DC1(3,1))^2);
    gradientDC1=(DC1(3,1))/(DC1(1,1));
    radinnerangleDC1=atan(gradientDC1);
    deginnerangleDC1=90-radinnerangleDC1/d2r;

    theta1=deggradient12-deginnerangleDC1;
    DC1rotated=[MagDC1*cos(theta1*d2r); 0; MagDC1*sin(theta1*d2r)]

    BC1=xzAD1-AB1-DC1rotated;

    Length1=norm(BC1);

    %Length2
    MagDC2 = sqrt((DC2(1,1)^2)+(DC2(3,1))^2);
    gradientDC2=(DC2(3,1))/(DC2(1,1));
    radinnerangleDC2=atan(gradientDC2);
    deginnerangleDC2=90+radinnerangleDC2/d2r;

    theta2=180-deggradient12-deginnerangleDC2;
    DC2rotated=[MagDC2*cos(theta2*d2r); 0; -MagDC2*sin(theta2*d2r)]

    BC2=xzAD2-AB2-DC2rotated;

    Length2=norm(BC2);
end
```

B.1.4 Function file – Negative gradient of the Joint D bracket for leg 3 and 4

```
function
[Length3,Length4]=NegGrad34(d2r,xzAD3top,xzAD3bottom,DC3,xzAD3,AB3,DC4,xzAD
4,AB4)
    %Length3
    gradient34=(xzAD3top(3,1)-xzAD3bottom(3,1))/(xzAD3top(1,1)-
xzAD3bottom(1,1));
    radgradient34=atan(gradient34);
```

```

deggradient34=radgradient34/d2r+180;

MagDC3 = sqrt((DC3(1,1)^2)+(DC3(3,1))^2);
gradientDC3=(DC3(3,1))/(DC3(1,1));
radinnerangleDC3=atan(gradientDC3);
deginnerangleDC3=90-radinnerangleDC3/d2r;

theta3=deggradient34-deginnerangleDC3;
DC3rotated=[MagDC3*cos(theta3*d2r); 0; MagDC3*sin(theta3*d2r)]

BC3=xzAD3-AB3-DC3rotated;

Length3=norm(BC3);

%Length4
MagDC4 = sqrt((DC4(1,1)^2)+(DC4(3,1))^2);
gradientDC4=(DC4(3,1))/(DC4(1,1));
radinnerangleDC4=atan(gradientDC4);
deginnerangleDC4=90+radinnerangleDC4/d2r;

theta4=180-deggradient34-deginnerangleDC4;
DC4rotated=[MagDC4*cos(theta4*d2r); 0; -MagDC4*sin(theta4*d2r)]

BC4=xzAD4-AB4-DC4rotated;

Length4=norm(BC4);
end

```

B.1.5 Function file – Negative gradient of the end effector for alpha rotations

```

function [Length5,Length6]=NegGrad56(alpha,d2r,DC5,yzAD5,AB5,DC6,yzAD6,AB6)
%Length 5
deggradient56=90+alpha/d2r;

MagDC5 = sqrt((DC5(2,1)^2)+(DC5(3,1))^2);
gradientDC5=(DC5(3,1))/(DC5(2,1));
radinnerangleDC5=atan(gradientDC5);
deginnerangleDC5=90-radinnerangleDC5/d2r;

theta5=deggradient56-deginnerangleDC5;
DC5rotated=[0; MagDC5*cos(theta5*d2r); MagDC5*sin(theta5*d2r)]

BC5=yzAD5-AB5-DC5rotated;
Length5=norm(BC5);

%Length 6
MagDC6=MagDC5;
gradientDC6=(DC6(3,1))/(DC6(2,1));
radinnerangleDC6=atan(gradientDC6);
deginnerangleDC6=radinnerangleDC6/d2r;

theta6=-(deginnerangleDC6+alpha/d2r);
DC6rotated=[0; -MagDC6*cos(theta6*d2r); MagDC6*sin(theta6*d2r)]

BC6=yzAD6-AB6-DC6rotated;
Length6=norm(BC6);
end

```


B.1.6 Function file – Positive gradient of the Joint D bracket for leg 1 and 2

```
function
[Length1,Length2]=PosGrad12(d2r,xzAD1top,xzAD1bottom,DC1,xzAD1,AB1,DC2,xzAD
2,AB2)
%Actuator 1
%Top Bracket gradient calculation
gradient12=(xzAD1top(3,1)-xzAD1bottom(3,1))/(xzAD1top(1,1)-
xzAD1bottom(1,1));
radgradient12=atan(gradient12);
deggradient12=radgradient12/d2r;

MagDC1 = sqrt((DC1(1,1)^2)+(DC1(3,1))^2);
gradientDC1=(DC1(3,1))/(DC1(1,1));
radinnerangleDC1=atan(gradientDC1);
deginnerangleDC1=90-radinnerangleDC1/d2r;

theta1=deggradient12-deginnerangleDC1;
DC1rotated=[MagDC1*cos(theta1*d2r); 0; MagDC1*sin(theta1*d2r)]

%Vector loop within a loop
BC1=xzAD1-AB1-DC1rotated;

%Final Actuator Length
Length1=norm(BC1);

%%%%%%%%%%%%%%%%%%%%%%%%%%%%%%%%%%%%%%%%%%%%%%%%%%%%%%%%%%%%%%%%%%%%%%%%
%Actuator 2
%Altered vector DC2
MagDC2 = sqrt((DC2(1,1)^2)+(DC2(3,1))^2);
gradientDC2=(DC2(3,1))/(DC2(1,1));
radinnerangleDC2=atan(gradientDC2);
deginnerangleDC2=90+radinnerangleDC2/d2r;

theta2=180-deggradient12-deginnerangleDC2;
DC2rotated=[MagDC2*cos(theta2*d2r); 0; -MagDC2*sin(theta2*d2r)]

%Vector loop within a loop
BC2=xzAD2-AB2-DC2rotated;

%Final Actuator Length
Length2=norm(BC2);
end
```

B.1.7 Function file – Positive gradient of the Joint D bracket for leg 3 and 4

```
function
[Length3,Length4]=PosGrad34(d2r,xzAD3top,xzAD3bottom,DC3,xzAD3,AB3,DC4,xzAD
4,AB4)
%Actuator 3 Length Calculations
%Top Bracket gradient calculation
gradient34=(xzAD3top(3,1)-xzAD3bottom(3,1))/(xzAD3top(1,1)-
xzAD3bottom(1,1));
radgradient34=atan(gradient34);
deggradient34=radgradient34/d2r;

%Altered vector DC3
MagDC3 = sqrt((DC3(1,1)^2)+(DC3(3,1))^2);
gradientDC3=(DC3(3,1))/(DC3(1,1));
```

```

radinnerangleDC3=atan (gradientDC3);
deginnerangleDC3=90-radinnerangleDC3/d2r;

theta3=deggradient34-deginnerangleDC3;
DC3rotated=[MagDC3*cos (theta3*d2r); 0; MagDC3*sin (theta3*d2r)]

%Vector loop within a loop
BC3=xzAD3-AB3-DC3rotated;

%Final Actuator Length
Length3=norm (BC3);

%%%%%%%%%%%%%%%%%%%%%%%%%%%%%%%%%%%%%%%%%%%%%%%%%%%%%%%%%%%%%%%%%%%%%%%%
%Actuator 4
%Altered vector DC4
MagDC4 = sqrt ((DC4 (1,1) ^2)+(DC4 (3,1) ) ^2);
gradientDC4=(DC4 (3,1) ) / (DC4 (1,1) );
radinnerangleDC4=atan (gradientDC4);
deginnerangleDC4=90+radinnerangleDC4/d2r;

theta4=180-deggradient34-deginnerangleDC4;
DC4rotated=[MagDC4*cos (theta4*d2r); 0; -MagDC4*sin (theta4*d2r)]

%Vector loop within a loop
BC4=xzAD4-AB4-DC4rotated;

%Final Actuator Length
Length4=norm (BC4);
end

```

B.1.8 Function file – Positive gradient of the end effector for alpha rotations

```

function [Length5,Length6]=PosGrad56 (alpha,d2r,DC5,yzAD5,AB5,DC6,yzAD6,AB6)
%Length 5
deggradient56=alpha/d2r;

MagDC5 = sqrt ((DC5 (2,1) ^2)+(DC5 (3,1) ) ^2);
gradientDC5=(DC5 (3,1) ) / (DC5 (2,1) );
radinnerangleDC5=atan (gradientDC5);
deginnerangleDC5=90-radinnerangleDC5/d2r;

theta5=90-deginnerangleDC5+deggradient56;
DC5rotated=[0; MagDC5*cos (theta5*d2r); MagDC5*sin (theta5*d2r)]

BC5=yzAD5-AB5-DC5rotated;
Length5=norm (BC5);

%Length 6
MagDC6=MagDC5;
gradientDC6=(DC6 (3,1) ) / (DC6 (2,1) );
radinnerangleDC6=atan (gradientDC6);
deginnerangleDC6=radinnerangleDC6/d2r;

theta6=- (deginnerangleDC6+ (alpha/d2r) );
DC6rotated=[0; -MagDC6*cos (theta6*d2r); MagDC6*sin (theta6*d2r)]

BC6=yzAD6-AB6-DC6rotated;

```

```
    Length6=norm(BC6);  
end
```

B.1.9 Mouse tracker code

```
t = timer('ExecutionMode', 'fixedRate', ...  
         'Period', 0.1, ... %Sampling rate  
         'TasksToExecute', 900, ...  
         'TimerFcn', @(~,~) fprintf('(X, Y) = (%g, %g)\n', get(0,  
'PointerLocation')));  
start(t); %will display mouse movements for 90 seconds
```

B.2 Inverse Kinematics: Arduino Code

```
// MultiStepper.pde

// -*- mode: C++ -*-

// Use MultiStepper class to manage multiple steppers and make them all move to
// the same position at the same time for linear 2d (or 3d) motion.

#include <AccelStepper.h>

#include <MultiStepper.h> //The Multistepper is a sub-class of the AccelStepper library therefore only called
after the AccelStepper library

// EG X-Y position bed driven by two steppers

AccelStepper stepper1(1,2,3); //The first value in brackets '1' means that a driver is being used to power the
stepper, The 2nd (CLK) and 3rd (CW) values are the PWM pins on the Arduino.

AccelStepper stepper2(1,4,5);

AccelStepper stepper3(1,6,7);

AccelStepper stepper4(1,8,9);

AccelStepper stepper5(1,10,11);

AccelStepper stepper6(1,12,13);

// Up to 10 steppers can be handled as a group by MultiStepper
MultiStepper steppers;

void setup() {
  Serial.begin(9600);

  // Configure each stepper
  stepper1.setMaxSpeed(200); //Steps per second
  stepper2.setMaxSpeed(200);
  stepper3.setMaxSpeed(200);
  stepper4.setMaxSpeed(200);
  stepper5.setMaxSpeed(200);
  stepper6.setMaxSpeed(200);

  // Then give them to MultiStepper to manage
```

```
steppers.addStepper(stepper1);
steppers.addStepper(stepper2);
steppers.addStepper(stepper3);
steppers.addStepper(stepper4);
steppers.addStepper(stepper5);
steppers.addStepper(stepper6);
}

void loop() {
  long positions[6]; // Array of stepper positions

  positions[0] = -5582; //references to a coordinate
  positions[1] = -5582;
  positions[2] = -5549;
  positions[3] = -5549;
  positions[4] = -9254;
  positions[5] = -9254;
  steppers.moveTo(positions);
  steppers.runSpeedToPosition(); // Blocks until all are in position
```

B.3 Forward kinematics MATLAB® Code

B.3.1 Translation

```
syms OPx OPy OPz theta1 theta3 theta5

d2r=pi/180;
alpha = 0;
beta = 0;

%User leg length inputs
length1=216.78;
length3=240.5;
length5=204.12;

%Constants of the system
%Parameters from equation 1 (for first pair of legs)
PD12x=-19.34;
PD12y=-33.50;
PD12z=0;

OA12x=-75;
OA12y=-129.9;
OA12z=0;

%Parameters from equation 2 (for second pair of legs)
PD34x=-19.34;
PD34y=33.50;
PD34z=0;

OA34x=-75;
OA34y=129.9;
OA34z=0;

%Parameters from equation 3 (for third pair of legs)
OA56x=150;
OA56y=0;
OA56z=60;

PDv1x=38.69;
PDv1y=0;
PDv1z=0;

%Functions
F1=(OPx+cos(beta)*PD12x+sin(beta)*sin(alpha)*PD12y+sin(beta)*cos(alpha)*PD12z-OA12x)^2 ...
    +(OPy+cos(alpha)*PD12y-sin(alpha)*PD12z-OA12y)^2 ...
    +(OPz-
sin(beta)*PD12x+cos(beta)*sin(alpha)*PD12y+cos(beta)*cos(alpha)*PD12z-OA12z)^2 ...
    -
    (((length1*cos(theta1)+61.5+43)^2)+((length1*sin(theta1)+85+40)^2));

F2=(OPx+cos(beta)*PD34x+sin(beta)*sin(alpha)*PD34y+sin(beta)*cos(alpha)*PD34z-OA34x)^2 ...
    +(OPy+cos(alpha)*PD34y-sin(alpha)*PD34z-OA34y)^2 ...
    +(OPz-
sin(beta)*PD34x+cos(beta)*sin(alpha)*PD34y+cos(beta)*cos(alpha)*PD34z-OA34z)^2 ...
    -
    (((length3*cos(theta3)+61.5+43)^2)+((length3*sin(theta3)+85+40)^2));
```

```

F3=(OPx+cos(beta)*PDvlx+sin(beta)*sin(alpha)*PDvly+sin(beta)*cos(alpha)*PDv
lz-OA56x)^2 ...
    +(OPy+cos(alpha)*PDvly-sin(alpha)*PDvlz-OA56y)^2 ...
    +(OPz-
sin(beta)*PDvlx+cos(beta)*sin(alpha)*PDvly+cos(beta)*cos(alpha)*PDvlz-
OA56z)^2 ...
    - (((length5*cos(theta5)+40-
40)^2)+((length5*sin(theta5)+22.5+22.5)^2));

F4=85+length1*sin(theta1)+40-OPz

F5=85+length3*sin(theta3)+40-OPz

F6=length5*cos(theta5)-OPy

F=[F1; F2; F3; F4; F5; F6]

U=[OPx; OPy; OPz; theta1; theta3; theta5]

j=jacobian(F,U)

V=[double(input('Please enter the initial guess for OPx ')),...
    double(input('Please enter the initial guess for OPy ')),...
    double(input('Please enter the initial guess for OPz ')),...
    double(input('Please enter the initial guess for theta1 in radians
')),...
    double(input('Please enter the initial guess for theta3 in radians
')),...
    double(input('Please enter the initial guess for theta5 in radians
'))]

i=0;
delta=100;
while (delta>1e-6)

    FnValues=[double(subs(F(1,1),U,V)),...
              double(subs(F(2,1),U,V)),...
              double(subs(F(3,1),U,V)),...
              double(subs(F(4,1),U,V)),...
              double(subs(F(5,1),U,V)),...
              double(subs(F(6,1),U,V))]

    jac=[double(subs(j(1,1),U,V)), double(subs(j(1,2),U,V)),
double(subs(j(1,3),U,V)), double(subs(j(1,4),U,V)),
double(subs(j(1,5),U,V)), double(subs(j(1,6),U,V));...
        double(subs(j(2,1),U,V)), double(subs(j(2,2),U,V)),
double(subs(j(2,3),U,V)), double(subs(j(2,4),U,V)),
double(subs(j(2,5),U,V)), double(subs(j(2,6),U,V));...
        double(subs(j(3,1),U,V)), double(subs(j(3,2),U,V)),
double(subs(j(3,3),U,V)), double(subs(j(3,4),U,V)),
double(subs(j(3,5),U,V)), double(subs(j(3,6),U,V));...
        double(subs(j(4,1),U,V)), double(subs(j(4,2),U,V)),
double(subs(j(4,3),U,V)), double(subs(j(4,4),U,V)),
double(subs(j(4,5),U,V)), double(subs(j(4,6),U,V));...
        double(subs(j(5,1),U,V)), double(subs(j(5,2),U,V)),
double(subs(j(5,3),U,V)), double(subs(j(5,4),U,V)),
double(subs(j(5,5),U,V)), double(subs(j(5,6),U,V));...

```

```

        double(subs(j(6,1),U,V)), double(subs(j(6,2),U,V)),
double(subs(j(6,3),U,V)), double(subs(j(6,4),U,V)),
double(subs(j(6,5),U,V)), double(subs(j(6,6),U,V))]

    NewV=V-jac\FnValues;

    predelta=abs(V-NewV);
    delta=max(predelta);
    V=NewV;
    i=i+1;
end

```

B.3.2 Alpha Rotation with Translation

```
syms OPx OPy OPz alpha theta1 theta3 theta5
```

```

d2r=pi/180;
beta=0;
gamma=0;

```

```

%User leg length inputs
length1=210.18;
length3=206.49;
length5=216.33;
%length6=10;

```

```

%Additional Parameters required to solve the system
DC1x=45.7182;
DC1z=36.8625;

```

```

DC3x=38.6652;
DC3z=44.2041;

```

```

DC5y=18.6792;
DC5z=19.5535;

```

```

%DC6y=38.9825;
%DC6z=43.9245;

```

```

gradient=-0.1763; %establish the gradient by using Point1 y and z (Mid EE
revolute LHS)-Mid EE revolute.

```

```

%Constants of the system
%Parameters from equation 1 (for first pair of legs)
PD12x=-19.34;
PD12y=-33.50;
PD12z=0;

```

```

OA12x=-75;
OA12y=-129.9;
OA12z=0;

```

```

%Parameters from equation 2 (for second pair of legs)
PD34x=-19.34;
PD34y=33.50;
PD34z=0;

```

```

OA34x=-75;
OA34y=129.9;
OA34z=0;

```



```

%Parameters from equation 3 (for third pair of legs)
OA5x=150;
OA5y=0;
OA5z=60;

PD5x=38.69;
PD5y=-25;
PD5z=0;

%Functions
F1=(OPx+cos(beta)*PD12x+sin(beta)*sin(alpha)*PD12y+sin(beta)*cos(alpha)*PD1
2z-OA12x)^2 ...
    + (OPy+cos(alpha)*PD12y-sin(alpha)*PD12z-OA12y)^2 ...
    + (OPz-
sin(beta)*PD12x+cos(beta)*sin(alpha)*PD12y+cos(beta)*cos(alpha)*PD12z-
OA12z)^2 ...
-
((length1*cos(theta1)+61.5+DC1x)^2)+((length1*sin(theta1)+85+DC1z)^2));

F2=(OPx+cos(beta)*PD34x+sin(beta)*sin(alpha)*PD34y+sin(beta)*cos(alpha)*PD3
4z-OA34x)^2 ...
    + (OPy+cos(alpha)*PD34y-sin(alpha)*PD34z-OA34y)^2 ...
    + (OPz-
sin(beta)*PD34x+cos(beta)*sin(alpha)*PD34y+cos(beta)*cos(alpha)*PD34z-
OA34z)^2 ...
-
((length3*cos(theta3)+61.5+DC3x)^2)+((length3*sin(theta3)+85+DC3z)^2));

F3=(OPx+cos(beta)*PD5x+sin(beta)*sin(alpha)*PD5y+sin(beta)*cos(alpha)*PD5z-
OA5x)^2 ...
    + (OPy+cos(alpha)*PD5y-sin(alpha)*PD5z-OA5y)^2 ...
    + (OPz-
sin(beta)*PD5x+cos(beta)*sin(alpha)*PD5y+cos(beta)*cos(alpha)*PD5z-OA5z)^2
...
-
((length5*cos(theta5)-
40+DC5y)^2)+((length5*sin(theta5)+22.5+DC5z)^2));

F4=85+length1*sin(theta1)+DC1z-(OPz-
sin(beta)*PD12x+cos(beta)*sin(alpha)*PD12y+cos(beta)*cos(alpha)*PD12z)

F5=85+length3*sin(theta3)+DC3z-(OPz-
sin(beta)*PD34x+cos(beta)*sin(alpha)*PD34y+cos(beta)*cos(alpha)*PD34z)

F6=-40+length5*cos(theta5)+DC5y-(OPy+cos(alpha)*PD5y-sin(alpha)*PD5z);

F7=gradient-tan(alpha);

F=[F1; F2; F3; F4; F5; F6; F7]

U=[OPx; OPy; OPz; alpha; theta1; theta3; theta5]

j=jacobian(F,U)

V=[double(input('Please enter the initial guess for OPx ')),...
    double(input('Please enter the initial guess for OPy ')),...
    double(input('Please enter the initial guess for OPz ')),...
    double(input('Please enter the initial guess for alpha in radians
')),...
    double(input('Please enter the initial guess for theta1 in radians
')),...
    double(input('Please enter the initial guess for theta3 in radians
')),...
    double(input('Please enter the initial guess for theta5 in radians
')),...
    double(input('Please enter the initial guess for theta1 in radians
')),...
    double(input('Please enter the initial guess for theta3 in radians
')),...
    double(input('Please enter the initial guess for theta5 in radians
'))];

```

```

    double(input('Please enter the initial guess for theta3 in radians
'),...
    double(input('Please enter the initial guess for theta5 in radians
'))]']

i=0;
delta=100;
while (delta>1e-6)

    FnValues=[double(subs(F(1,1),U,V)),...
    double(subs(F(2,1),U,V)),...
    double(subs(F(3,1),U,V)),...
    double(subs(F(4,1),U,V)),...
    double(subs(F(5,1),U,V)),...
    double(subs(F(6,1),U,V)),...
    double(subs(F(7,1),U,V))]']

    jac=[double(subs(j(1,1),U,V)), double(subs(j(1,2),U,V)),
double(subs(j(1,3),U,V)), double(subs(j(1,4),U,V)),
double(subs(j(1,5),U,V)), double(subs(j(1,6),U,V)),
double(subs(j(1,7),U,V));...
    double(subs(j(2,1),U,V)), double(subs(j(2,2),U,V)),
double(subs(j(2,3),U,V)), double(subs(j(2,4),U,V)),
double(subs(j(2,5),U,V)), double(subs(j(2,6),U,V)),
double(subs(j(2,7),U,V));...
    double(subs(j(3,1),U,V)), double(subs(j(3,2),U,V)),
double(subs(j(3,3),U,V)), double(subs(j(3,4),U,V)),
double(subs(j(3,5),U,V)), double(subs(j(3,6),U,V)),
double(subs(j(3,7),U,V));...
    double(subs(j(4,1),U,V)), double(subs(j(4,2),U,V)),
double(subs(j(4,3),U,V)), double(subs(j(4,4),U,V)),
double(subs(j(4,5),U,V)), double(subs(j(4,6),U,V)),
double(subs(j(4,7),U,V));...
    double(subs(j(5,1),U,V)), double(subs(j(5,2),U,V)),
double(subs(j(5,3),U,V)), double(subs(j(5,4),U,V)),
double(subs(j(5,5),U,V)), double(subs(j(5,6),U,V)),
double(subs(j(5,7),U,V));...
    double(subs(j(6,1),U,V)), double(subs(j(6,2),U,V)),
double(subs(j(6,3),U,V)), double(subs(j(6,4),U,V)),
double(subs(j(6,5),U,V)), double(subs(j(6,6),U,V)),
double(subs(j(6,7),U,V));...
    double(subs(j(7,1),U,V)), double(subs(j(7,2),U,V)),
double(subs(j(7,3),U,V)), double(subs(j(7,4),U,V)),
double(subs(j(7,5),U,V)), double(subs(j(7,6),U,V)),
double(subs(j(7,7),U,V))]

    NewV=V-jac\FnValues;

    predelta=abs(V-NewV);
    delta=max(predelta);
    V=NewV;
    i=i+1;
end

```

B.3.3 Beta Rotation with Translation

```
syms OPx OPy OPz beta theta1 theta3 theta5

d2r=pi/180;
alpha = 0;
gamma=0;

%User leg length inputs
length1=245.97;
length3=227.47;
length5=234.49;

%Additional Parameters required to solve the system
DC1x=34.9941;
DC1z=47.1637;

DC3x=33.8522;
DC3z=47.9899;

gradient=-0.2178; %establish the gradient by using OPx, OPz, PD12x, PD12z

%Constants of the system
%Parameters from equation 1 (for first pair of legs)
PD12x=-19.34;
PD12y=-33.50;
PD12z=0;

OA12x=-75;
OA12y=-129.9;
OA12z=0;

%Parameters from equation 2 (for second pair of legs)
PD34x=-19.34;
PD34y=33.50;
PD34z=0;

OA34x=-75;
OA34y=129.9;
OA34z=0;

%Parameters from equation 3 (for third pair of legs)
OAv1x=150;
OAv1y=0;
OAv1z=60;

PDv1x=38.69;
PDv1y=0;
PDv1z=0;

%Functions
F1=(OPx+cos(beta)*PD12x+sin(beta)*sin(alpha)*PD12y+sin(beta)*cos(alpha)*PD12z-OA12x)^2 ...
    + (OPy+cos(alpha)*PD12y-sin(alpha)*PD12z-OA12y)^2 ...
    + (OPz-
sin(beta)*PD12x+cos(beta)*sin(alpha)*PD12y+cos(beta)*cos(alpha)*PD12z-OA12z)^2 ...
    -
    (((length1*cos(theta1)+61.5+DC1x)^2)+((length1*sin(theta1)+85+DC1z)^2));

F2=(OPx+cos(beta)*PD34x+sin(beta)*sin(alpha)*PD34y+sin(beta)*cos(alpha)*PD34z-OA34x)^2 ...
```

```

        + (OPy+cos(alpha)*PD34y-sin(alpha)*PD34z-OA34y)^2 ...
        + (OPz-
sin(beta)*PD34x+cos(beta)*sin(alpha)*PD34y+cos(beta)*cos(alpha)*PD34z-
OA34z)^2 ...
        -
((length3*cos(theta3)+61.5+DC3x)^2)+((length3*sin(theta3)+85+DC3z)^2));

F3=(OPx+cos(beta)*PDv1x+sin(beta)*sin(alpha)*PDv1y+sin(beta)*cos(alpha)*PDv
lz-OAv1x)^2 ...
        + (OPy+cos(alpha)*PDv1y-sin(alpha)*PDv1z-OAv1y)^2 ...
        + (OPz-
sin(beta)*PDv1x+cos(beta)*sin(alpha)*PDv1y+cos(beta)*cos(alpha)*PDv1z-
OAv1z)^2 ...
        - ((length5*cos(theta5)-
40+40)^2)+((length5*sin(theta5)+22.5+22.5)^2));

F4=85+length1*sin(theta1)+DC1z-(OPz-
sin(beta)*PD12x+cos(beta)*sin(alpha)*PD12y+cos(beta)*cos(alpha)*PD12z)

F5=85+length3*sin(theta3)+DC3z-(OPz-
sin(beta)*PD34x+cos(beta)*sin(alpha)*PD34y+cos(beta)*cos(alpha)*PD34z)

F6=length5*cos(theta5)-OPy;

F7=gradient-tan(beta);

F=[F1; F2; F3; F4; F5; F6; F7]

U=[OPx; OPy; OPz; beta; theta1; theta3; theta5]

j=jacobian(F,U)

V=[double(input('Please enter the initial guess for OPx ')),...
double(input('Please enter the initial guess for OPy ')),...
double(input('Please enter the initial guess for OPz ')),...
double(input('Please enter the initial guess for beta in radians
')),...
double(input('Please enter the initial guess for theta1 in radians
')),...
double(input('Please enter the initial guess for theta3 in radians
')),...
double(input('Please enter the initial guess for theta5 in radians
'))]']

i=0;
delta=100;
while (delta>1e-6)

    FnValues=[double(subs(F(1,1),U,V)),...
double(subs(F(2,1),U,V)),...
double(subs(F(3,1),U,V)),...
double(subs(F(4,1),U,V)),...
double(subs(F(5,1),U,V)),...
double(subs(F(6,1),U,V)),...
double(subs(F(7,1),U,V))]']

    jac=[double(subs(j(1,1),U,V)), double(subs(j(1,2),U,V)),
double(subs(j(1,3),U,V)), double(subs(j(1,4),U,V)),
double(subs(j(1,5),U,V)), double(subs(j(1,6),U,V)),
double(subs(j(1,7),U,V))];...

```

```

        double(subs(j(2,1),U,V)), double(subs(j(2,2),U,V)),
double(subs(j(2,3),U,V)), double(subs(j(2,4),U,V)),
double(subs(j(2,5),U,V)), double(subs(j(2,6),U,V)),
double(subs(j(2,7),U,V));...
        double(subs(j(3,1),U,V)), double(subs(j(3,2),U,V)),
double(subs(j(3,3),U,V)), double(subs(j(3,4),U,V)),
double(subs(j(3,5),U,V)), double(subs(j(3,6),U,V)),
double(subs(j(3,7),U,V));...
        double(subs(j(4,1),U,V)), double(subs(j(4,2),U,V)),
double(subs(j(4,3),U,V)), double(subs(j(4,4),U,V)),
double(subs(j(4,5),U,V)), double(subs(j(4,6),U,V)),
double(subs(j(4,7),U,V));...
        double(subs(j(5,1),U,V)), double(subs(j(5,2),U,V)),
double(subs(j(5,3),U,V)), double(subs(j(5,4),U,V)),
double(subs(j(5,5),U,V)), double(subs(j(5,6),U,V)),
double(subs(j(5,7),U,V));...
        double(subs(j(6,1),U,V)), double(subs(j(6,2),U,V)),
double(subs(j(6,3),U,V)), double(subs(j(6,4),U,V)),
double(subs(j(6,5),U,V)), double(subs(j(6,6),U,V)),
double(subs(j(6,7),U,V));...
        double(subs(j(7,1),U,V)), double(subs(j(7,2),U,V)),
double(subs(j(7,3),U,V)), double(subs(j(7,4),U,V)),
double(subs(j(7,5),U,V)), double(subs(j(7,6),U,V)),
double(subs(j(7,7),U,V))]

```

```

NewV=V-jac\FnValues;

```

```

predelta=abs(V-NewV);

```

```

delta=max(predelta);

```

```

V=NewV;

```

```

i=i+1;

```

```

end

```

B.4 Workspace MATLAB® Code

The following sections of code were extensions to the inverse kinematic code for the translation analysis. This was similarly employed for the alpha rotation with translation and the beta rotation with translation.

```
a=46.5; %Lower limit x
b=235.14; %Upper limit x
c=-136.12; %Lower limit y
d=136.12; %Upper limit y
e=262.08; %Lower limit z
f=356.68; %Upper limit z
storage = {

i=0
while (i<1500)
xf=a + (b-a)*rand(1);
yf=c + (d-c)*rand(1);
zf=e + (f-e)*rand(1);

%Inverse Kinematic Code
end

%Inner Vector loops
%Length1
BC1=xzAD1-AB1-DC1;
Length1=norm(BC1);
phi1=(atan(BC1(3,1)/BC1(1,1)))*r2d;

%Length2
BC2=xzAD2-AB2-DC2;
Length2=norm(BC2);
phi2=(atan(BC2(3,1)/BC2(1,1)))*r2d;

%Length3
BC3=xzAD3-AB3-DC3;
Length3=norm(BC3);
phi3=(atan(BC3(3,1)/BC3(1,1)))*r2d;

%Length4
BC4=xzAD4-AB4-DC4;
Length4=norm(BC4);
phi4=(atan(BC4(3,1)/BC4(1,1)))*r2d;

%Length5
BC5=yzAD5-AB5-DC5;
Length5=norm(BC5);
phi5prelim=(atan(BC5(3,1)/BC5(2,1)))*r2d;

if phi5prelim<0
phi5=phi5prelim+180;
elseif phi5prelim>0
phi5=phi5prelim;
end

%Length6
BC6=yzAD6-AB6-DC6;
Length6=norm(BC6);
```

```

phi6prelim=(atan(BC6(3,1)/BC6(2,1)))*r2d;

if phi6prelim<0
    phi6=phi6prelim+180;
elseif phi6prelim>0
    phi6=phi6prelim;
end

if Length1>184 && Length1<244 && Length2>184 && Length2<244 &&
Length3>184 && Length3<244 && Length4>184 ...
    && Length4<244 && Length5>192 && Length5<252 && Length6>192 &&
Length6<252 && phi1>34.18 && phi1<78.73...
    && phi2>34.18 && phi2<78.73 && phi3>34.18 && phi3<78.73 &&
phi4>34.18 && phi4<78.73...
    && phi5>56.43 && phi5<123.57 && phi5>56.43 && phi5<123.57

subplot(2,2,1)
scatter3(xf,yf,zf, '.')
title('Point Cloud')
storage = [storage; {xf yf zf }]; %Growing array of valid coordinates
hold on
i=i+1

xlabel('X axis')
ylabel('Y axis')
zlabel('Z axis')

view(0,0)
end

subplot(2,2,2)
CC=cell2mat(storage);
DT=delaunayTriangulation(CC);
[K,v]=convexHull(DT);
trisurf(K,DT.Points(:,1),DT.Points(:,2),DT.Points(:,3))
view(0,0)
title('Convex Hull')
xlabel('X Axis')
ylabel('Y Axis')
zlabel('Z Axis')

subplot(2,2,3)
h = histogram2(CC(:,1),CC(:,2),24,'FaceColor','flat');
colorbar
view(0,0)
title('Point Cloud Distribution')
xlabel('X Axis')
ylabel('Y Axis')
zlabel('Z Axis')

```

Appendix C – Calculations

C.1. Power Screw Analysis

The power screw calculations were performed on the threaded rod of the linear actuator to understand its performance characteristics. Power screw calculations were useful in the analysis of PKMs due to its higher load bearing advantage over serial robots.

$$M_t = \frac{Wd_m}{2} \left[\frac{f\pi d_m + Lead(\cos\alpha_n)}{\pi d_m \cos\alpha_n - fLead} \right] + \frac{Wf_c d_c}{2}$$

The linear actuator did not possess a collar and this is shown in Appendix H Drawing 6. The collar variables are therefore not considered. The pitch diameter was used instead of the mean diameter. The formula was obtained from Shigley [165].

$$d_m = d_p = d - 0.649519p$$

$$d_p = 8 - 0.649519(1.25) = 7.19 \text{ mm}$$

$$W = \frac{2M_t}{d_p \left[\frac{f\pi d_p + Lead(\cos\alpha_n)}{\pi d_p \cos\alpha_n - fLead} \right]}$$

The torque, M_t , was obtained from the graphs of torque vs. pulse per second for the stepper motors. The stepper motors rotated at 200 steps per second, which translates to 200 pulses per second. The torques from the graphs were estimated at 29 Ncm for actuators 1 to 4 and 24 Ncm for actuator 5 and 6. The value of 24 Ncm was carried forward for the calculation. The friction value, f , was approximated to be 0.15 and the thread angle was 60° [165].

$$W = \frac{2 \times (24 \times 10^{-2})}{7.19 \times 10^{-3} \left[\frac{0.15\pi(7.19 \times 10^{-3}) + 1.25 \times 10^{-3} \left(\cos \frac{60}{2} \right)}{\pi(7.19 \times 10^{-3}) \left(\cos \frac{60}{2} \right) - 0.15(1.25 \times 10^{-3})} \right]}$$

$$W = 289 \text{ N}$$

Considering friction from the guides of the telescoping arm, 10% friction is accounted for.

$$W = 289 \times 0.9 = 260.1 \text{ N}$$

The efficiency of the linear actuators, η , was calculated as follows:

$$\eta = \frac{WLead}{2\pi M_t} = \frac{260.1 \times 1.25 \times 10^{-3}}{2\pi \times (24 \times 10^{-2})} = 0.2156 = 21.56\%$$

C.2. Steps per Linear Movement

The calculations regarding the steps per linear movement were required to conduct the accuracy and repeatability tests documented in Section 8.6. The number of steps per revolution of the stepper motors is presented below. Actuator 1 to 4 possesses stepper motors with a resolution of 1.8° per step while actuator 5 and 6 possess stepper motors with a resolution of 0.9° per step.

$$\text{steps per rev}_{1-4} = \frac{360^\circ}{1.8^\circ \text{ per step}} = 200 \text{ steps}$$

$$\text{steps per rev}_{5,6} = \frac{360^\circ}{0.9^\circ \text{ per step}} = 400 \text{ steps}$$

An M8 threaded rod was used as the lead screw with a pitch of 1.25 mm. The CR values for the two different types of stepper motors were calculated and is presented.

$$CR_{1-4} = \frac{\text{pitch of threaded rod}}{\text{steps/rev of stepper motor}} = \frac{1.25 \text{ mm}}{200} = 0.00625 \text{ mm/step}$$

$$CR_{5,6} = \frac{\text{pitch of threaded rod}}{\text{steps/rev of stepper motor}} = \frac{1.25 \text{ mm}}{400} = 0.003125 \text{ mm/step}$$

The number of steps to move the stepper motor shaft to result in a specific stroke length was calculated, as shown below.

$$\Delta \text{length} = |\overline{BC}_f| - |\overline{BC}_i|$$

Where:

- $|\overline{BC}_f|$ = Magnitude of the BC vector at is the final position
- $|\overline{BC}_i|$ = Magnitude of the BC vector at is the initial position

Finally calculating the number of steps for the stepper motor shaft to turn:

$$\text{Steps to move} = \frac{\Delta \text{length}}{CR}$$

For example, if the change in length recorded for actuator 1 were 50 mm, the number of steps would be calculated as follows:

$$\text{Steps to move} = \frac{\Delta \text{length}}{CR_{1-4}} = \frac{50 \text{ mm}}{0.00625 \text{ mm/step}} = 8000 \text{ steps}$$

C.3. Buckling Analysis

The buckling calculation was performed on the threaded rod of the linear actuator to determine the maximum load and stress that can be placed upon the threaded rod. These calculations were required to determine the limiting factor of the PKM in load bearing applications. The threaded rod was considered as free and fixed end support therefore $K = 2$. The length of the threaded rod was 78 mm therefore $L = 78 \text{ mm}$. $E = 206 \text{ GPa}$ because a steel threaded rod was used [166]. The calculations are as follows.

$$P_{cr} = \frac{\pi^2 EI}{(KL)^2}$$

$$P_{cr} = \frac{\pi^2(206 \times 10^9) \frac{\pi d^4}{64}}{(2 \times 0.078)^2}$$

$$P_{cr} = \frac{\pi^2(206 \times 10^9) \frac{\pi \times 0.008^4}{64}}{(2 \times 0.078)^2} = 16.80 \text{ kN}$$

The radius of gyration, r , was calculated as follows:

$$r = \sqrt{\frac{I}{A}} = \sqrt{\frac{\frac{\pi d^4}{64}}{36.6 \times 10^{-6}}} = \sqrt{\frac{\pi \times 0.008^4}{64}} = 2.34 \text{ mm}$$

The slenderness ratio calculation is presented below.

$$\frac{KL}{r} = \frac{2 \times 78 \text{ mm}}{2.34 \text{ mm}} = 66.67$$

The critical stress for the M8 threaded rod is shown below.

$$\sigma_{cr} = \frac{\pi^2 E}{\left(\frac{KL}{r}\right)^2} = \frac{\pi^2 \times 206 \times 10^9}{(66.67)^2} = 457.41 \text{ MPa}$$

C.4. Rotated CD Vector Analysis

The rotated \overrightarrow{CD} vector calculations were required to perform the forward and inverse kinematic analysis of the rotation of the end effector. The calculations were also required when performing the workspace analysis. When the end effector performs α or β rotation, the Joint D bracket leans forward or backward and changes the vector components in the different directions. The different cases are presented and the changes in vector components are calculated.

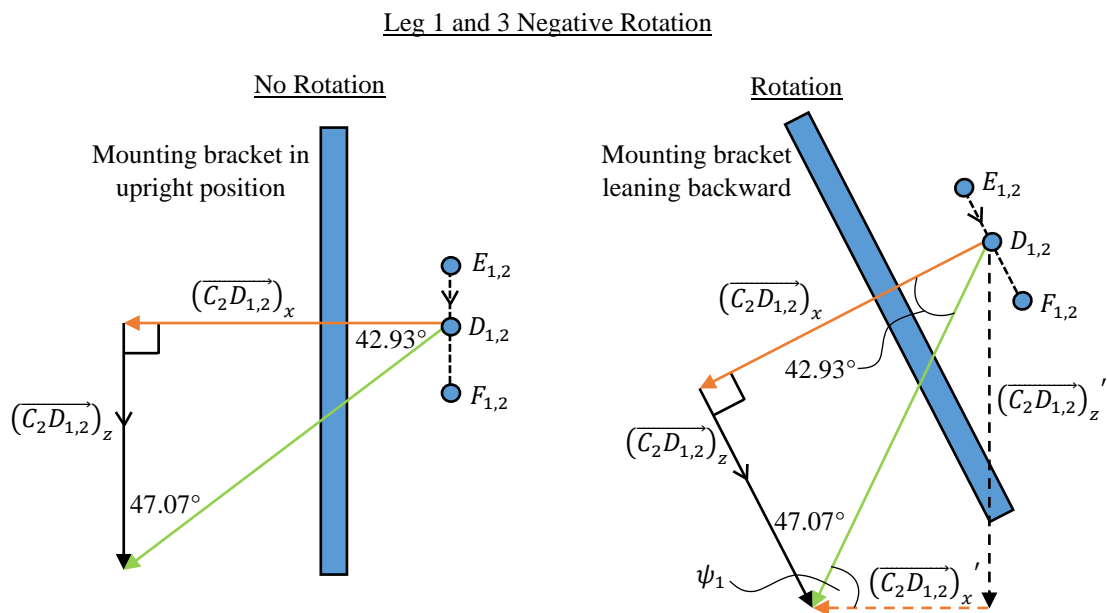


Figure C.1: Leg 1 and leg 3 negative rotation of the Joint D bracket

$$m_1 = \frac{\Delta z}{\Delta x} = \frac{(\overrightarrow{PE_{1,2}} - \overrightarrow{PF_{1,2}})_z}{(\overrightarrow{PE_{1,2}} - \overrightarrow{PF_{1,2}})_x}$$

$$\lambda_1 = \tan^{-1}(m_1)$$

$$\xi_1 = 180^\circ - |\lambda_1|$$

$$\psi_1 + 47.07^\circ = \xi_1$$

$$\therefore \psi_1 = \xi_1 - 47.07^\circ$$

The following equations solve the new x and z components of the vector $\overrightarrow{C_1D_{1,2}}$.

$$(\overrightarrow{C_1D_{1,2}})_x' = |\overrightarrow{C_1D_{1,2}}| \cos \psi_1$$

$$(\overrightarrow{C_1D_{1,2}})_z' = |\overrightarrow{C_1D_{1,2}}| \sin \psi_1$$

Leg 2 and 4 Positive Rotation

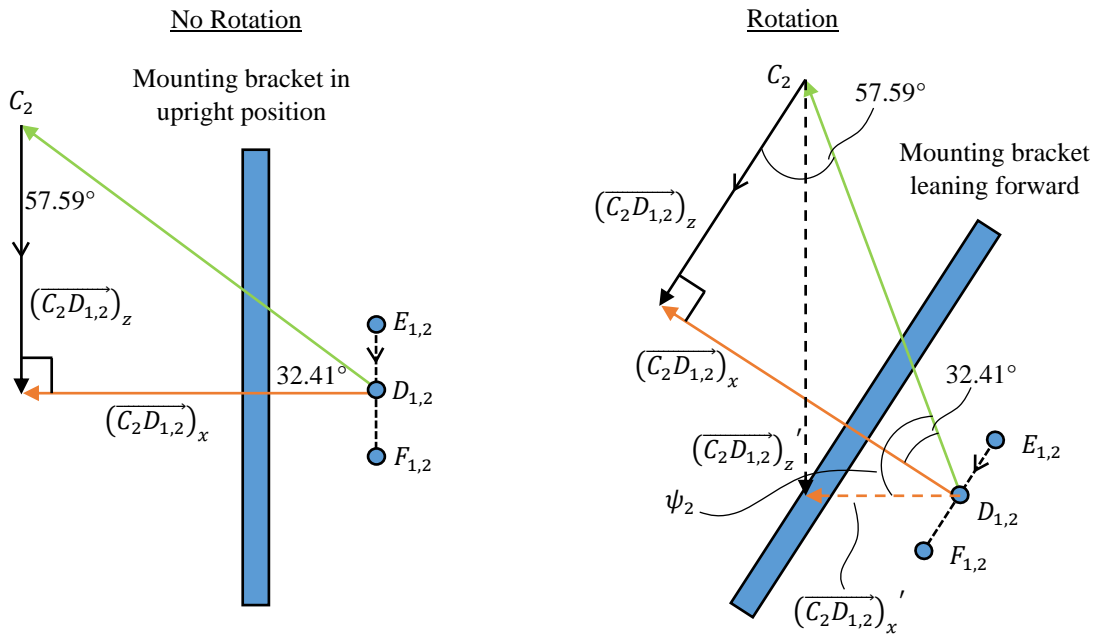


Figure C.2: Leg 2 and leg 4 positive rotation of the Joint D bracket

$$m_2 = \frac{\Delta z}{\Delta x} = \frac{(\overrightarrow{PE_{1,2}} - \overrightarrow{PF_{1,2}})_z}{(\overrightarrow{PE_{1,2}} - \overrightarrow{PF_{1,2}})_x}$$

$$\lambda_2 = \tan^{-1}(m_2)$$

$$\psi_2 + \lambda_2 + 57.59^\circ = 180^\circ$$

$$\therefore \psi_2 = 180^\circ - \lambda_2 - 57.59^\circ$$

The following equations solve the new x and z components of the vector $\overrightarrow{C_1D_{1,2}}$.

$$(\overrightarrow{C_1D_{1,2}})'_x = |\overrightarrow{C_1D_{1,2}}| \cos \psi_2$$

$$(\overrightarrow{C_1D_{1,2}})'_z = |\overrightarrow{C_1D_{1,2}}| \sin \psi_2$$

Leg 2 and 4 Negative Rotation

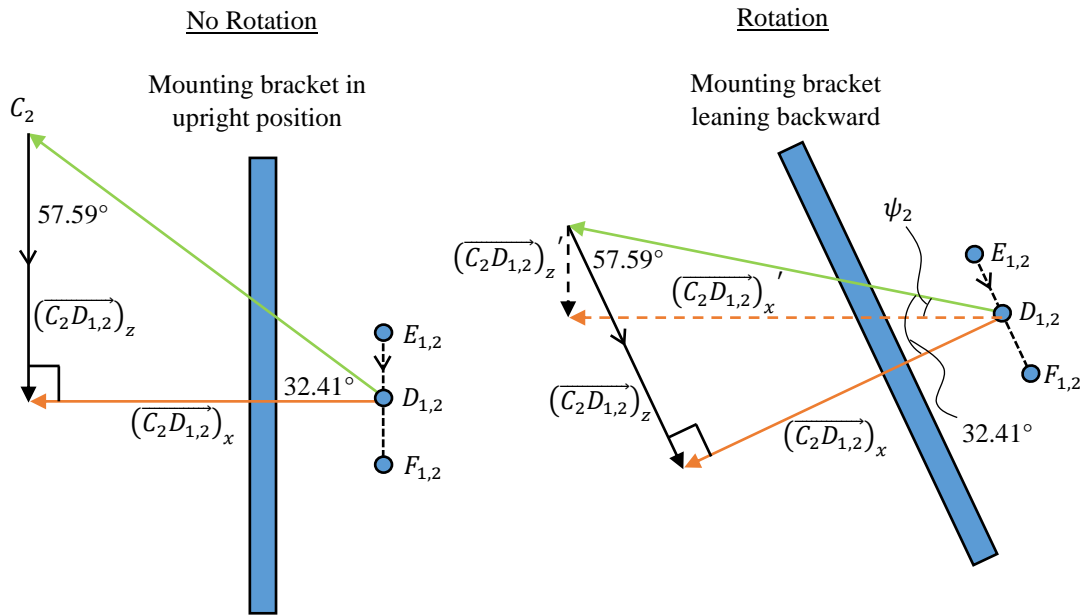


Figure C.3: Leg 2 and leg 4 negative rotation of the Joint D bracket

$$m_2 = \frac{\Delta z}{\Delta x} = \frac{(\overrightarrow{PE_{1,2}} - \overrightarrow{PF_{1,2}})_z}{(\overrightarrow{PE_{1,2}} - \overrightarrow{PF_{1,2}})_x}$$

$$\lambda_2 = \tan^{-1}(m_2)$$

$$\psi_2 = |\lambda_2| - 57.59^\circ$$

The following equations solve the new x and z components of the vector $\overrightarrow{C_1D_{1,2}}$.

$$(\overrightarrow{C_1D_{1,2}})'_x = |\overrightarrow{C_1D_{1,2}}| \cos \psi_2$$

$$(\overrightarrow{C_1D_{1,2}})'_z = |\overrightarrow{C_1D_{1,2}}| \sin \psi_2$$

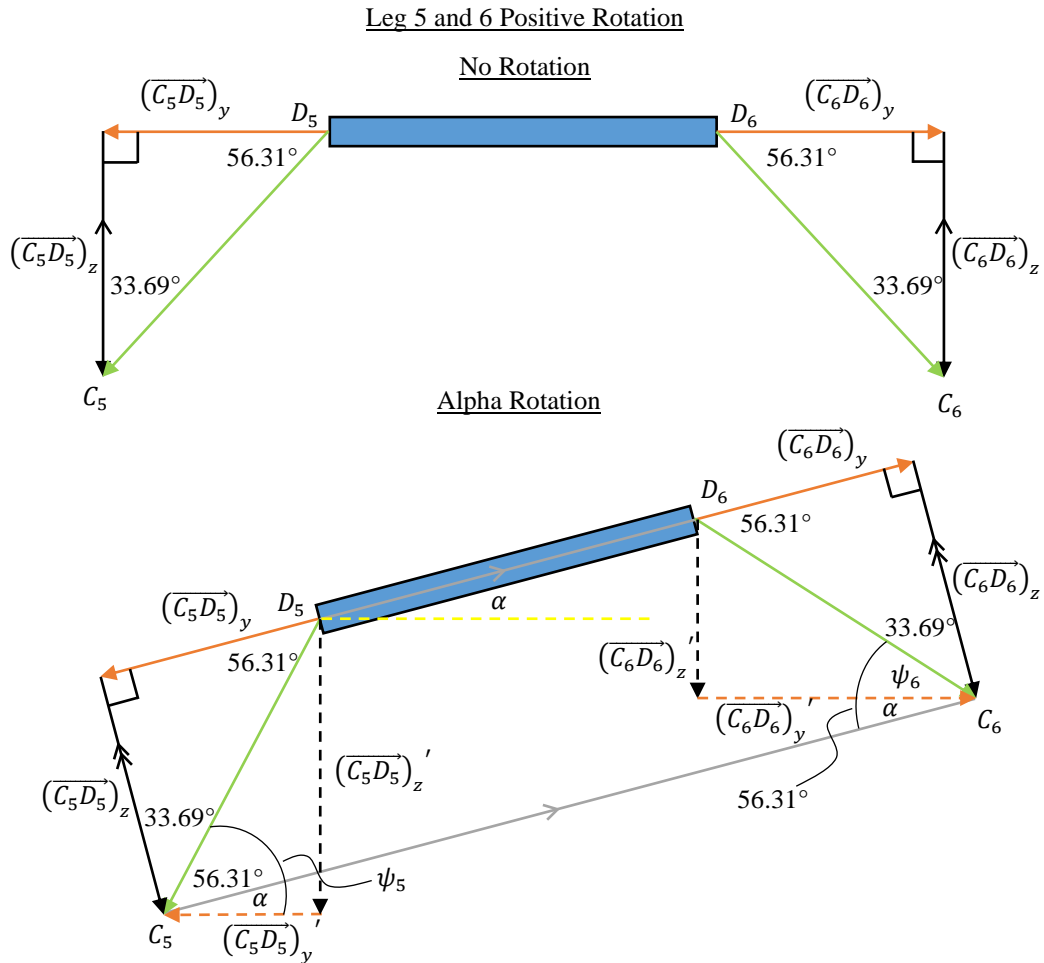


Figure C.4: Leg 5 and leg 6 positive alpha rotation of the end effector

$$\psi_5 = 56.13^\circ + \alpha$$

The following equations solve the new y and z components of the vector $\overline{C_5D_5}$.

$$(\overline{C_5D_5})'_y = |\overline{C_5D_5}| \cos \psi_5$$

$$(\overline{C_5D_5})'_z = |\overline{C_5D_5}| \sin \psi_5$$

Concerning ψ_6 , the following equations solve the new y and z components of the vector $\overline{C_6D_6}$.

$$\psi_6 = 90^\circ - 33.69^\circ - \alpha$$

$$(\overline{C_6D_6})'_y = |\overline{C_6D_6}| \cos \psi_6$$

$$(\overline{C_6D_6})'_z = |\overline{C_6D_6}| \sin \psi_6$$

Leg 5 and 6 Negative Rotation

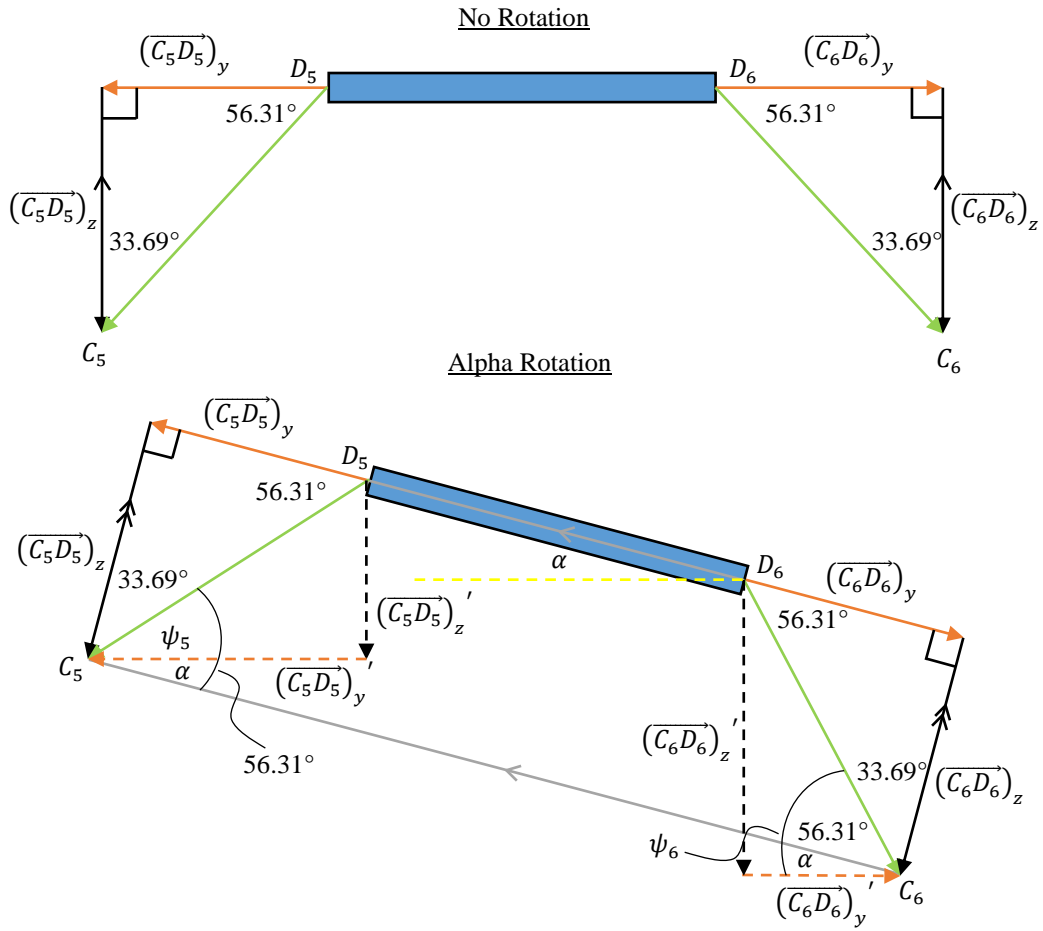


Figure C.5: Leg 5 and leg 6 negative alpha rotation of the end effector

$$\psi_5 + \alpha + 33.69^\circ = 90^\circ$$

$$\therefore \psi_5 = 90^\circ - \alpha - 33.69^\circ$$

The following equations solve the new y and z components of the vector $\overrightarrow{C_5 D_5}$.

$$(\overrightarrow{C_5 D_5})'_y = |\overrightarrow{C_5 D_5}| \cos \psi_5$$

$$(\overrightarrow{C_5 D_5})'_z = |\overrightarrow{C_5 D_5}| \sin \psi_5$$

Concerning ψ_6 , the following equations solve the new y and z components of the vector $\overrightarrow{C_6 D_6}$.

$$\psi_6 = 56.13^\circ + \alpha$$

$$(\overrightarrow{C_6 D_6})'_y = |\overrightarrow{C_6 D_6}| \cos \psi_6$$

$$(\overrightarrow{C_6 D_6})'_z = |\overrightarrow{C_6 D_6}| \sin \psi_6$$

Appendix D – Quality Function Deployment

Figure D.1 to Figure D.5 illustrates excerpts of the QFD.

Legend		
⊖	Strong Relationship	9
○	Moderate Relationship	3
▲	Weak Relationship	1
++	Strong Positive Correlation	
+	Positive Correlation	
-	Negative Correlation	
▼	Strong Negative Correlation	
▼	Objective Is To Minimize	
▲	Objective Is To Maximize	
X	Objective Is To Hit Target	

Figure D.1: The Legend for the QFD

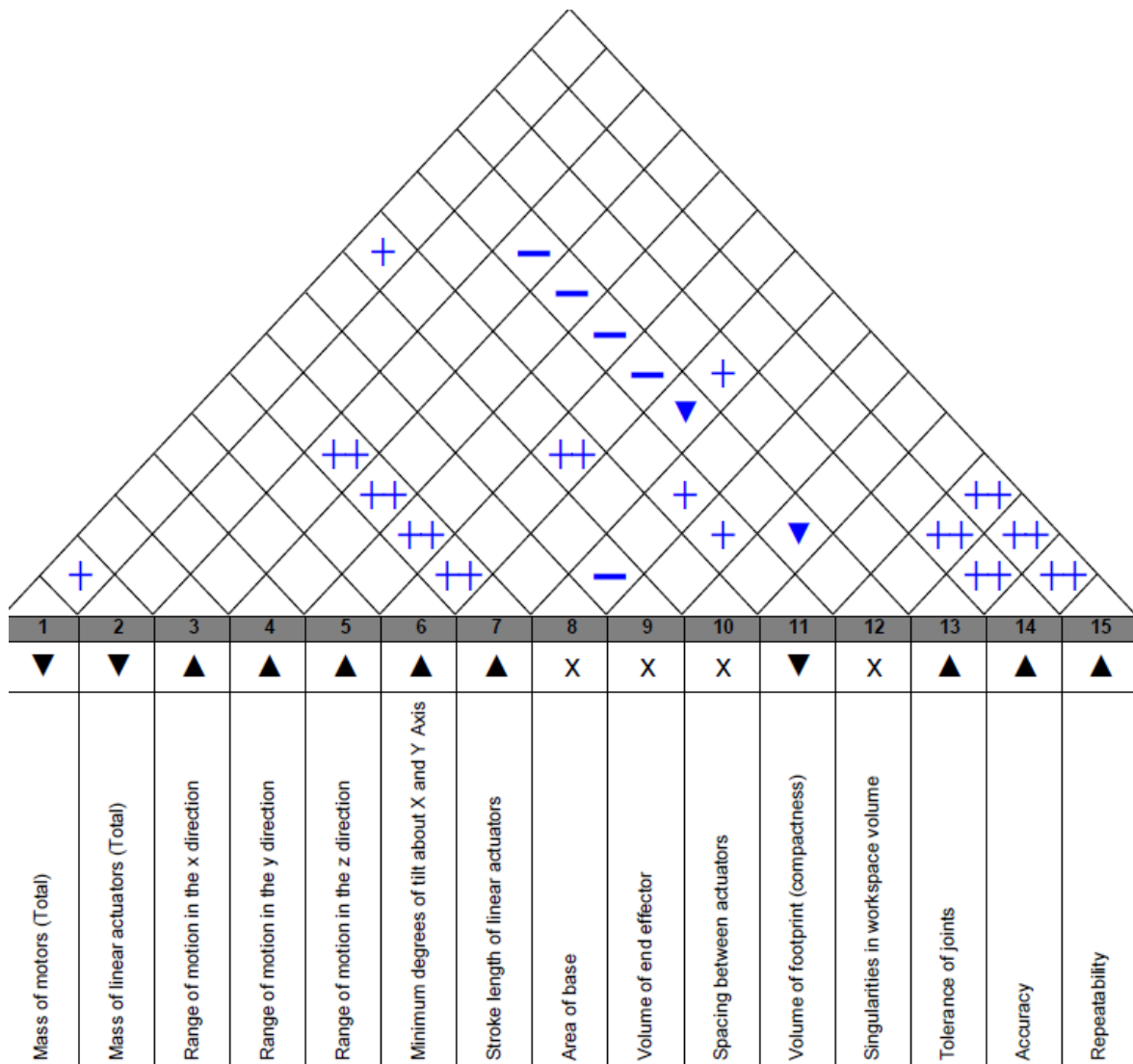


Figure D.2: Relationships between the different engineering metrics

Row #	Max Relationship Value in Row	Relative Weight	Weight/ Importance	Direction of Improvement: Minimize (▼), Maximize (▲), or Target (x)	Column #	1	2	3	4	5	6	7	8	9	10	11	12	13	14	15	
				D demanded Quality (a.k.a. "Customer Requirements" or "Whats")	Quality Characteristics (a.k.a. "Functional Requirements" or "Hows")	1	2	3	4	5	6	7	8	9	10	11	12	13	14	15	
1	9	9,7	3,0			Lightweight	Mass of motors (Total)	○													
2	9	12,9	4,0	Translation along X,Y & Z axes	Mass of linear actuators (Total)	○	○	○	○	○											
3	9	12,9	4,0	Rotation about X and Y axes	Range of motion in the x direction		○	○	○	○											
4	9	12,9	4,0	Durable	Range of motion in the y direction																
5	9	12,9	4,0	High precision	Range of motion in the z direction																
6	9	12,9	4,0	Low cost	Minimum degrees of tilt about X and Y Axis																
7	9	9,7	3,0	Used for different applications	Stroke length of linear actuators							○									
8	9	6,5	2,0	Modular	Area of base								○								
9	9	9,7	3,0	Portable	Volume of end effector									○							
10					Spacing between actuators									○							
					Volume of footprint (compactness)																
					Tolerance of joints																
					Accuracy																
					Repeatability																

Figure D.3: Relationships between customer requirements and engineering metrics

Column #	1	2	3	4	5	6	7	8	9	10	11	12	13	14	15
Direction of Improvement: Minimize (▼), Maximize (▲), or Target (X)	▼	▼	▲	▲	▲	▲	▲	X	X	X	▼	X	▲	▲	▲
	▲	▲	▲	▲	▲	▲	▲	X	X	X	▼	X	▲	▲	▲
Quality Characteristics (a.k.a. "Functional Requirements" or "How's")	Mass of motors (Total)	Mass of linear actuators (Total)	Range of motion in the x direction	Range of motion in the y direction	Range of motion in the z direction	Minimum degrees of tilt about X and Y Axis	Stroke length of linear actuators	Area of base	Volume of end effector	Spacing between actuators	Volume of footprint (compactness)	Singularities in workspace volume	Tolerance of joints	Accuracy	Repeatability
	2 kg	4 kg	200 mm	250 mm	100 mm	60 degrees	65 mm	1 m ²	0,00004 m ³	80 mm	0,003 m ³	0	Less than 1 mm	2 mm and 2 degrees	2 mm and 2 degrees
Target or Limit Value	2	2	7	7	7	8	4	2	4	1	6	9	7	8	8
	9	9	9	9	9	9	9	9	9	9	9	9	9	9	9
Difficulty (0=Easy to Accomplish, 10=Extremely Difficult)	193,5	180,6	319,4	319,4	319,4	203,2	464,5	212,9	154,8	135,5	87,1	145,2	348,4	358,1	358,1
Max Relationship Value in Column	5,1	4,8	8,4	8,4	8,4	5,3	12,2	5,6	4,1	3,6	2,3	3,8	9,2	9,4	9,4
Weight / Importance															
Relative Weight															

Figure D.4: Target specifications for the engineering metrics

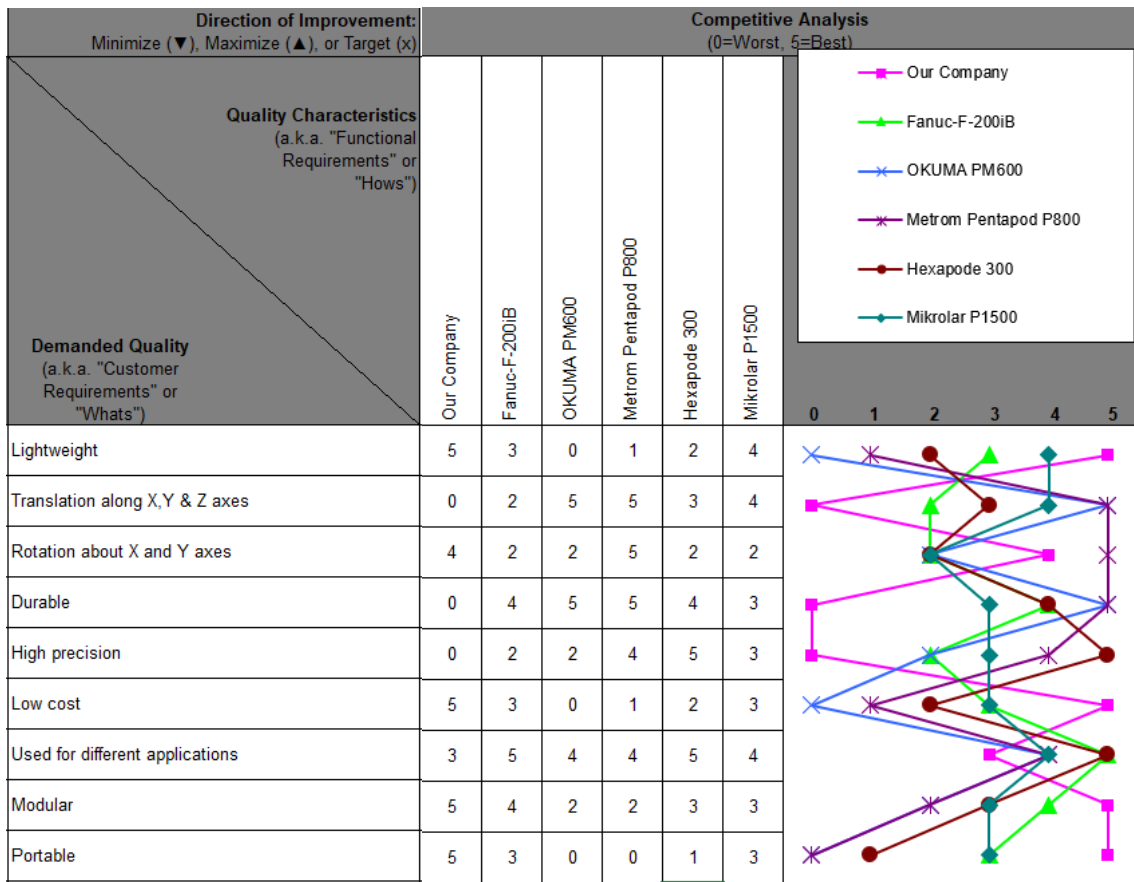


Figure D.5: Competitive analysis between industrial PKMs and the PKM developed in this study

Appendix E – Project Costs

Table E.1 lists the cost of components for this research.

Table E.1: Cost of components

Component	Price / Unit	Quantity	Cost
Additive Manufacturing			
Filament for additive manufactured components – eSun 1kg	R 300.00	6	R 1800.00
Magigoo Pen – bonding agent for machine bed	R 600.00	1	R 600.00
Mechanical			
M8 chromed linear shafts	R 140.00	2	R 280.00
SK8 linear shaft support	R 26.00	8	R 208.00
Linear bearings – LMK8UU	R 85.00	4	R 340.00
Radial bearing – 608 ZZ	R 13.00	4	R 52.00
Thrust bearings – NSK 51103	R 120.00	2	R 240.00
M8 steel threaded rod	R 35.00	2	R 70.00
Aluminium flexible couplers (5mm/8mm)	R 40.00	6	R 240.00
Aluminium solid couplers (5mm/8mm)	R 40.00	6	R 240.00
Bolts, washers and nuts (assorted)	R 250.00		R 250.00
Modular extrusions and related components			
Aluminium extruded profile PG30 T – slot	R 150.00	8	R 1200.00
PG30 corner brackets	R 14.74	15	R 221.09
PG30 tee nuts – M5	R 4.95	60	R 297.00
Electronics			
42BYGHW609 stepper motors	R 240.00	4	R 960.00
42BYGHM809 stepper motors	R 240.00	2	R 480.00
Arduino Mega 2560	R 250.00	1	R 250.00
24V 12.5A power supply units (Mean Well S-320-24-D)	R 896.00	2	R 1792.00
TB6560 stepper motor driver	R 140.00	6	R 840.00
Jumper Wires (Packs)	R 30.00	2	R 60.00
Breadboard 400 PT	R 22.00	2	R 44.00
5-P in-line microphone male plugs	R 26.15	6	R 156.90
5-P in-line microphone female plugs	R 20.85	6	R 125.10
Computer fan	R 40.00	1	R 40.00
Heatshrink wire cover kit	R 95.00	1	R 95.00
EasyHold plastic box (control box) – 345x310x135	R 332.00	1	R 332.00
Mains lead plug to socket	R 60.00	2	R 120.00
IEC plug – male flange mounted	R 7.74	2	R 15.48
Tools and equipment			
Hole saw set - 16 piece	R 350.00	1	R 350.00
Bosch hand drill – 750W GSB16RE	R 1200.00	1	R 1200.00
Digital Vernier calliper	R 285.00	1	R 285.00
Wire stripper	R 150.00	1	R 150.00
Miscellaneous			
Wooden platform	R 68.00	1	R 68.00
TOTAL			R 13401.57

Appendix F – Linear Actuator Concepts

F.1 Concept 1: Aluminium Sheet Concept

This concept used an aluminium sheet folded at each of its ends. One end supported a linear and radial bearing and the other end allowed the stepper motor to be mounted. The length of the actuator could be altered by changing the length of the aluminium sheet. This design uses wear strips to reduce the friction between the additive manufactured slider and the aluminium sheet. The telescoping arm is an aluminium rod. An advantage of this design is that it is lightweight and cost-effective. A disadvantage of this design is that it possessed low mechanical rigidity. Warpage could also occur if the aluminium sheet is too thin. Figure F.1 displays the design.

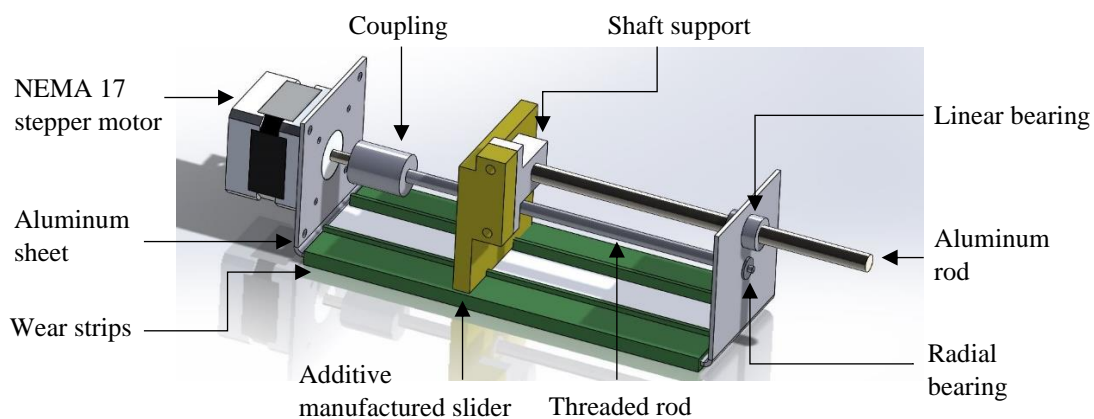


Figure F.1: Linear actuator concept 1

F.2 Concept 2: Additive Manufactured Bracket Concept

This concept uses three additive manufactured brackets to link all actuator components. Instead of using an aluminium sheet, the aluminium telescoping arm, threaded rod and aluminium guide rod increases the mechanical rigidity of the actuator. This concept, however, requires more shaft supports and bearings. The length of the actuator can be altered by the length of the threaded rod and guide rod. The advantage of this concept is that it is more rigid than Concept 1 and the telescoping arm has two supports. The disadvantage is that the additional aluminium guide rod and the additional bearings make this concept heavier and more expensive. Figure F.2 shows the design concept.

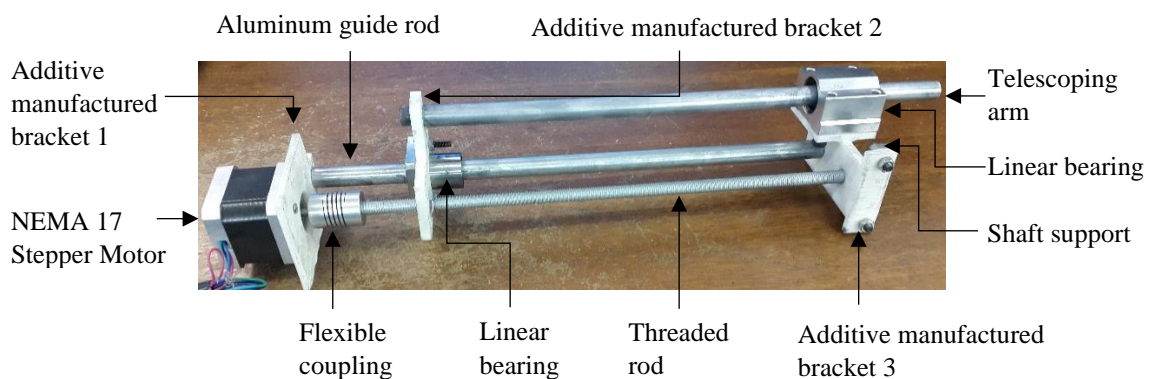


Figure F.2: Linear actuator concept 2

F.3 Concept 3: Additive Manufactured Casing with Guides and Slots

Concept 3, illustrated in Figure F.3, makes use of AM for the majority of the design. The design aimed to be compact, lightweight, cost-effective and easy to manufacture. The outer casing, the telescoping arm and the revolute joint attachments at the back and front of the actuator are designed for AM. The nut is fixed to the bottom of the telescoping arm and the threaded rod rotates within the nut which causes the linear displacement of the telescoping arm. The square-shaped design restricts the relative rotation between the telescoping arm and the outer casing. This was aided by the guides of the outer casing and the slots on the telescoping arm. The guides and slots were designed for two sides of the outer casing and telescoping arm.

The disadvantage of the design is that the telescoping arm is only supported by the contact between the nut and threaded rod. The outer casing, motor and motor backplate are all held together with M3 threaded rods which run through the length of the motor body. An M8 threaded rod is used as the lead screw and a flexible coupler attaches the motor shaft to the M8 threaded rod.

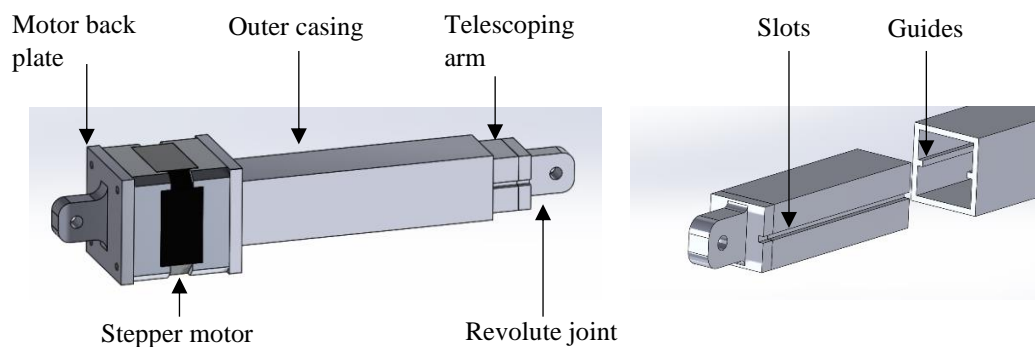


Figure F.3: Linear actuator concept 3

F.4 Linear Actuator Pugh Selection Matrix

Table F.1 displays the criteria and the scores of each of the concepts. Concept 4 was selected.

Table F.1: Linear actuator selection matrix

Aspect	Relative importance (1-5)	Concepts			
		1 (Baseline)	2	3	4
Compact	4	0	-1	1	1
Cost Effective	5	0	-1	1	1
Lightweight	3	0	-1	1	1
Easy to manufacture	3	0	1	0	0
Rigidity	5	0	1	0	1
Easy to assemble	2	0	1	0	0
Good accuracy	4	0	1	1	1
Easy to interface with joints	3	0	0	1	1
Total		0	2	19	24

Appendix G – PKM DOFs

G.1 Alpha Rotation

Figure G.1a depicts the isometric view of the PKM in its maximum alpha tilt pose. Figure G.1b depicts the front view of the PKM performing the maximum alpha tilt pose. For this condition to occur, leg 2 is closed and leg 4 and leg 6 are at a maximum stroke length. The maximum tilt angled observed is 35.73° . The minimum alpha rotation is a reflection across its x-axis; therefore, the minimum tilt angle is -35.73° . This condition occurs when leg 4 is fully retracted and leg 2 and leg 5 are fully extended.

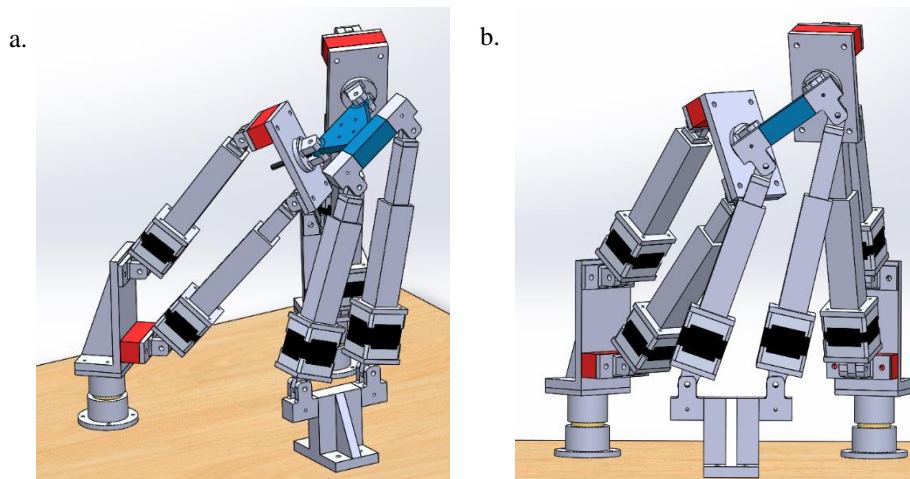


Figure G.1: Maximum alpha rotation

- Isometric view of the pose for maximum alpha rotation.
- Front view of the pose for maximum alpha rotation.

G.2 Beta Rotation

Figure G.2 shows the different views of the pose when performing the minimum beta rotation. For this pose to occur, leg 5 and leg 6 are fully extended and parallel whilst leg 2 and leg 4 are fully retracted. The bottom corners of the joint D brackets are 1 mm apart. The angle of the tilt observed is -36.8° .

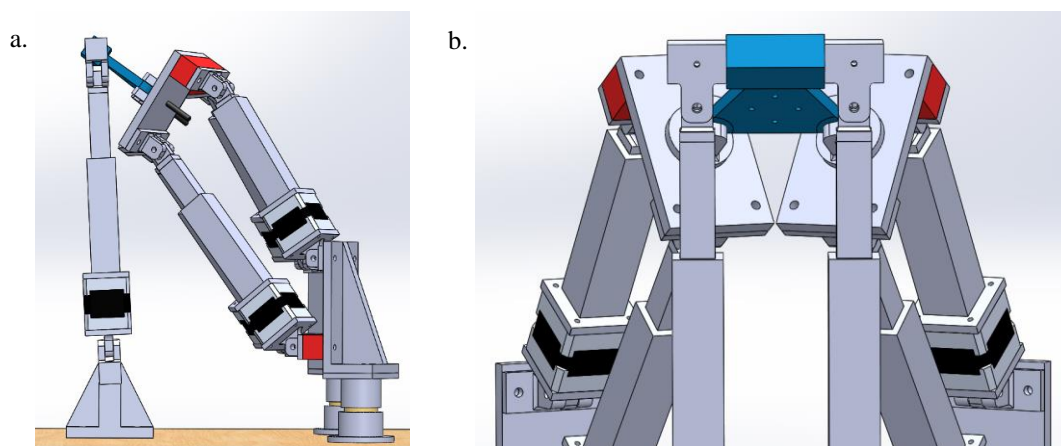


Figure G.2: Minimum beta rotation

- Side view of the pose for minimum beta rotation.
- Front view of the pose for minimum beta rotation.

The maximum beta tilt angle was 27.17° as depicted in Figure G.3. In this pose, leg 5 and leg 6 are fully retracted and leg 2 and leg 4 are fully extended. Part 2 of joint C of leg 1 and leg 2 actuator casing are 1mm apart. Part 2 of joint C of leg 3 and the actuator casing of leg 4 are 1 mm apart as shown in Figure G.3c.

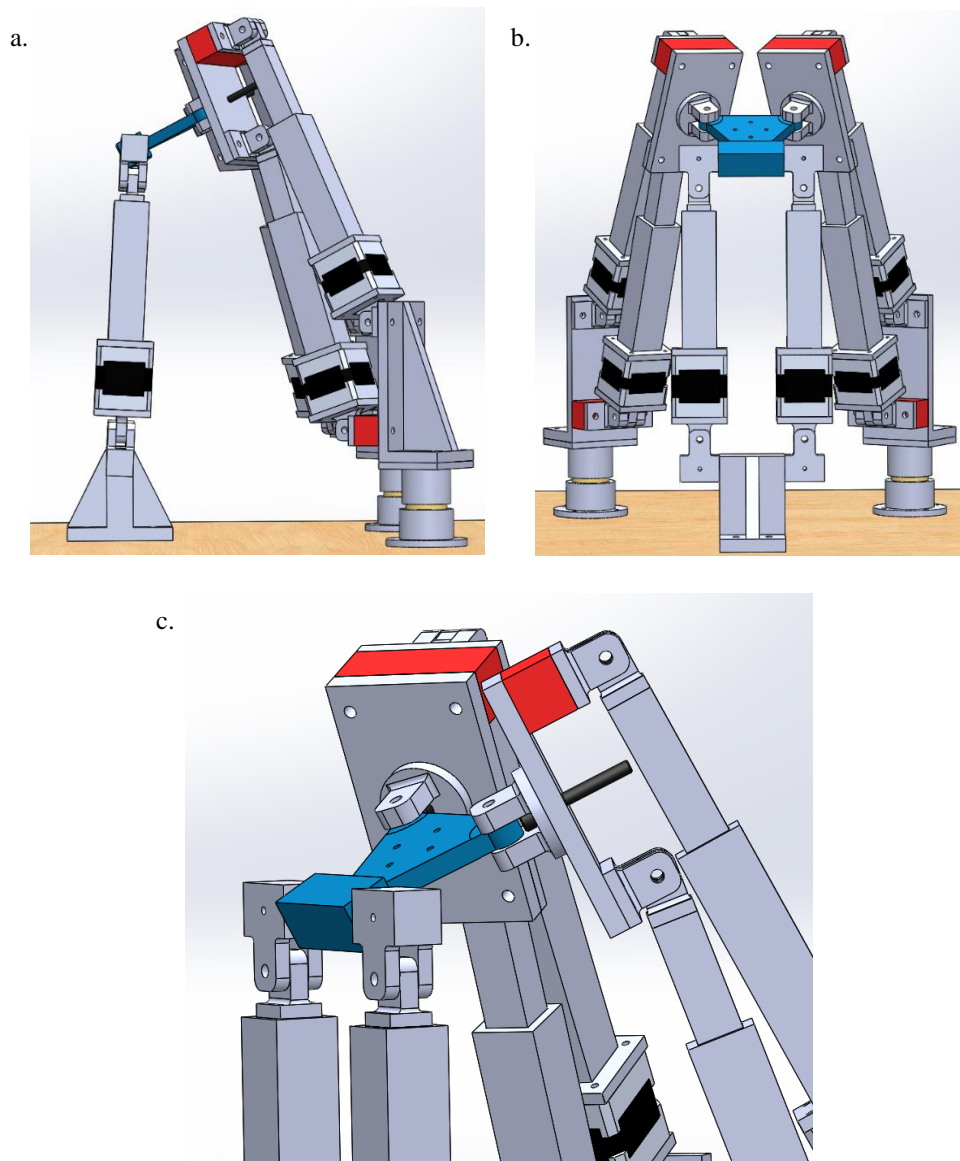


Figure G.3: Maximum beta rotation

- a. Side view of the pose for maximum beta rotation.
- b. Front view of the pose for maximum beta rotation.
- c. Close-up view of the pose for maximum beta rotation depicting the 1 mm clash clearance between leg 3 and 4.

G.3 Parasitic Gamma Rotation

Parasitic motion (rotation) only occurred when the PKM performed alpha and beta rotations simultaneously. Figure G.4a depicts an example of parasitic motion where a gamma rotation of -8.02° is induced when $\alpha = 35.83^\circ$ and $\beta = -7.36^\circ$. Figure G.4b and Figure G.4c depicts the front and side views respectively which exhibits 5 independent motions and 1 parasitic motion.

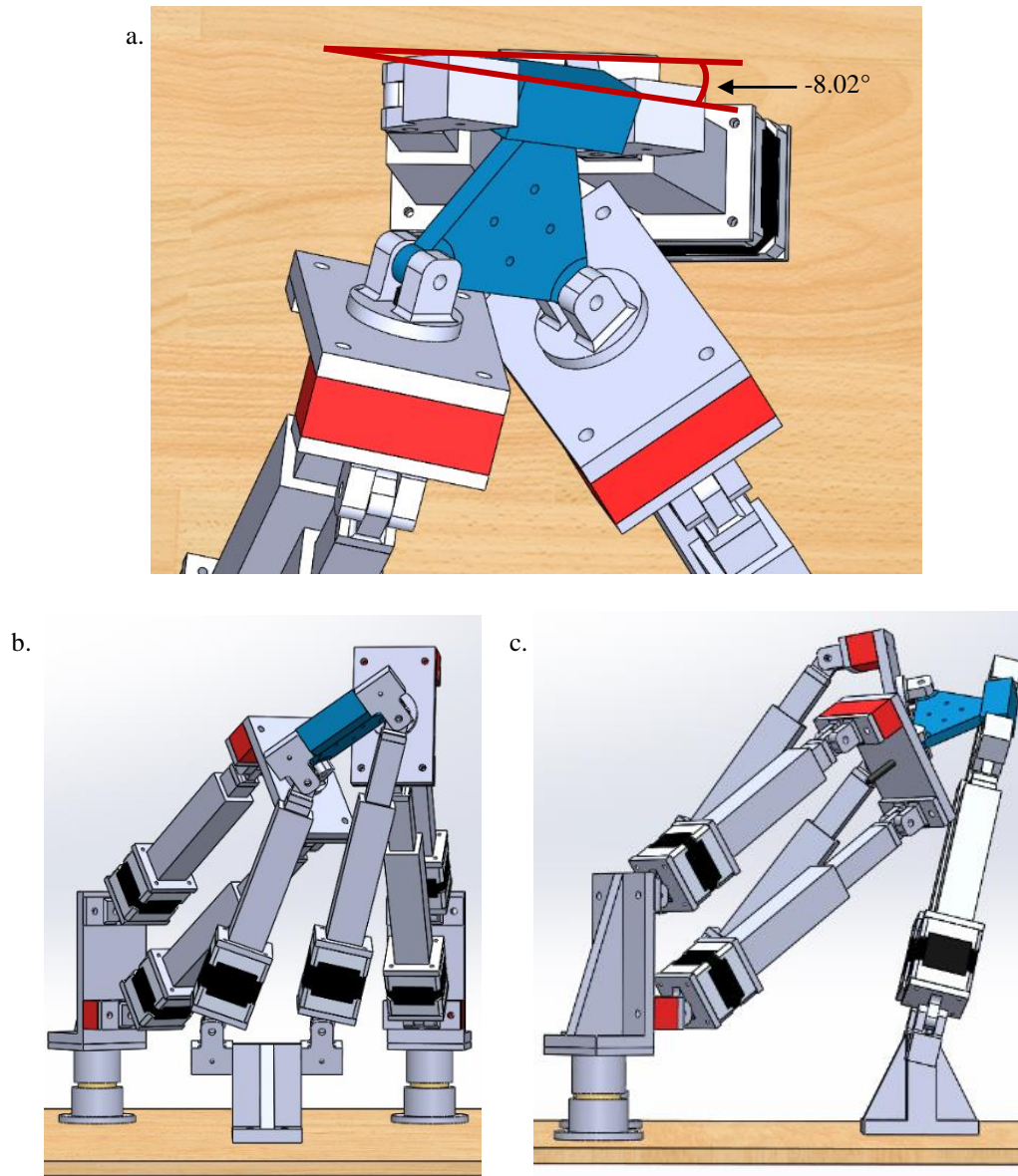


Figure G.4: Existence of parasitic motion

- Close-up view of the end effector in relation to the Joint *B* bracket variation 2 illustrating parasitic rotation.
- Front view pose exhibiting 5 independent motions and 1 parasitic motion.
- Side view pose exhibiting 5 independent motions and 1 parasitic motion.

G.4 Translation along x, y and z Axes

Figure G.5a depicts the translation along the positive x-axis. Figure G.5b illustrates the translation along the positive y-axis and Figure G.5c depicts the translation of the end effector along the positive z-axis. Figure G.5 illustrates translation without any rotation of the end effector.

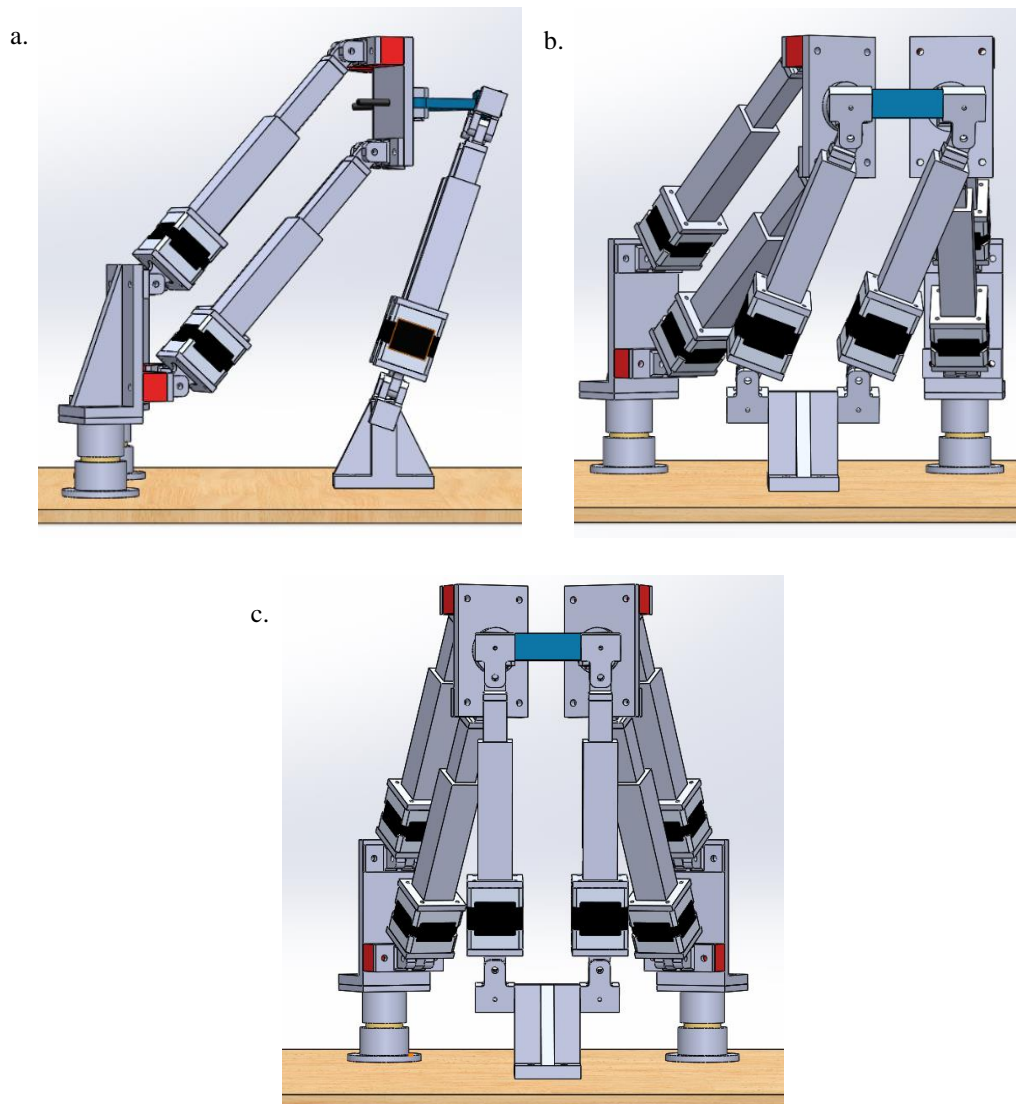
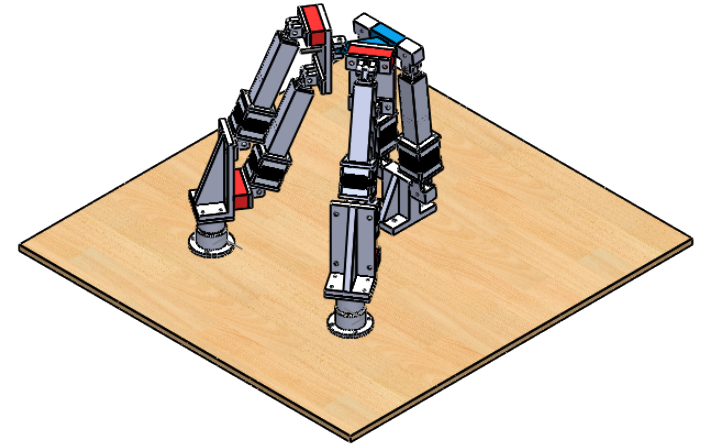


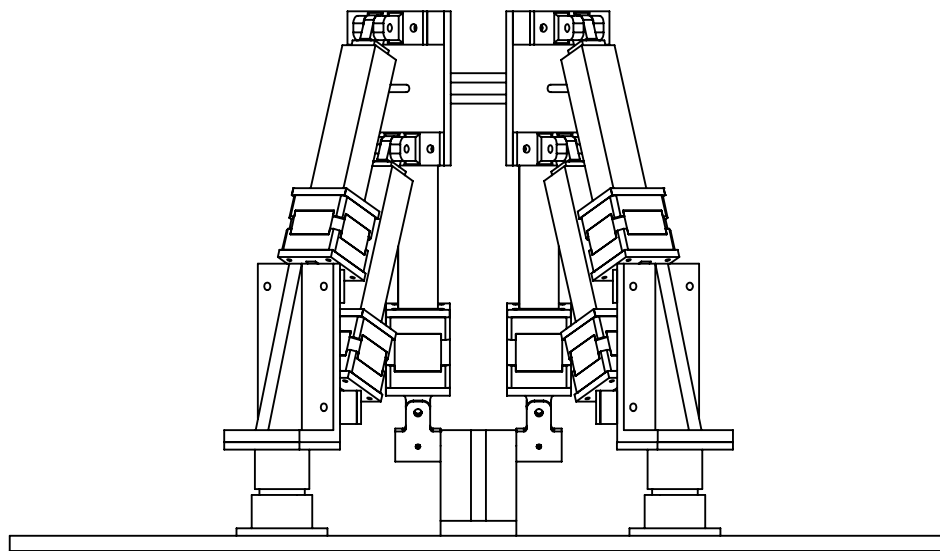
Figure G.5: Translation along the different axes

- a. Translation along the x-axis.
- b. Translation along the y-axis.
- c. Translation along the z-axis.

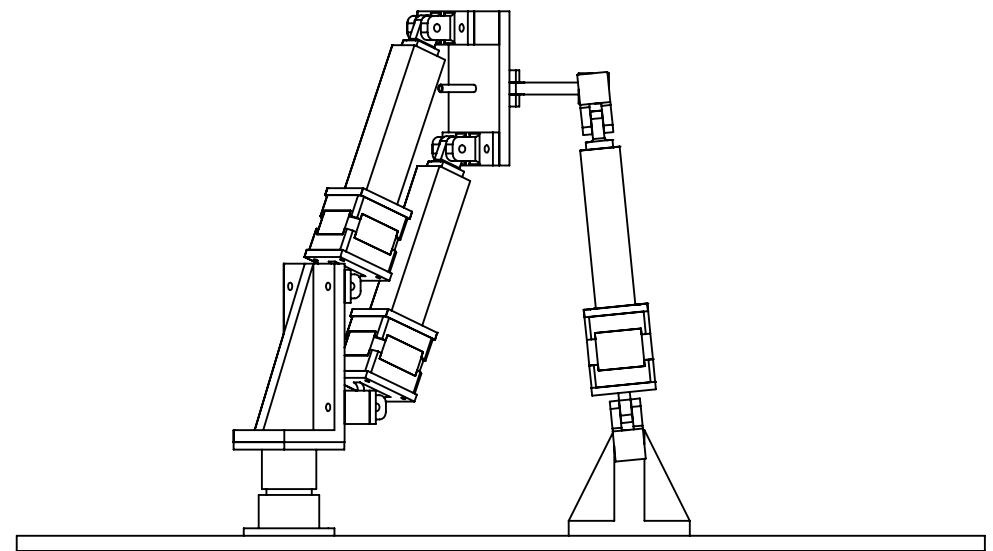
Appendix H – Engineering Drawings



ISOMETRIC VIEW
SCALE 1:10



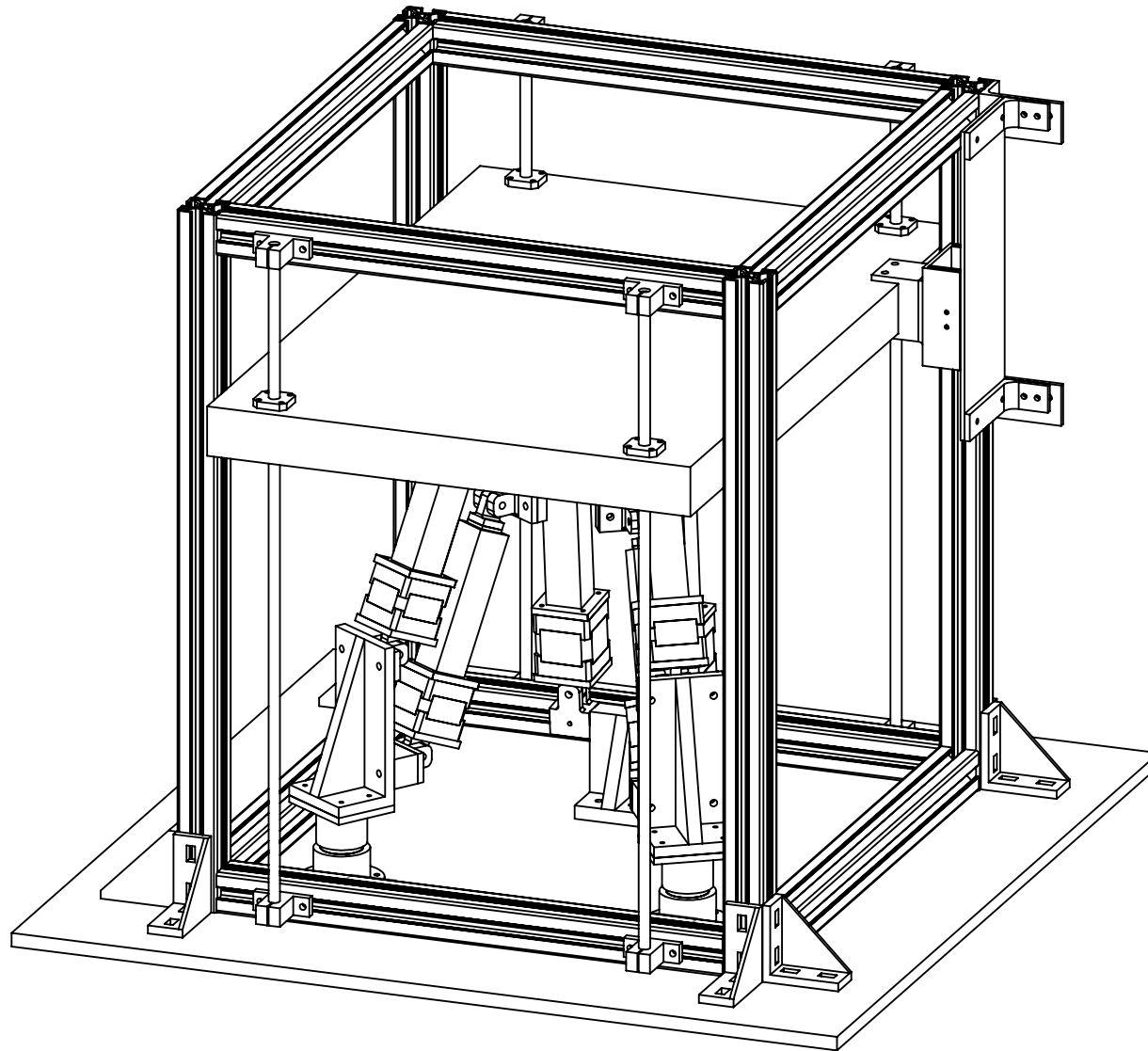
FRONT VIEW



LEFT VIEW

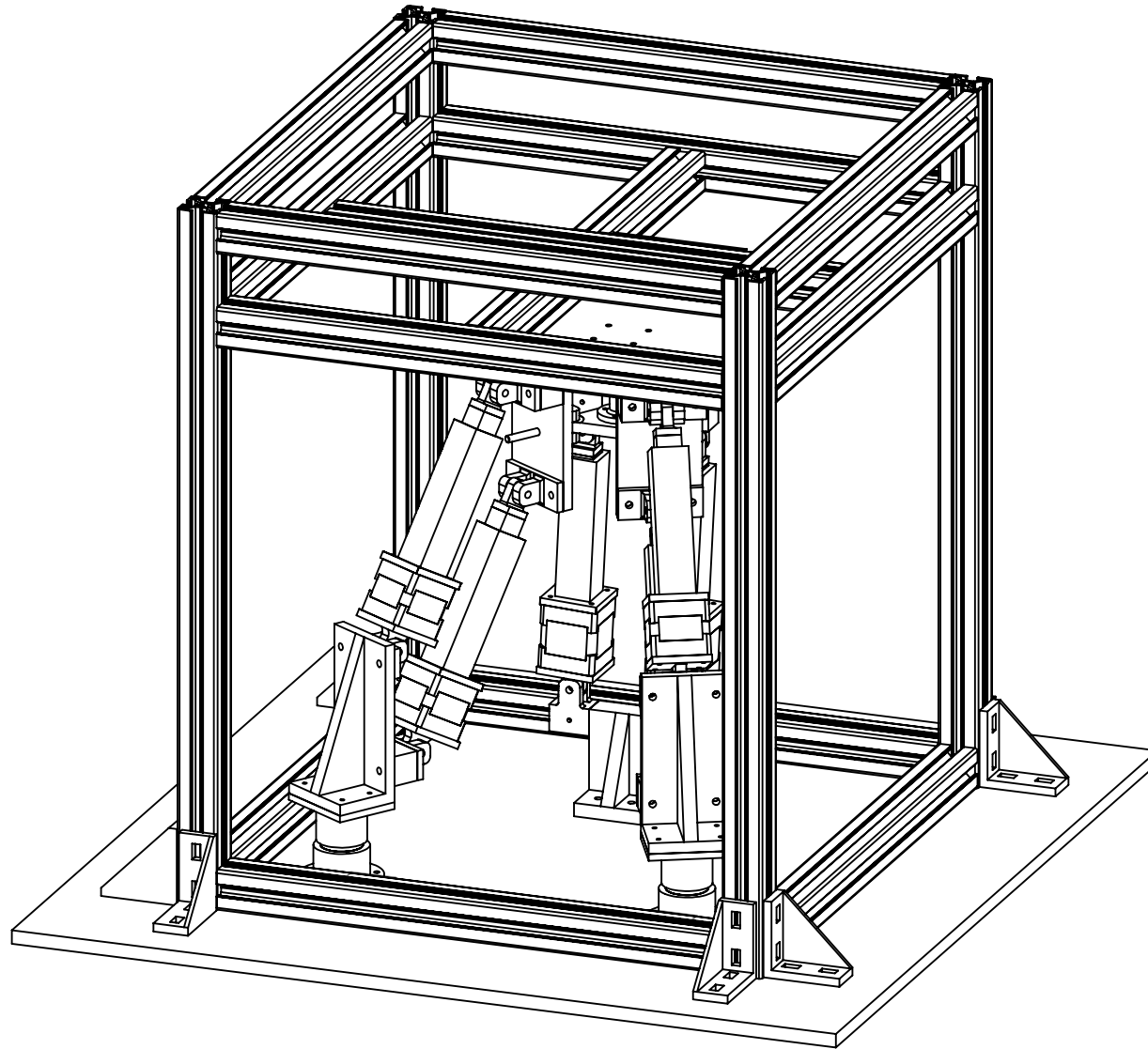
UNLESS OTHERWISE
STATED GENERAL
TOLERANCES : ± 0.25 mm
ANGLES : $\pm 0.25^\circ$

UNIVERSITY OF KWAZULU-NATAL SCHOOL OF ENGINEERING MECHANICAL ENGINEERING	MAT.: N/A	No. REQ.: 1	SCALE: 1:5	UNITS: mm	PROJECT: PKM	No.:
		DATE	CHECKED	STUDENT NAME: WESLEY DHARMALINGUM		1 / 28
	PROJECT SUPERVISOR			STUDENT No.: 209516218	TITLE: ASSEMBLY DRAWING	
	WORKSHOP TECHNICIAN			E-MAIL:		
TECHNICAL OFFICER			TEL. No.:			



UNLESS OTHERWISE
STATED GENERAL
TOLERANCES : ± 0.25 mm
ANGLES : $\pm 0.25^\circ$

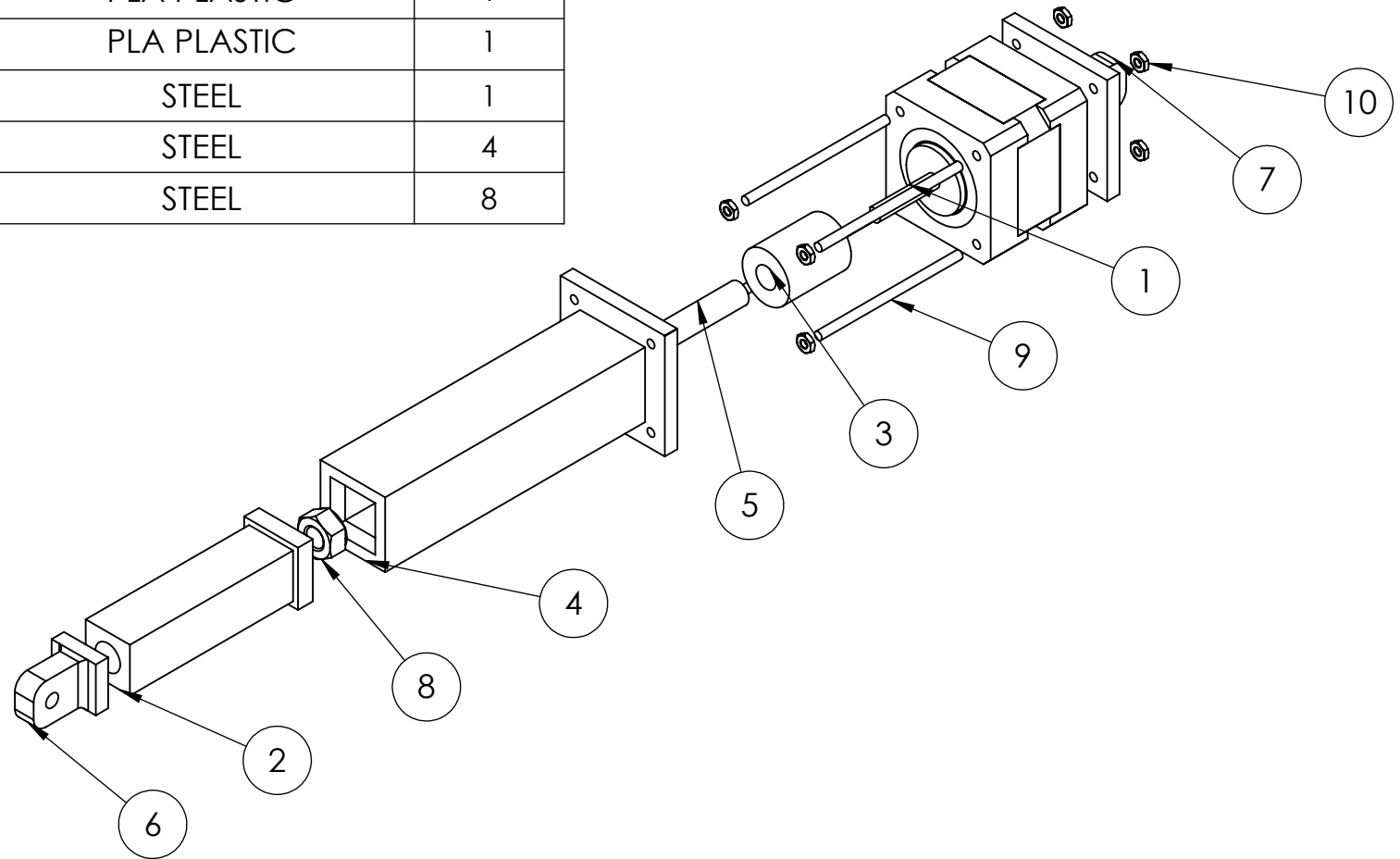
UNIVERSITY OF KWAZULU-NATAL SCHOOL OF ENGINEERING MECHANICAL ENGINEERING	MAT.: N/A	No. REQ.: 1	SCALE: 1:5	UNITS: mm	PROJECT: PKM WITH TESTING FRAME AND SENSORS	No.: 2 / 28
	DATE	CHECKED	STUDENT NAME: WESLEY DHARMALINGUM			
	PROJECT SUPERVISOR		STUDENT No.: 209516218		TITLE: ASSEMBLY DRAWING	
WORKSHOP TECHNICIAN		E-MAIL:				
TECHNICAL OFFICER			TEL. No.:			



UNLESS OTHERWISE
STATED GENERAL
TOLERANCES : ± 0.25 mm
ANGLES : $\pm 0.25^\circ$

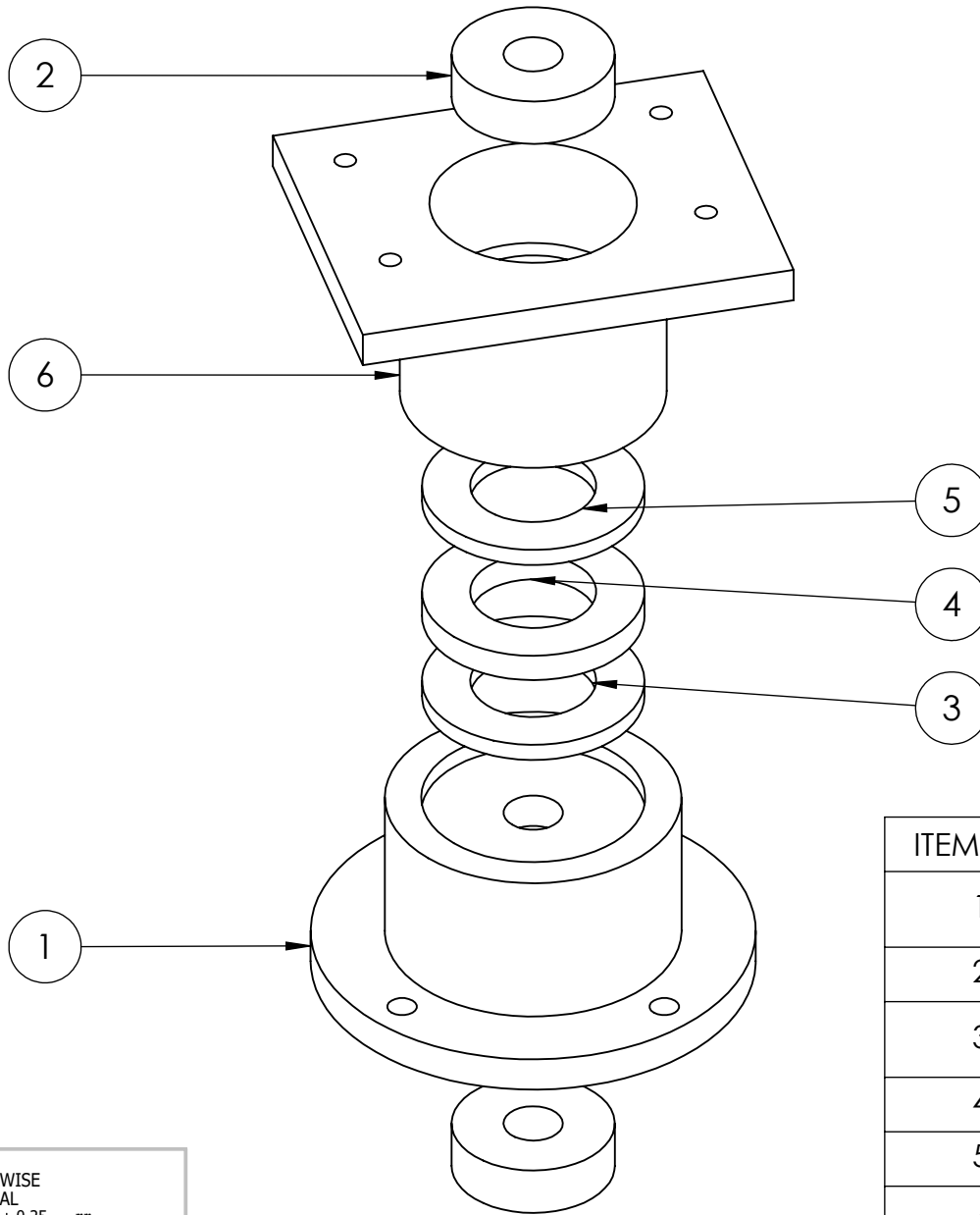
UNIVERSITY OF KWAZULU-NATAL SCHOOL OF ENGINEERING MECHANICAL ENGINEERING	MAT.: N/A	No. REQ.: 1	SCALE: 1:5	UNITS: mm	PROJECT: PKM WITH ROTATIONAL TESTING FRAME AND SENSORS	No.: 3 / 28
	DATE	CHECKED	STUDENT NAME: WESLEY DHARMALINGUM			
	PROJECT SUPERVISOR		STUDENT No.: 209516218		TITLE: ASSEMBLY DRAWING	
	WORKSHOP TECHNICIAN		E-MAIL:			
TECHNICAL OFFICER			TEL. No.:			

ITEM NO.	PART NUMBER	MATERIAL	QTY.
1	nema_17_39mm	N/A	1
2	Telescoping arm	PLA PLASTIC	1
3	Flexible Coupler	ALUMINIUM	1
4	Actuator outer casing	PLA PLASTIC	1
5	Threaded rod	STEEL	1
6	Joint C part 2	PLA PLASTIC	1
7	Joint B part 2	PLA PLASTIC	1
8	ISO - 4032 - M8 - W - N	STEEL	1
9	M3 threaded rod	STEEL	4
10	ISO - 4035 - M3 - N	STEEL	8



UNLESS OTHERWISE
STATED GENERAL
TOLERANCES : ± 0.25 mm
ANGLES : $\pm 0.25^\circ$

UNIVERSITY OF KWAZULU-NATAL SCHOOL OF ENGINEERING MECHANICAL ENGINEERING	MAT.: N/A	No. REQ.: 6	SCALE: 1:2	UNITS: mm	PROJECT: LINEAR ACTUATOR	No.:
	DATE	CHECKED	STUDENT NAME: WESLEY DHARMALINGUM			4 / 28
	PROJECT SUPERVISOR		STUDENT No.: 209516218		TITLE: EXPLODED VIEW	
	WORKSHOP TECHNICIAN		E-MAIL:			
TECHNICAL OFFICER			TEL. No.:			

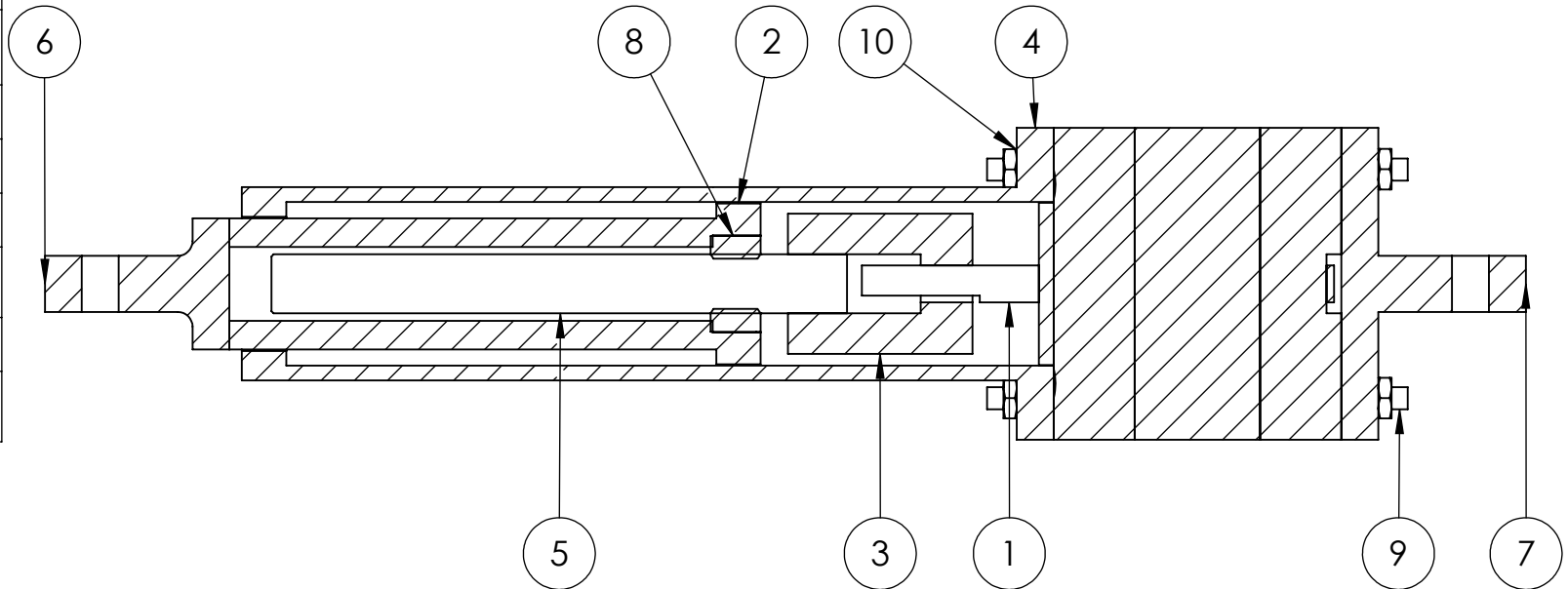


ITEM NO.	PART NUMBER	MATERIAL	QTY.
1	thrust bearing bottom bracket	PLA PLASTIC	1
2	Radial bearing	STEEL	2
3	Thrust bearing bottom	STEEL	1
4	Thrust bearing middle	STEEL	1
5	Thrust bearing top	STEEL	1
6	thrust bearing top bracket	PLA PLASTIC	1

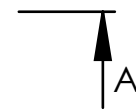
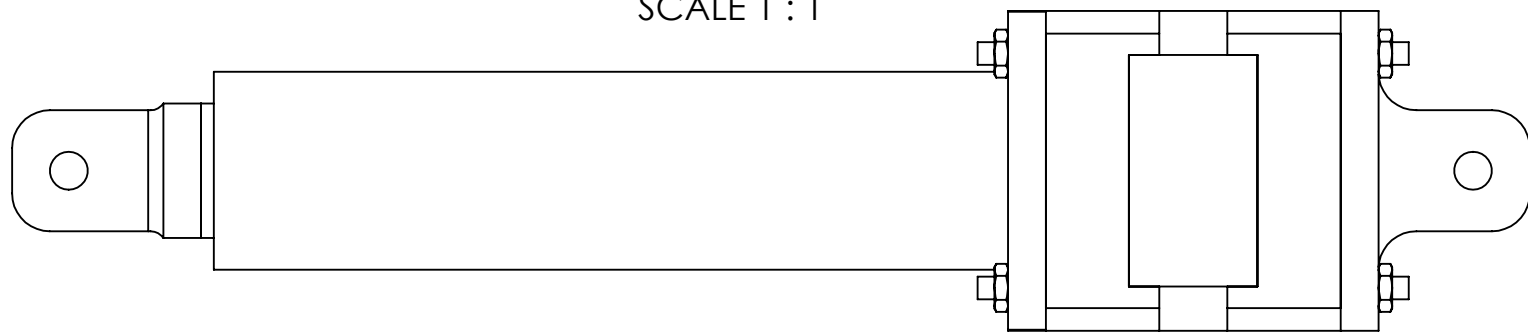
UNLESS OTHERWISE STATED GENERAL TOLERANCES : ± 0.25 mm ANGLES : $\pm 0.25^\circ$

UNIVERSITY OF KWAZULU-NATAL SCHOOL OF ENGINEERING MECHANICAL ENGINEERING	MAT.: N/A	No. REQ.: 2	SCALE: 1:1	UNITS: mm	PROJECT: THRUST BEARING JOINT	No.: 5 / 28
	DATE	CHECKED	STUDENT NAME: WESLEY DHARMALINGUM			
	PROJECT SUPERVISOR		STUDENT No.: 209516218		TITLE: EXPLODED VIEW	
	WORKSHOP TECHNICIAN		E-MAIL:			
TECHNICAL OFFICER			TEL. No.:			

ITEM NO.	PART NUMBER
1	nema_17_39mm
2	Telescoping arm
3	Flexible Coupler
4	Actuator outer casing
5	Threaded rod
6	Joint C part 2
7	Joint B part 2
8	ISO - 4032 - M8 - W - N
9	M3 threaded rod
10	ISO - 4035 - M3 - N

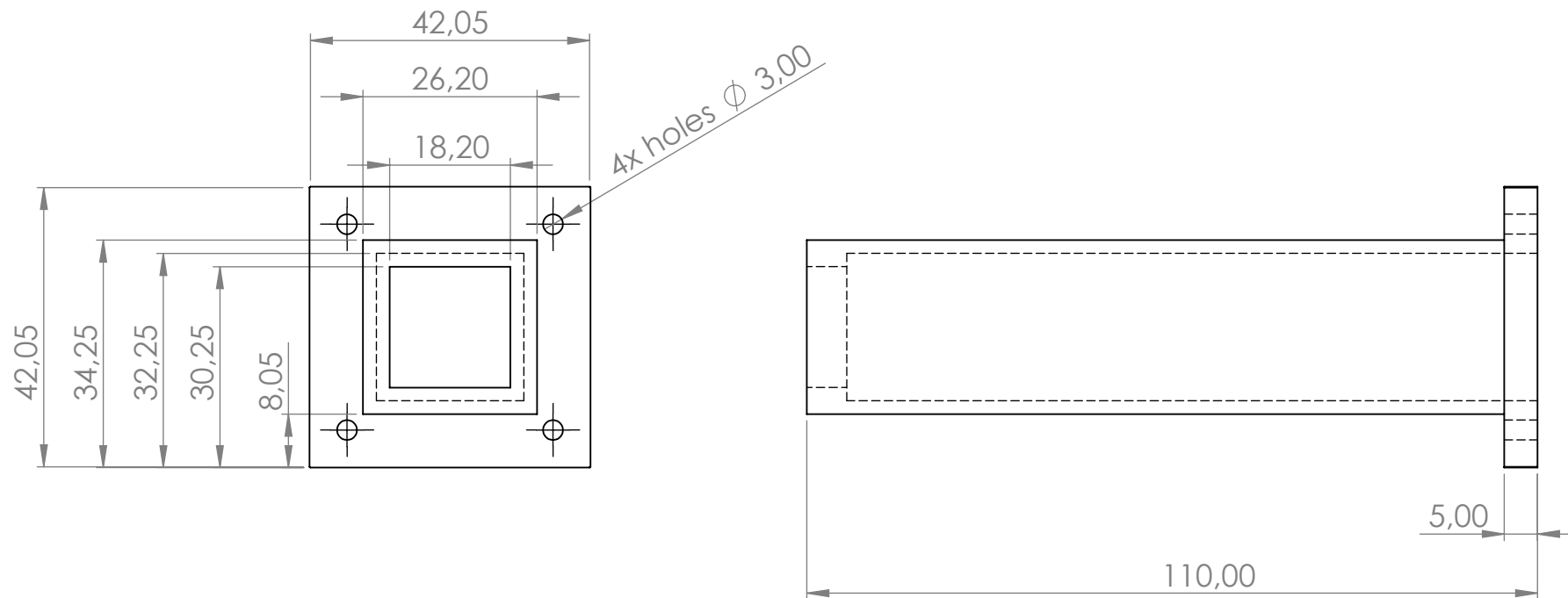


SECTION A-A
SCALE 1 : 1



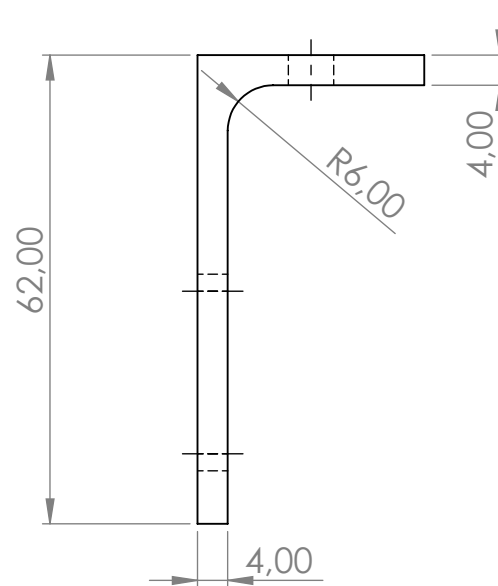
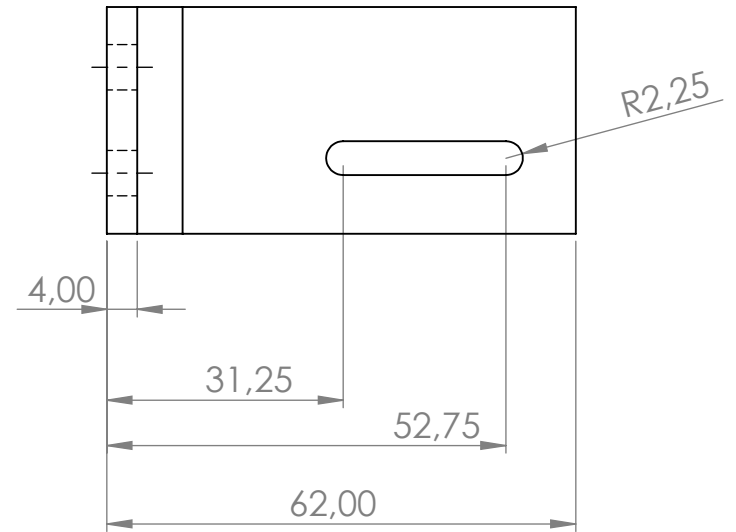
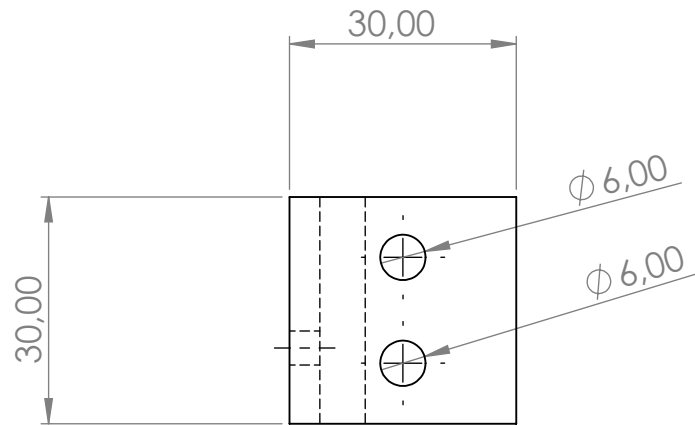
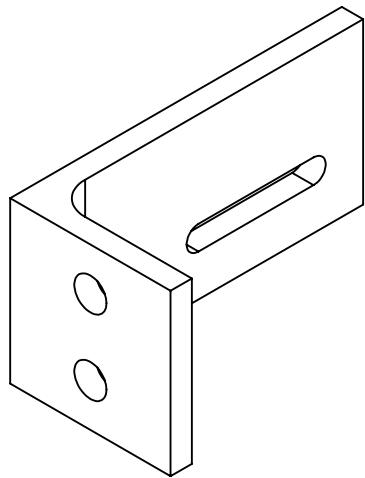
UNLESS OTHERWISE STATED GENERAL TOLERANCES : ± 0.25 mm
ANGLES : $\pm 0.25^\circ$

UNIVERSITY OF KWAZULU-NATAL SCHOOL OF ENGINEERING MECHANICAL ENGINEERING	MAT.: N/A	No. REQ.: 6	SCALE: 1:1	UNITS: mm	PROJECT: LINEAR ACTUATOR	No.:
		DATE	CHECKED	STUDENT NAME: WESLEY DHARMALINGUM		6 / 28
	PROJECT SUPERVISOR			STUDENT No.: 209516218	TITLE: SECTIONED VIEW	
	WORKSHOP TECHNICIAN			E-MAIL:		
TECHNICAL OFFICER				TEL. No.:		



UNLESS OTHERWISE
STATED GENERAL
TOLERANCES : $\pm 0,25$ mm
ANGLES : $\pm 0,25^\circ$

UNIVERSITY OF KWAZULU-NATAL SCHOOL OF ENGINEERING MECHANICAL ENGINEERING	MAT.: PLA PLASTIC	No. REQ.: 6	SCALE: 1:1	UNITS: mm	PROJECT: ACTUATOR OUTER CASING	No.: 7 / 28
		DATE	CHECKED	STUDENT NAME: WESLEY DHARMALINGUM	TITLE: DETAILED DRAWING	
	PROJECT SUPERVISOR			STUDENT No.: 209516218		
	WORKSHOP TECHNICIAN			E-MAIL:		
	TECHNICAL OFFICER			TEL. No.:		



UNLESS OTHERWISE
STATED GENERAL
TOLERANCES : $\pm 0,25$ mm
ANGLES : $\pm 0,25^\circ$

UNIVERSITY OF KWAZULU-NATAL

SCHOOL OF ENGINEERING

MECHANICAL ENGINEERING

MAT.: PLA PLASTIC

DATE

PROJECT SUPERVISOR

WORKSHOP TECHNICIAN

TECHNICAL OFFICER

No. REQ.: 2

CHECKED

SCALE: 1:1

STUDENT NAME: WESLEY DHARMALINGUM

STUDENT No.: 209516218

E-MAIL:

TEL. No.:

UNITS: mm

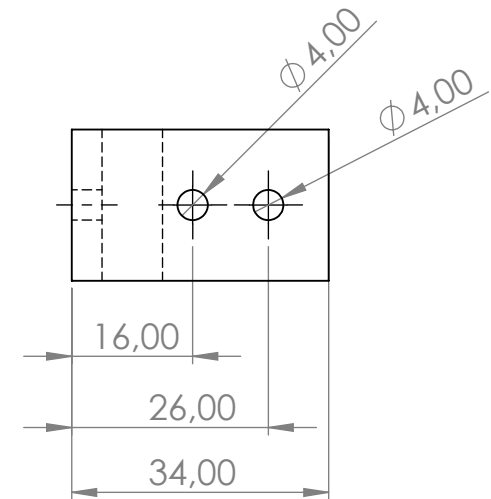
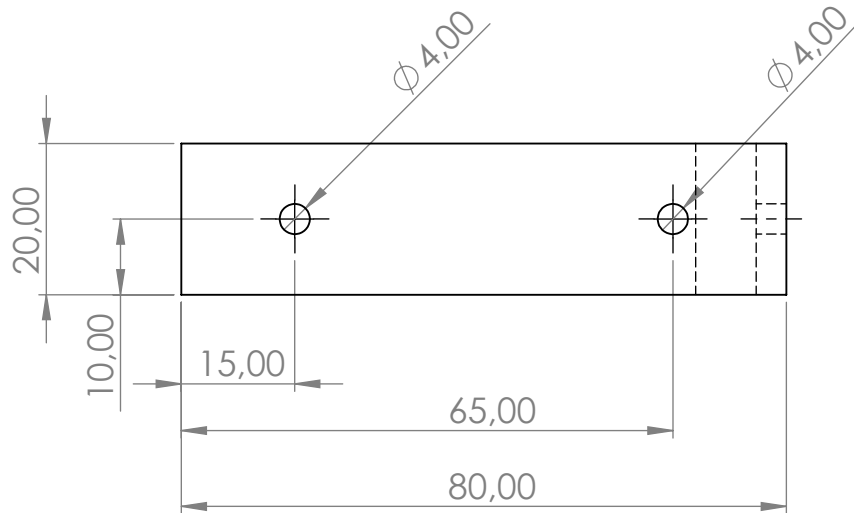
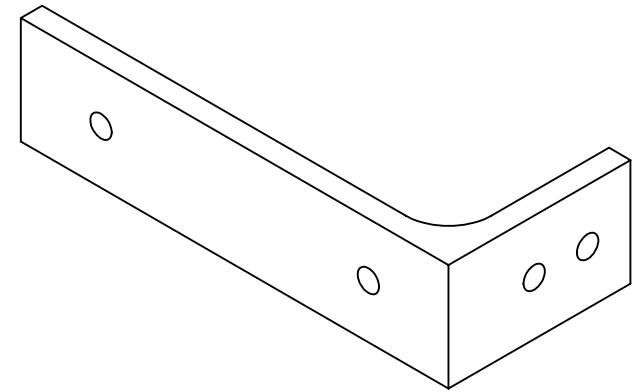
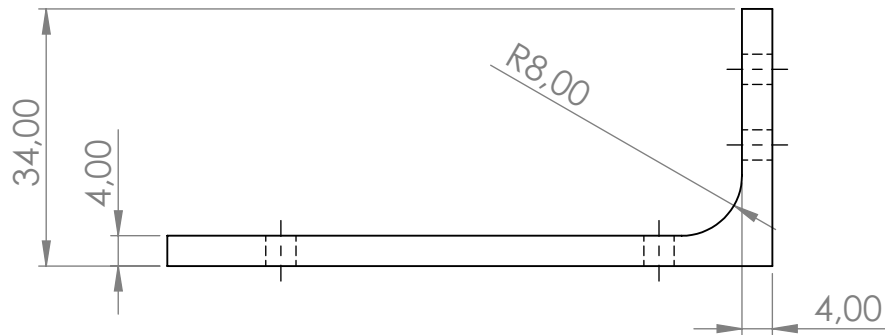
PROJECT: ADJUSTABLE BRACKET PART 1

TITLE: DETAILED DRAWING

No.:

8 / 28





UNLESS OTHERWISE
STATED GENERAL
TOLERANCES : $\pm 0,25$ mm
ANGLES : $\pm 0,25^\circ$

UNIVERSITY OF KWAZULU-NATAL
SCHOOL OF ENGINEERING
MECHANICAL ENGINEERING

MAT.: PLA PLASTIC

No. REQ.: 2

SCALE: 1:1

UNITS: mm

PROJECT: ADJUSTABLE BRACKET PART 2

No.:

DATE

CHECKED

STUDENT NAME: WESLEY DHARMALINGUM

9 / 28

PROJECT SUPERVISOR

STUDENT No.: 209516218

WORKSHOP TECHNICIAN

E-MAIL:

TITLE: DETAILED DRAWING

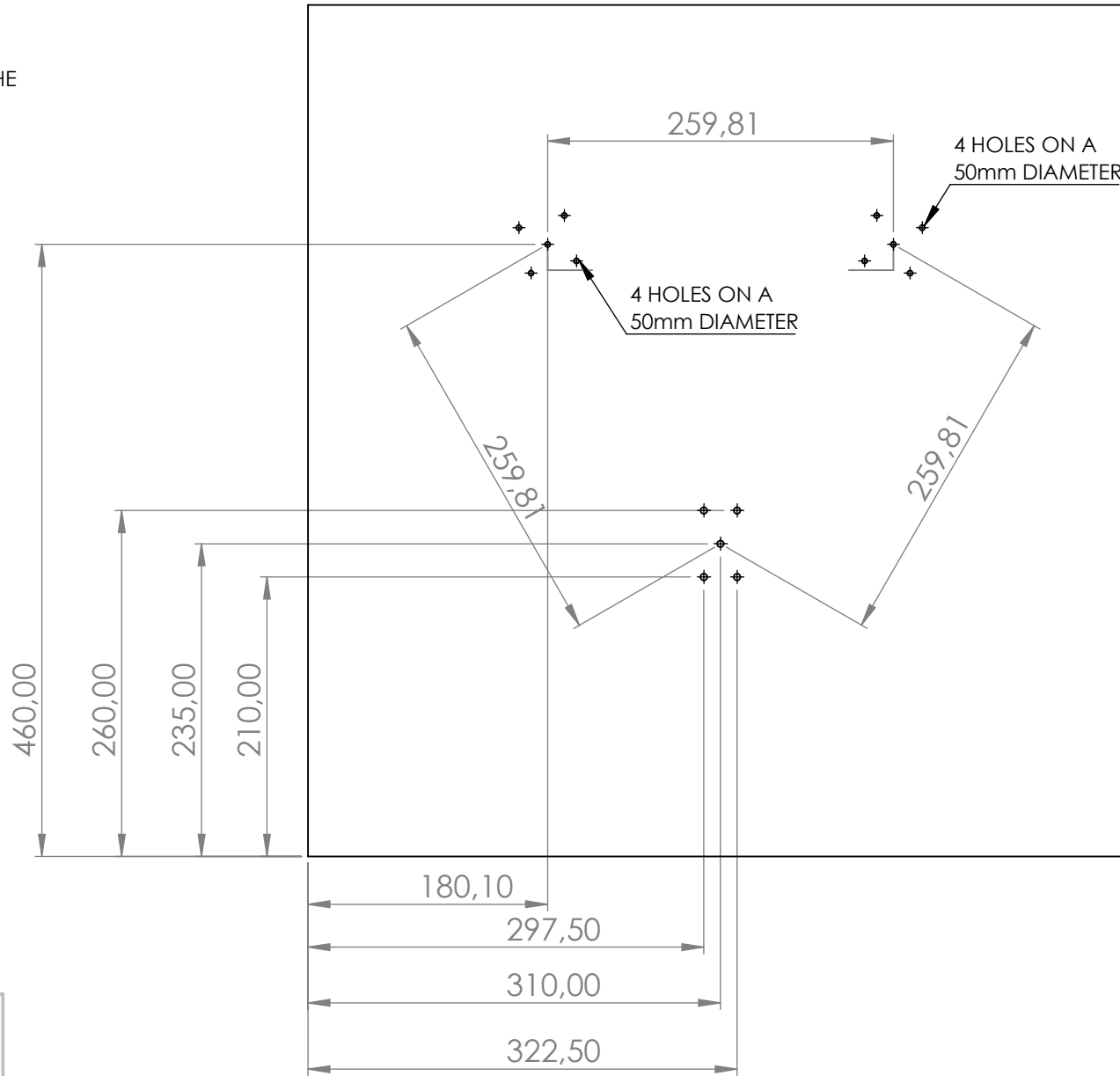
TECHNICAL OFFICER

TEL. No.:



ALL HOLES HAVE A DIAMETER OF 4 mm

THE THICKNESS OF THE BASE IS 10 mm



UNLESS OTHERWISE STATED GENERAL TOLERANCES : $\pm 0,25$ mm ANGLES : $\pm 0,25^\circ$

UNIVERSITY OF KWAZULU-NATAL

SCHOOL OF ENGINEERING

MECHANICAL ENGINEERING

MAT.: PLA PLASTIC

DATE

PROJECT SUPERVISOR

WORKSHOP TECHNICIAN

TECHNICAL OFFICER

No. REQ.: 1

CHECKED

SCALE: 1:5

STUDENT NAME: WESLEY DHARMALINGUM

STUDENT No.: 209516218

E-MAIL:

TEL. No.:

UNITS: mm

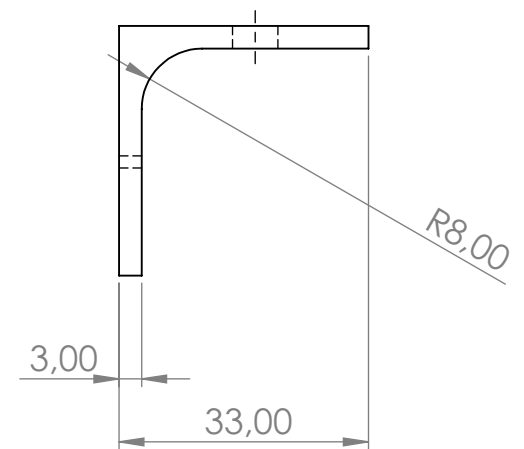
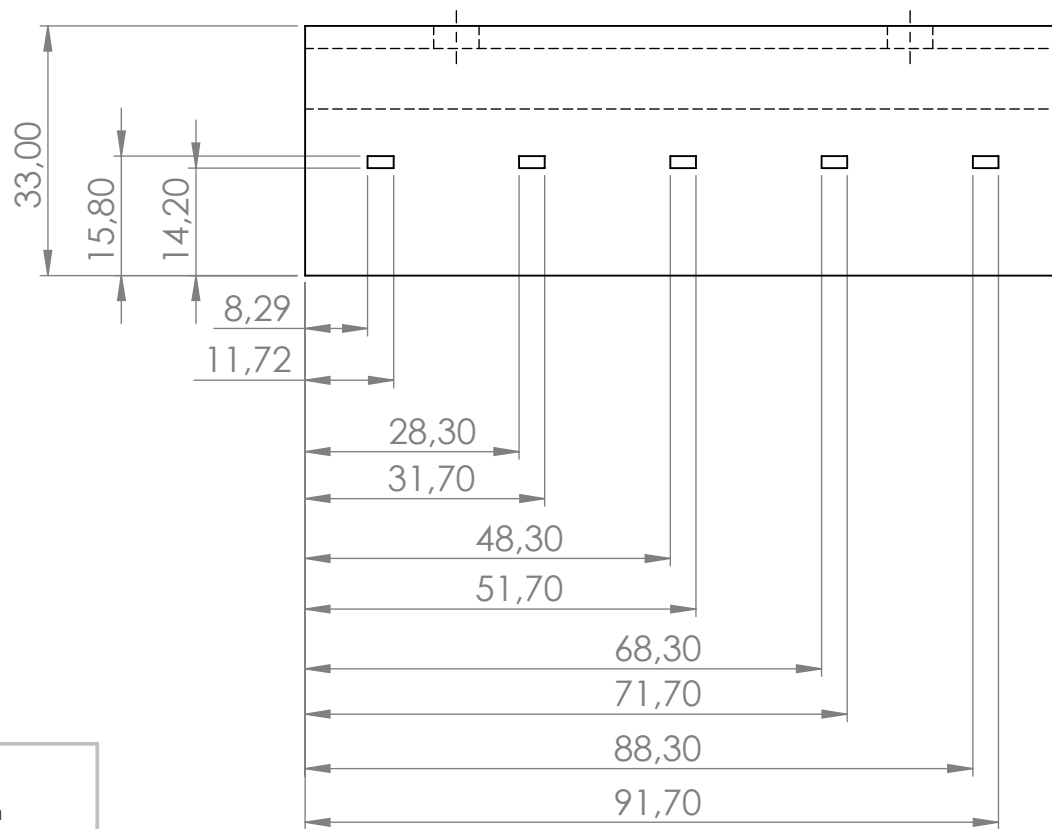
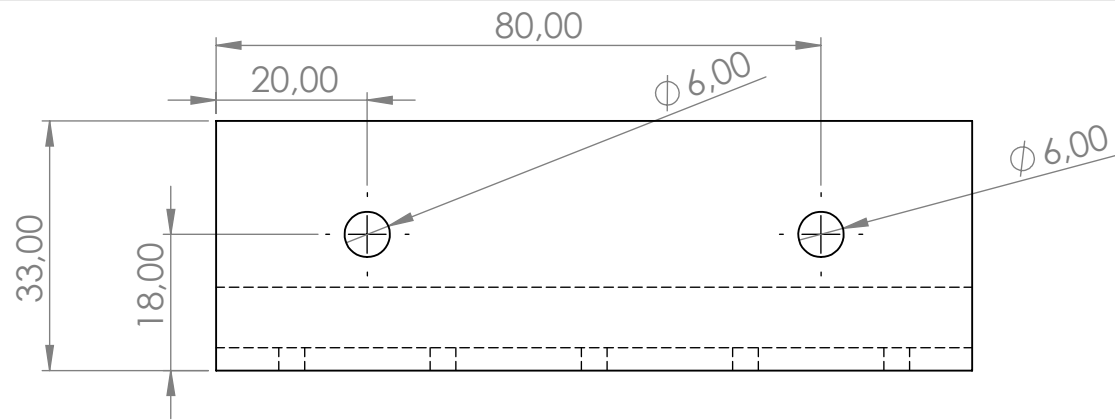
PROJECT: BASE

TITLE: DETAILED DRAWING

No.:

10 / 28





UNLESS OTHERWISE
STATED GENERAL
TOLERANCES : $\pm 0,25$ mm
ANGLES : $\pm 0,25^\circ$

UNIVERSITY OF KWAZULU-NATAL

SCHOOL OF ENGINEERING

MECHANICAL ENGINEERING

MAT.: PLA PLASTIC

DATE

PROJECT SUPERVISOR

WORKSHOP TECHNICIAN

TECHNICAL OFFICER

No. REQ.: 2

CHECKED

SCALE: 1:1

STUDENT NAME: WESLEY DHARMALINGUM

STUDENT No.: 209516218

E-MAIL:

TEL. No.:

UNITS: mm

PROJECT: DEPTH MEASURING BRACKET

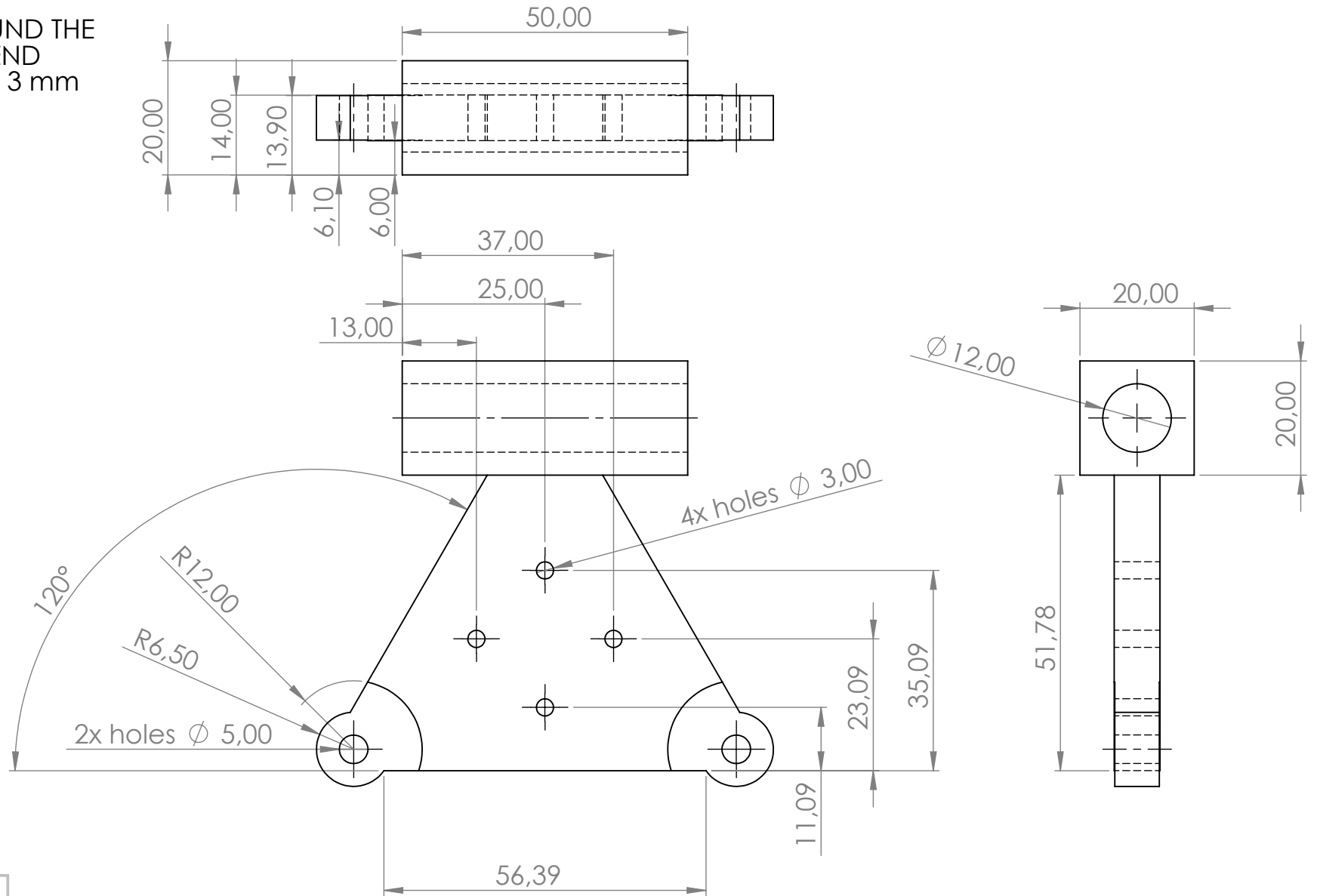
TITLE: DETAILED DRAWING

No.:

11 / 28



ALL HOLES AROUND THE CENTRE OF THE END EFFECTOR HAS A 3 mm DIAMETER



UNLESS OTHERWISE STATED GENERAL TOLERANCES : $\pm 0,25$ mm ANGLES : $\pm 0,25^\circ$

UNIVERSITY OF KWAZULU-NATAL

SCHOOL OF ENGINEERING

MECHANICAL ENGINEERING

MAT.: PLA PLASTIC

DATE

PROJECT SUPERVISOR

WORKSHOP TECHNICIAN

TECHNICAL OFFICER

No. REQ.: 1

CHECKED

SCALE: 1:1

STUDENT NAME: WESLEY DHARMALINGUM

STUDENT No.: 209516218

E-MAIL:

TEL. No.:

UNITS: mm

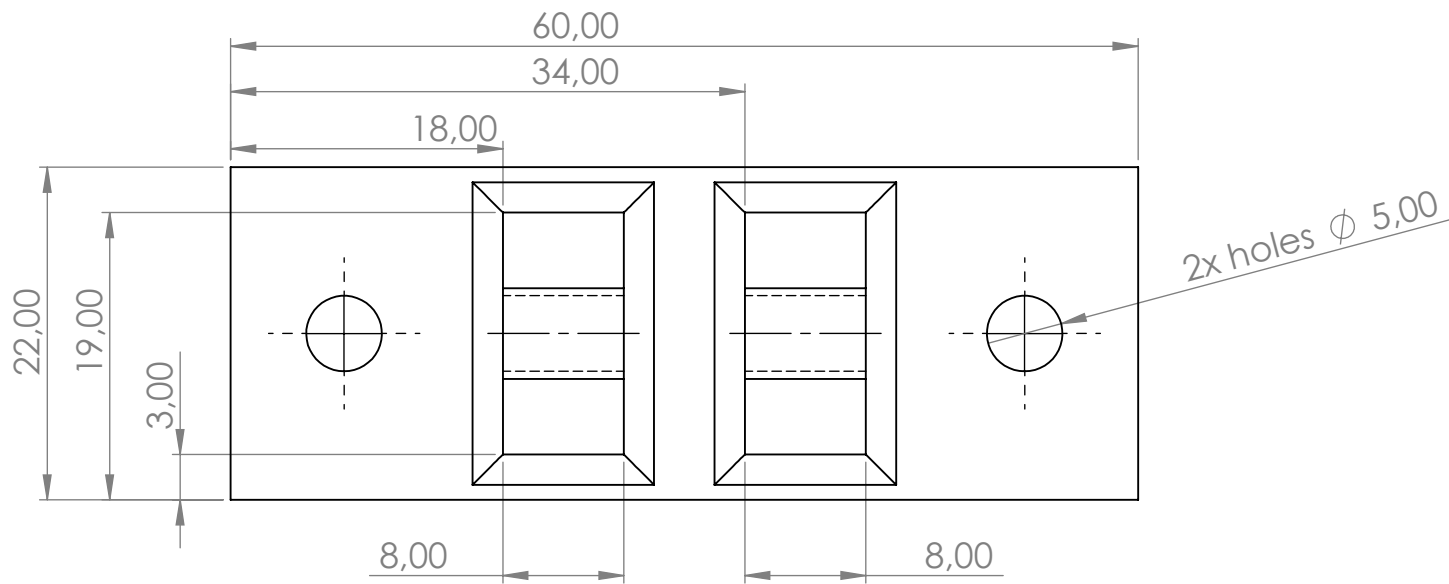
PROJECT: END EFFECTOR

TITLE: DETAILED DRAWING

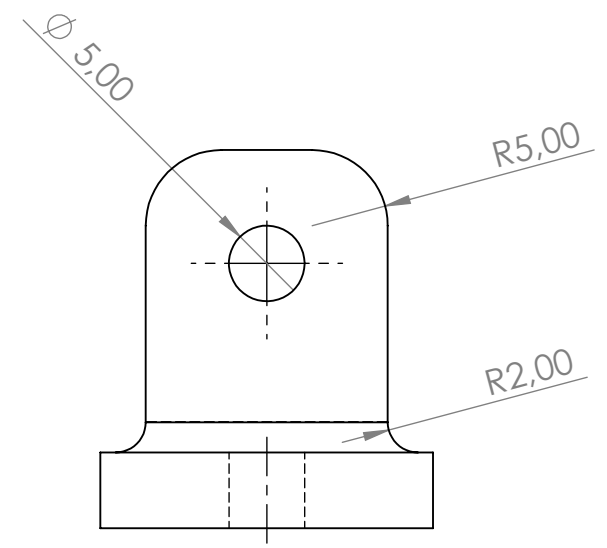
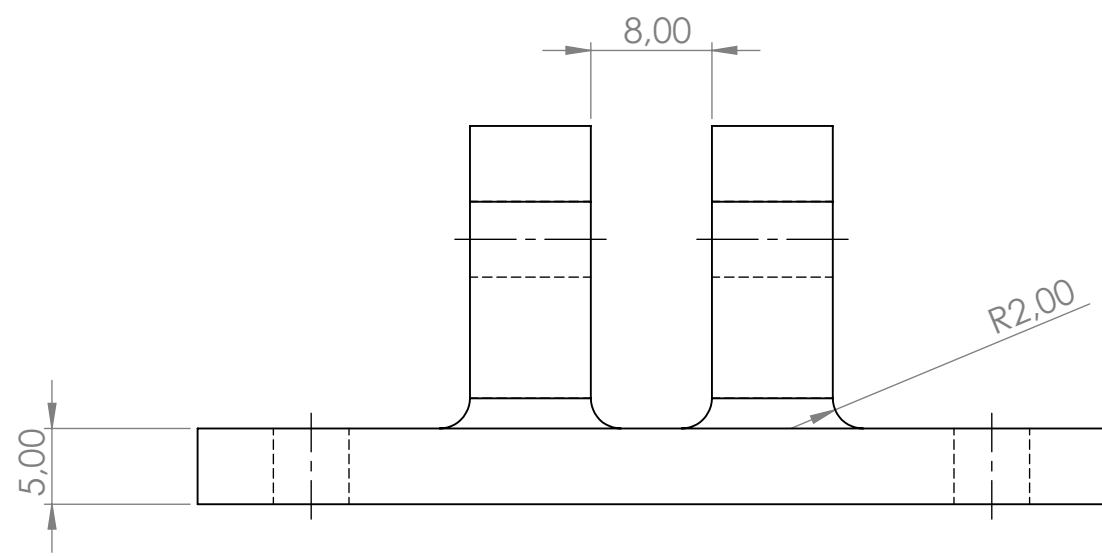
No.:

12 / 28



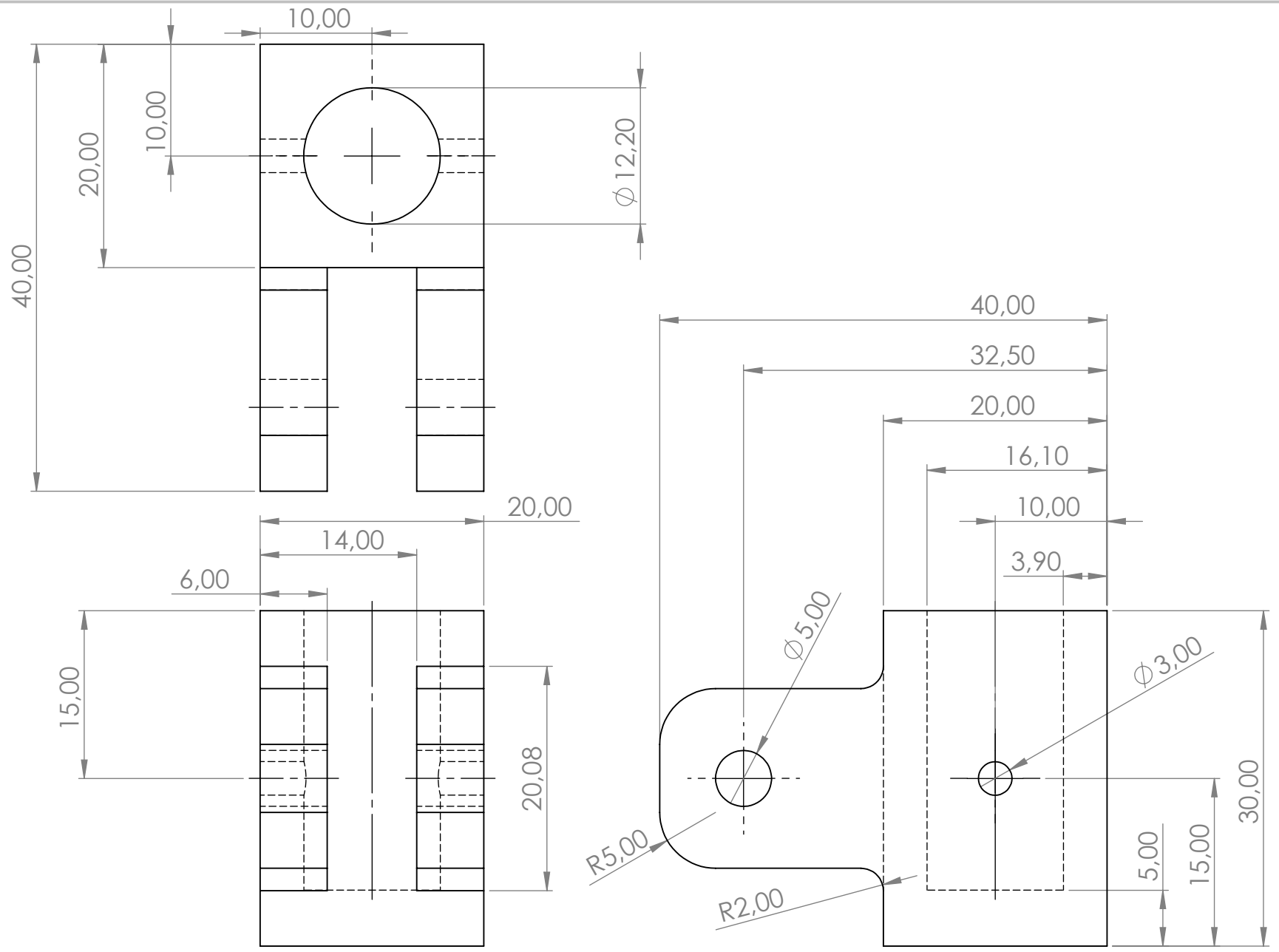


2x holes ϕ 5,00



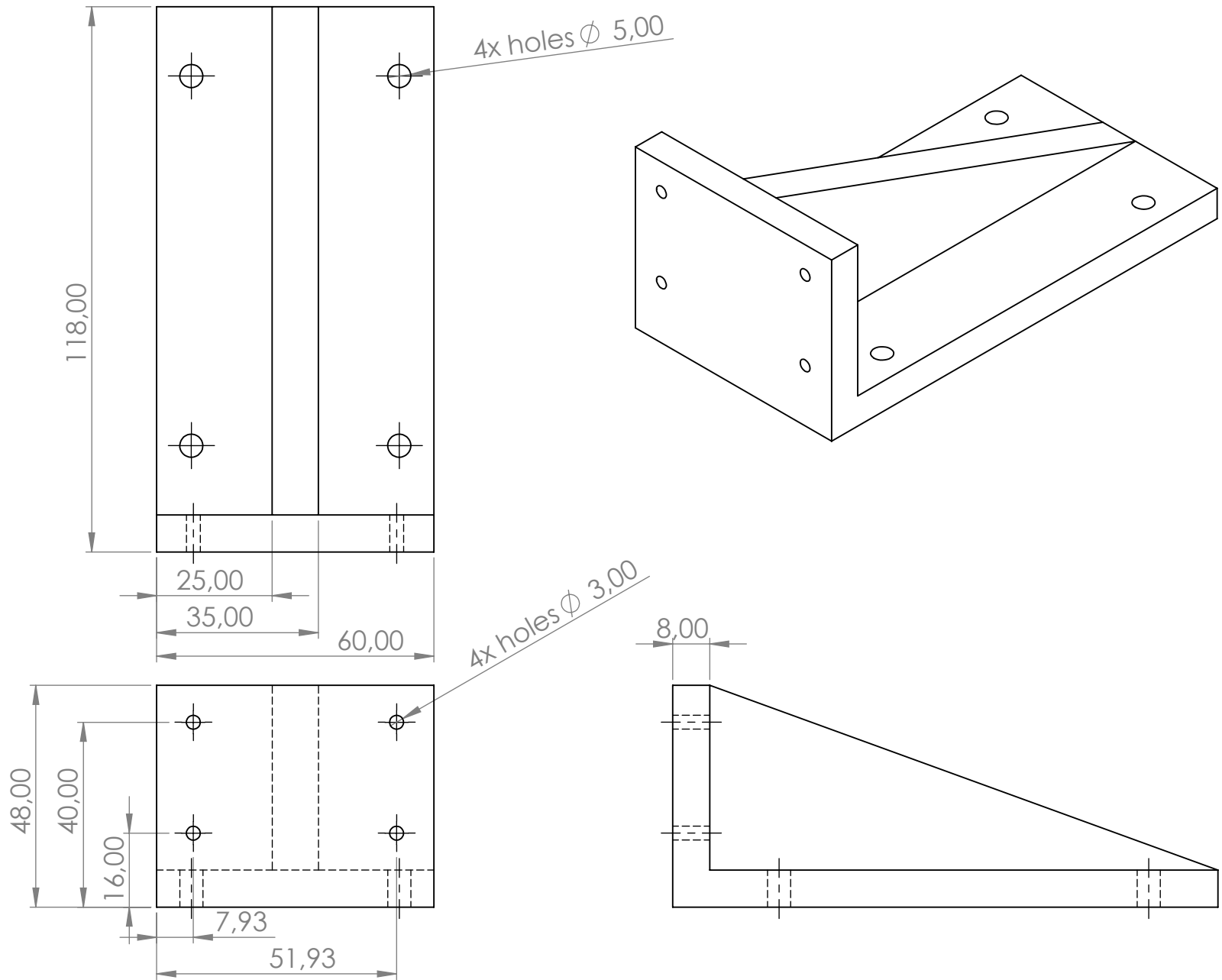
UNLESS OTHERWISE
STATED GENERAL
TOLERANCES : $\pm 0,25$ mm
ANGLES : $\pm 0,25^\circ$

UNIVERSITY OF KWAZULU-NATAL SCHOOL OF ENGINEERING MECHANICAL ENGINEERING	MAT.: PLA PLASTIC	No. REQ.: 8	SCALE: 2 : 1	UNITS: mm	PROJECT: JOINT B AND C VARIATION 1 PART 1	No.: 13 / 28
	DATE	CHECKED	STUDENT NAME: WESLEY DHARMALINGUM			
	PROJECT SUPERVISOR		STUDENT No.: 209516218		TITLE: DETAILED DRAWING	
	WORKSHOP TECHNICIAN		E-MAIL:			
TECHNICAL OFFICER			TEL. No.:			



UNLESS OTHERWISE STATED GENERAL TOLERANCES : $\pm 0,25$ mm ANGLES : $\pm 0,25^\circ$

UNIVERSITY OF KWAZULU-NATAL SCHOOL OF ENGINEERING MECHANICAL ENGINEERING	MAT.: PLA PLASTIC	No. REQ.: 4	SCALE: 2:1	UNITS: mm	PROJECT: JOINT B AND C VARIATION 2 PART 1	No.: 14 / 28
	DATE	CHECKED	STUDENT NAME: WESLEY DHARMALINGUM			
	PROJECT SUPERVISOR		STUDENT No.: 209516218		TITLE: DETAILED DRAWING	
	WORKSHOP TECHNICIAN		E-MAIL:			
TECHNICAL OFFICER			TEL. No.:			



UNLESS OTHERWISE
STATED GENERAL
TOLERANCES : $\pm 0,25$ mm
ANGLES : $\pm 0,25^\circ$

UNIVERSITY OF KWAZULU-NATAL

SCHOOL OF ENGINEERING

MECHANICAL ENGINEERING

MAT.: PLA PLASTIC

DATE

PROJECT SUPERVISOR

WORKSHOP TECHNICIAN

TECHNICAL OFFICER

No. REQ.: 2

CHECKED

SCALE: 1 : 1.25

UNITS: mm

STUDENT NAME: WESLEY DHARMALINGUM

STUDENT No.: 209516218

E-MAIL:

TEL. No.:

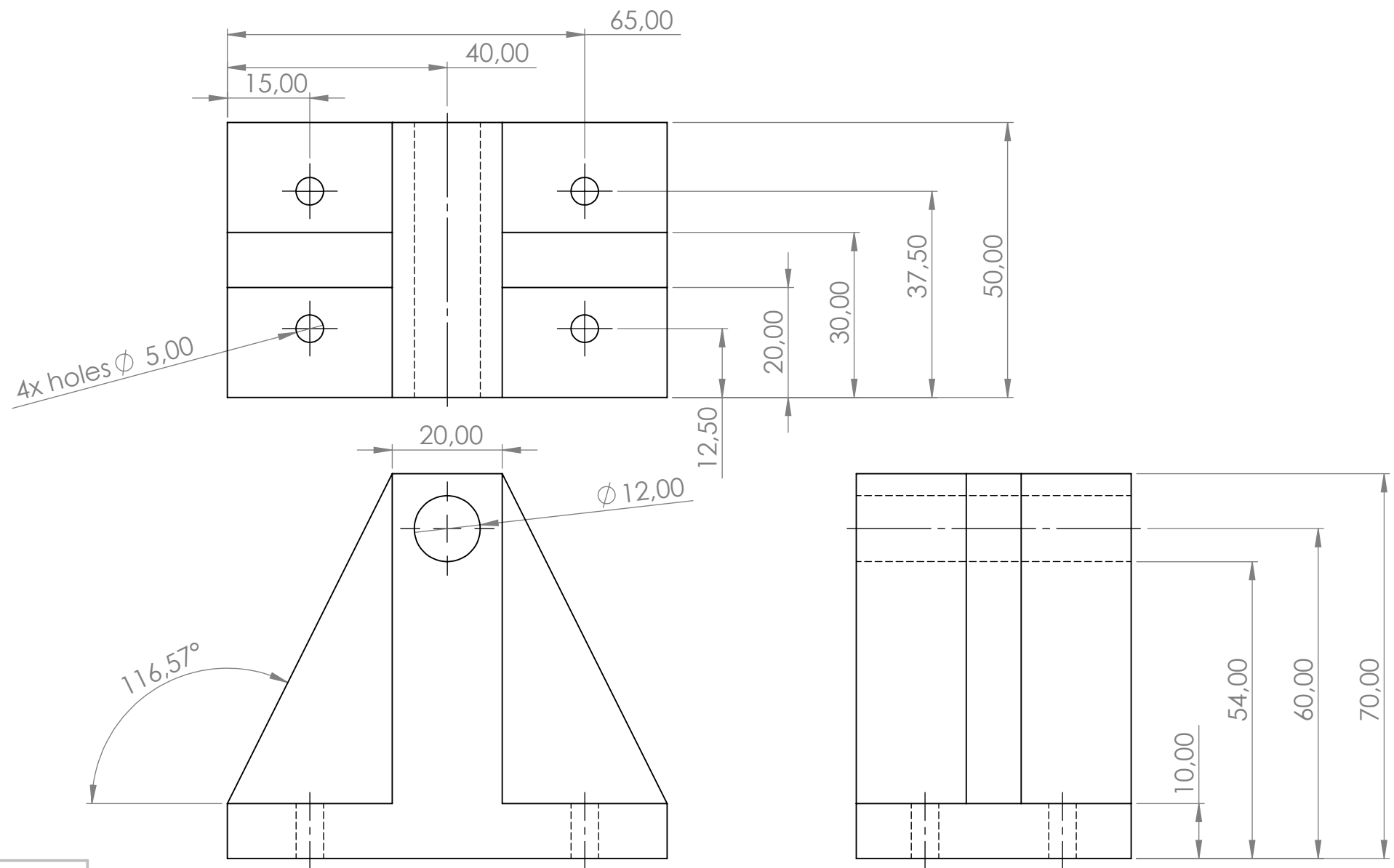
PROJECT: JOINT B BRACKET VARIATION 1

TITLE: DETAILED DRAWING

No.:

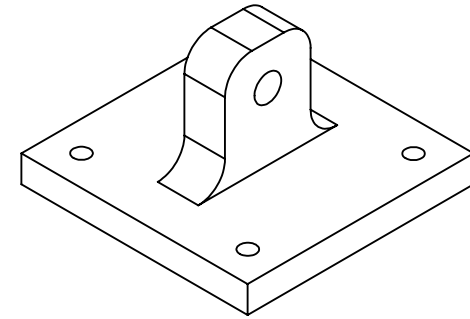
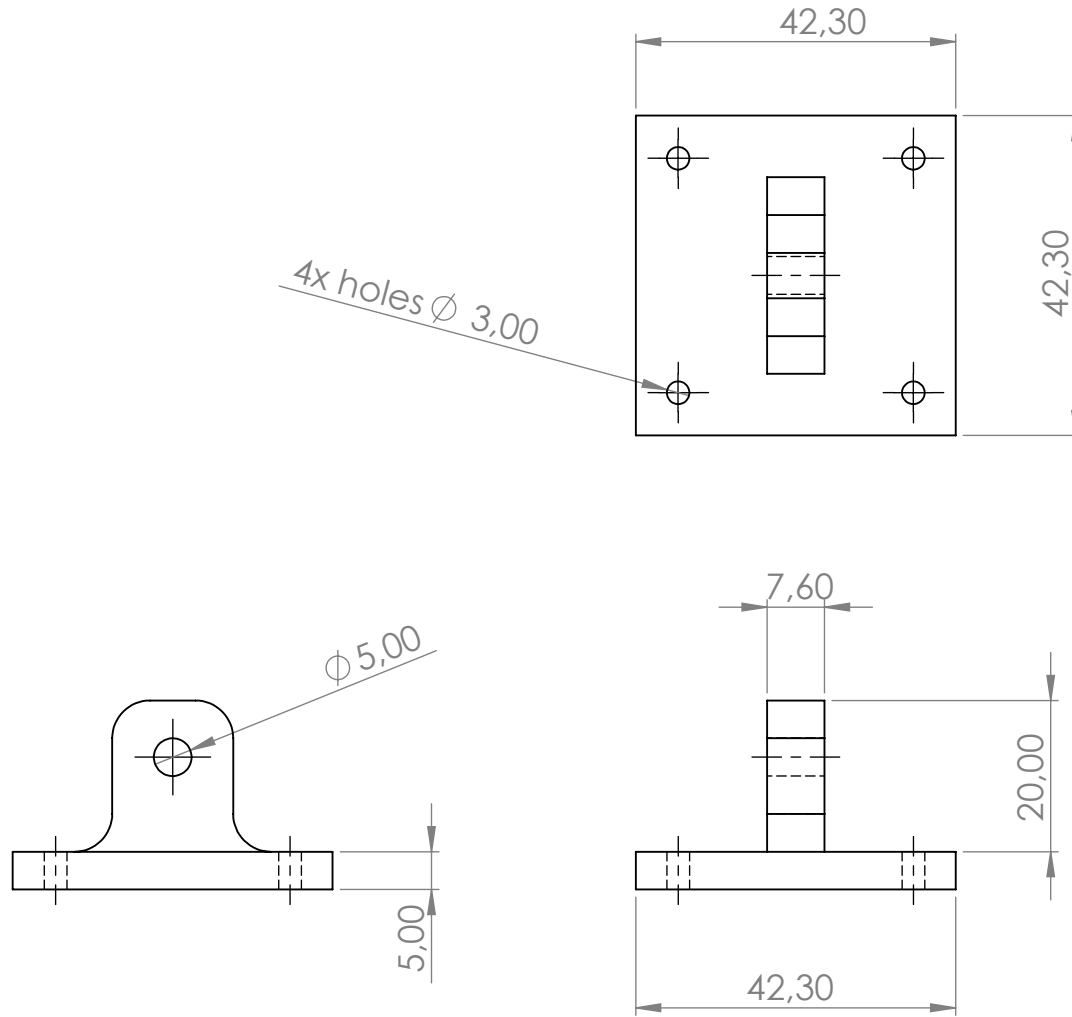
15 / 28





UNLESS OTHERWISE
STATED GENERAL
TOLERANCES : $\pm 0,25$ mm
ANGLES : $\pm 0,25^\circ$

UNIVERSITY OF KWAZULU-NATAL SCHOOL OF ENGINEERING MECHANICAL ENGINEERING	MAT.: PLA PLASTIC		No. REQ.: 1	SCALE: 1:1	UNITS: mm	PROJECT: JOINT B BRACKET VARIATION 2	No.:
		DATE	CHECKED	STUDENT NAME: WESLEY DHARMALINGUM		TITLE: DETAILED DRAWING	16 / 28
	PROJECT SUPERVISOR			STUDENT No.: 209516218			
	WORKSHOP TECHNICIAN			E-MAIL:			
TECHNICAL OFFICER				TEL. No.:			



UNLESS OTHERWISE
STATED GENERAL
TOLERANCES : $\pm 0,25$ mm
ANGLES : $\pm 0,25^\circ$

UNIVERSITY OF KWAZULU-NATAL

SCHOOL OF ENGINEERING

MECHANICAL ENGINEERING

MAT.: PLA PLASTIC

PROJECT SUPERVISOR

WORKSHOP TECHNICIAN

TECHNICAL OFFICER

DATE

No. REQ.: 6

CHECKED

SCALE: 1:1

STUDENT NAME: WESLEY DHARMALINGUM

STUDENT No.: 209516218

E-MAIL:

TEL. No.:

UNITS: mm

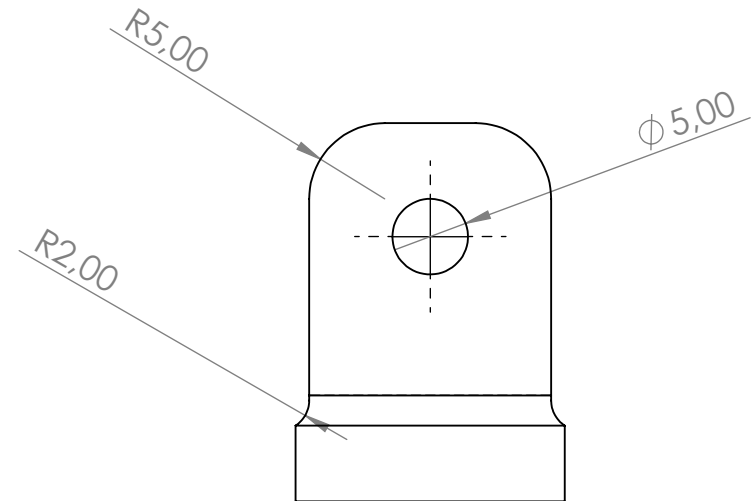
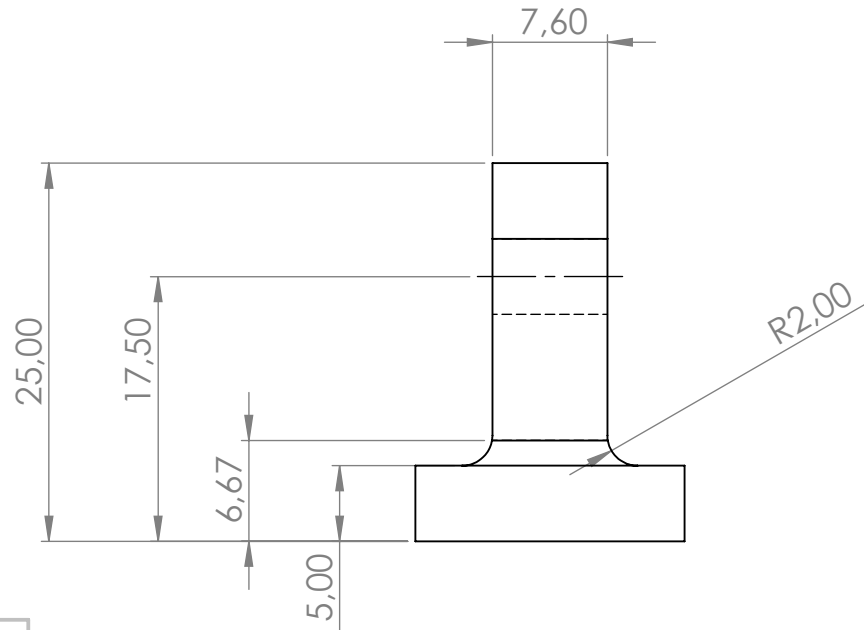
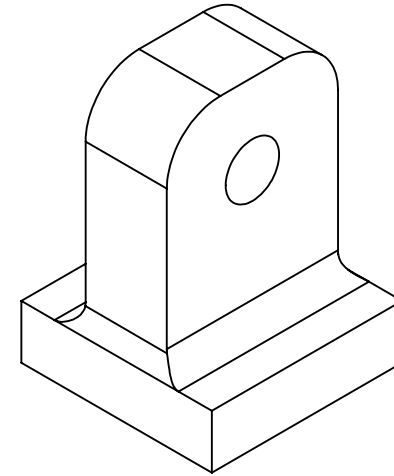
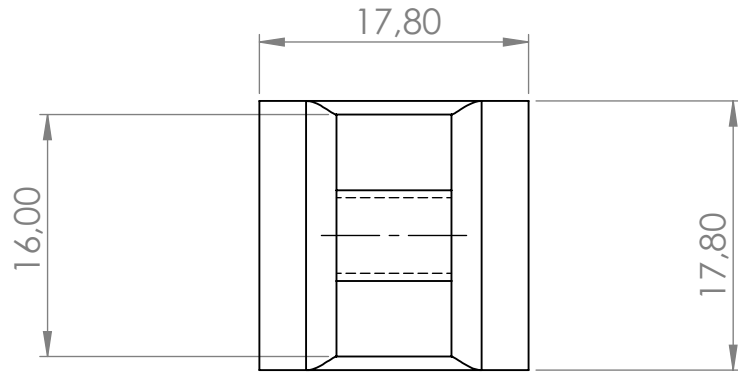
PROJECT: JOINT B PART 2

TITLE: DETAILED DRAWING

No.:

17 / 28





UNLESS OTHERWISE
STATED GENERAL
TOLERANCES : $\pm 0,25$ mm
ANGLES : $\pm 0,25^\circ$

UNIVERSITY OF KWAZULU-NATAL

MAT.: PLA PLASTIC

No. REQ.: 6

SCALE: 2:1

UNITS: mm

PROJECT: JOINT C PART 2

No.:

SCHOOL OF ENGINEERING

PROJECT SUPERVISOR

DATE

CHECKED

STUDENT NAME: WESLEY DHARMALINGUM

18 / 28

MECHANICAL ENGINEERING

WORKSHOP TECHNICIAN

STUDENT No.: 209516218

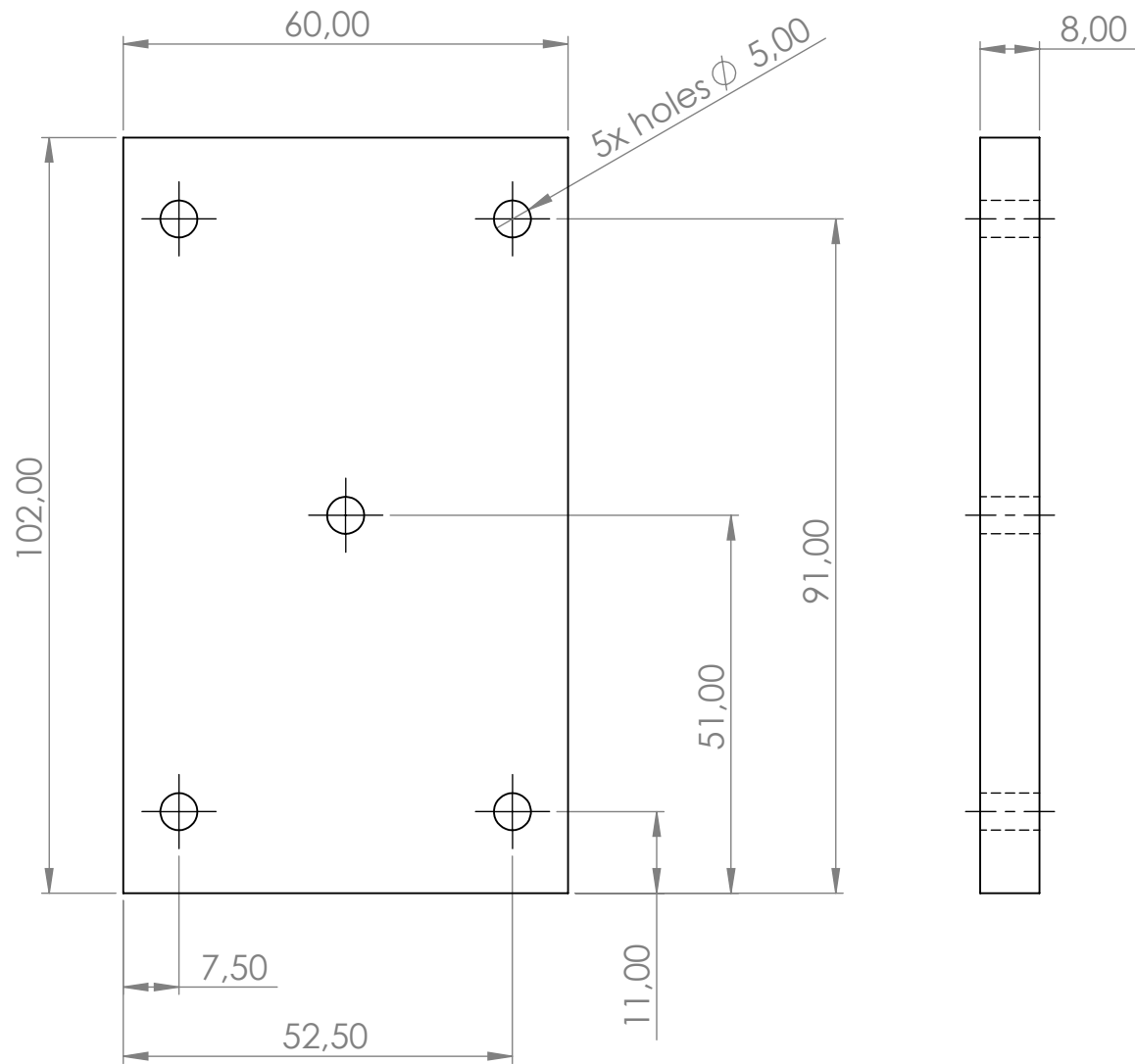
TITLE: DETAILED DRAWING

TECHNICAL OFFICER

E-MAIL:

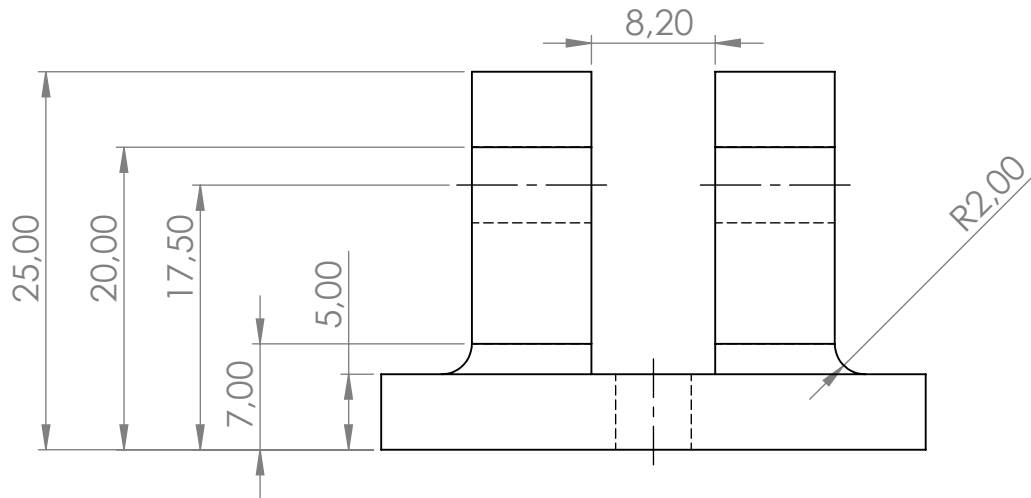
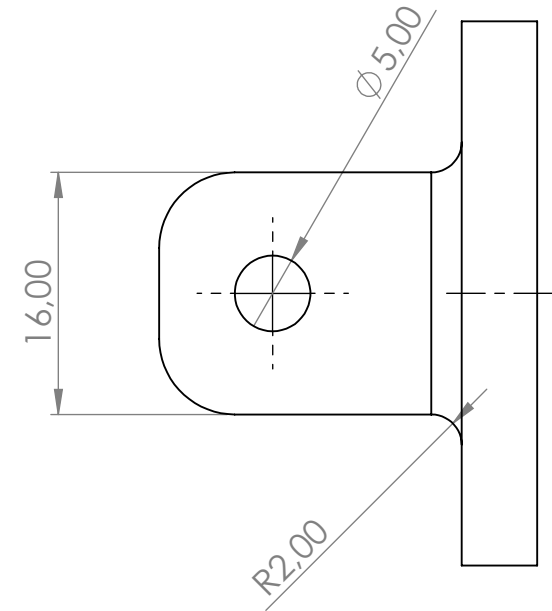
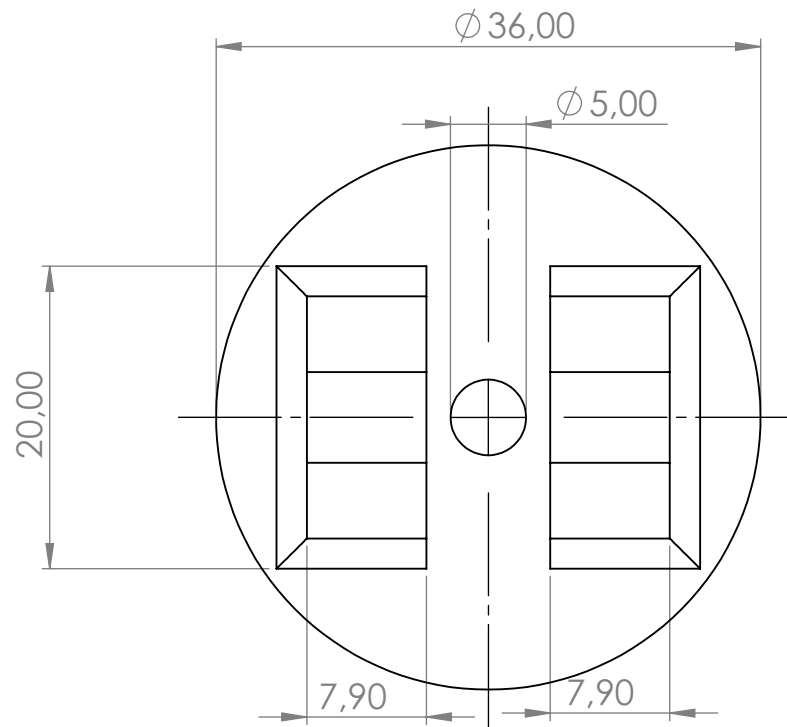
TEL. No.:





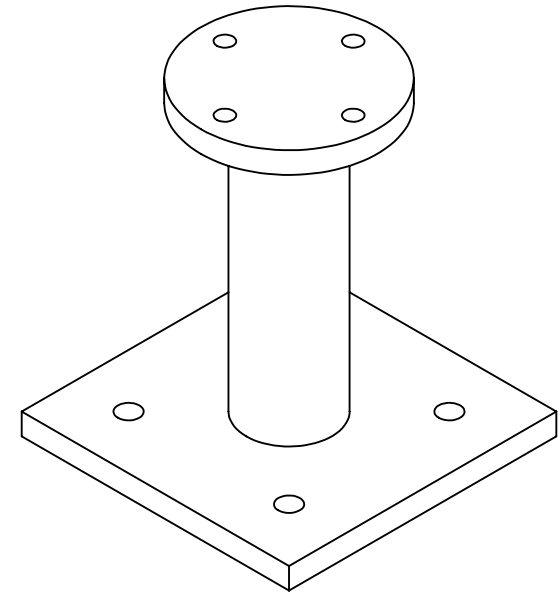
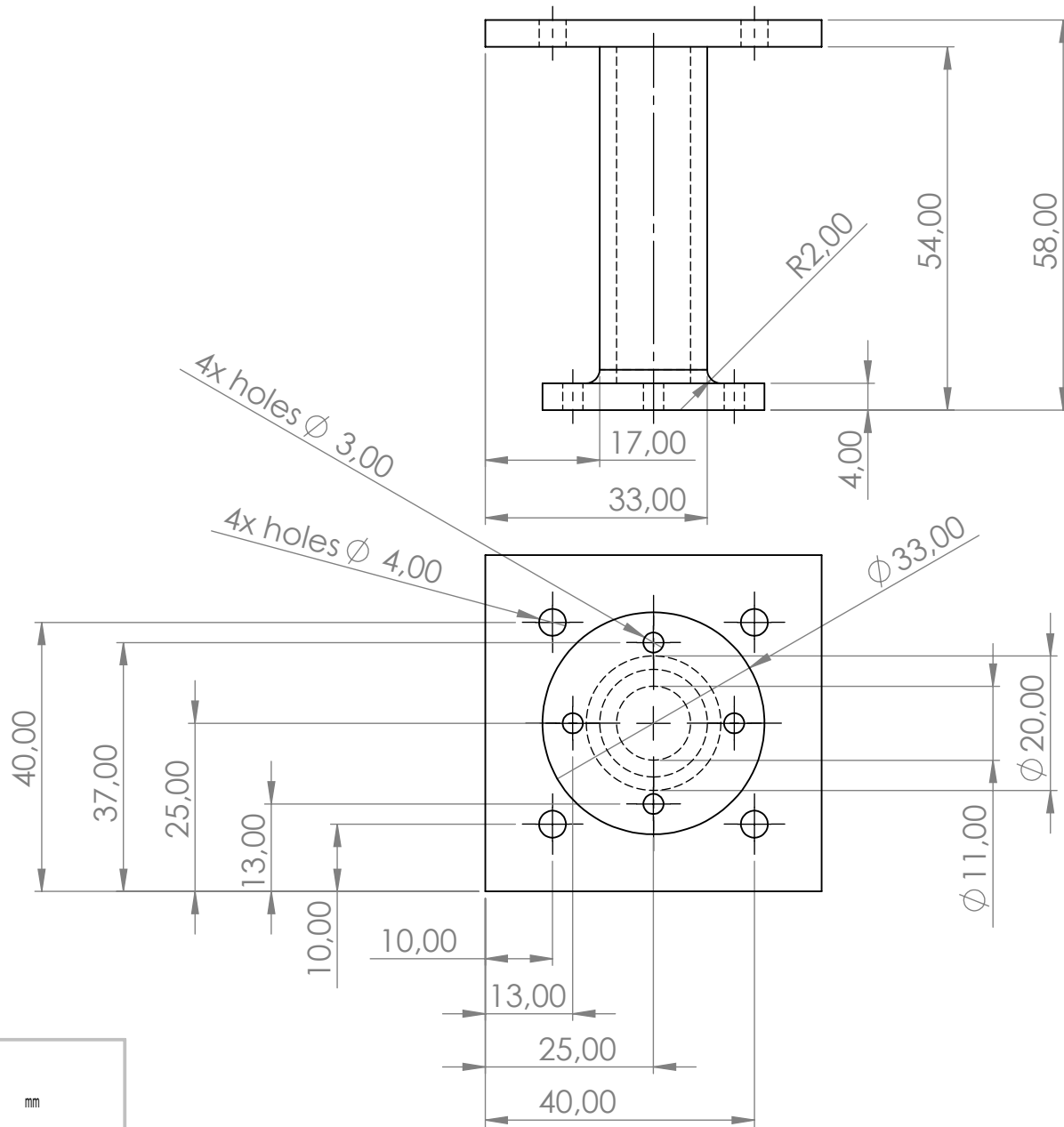
UNLESS OTHERWISE
 STATED GENERAL
 TOLERANCES : $\pm 0,25$ mm
 ANGLES : $\pm 0,25^\circ$

UNIVERSITY OF KWAZULU-NATAL SCHOOL OF ENGINEERING MECHANICAL ENGINEERING	MAT.: PLA PLASTIC	No. REQ.: 2	SCALE: 1:1	UNITS: mm	PROJECT: JOINT D BRACKET	No.:
	DATE	CHECKED	STUDENT NAME: WESLEY DHARMALINGUM			19 / 28
	PROJECT SUPERVISOR		STUDENT No.: 209516218		TITLE: DETAILED DRAWING	
	WORKSHOP TECHNICIAN		E-MAIL:			
TECHNICAL OFFICER			TEL. No.:			



UNLESS OTHERWISE STATED GENERAL TOLERANCES : ± 0.25 mm ANGLES : $\pm 0.25^\circ$

UNIVERSITY OF KWAZULU-NATAL SCHOOL OF ENGINEERING MECHANICAL ENGINEERING	MAT.: PLA PLASTIC	No. REQ.: 2	SCALE: 2:1	UNITS: mm	PROJECT: JOINT D FORKED ATTACHMENT	No.: 20 / 28
	DATE	CHECKED	STUDENT NAME: WESLEY DHARMALINGUM			
	PROJECT SUPERVISOR		STUDENT No.: 209516218		TITLE: DETAILED DRAWING	
	WORKSHOP TECHNICIAN		E-MAIL:			
TECHNICAL OFFICER			TEL. No.:			



UNLESS OTHERWISE
STATED GENERAL
TOLERANCES : ± 0.25 mm
ANGLES : $\pm 0.25^\circ$

UNIVERSITY OF KWAZULU-NATAL

SCHOOL OF ENGINEERING

MECHANICAL ENGINEERING

MAT.: PLA PLASTIC

DATE

PROJECT SUPERVISOR

WORKSHOP TECHNICIAN

TECHNICAL OFFICER

No. REQ.: 1

CHECKED

SCALE: 1:1

STUDENT NAME: WESLEY DHARMALINGUM

STUDENT No.: 209516218

E-MAIL:

TEL. No.:

UNITS: mm

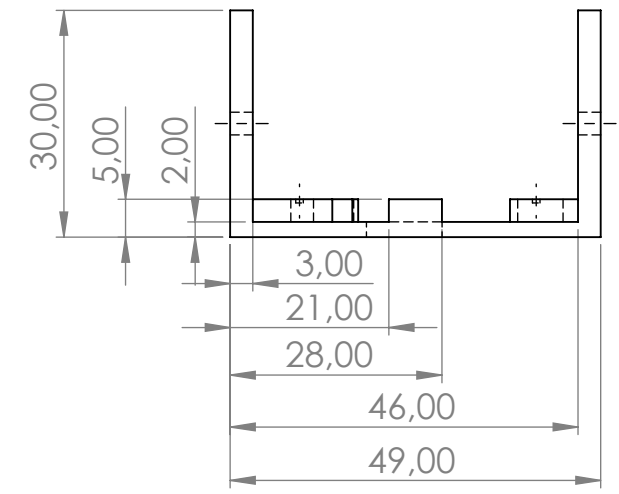
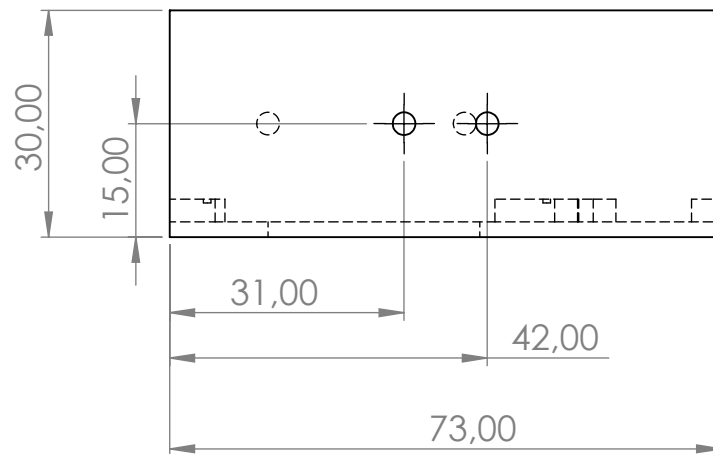
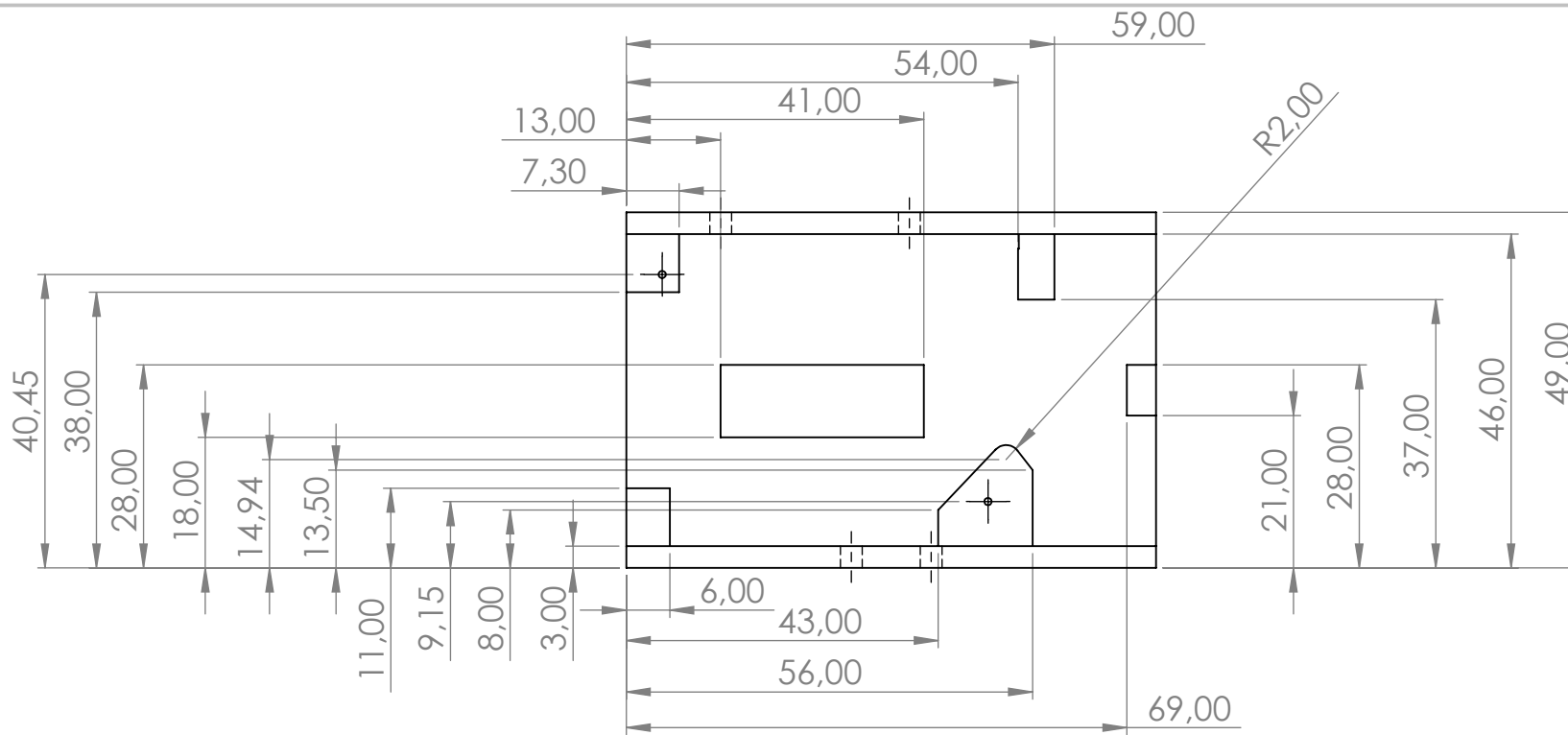
PROJECT: MIRROR MOUNTING BRACKET

TITLE: DETAILED DESIGN

No.:

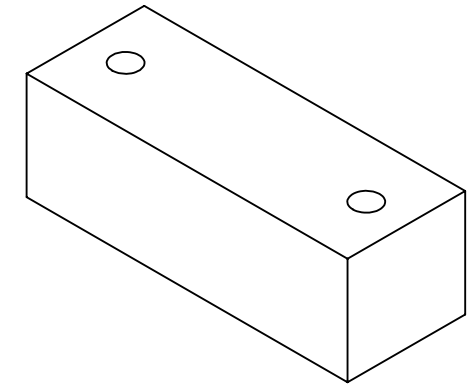
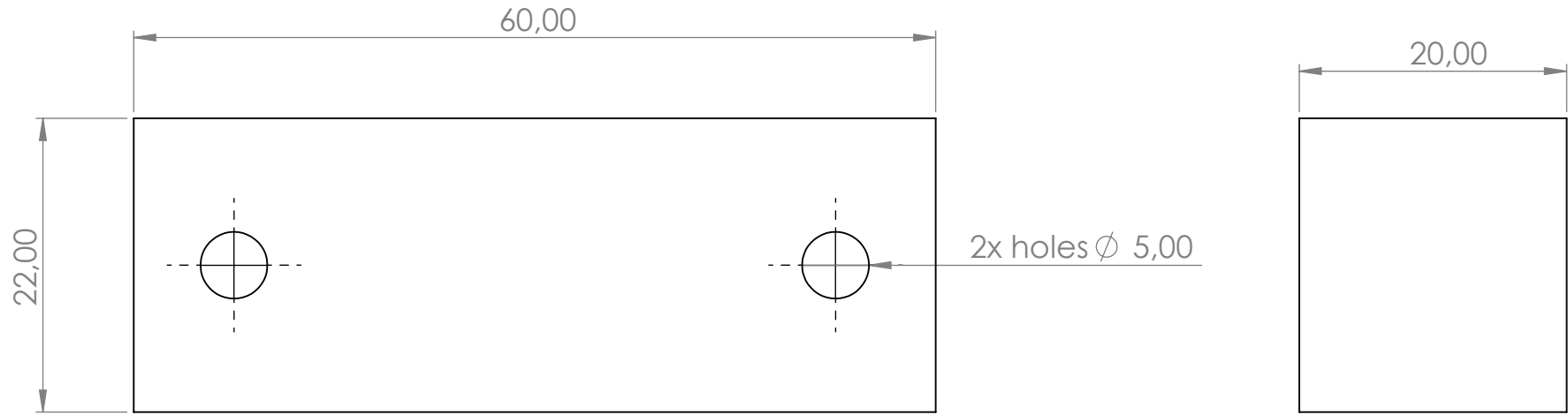
21 / 28





UNLESS OTHERWISE STATED GENERAL TOLERANCES : ± 0,25 mm ANGLES : ± 0,25 °

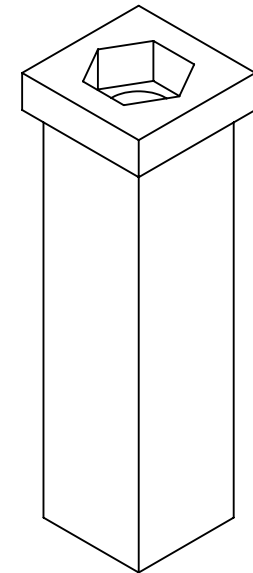
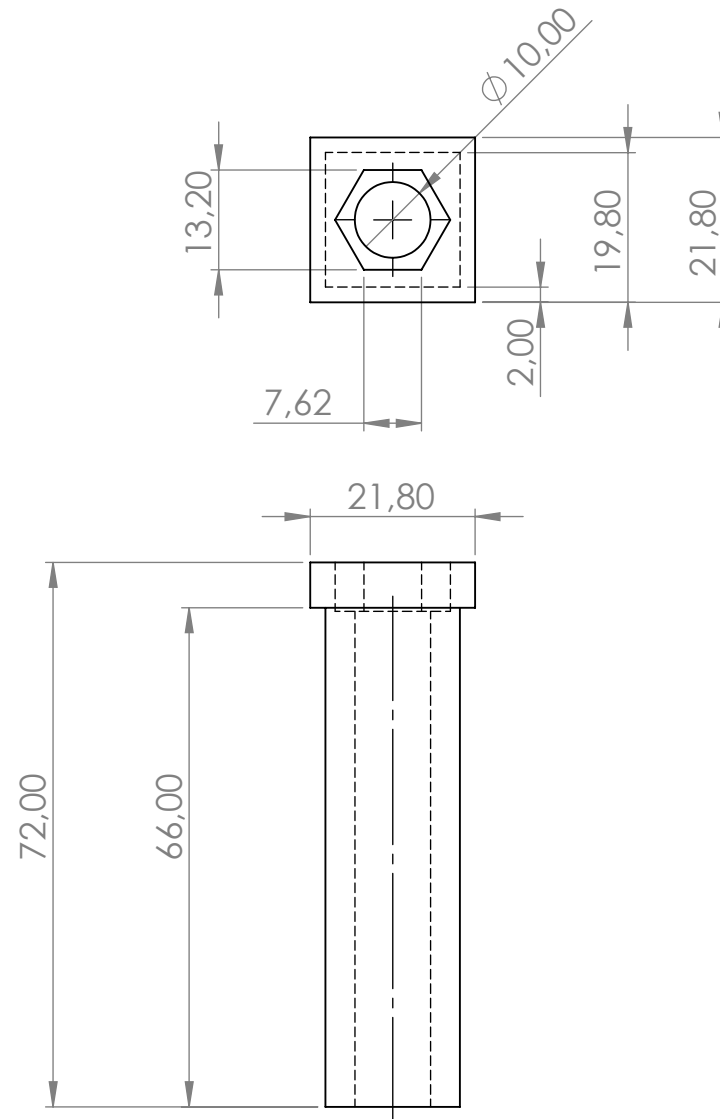
UNIVERSITY OF KWAZULU-NATAL SCHOOL OF ENGINEERING MECHANICAL ENGINEERING	MAT.: PLA PLASTIC	No. REQ.: 2	SCALE: 1:1	UNITS: mm	PROJECT: OCM SENSOR HOUSING PART 1	No.: 22 / 28
	DATE	CHECKED	STUDENT NAME: WESLEY DHARMALINGUM		TITLE: DETAILED DRAWING	
	PROJECT SUPERVISOR		STUDENT No.: 209516218			
	WORKSHOP TECHNICIAN		E-MAIL:			
TECHNICAL OFFICER			TEL. No.:			



ISOMETRIC VIEW
SCALE 1:1

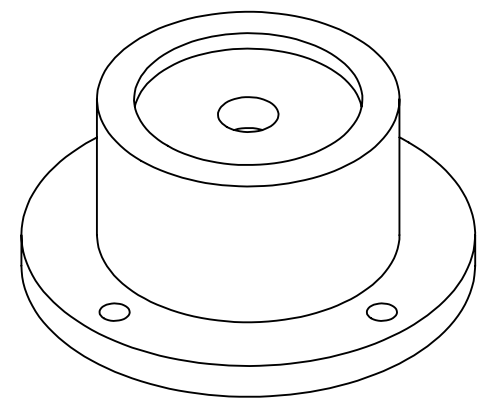
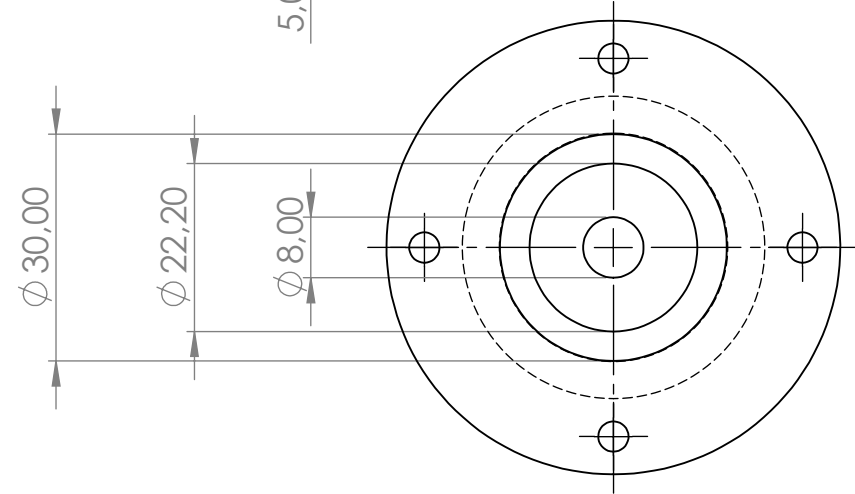
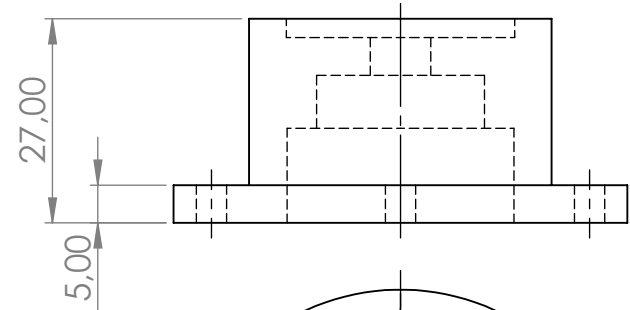
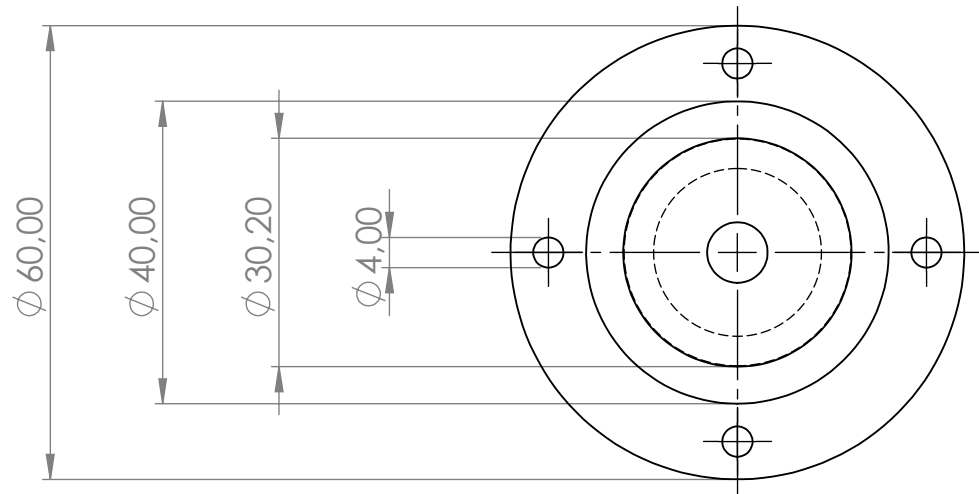
UNLESS OTHERWISE
STATED GENERAL
TOLERANCES : $\pm 0,25$ mm
ANGLES : $\pm 0,25^\circ$

UNIVERSITY OF KWAZULU-NATAL SCHOOL OF ENGINEERING MECHANICAL ENGINEERING	MAT.: PLA PLASTIC		No. REQ.: 4	SCALE: 2:1	UNITS: mm	PROJECT: SPACER	No.:
		DATE	CHECKED	STUDENT NAME: WESLEY DHARMALINGUM			23 / 28
	PROJECT SUPERVISOR			STUDENT No.: 209516218		TITLE: DETAILED DRAWING	
	WORKSHOP TECHNICIAN			E-MAIL:			
TECHNICAL OFFICER			TEL. No.:				



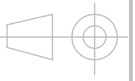
UNLESS OTHERWISE
STATED GENERAL
TOLERANCES : ± 0.25 mm
ANGLES : $\pm 0.25^\circ$

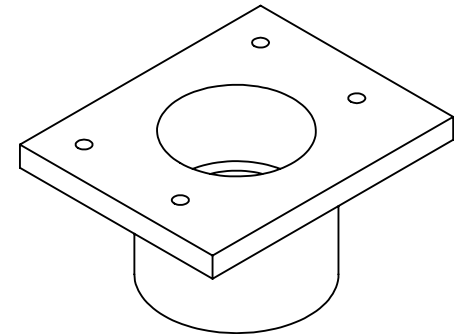
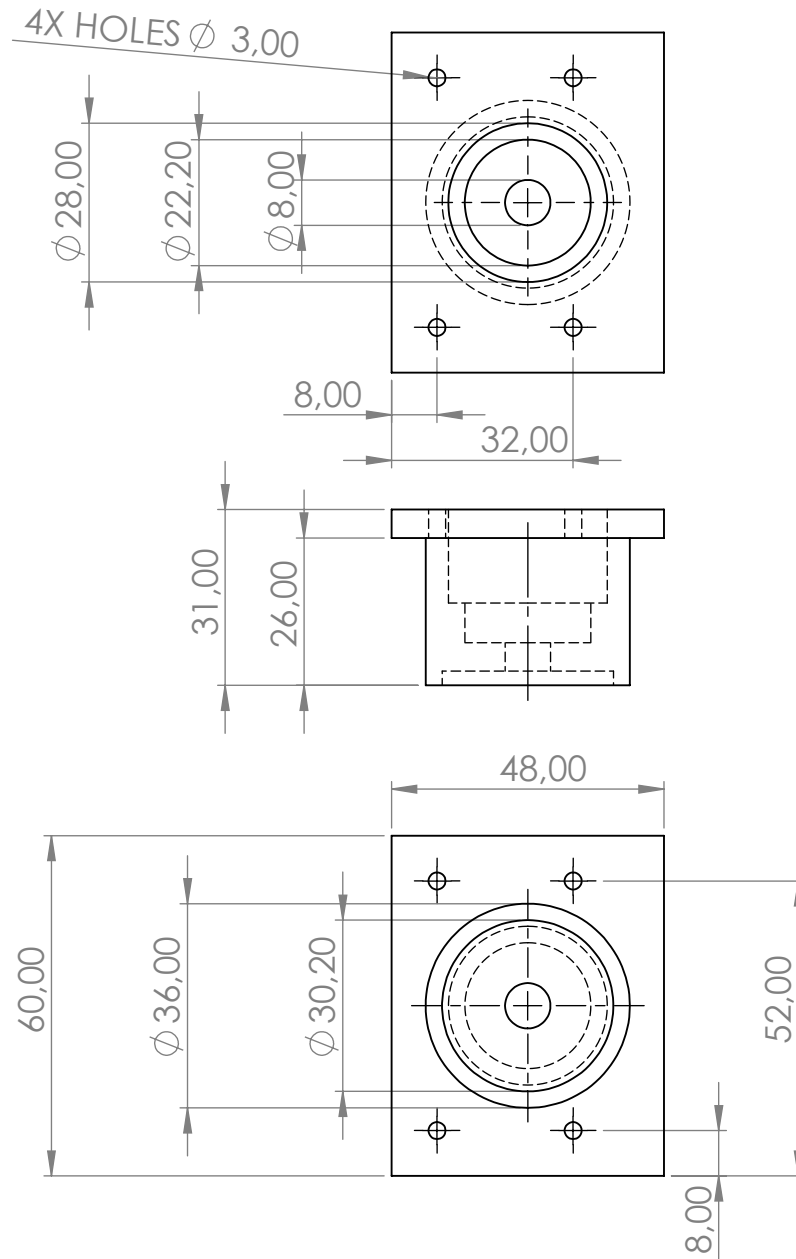
UNIVERSITY OF KWAZULU-NATAL SCHOOL OF ENGINEERING MECHANICAL ENGINEERING	MAT.: PLA PLASTIC		No. REQ.: 6	SCALE: 1:1	UNITS: mm	PROJECT: TELESCOPING ARM	No.:
		DATE	CHECKED	STUDENT NAME: WESLEY DHARMALINGUM			24 / 28
	PROJECT SUPERVISOR			STUDENT No.: 209516218		TITLE: DETAILED DRAWING	
	WORKSHOP TECHNICIAN			E-MAIL:			
TECHNICAL OFFICER				TEL. No.:			



UNLESS OTHERWISE
STATED GENERAL
TOLERANCES : ± 0.25 mm
ANGLES : $\pm 0.25^\circ$

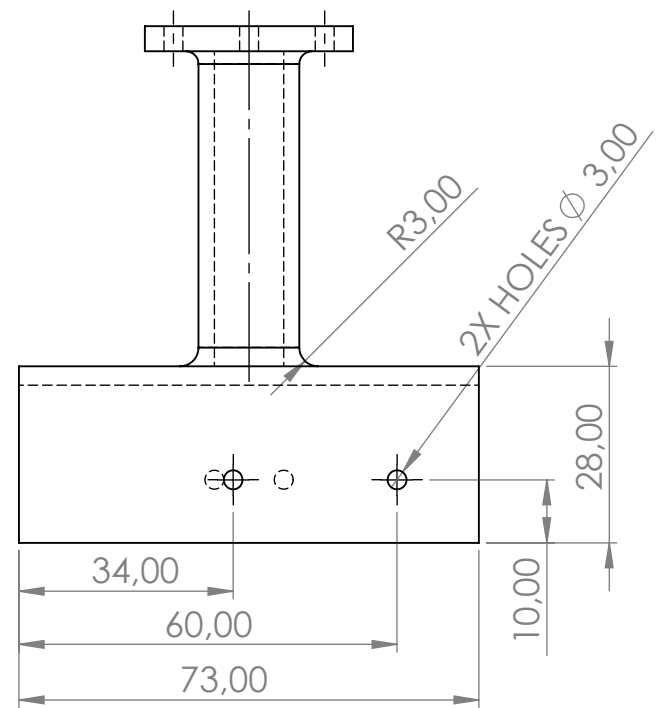
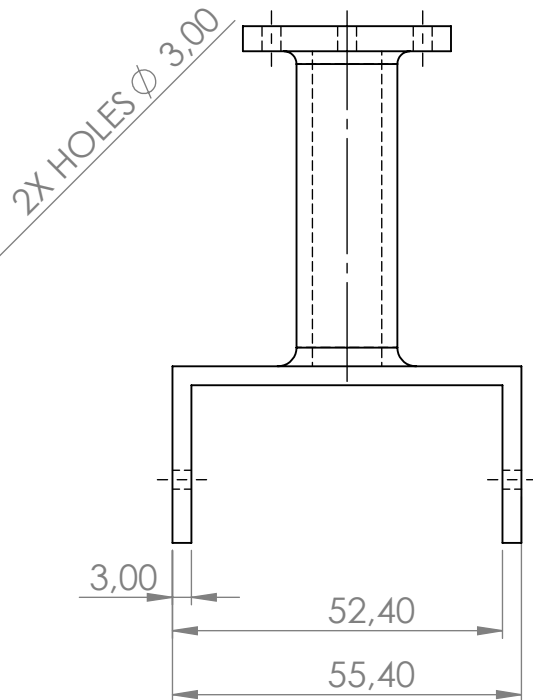
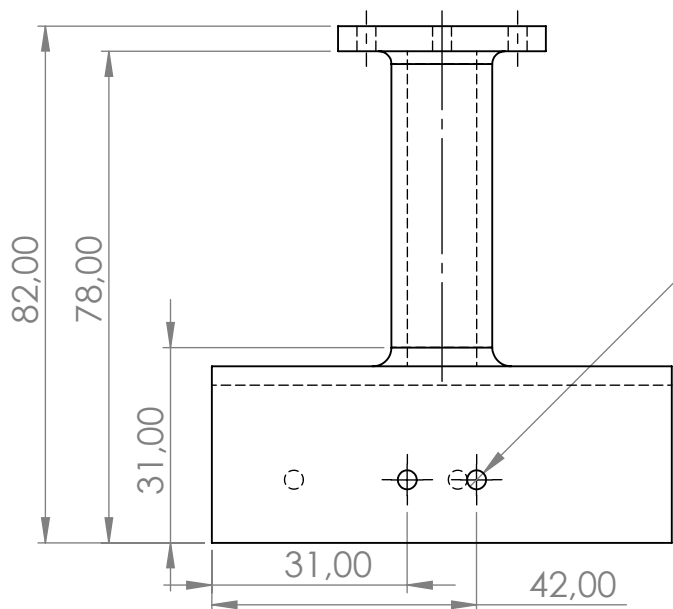
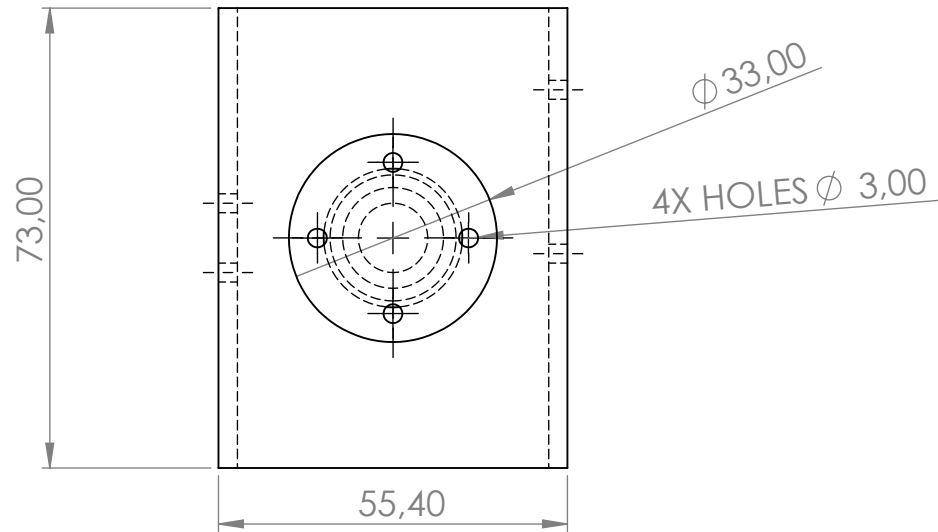
UNIVERSITY OF KWAZULU-NATAL SCHOOL OF ENGINEERING MECHANICAL ENGINEERING	MAT.: PLAPLASTIC	No. REQ.: 2	SCALE: 1:1	UNITS: mm	PROJECT: THRUST BEARING BOTTOM BRACKET	No.: 25 / 28
	DATE	CHECKED	STUDENT NAME: WESLEY DHARMALINGUM			
	PROJECT SUPERVISOR		STUDENT No.: 209516218		TITLE: DETAILED DRAWING	
	WORKSHOP TECHNICIAN		E-MAIL:			
TECHNICAL OFFICER			TEL. No.:			





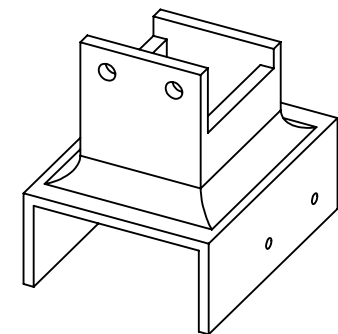
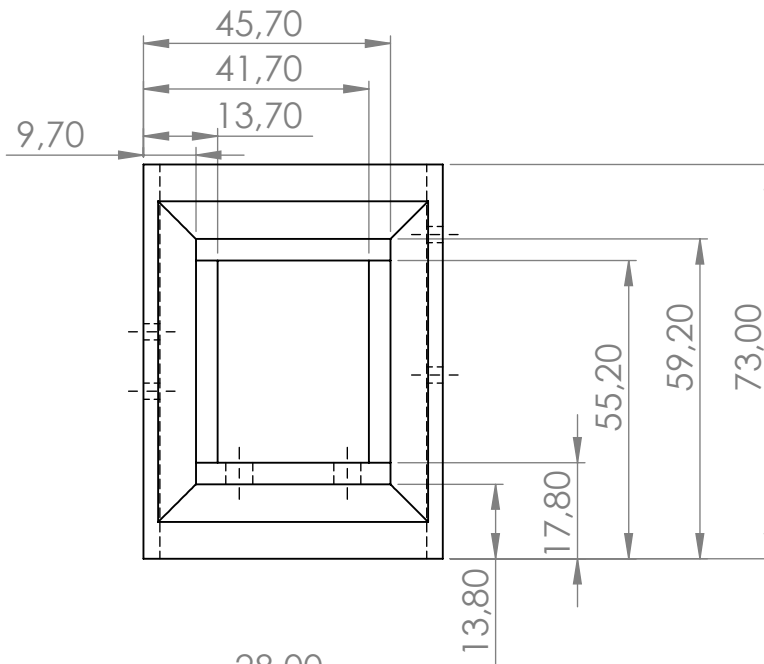
UNLESS OTHERWISE
STATED GENERAL
TOLERANCES : \pm 0,25 mm
ANGLES : \pm 0,25 $^{\circ}$

UNIVERSITY OF KWAZULU-NATAL SCHOOL OF ENGINEERING MECHANICAL ENGINEERING	MAT.: PLA PLASTIC		No. REQ.: 2	SCALE: 0.75 : 1	UNITS: mm	PROJECT: THRUST BEARING TOP BRACKET	No.:
	DATE	CHECKED	STUDENT NAME: WESLEY DHARMALINGUM				TITLE: DETAILED DRAWING
	PROJECT SUPERVISOR		STUDENT No.: 209516218				
	WORKSHOP TECHNICIAN		E-MAIL:				
TECHNICAL OFFICER		TEL. No.:					

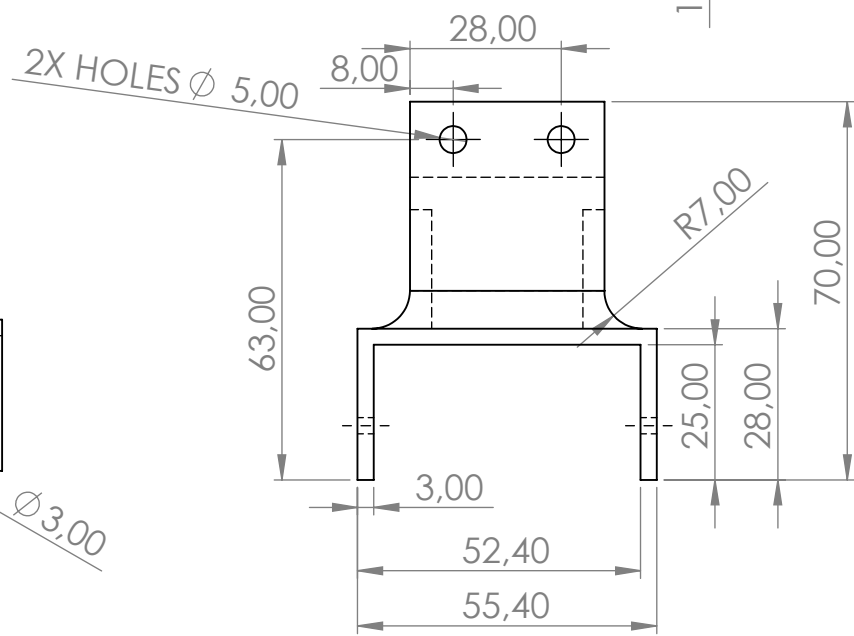
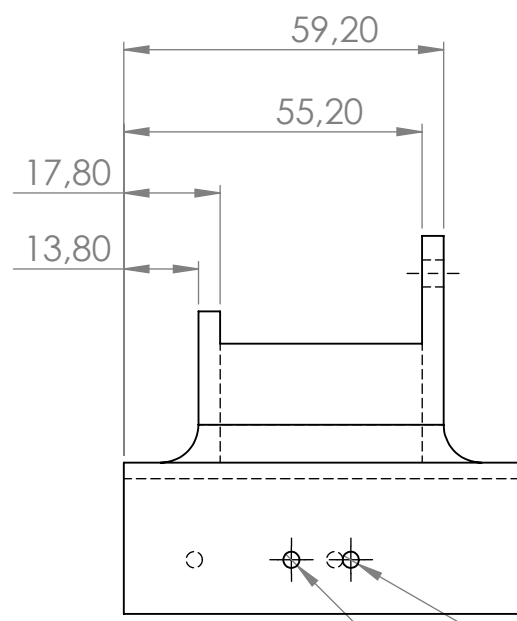


UNLESS OTHERWISE
STATED GENERAL
TOLERANCES : $\pm 0,25$ mm
ANGLES : $\pm 0,25^\circ$

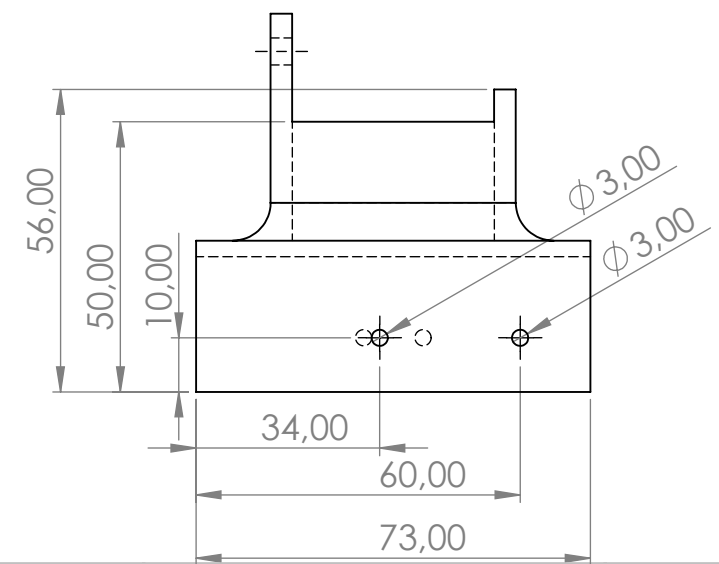
UNIVERSITY OF KWAZULU-NATAL	MAT.: PLA PLASTIC		No. REQ.: 1	SCALE: 1:1.2	UNITS: mm	PROJECT: XY OCM SENSOR HOUSING PART 2	No.: 27 / 28
	SCHOOL OF ENGINEERING	DATE	CHECKED	STUDENT NAME: WESLEY DHARMALINGUM			
MECHANICAL ENGINEERING	PROJECT SUPERVISOR			STUDENT No.: 209516218		TITLE: DETAILED DRAWING	
	WORKSHOP TECHNICIAN			E-MAIL:			
	TECHNICAL OFFICER			TEL. No.:			



ISOMETRIC VIEW
SCALE 1:2



2X HOLES ϕ 5,00



UNLESS OTHERWISE
STATED GENERAL
TOLERANCES : \pm 0,25 mm
ANGLES : \pm 0,25 °

UNIVERSITY OF KWAZULU-NATAL SCHOOL OF ENGINEERING MECHANICAL ENGINEERING	MAT.: PLA PLASTIC	No. REQ.: 1	SCALE: 1:1.4	UNITS: mm	PROJECT: Z OCM SENSOR HOUSING PART 2	No.: 28 / 28
	DATE	CHECKED	STUDENT NAME: WESLEY DHARMALINGUM			
	PROJECT SUPERVISOR		STUDENT No.: 209516218		TITLE: DETAILED DRAWING	
	WORKSHOP TECHNICIAN		E-MAIL:			
TECHNICAL OFFICER			TEL. No.:			